

# Fast ion generation with ICRF waves and beams in the Wendelstein 7-X stellarator

Présentée le 11 mai 2023

Faculté des sciences de base  
SPC - Théorie  
Programme doctoral en physique

pour l'obtention du grade de Docteur ès Sciences

par

**Mike MACHIELSEN**

Acceptée sur proposition du jury

Prof. V. Savona, président du jury  
Prof. J. Graves, directeur de thèse  
Dr D. van Eester, rapporteur  
Dr J. Geiger, rapporteur  
Dr S. Coda, rapporteur



*“It is faster to make a four-inch mirror  
then a six-inch mirror  
than to make a six-inch mirror.”*  
- Bill McKeeman -





# Abstract

The largest operating stellarator, Wendelstein 7-X, is of the quasi-isodynamic type. For this design to scale up to a fusion reactor, several criteria must be met, one of them being good fast ion confinement. The latter still has to be tested experimentally, preferably before actually building a reactor. To this end fast ions have to be generated in present day machines. W7-X can use radio waves in the ICRF and neutral beams, the effectiveness of both is assessed in this work using the SCENIC package, combining the three different codes: VMEC (magnetic equilibrium), LEMan (full-wave) and VENUS-LEVIS (particle orbit following), used iteratively to find a self-consistent steady state. The propagation of radio waves in a plasma is described by Maxwell's equations, combined with the linearised Vlasov equation. Since these equations combine to form a linear time-invariant system, the natural approach is to solve the problem in the frequency domain. The main difficulty stems from the fact that the induced charges and currents are a non-local functional of the electric field. To address this problem directly, a new expression is derived for this constitutive relation in configuration space, and the resulting dielectric kernel is applied to mode conversion in simplified geometry. Such advanced wave physics is beyond the needs of heating schemes usually considered for tokamaks and stellarators, so it is reasonable that the full wave code LEMan has a number of approximations. Despite this LEMan is nevertheless capable of modelling minority, three-ion and synergetic RF-NBI heating schemes in 3D, now with the addition of hot plasma effects. Standard minority heating does produce fast ions in W7-X, but in limited quantities because the enhanced perpendicular velocity leads to a significant amount of trapped particles. These are lost far more rapidly in W7-X than in a tokamak. One way to remedy this is by instead accelerating ions that are born from the neutral beam. These particles are already fast, but under the right conditions their energy is increased considerably, which lends confidence in future fast ion generation experiments in W7-X.

**Key words:** Stellarator, tokamak, hot plasma, ICRH, ICRF, radio frequency, radio waves, full-wave, NBI, neutral beams, plasma heating, fast ions



## Résumé

Le plus grand stellarator en service, le Wendelstein 7-X, est de type quasi-isodynamique. Pour que cette conception puisse être transposée en réacteur de fusion, plusieurs critères doivent être remplis, l'un d'entre eux étant un bon confinement des ions rapides. Ce dernier doit encore être testé expérimentalement, de préférence avant la construction d'un réacteur. À cette fin, des ions rapides doivent être générés dans des machines actuelles. W7-X peut utiliser des ondes radio dans l'ICRF et des faisceaux neutres. L'efficacité des deux est évaluée dans ce travail à l'aide du paquet SCENIC, qui combine les trois différents codes : VMEC (équilibre magnétique), LEMan (pleine onde) et VENUS-LEVIS (suivi d'orbite de particules), utilisés de manière itérative pour trouver un état stable autoconsistant. La propagation des ondes radio dans un plasma est décrite par les équations de Maxwell, combinées à l'équation de Vlasov linéarisée. Comme ces équations se combinent pour former un système linéaire invariant dans le temps, l'approche naturelle consiste à résoudre le problème dans le domaine des fréquences. La principale difficulté provient du fait que les charges et les courants induits sont une fonction non locale du champ électrique. Pour aborder ce problème directement, une nouvelle expression est dérivée pour cette relation constitutive dans l'espace de configuration, et le noyau diélectrique résultant est appliqué à la conversion de mode dans une géométrie simplifiée. Une physique ondulatoire aussi avancée dépasse les besoins des schémas de chauffage généralement considérés pour les tokamaks et les stellarators, il est donc raisonnable que le code d'onde complet LEMan comporte un certain nombre d'approximations. Malgré cela, LEMan est néanmoins capable de modéliser en 3D des schémas de chauffage minoritaire, à trois ions et synergique RF-NBI, en y ajoutant maintenant les effets de plasma chaud. Le chauffage minoritaire standard produit des ions rapides dans W7-X, mais en quantités limitées car la vitesse perpendiculaire accrue entraîne une quantité importante de particules piégées. Celles-ci sont perdues beaucoup plus rapidement dans le W7-X que dans un tokamak. Une façon de remédier à ce problème est d'accélérer plutôt les ions qui naissent du faisceau neutre. Ces particules sont déjà rapides, mais dans les bonnes conditions leur énergie est considérablement augmentée, ce qui donne confiance dans les futures expériences de génération d'ions rapides dans W7-X.

**Mots clés :** Stellarator, tokamak, hot plasma, ICRH, ICRF, radio frequency, radio waves, full-wave, NBI, neutral beams, plasma heating, fast ions



# Acronyms

**CDF:** Cumulative Distribution Function  
**DOF:** Degree Of Freedom  
**ELD:** Electron Landau Damping  
**FEM:** Finite Element Method  
**FLR:** Finite Larmor Radius  
**HFS:** High Field Side  
**IBW:** Ion Bernstein Wave  
**ICRF:** Ion Cyclotron Range of Frequencies  
**ICRH:** Ion Cyclotron Resonance Heating  
**ITER:** International Thermonuclear Experimental Reactor  
**JET:** Joint European Torus  
**LCFS:** Last Closed Flux Surface  
**LFS:** Low Field Side  
**LHS:** Left Hand Side  
**MHD:** Magnetohydrodynamics  
**MPI:** Message Passing Interface  
**NBI:** Neutral Beam Injection  
**ODE:** Ordinary Differential Equation  
**PDE:** Partial Differential Equation  
**PDF:** Plasma Dispersion Function  
**QI:** Quasi-isodynamic  
**RF:** Radio Frequency  
**RHS:** Right Hand Side  
**SD:** Slowing Down  
**TTMP:** Transit Time Magnetic Pumping  
**u.p.t.:** Unperturbed trajectory  
**W7-X:** Wendelstein 7-X



# Contents

<b>Abstract (English/Français)</b>	<b>i</b>
<b>Acronyms</b>	<b>v</b>
<b>1 Introduction</b>	<b>1</b>
1.1 Tokamak and stellarator . . . . .	1
1.2 Fast ion generation . . . . .	3
1.3 Thesis contribution . . . . .	3
1.4 Outline . . . . .	4
<b>2 ICRF physics</b>	<b>5</b>
2.1 Maxwell equations . . . . .	5
2.1.1 Potential formulation . . . . .	6
2.1.2 Boundary conditions . . . . .	7
2.2 Constitutive relation . . . . .	8
2.2.1 Linearised Vlasov equation . . . . .	8
2.2.2 Dielectric tensor . . . . .	12
2.2.3 Bi-Maxwellian . . . . .	16
2.3 Cold plasma . . . . .	19
2.3.1 Dispersion relation . . . . .	19
2.3.2 ICRH schemes . . . . .	22
2.4 LEMan . . . . .	25
2.4.1 Weak form . . . . .	25
2.4.2 Optimisations for axisymmetry . . . . .	27
2.4.3 Mode families . . . . .	27
2.5 SCENIC . . . . .	28
2.6 Summary . . . . .	29
<b>3 Configuration space conductivity kernel</b>	<b>31</b>
3.1 Inverse Fourier transform . . . . .	32
3.1.1 Transform perpendicular direction . . . . .	34
3.1.2 Transform parallel direction . . . . .	35
3.1.3 Explicit form of the configuration space kernel . . . . .	38
3.2 Application in 1D . . . . .	40

## Contents

---

3.3	Hierarchical matrices . . . . .	43
3.4	Summary . . . . .	45
<b>4</b>	<b>Applications of the hot plasma dielectric tensor</b>	<b>47</b>
4.1	Distribution functions . . . . .	47
4.1.1	Maxwellian and its variations . . . . .	47
4.1.2	Marker distribution function . . . . .	51
4.2	Derivation of the dielectric tensor . . . . .	53
4.2.1	Modified bi-Maxwellian . . . . .	53
4.2.2	Marker distribution . . . . .	58
4.3	Comparison of plasma models using axisymmetric JET-like geometry . . . . .	60
4.4	LEMan runs for W7-X . . . . .	66
4.5	Full SCENIC runs in JET . . . . .	71
4.6	Summary . . . . .	74
<b>5</b>	<b>Combined RF-NBI heating</b>	<b>75</b>
5.1	Neutral beam injection . . . . .	75
5.1.1	NBI model . . . . .	76
5.1.2	Limitations of the NBI model . . . . .	78
5.1.3	NBI deposition in W7-X . . . . .	79
5.1.4	Slowing down distribution . . . . .	82
5.2	Monte Carlo operators . . . . .	84
5.2.1	Coulomb collisions . . . . .	84
5.2.2	Anomalous diffusion . . . . .	87
5.2.3	Wave-particle interaction . . . . .	89
5.3	Model difficulties with combined RF-NBI . . . . .	91
5.4	RF-NBI results W7-X . . . . .	92
5.4.1	Wave field . . . . .	93
5.4.2	Fast ions . . . . .	99
5.5	Discussion . . . . .	102
5.6	Summary . . . . .	103
<b>6</b>	<b>Conclusion &amp; summary</b>	<b>105</b>
6.1	Future work . . . . .	106
6.1.1	ICRF waves . . . . .	106
6.1.2	Fast ions . . . . .	106
<b>A</b>	<b>Appendix</b>	<b>109</b>
A.1	Metric tensor . . . . .	109
A.2	Bessel functions . . . . .	111
A.3	Plasma dispersion function . . . . .	112
A.3.1	Hilbert transform . . . . .	113



A.3.2 Generalised plasma dispersion function . . . . .	114
A.4 Hot plasma dispersion relation . . . . .	116
A.5 Expressions H functions . . . . .	117
A.6 Expressions S functions . . . . .	119
A.7 Modified bi-Maxwellian coefficients . . . . .	120
A.7.1 Warm plasma limit LFS . . . . .	120
A.8 Marker distribution coefficients . . . . .	123
A.9 Future ICRH models . . . . .	126
<b>Acknowledgements</b>	<b>129</b>
<b>Bibliography</b>	<b>137</b>
<b>Curriculum Vitae</b>	<b>139</b>



# 1 Introduction

Nuclear fusion is the process in which atomic nuclei are merged together to form heavier nuclei. Based on the mass difference between the reactants and products this reaction either consumes or releases energy. For example, the fusion of hydrogen is what powers the sun (mainly the proton-proton chain to be precise), which releases net energy. Scientists and engineers have sought to replicate this process on earth, with the aim of harnessing this power.

Controlled thermonuclear fusion requires the fuel to be confined long enough so that it can fuse. Different techniques exist to achieve this in the laboratory, some notable ones listed below (examples in parentheses):

- Electrical confinement (fusor, polywell)
- Inertial confinement (laser beams, Z pinch)
- Magnetic confinement (mirror, cusp, tokamak, stellarator)

The sun uses gravitational confinement, which is omitted from the list as it obviously cannot be used in the lab. In addition, the proton-proton fusion is not necessarily optimal for the use in a reactor. Fusion of deuterium and tritium (heavy hydrogen isotopes) is a more attractive reaction because of its large fusion cross section. Moreover, magnetic confinement fusion experiments require a temperature of about 150 million Kelvin<sup>1</sup>, roughly ten times the temperature in the core of the sun.

## 1.1 Tokamak and stellarator

The most mature of the above techniques is arguably the tokamak, which uses a set of electromagnets to produce, together with the plasma current, a helical magnetic field confining the plasma. A purely toroidal magnetic field would be simpler, but the resulting particle

---

<sup>1</sup>Using the Lawson criterion the minimal fusion triple product is found at a thermal energy of about 14 keV.

## Introduction

---

drift leads to charge accumulation. This would eventually generate an  $\mathbf{E} \times \mathbf{B}$  drift that kills the plasma. Some amount of poloidal field is essential for plasma confinement because it effectively short-circuits the top and bottom of the plasma, preventing charge accumulation. In order to generate this field, the tokamak requires a toroidal plasma current. This is driven by the central solenoid, which acts as a transformer inducing a loop voltage. However, the induced current comes at a price: the device cannot operate in steady state, as it requires a continuous current ramp in the central solenoid. Steady state operation is desirable for a power plant, but running in pulsed mode should still enable electricity production. Also, it is possible to overcome this limitation by maximizing bootstrap current, a current generated by the plasma itself [1, section 4.9], and using non-inductive current drive. Fully non-inductive operation has already been demonstrated in practice, see e.g. [2]. However, such auxiliary current drive is expensive (in terms of Amperes driven per Watt) [3, section 6.8]. But there is another issue with the tokamak design, this induced current is a source of MHD instabilities [4], [5]. Even when it isn't a source, the large current makes disruptions potentially more damaging to the first wall; the induced current can lead to runaway electrons during plasma disruption.

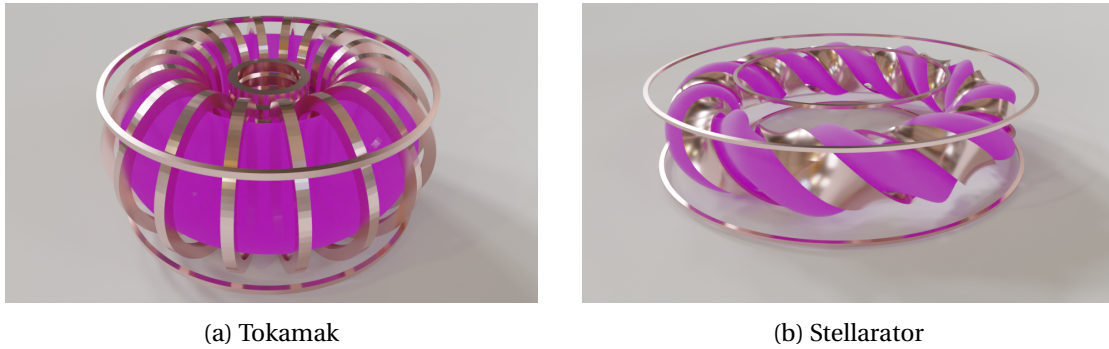


Figure 1.1: Simplified illustration of two magnetic confinement devices. The coils wrap around the plasma, shown in pink.

The stellarator design aims to sidestep these problems by using a special geometry that inherently produces the desired, steady state, helical magnetic field, see Fig. 1.1. Stellarators typically have little to no net toroidal plasma current. But the trade-off is added complexity. Also there are concerns regarding the fast ion confinement. Due to the axisymmetry of a tokamak trapped ions are well confined because their orbits are closed when projected onto the poloidal plane. I.e., if it was not for collisions, the ions would return to where they started. This is a very desirable feature because in a burning plasma the fusion alphas will need to be confined long enough to transfer their energy to the bulk plasma before being lost.

Stellarators are not axisymmetric, but they can have hidden symmetries. So called quasi-axisymmetric or quasi-helical configurations exploit a symmetry in Boozer coordinates (specific magnetic coordinates) that results in constant longitudinal adiabatic invariant on flux surfaces. This implies that the net radial drift almost vanishes over one bounce period, re-

sulting in good particle confinement. Wendelstein 7-X (W7-X) takes a different approach: It too aims for constant longitudinal adiabatic invariant on flux surfaces, but without using a quasi-symmetry. Its configuration follows from a different type of optimisation, known as a quasi-isodynamic (QI) design [6].

But it is challenging to find the optimal configuration to all the design criteria [7], [8]. One of them being fast ion confinement, which is much better than in previous Wendelstein machines, but not yet perfect [9]. The design of W7-X is an approximation of QI; it aims to minimise radial drift of trapped particles over many bounce periods. Some trapped particles however, are rapidly lost [10].

## 1.2 Fast ion generation

Proper confinement of fast ions in QI configurations still has to be demonstrated experimentally. But this has to be done already in current devices, as it is vital for the design of a future stellarator reactor. Since W7-X is not a reactor, the fast ions have to be generated via auxiliary means. In some respects these can then be used to mimic fusion alphas. W7-X can make use of NBI (neutral beam injection), which provides ions that are already fast by birth. The proton injection energy is 55 keV, with some protons coming from the dissociation of  $H_2^+$ / $H_3^+$ , and thus having one half/third that energy.

Waves in the ion cyclotron range of frequencies (ICRF) are another approach to generate fast ions. These waves are launched from an antenna inside the vacuum vessel and propagate into the plasma until a certain resonance condition is met. In order to have good wave polarisation, some small amount of impurities are often added to the plasma, called minority heating. It is this small population that usually absorbs most of the power, leading to not just bulk plasma heating, but also the generation of a fast ion population, with typically greatly enhanced perpendicular velocities. It is furthermore possible to combine these two techniques in what is called the RF-NBI scheme, which has some attractive properties compared to using only NBI or only RF (section 5.4).

## 1.3 Thesis contribution

The main goal of this thesis is to study the effectiveness of various approaches in terms of plasma heating and fast ion generation capabilities, using large scale simulations. The primary difficulty with these simulations is that different aspects of the physics couple together: The magnetic equilibrium, the perturbations in the electromagnetic fields, the beam deposition and the fast ion distribution function are all linked in a non-trivial way<sup>2</sup>. Over the years different tools have been developed to model each of these areas in isolation. But, given that

---

<sup>2</sup>This list could be expanded to include the plasma profiles of the majority species (affected by transport), antenna coupling, and edge effects such as the plasma sheath and eddy currents in the wall. However, that is beyond the scope of this work.

the time scales relating to these various physical phenomena are distinct, the models can be strung together and solved iteratively in order to find a self-consistent solution.

One particularly challenging aspect is the RF wave modelling; the plasma is inhomogeneous, anisotropic and 3D. Moreover, the dielectric response is non-local. To this end a considerable portion of this thesis is dedicated to improving the understanding of the plasma's dielectric properties, contained in the dielectric tensor (or conductivity tensor). Studying this in configuration space instead of the usual Fourier space provides new insight and modelling options.

In addition, the beams and/or ICRF waves are known to produce non-Maxwellian species. In order to capture the effects of these species on wave propagation, polarisation and absorption in the simulation, new dielectric tensors have to be derived and implemented. These need to include finite Larmor radius (FLR) effects in order to accurately predict the power deposition in a hot plasma.

Finally, using this knowledge and code upgrades, the capability of generating fast ions in W7-X using beams and ICRF waves is assessed.

## 1.4 Outline

This thesis consists of four main parts: in chapter 2 the physics of radio waves is discussed. A brief description of the primary software tools is given as well, including the full-wave code LEMan and SCENIC. A highly detailed derivation of the dielectric properties of the plasma is also presented in chapter 2, since it will be needed in the novel results and development of chapter 3. Most of the RF modelling in this thesis (chapters 4, 5) was done with LEMan, and like many other full-wave codes it uses a description of the dielectric tensor derived in Fourier space. It may however be better to use an expression for this tensor in configuration space, as this works well with the finite element method. To this end such an expression is derived from first principles in chapter 3, and it is applied to mode conversion.

For the purpose of investigating the relevant schemes in W7-X, mode conversion is estimated to play a minor role. Hence, LEMan is a suitable choice of full-wave code for the last chapters of this thesis, especially since it is already integrated in SCENIC. Nevertheless, some of the relevant heating schemes involve higher harmonic heating. So in order to more accurately resolve the physics of a hot plasma, it was found necessary to upgrade LEMan, see chapter 4. Several test cases for both tokamaks and stellarators are also presented in chapter 4. Besides radio wave heating, NBI provides another way to generate fast ions. These two mechanisms can also work together synergetically, as explained in chapter 5, with application to W7-X. In order to realise these simulations a few key upgrades to the VENUS-LEVIS code had to be implemented, which include the addition of a radial diffusion model. Lastly, chapter 6 concludes this thesis and provides some ideas for further work.

## 2 ICRF physics

Ion cyclotron resonance heating (ICRH) is a common auxiliary heating method in magnetic confinement fusion. It exploits the resonance where the driving frequency, i.e. that of an antenna, matches that of the rapid gyro motion of the ions (or any of its harmonics). Not all particles are accelerated equally, which typically leads to enhanced fast ion tails. In order to understand this behaviour extensive modelling is used. This starts with solving Maxwell's equations. The main difficulty stems from the constitutive relation, which is the equation relating the induced plasma current to a given electric field. This relation is complicated, and non-local in nature. Substitution into Maxwell's equations results in an integro-differential problem.

This chapter revisits basic plasma wave theory, which lays the groundwork for the next chapter. In addition, the cold limit is investigated which helps to understand what makes a good ICRH scheme. Lastly, the main software tools are introduced.

### 2.1 Maxwell equations

Maxwell's equations in SI units are as follows:

$$\nabla \cdot \mathbf{E} = \rho / \epsilon_0 \quad (2.1a)$$

$$\nabla \cdot \mathbf{B} = 0 \quad (2.1b)$$

$$\nabla \times \mathbf{E} = -\frac{\partial \mathbf{B}}{\partial t} \quad (2.1c)$$

$$\nabla \times \mathbf{B} = \mu_0 \mathbf{J} + \frac{1}{c^2} \frac{\partial \mathbf{E}}{\partial t}. \quad (2.1d)$$

With  $\mathbf{E}$  the electric field,  $\mathbf{B}$  the magnetic field,  $\rho$  the charge density and  $\mathbf{J}$  the current density. Taking the curl of Faraday's law, and substituting in Ampere's law yields the following double curl equation:

$$\nabla \times (\nabla \times \mathbf{E}) + \frac{1}{c^2} \frac{\partial^2 \mathbf{E}}{\partial t^2} = -\mu_0 \frac{\partial \mathbf{J}}{\partial t}, \quad (2.2)$$

which in the frequency domain can be written as follows:

$$\nabla \times (\nabla \times \mathbf{E}) - \frac{\omega^2}{c^2} \mathbf{E} - i\mu_0\omega \mathbf{J}_p = i\mu_0\omega \mathbf{J}_{ant}. \quad (2.3)$$

Equation (2.2) (or (2.3)) is advantageous compared to the original Maxwell's equations because it gives an expression which can be solved to obtain  $\mathbf{E}$ , without explicitly needing  $\mathbf{B}$  and  $\rho$ . However, this equation permits spurious solutions in addition to the real solution [11]. See section 2.1.1 for further discussion.

The current density consists of a contribution due to the antenna, plus the plasma response:

$$\mathbf{J} = \mathbf{J}_{ant} + \mathbf{J}_p. \quad (2.4)$$

The antenna current  $\mathbf{J}_{ant}$  is something the experimentalist controls, a “free” current, hence it is assumed to be a given function of position <sup>1</sup>. The plasma response  $\mathbf{J}_p$  is often referred to as the plasma current, not to be confused with the steady state plasma current required by the corresponding MHD-equilibrium. The latter is an equilibrium quantity, while  $\mathbf{J}_p$  oscillates with frequency  $\omega$ . This plasma current depends on  $\mathbf{E}$  via the constitutive relation, see Eq. (2.30) in section 2.2. Thus Maxwell's equations must be solved self-consistently with the plasma response. This is guaranteed by substituting the constitutive relation into Eq. (2.2), or (2.3) for the frequency domain.

### 2.1.1 Potential formulation

As mentioned before, the double curl equation Eq. (2.3) permits additional, non-physical solutions. This is because its solution does not necessarily satisfy all of Maxwell's equations; the divergence equations cannot just be ignored [11]. Leaving this untreated is dangerous because increasing the mesh resolution does not guarantee convergence to the exact solution. This is sometimes referred to as “numerical pollution”, and has been studied thoroughly in the past (in the context of wave modelling see e.g. [12]–[16]). Many techniques have been developed to deal with this issue, the one adopted by LEMan is to solve for the potentials, instead of the electric field [17]:

$$\nabla^2 \mathbf{A} - c^{-2} \partial_t^2 \mathbf{A} - \nabla (\nabla \cdot \mathbf{A} + c^{-2} \partial_t \phi) = -\mu_0 \mathbf{J} \quad (2.5a)$$

$$\nabla^2 \phi + \partial_t \nabla \cdot \mathbf{A} = -\rho / \epsilon_0, \quad (2.5b)$$

using the vector Laplacian  $\nabla^2 \mathbf{a} = \nabla (\nabla \cdot \mathbf{a}) - \nabla \times (\nabla \times \mathbf{a})$ . The fields are recovered using

$$\mathbf{E} = -\nabla \phi - \partial_t \mathbf{A}$$

$$\mathbf{B} = \nabla \times \mathbf{A}.$$

---

<sup>1</sup>Ignoring here the complicated eddy currents that may be induced in the antenna.



Recall that  $\nabla \cdot (\nabla \times \mathbf{A}) = 0$  and  $\nabla \times \nabla \phi = \mathbf{0}$  are general vector identities, so Eqs. (2.1b) and (2.1c) are automatically satisfied. Hence, a solution to Eqs. (2.5) inherently satisfies all four of the original Maxwell equations (Eqs. (2.1)).

Using the Coulomb gauge, and switching to the frequency domain gives:

$$\nabla^2 \mathbf{A} + \omega^2 c^{-2} \mathbf{A} + i\omega c^{-2} \nabla \phi + \mu_0 \mathbf{J}_p = -\mu_0 \mathbf{J}_{ant} \quad (2.6a)$$

$$\nabla^2 \phi - i\omega \nabla \cdot \mathbf{A} + \varepsilon_0^{-1} \rho_p = -\varepsilon_0^{-1} \rho_{ant}. \quad (2.6b)$$

This Coulomb formulation is also used by the PENN code [15]. The numerical pollution is eliminated as long as the gauge condition is satisfied. The divergence of  $\mathbf{A}$  is retained in Eq. (2.6b) because the two equations combine to give

$$\nabla^2 (\nabla \cdot \mathbf{A}) = 0. \quad (2.7)$$

To derive this take the divergence of Eq. (2.6a), add  $-i\omega/c^2$  times Eq. (2.6b) and use charge conservation ( $i\omega \rho = \nabla \cdot \mathbf{J}$ ). Equation (2.7) is simply the Laplace equation for  $\nabla \cdot \mathbf{A}$  with homogeneous Dirichlet BCs. If the gauge is enforced on the boundary of the domain, it will be satisfied in the interior as well<sup>2</sup>. A downside of using the potential formulation is that we have to deal with four variables instead of three, so the number of degrees of freedom in the model will be increased, compared to solving for just the electric field.

### 2.1.2 Boundary conditions

In order to solve Maxwell's equations in the bounded domain, they must be supplemented by boundary conditions. The metal wall marks the model boundary<sup>3</sup>, which is assumed to be a perfectly electric conductor (PEC). This means that the electric field rapidly decays in strength as it penetrates into the wall. From the interface conditions for electromagnetic fields we know that the component of  $\mathbf{E}$  tangent to the wall is continuous, so it must be zero at the interface. More explicitly,

$$\mathbf{E} \times \mathbf{n}_w = \mathbf{0}, \quad (2.8)$$

with  $\mathbf{n}_w$  the normal vector of the wall. No boundary condition is needed for the normal component  $\mathbf{E} \cdot \mathbf{n}_w$ , the weak form of the boundary value problem already has a unique solution. See [18, section 4.6] for a proof. The condition from Eq. (2.8) will be satisfied by imposing  $\mathbf{A} \times \mathbf{n}_w = \mathbf{0}$  and  $\phi = 0$  on the wall. In conclusion the boundary conditions for the potentials are:

$$\nabla \cdot \mathbf{A} = 0, \quad \mathbf{A} \times \mathbf{n}_w = \mathbf{0}, \quad \phi = 0. \quad (2.9)$$

Note that due to the choice of coordinates in LEMan, there is an additional “boundary” at the magnetic axis, see [17] for more details.

<sup>2</sup>Of course the approximate numerical solution will not perfectly satisfy  $\nabla \cdot \mathbf{A} = 0$ , however this procedure ensures it is minimised along with the residual.

<sup>3</sup>In this work the boundary is furthermore assumed to be located at the LCFS, so the SOL is not treated.

## 2.2 Constitutive relation

The relevant equations and boundary conditions to construct a full-wave code have been defined in the previous section. However, one piece of information is still missing, the constitutive relation, which links  $\rho_p, \mathbf{J}_p$  to the electric field. The goal of this section is deriving such a relation. Note, this material is mostly based on [19, section 4.3] and [20].

### 2.2.1 Linearised Vlasov equation

The desired quantities  $\rho_p, \mathbf{J}_p$  are moments of the perturbed distribution function. So in order to find a constitutive relation, let us start with the non-relativistic Vlasov equation:

$$\frac{df}{dt} = \frac{\partial f}{\partial t} + \mathbf{v} \cdot \nabla f + \frac{q}{m} (\mathbf{E} + \mathbf{v} \times \mathbf{B}) \cdot \nabla_v f = 0, \quad (2.10)$$

with  $f$  the distribution function,  $t$  time,  $\mathbf{v}$  the velocity,  $q$  the charge of the particle and  $m$  the mass. Note, we are merely interested in the periodic state which sets in after the transient of the antenna initialisation has died down. This requires the wave to bounce around the machine several times which typically takes a few antenna periods. Because of this separation of time scales,  $\omega \gg \omega_{coll}$ , it is justified to neglect the contribution of collisions, which would normally appear on the RHS in Eq. (2.10). In addition, relativistic effects are neglected. The distribution function cannot change significantly on the time scale  $1/\omega$ , therefore it is also justified to linearise<sup>4</sup> Eq. (2.10) about the unperturbed variables  $f_0, \mathbf{E}_0, \mathbf{B}_0$ :

$$\begin{aligned} f &= f_0 + f_1 \\ \mathbf{E} &= \mathbf{E}_1 \\ \mathbf{B} &= \mathbf{B}_0 + \mathbf{B}_1. \end{aligned}$$

Note, for simplicity any background (zeroth-order) electric field is ignored. To zeroth-order, the Vlasov equation reads:

$$\left. \frac{df_0}{dt} \right|_{u.p.t.} = \frac{\partial f_0}{\partial t} + \mathbf{v} \cdot \nabla f_0 + \frac{q}{m} (\mathbf{v} \times \mathbf{B}_0) \cdot \nabla_v f_0 = 0, \quad (2.11)$$

where u.p.t. stands for unperturbed trajectory, indicating that this is the solution where the “perturbations”  $\mathbf{E}_1, \mathbf{B}_1$  are absent. This trajectory is described by the following set of ODEs:

$$\begin{aligned} \frac{d\mathbf{r}}{dt} &= \mathbf{v} \\ \frac{d\mathbf{v}}{dt} &= \frac{q}{m} (\mathbf{v} \times \mathbf{B}_0). \end{aligned} \quad (2.12)$$

---

<sup>4</sup>In MHD it is common to linearise also the fluid velocity. However, here  $\mathbf{v}$  represents the velocity of a particle, not that of the fluid. So there is no such thing as the zeroth-order velocity  $\mathbf{v}_0$ , it is an independent phase-space coordinate, hence  $\mathbf{v}$  is not linearised.

As  $f_0$  is the steady state solution,  $\partial f_0 / \partial t = 0$ . If it is furthermore a homogeneous plasma,  $\nabla f_0 = \mathbf{0}$ , so that

$$(\mathbf{v} \times \mathbf{B}_0) \cdot \nabla_v f_0 = 0. \quad (2.13)$$

Note that in right-handed cylindrical coordinates (perpendicular velocity, gyro angle, parallel velocity),  $(v_\perp, \phi, v_\parallel)$ :

$$\nabla_v f = \frac{\partial f}{\partial v_\perp} \mathbf{e}_{v_\perp} + \frac{1}{v_\perp} \frac{\partial f}{\partial \phi} \mathbf{e}_\phi + \frac{\partial f}{\partial v_\parallel} \mathbf{e}_{v_\parallel} \quad (2.14)$$

so  $(\mathbf{v} \times \mathbf{B}_0) \cdot \nabla_v f_0 = -B_0 \frac{\partial f_0}{\partial \phi}$ . Which means Eq. (2.13) leads to

$$\frac{\partial f_0}{\partial \phi} = 0. \quad (2.15)$$

Of course, a different coordinate system could have been chosen, e.g.  $(v_\perp, v_\parallel, \phi)$  which does not have the minus sign in front of  $B_0$ , but the conclusion is the same. The steady state background distribution function is isotropic in gyro-angle.

Going back to the more general case of an inhomogeneous  $f_0$ , Eq. (2.10) reads to first order:

$$\begin{aligned} \frac{df}{dt} = & \underbrace{\frac{\partial f_1}{\partial t} + \mathbf{v} \cdot \nabla f_1 + \frac{q}{m} \mathbf{v} \times \mathbf{B}_0 \cdot \nabla_v f_1}_{=df_1/dt|_{u.p.t.}} + \underbrace{\frac{q}{m} (\mathbf{E}_1 + \mathbf{v} \times \mathbf{B}_1) \cdot \nabla_v f_1}_{\text{2nd order, so } \approx 0} \\ & + \underbrace{\frac{\partial f_0}{\partial t} + \mathbf{v} \cdot \nabla f_0 + \frac{q}{m} \mathbf{v} \times \mathbf{B}_0 \cdot \nabla_v f_0}_{=df_0/dt|_{u.p.t.}=0} + \frac{q}{m} (\mathbf{E}_1 + \mathbf{v} \times \mathbf{B}_1) \cdot \nabla_v f_0 = 0. \end{aligned} \quad (2.16)$$

But this can be refactored using the definition of the u.p.t. This is a powerful tool, the perturbed trajectory requires  $\mathbf{E}_1, \mathbf{B}_1$ , the very thing we are trying to solve for in the end. Clearly, we do not yet have this information, but the only thing that remains in Eq. (2.16) is the total derivative of  $f_1$  along the u.p.t. This only requires zeroth-order quantities, which are assumed to be known

$$\left. \frac{df_1}{dt} \right|_{u.p.t.} = -\frac{q}{m} (\mathbf{E}_1 + \mathbf{v} \times \mathbf{B}_1) \cdot \nabla_v f_0. \quad (2.17)$$

This can be solved using the method of characteristics,

$$f_1(\mathbf{r}, \mathbf{v}, t) = -\frac{q}{m} \int_{-\infty}^t [\mathbf{E}_1(\mathbf{r}', t') + \mathbf{v}' \times \mathbf{B}_1(\mathbf{r}', t')] \cdot \nabla_{v'} f_0(\mathbf{r}', \mathbf{v}') dt'. \quad (2.18)$$

The coordinates  $(\mathbf{r}', \mathbf{v}')$  indicate the position of a particle in phase-space at time  $t'$ , which ends up in  $(\mathbf{r}, \mathbf{v})$  at time  $t$ . In this last equation the antenna is assumed to be turned on infinitely long ago, where the frequency  $\omega$  has an infinitesimal positive imaginary part. This conveniently eliminates the dependency on the initial condition. For a more thorough discussion about the justification of this, see [21, section 10.4].

In order to keep the derivation tractable, a homogeneous plasma is once again assumed. I.e.

the background quantities do not depend on position. In addition, Cartesian coordinates are used, with the  $z$  axis aligned with  $\mathbf{B}_0$ . Moreover, the perturbation is assumed to be of the form:

$$\begin{aligned}\mathbf{E}_1(\mathbf{r}, t) &= \tilde{\mathbf{E}}_1 e^{i(\mathbf{k} \cdot \mathbf{r} - \omega t)} \\ \mathbf{B}_1(\mathbf{r}, t) &= \tilde{\mathbf{B}}_1 e^{i(\mathbf{k} \cdot \mathbf{r} - \omega t)} \\ f_1(\mathbf{r}, t) &= \tilde{f}_1 e^{i(\mathbf{k} \cdot \mathbf{r} - \omega t)}.\end{aligned}$$

More formally, a Fourier-Laplace transform is used. The  $\nabla$  takes on a factor  $i\mathbf{k}$  and  $\partial/\partial t$  a factor  $-i\omega$ , so  $\mathbf{B}_1$  can be eliminated from Eq. (2.18) using Faraday's law,

$$f_1(\mathbf{r}, \mathbf{v}, t) = -\frac{q}{m} \int_{-\infty}^t \tilde{\mathbf{E}}_1 \cdot \left[ I \left( 1 - \frac{\mathbf{v}' \cdot \mathbf{k}}{\omega} \right) + \frac{\mathbf{v}' \cdot \mathbf{k}}{\omega} \right] \cdot \nabla_{\mathbf{v}'} f_0(\mathbf{v}') e^{i(\mathbf{k} \cdot \mathbf{r}' - \omega t')} dt'. \quad (2.19)$$

This simplifies considerably in case  $f_0$  is an isotropic Maxwellian, since the contribution of  $\mathbf{B}_1$  drops out ( $\nabla_{\mathbf{v}} f_0 \propto \mathbf{v}$ ). However, Eq. (2.19) will be kept general for now. Using  $\tau = t - t'$  it can be written as:

$$\tilde{f}_1 = -\frac{q}{m} \int_0^\infty \tilde{\mathbf{E}}_1 \cdot \left[ I \left( 1 - \frac{\mathbf{v}' \cdot \mathbf{k}}{\omega} \right) + \frac{\mathbf{v}' \cdot \mathbf{k}}{\omega} \right] \cdot \nabla_{\mathbf{v}'} f_0(\mathbf{v}') e^{i\omega\tau + i\mathbf{k} \cdot (\mathbf{r}' - \mathbf{r})} d\tau. \quad (2.20)$$

The unperturbed trajectories can be written using rotation matrix  $A$ ,

$$\begin{aligned}\frac{d\mathbf{v}'}{d\tau} &= \Omega A \cdot \mathbf{v}' = -\frac{d\mathbf{v}'}{d\tau}, \\ A &= \begin{pmatrix} 0 & 1 & 0 \\ -1 & 0 & 0 \\ 0 & 0 & 0 \end{pmatrix},\end{aligned} \quad (2.21)$$

where  $\Omega = qB_0/m$  is the cyclotron frequency, *including* the charge sign<sup>5</sup>, meaning that  $\Omega < 0$  if  $q < 0$ . Equation (2.21) is a first order ODE with a matrix with constant coefficients, so it can be solved using the matrix exponential,

$$\mathbf{v}' = e^{-\Omega A \tau} \cdot \mathbf{v} = R \cdot \mathbf{v}, \quad (2.22)$$

with matrix  $R$  defined as:

$$R = \begin{pmatrix} \cos(\Omega\tau) & -\sin(\Omega\tau) & 0 \\ \sin(\Omega\tau) & \cos(\Omega\tau) & 0 \\ 0 & 0 & 1 \end{pmatrix}.$$

The position  $\mathbf{r}'$  is then found by integrating once more,

$$\mathbf{r}' = \mathbf{r} - Q \cdot \mathbf{v}, \quad (2.23)$$

---

<sup>5</sup>Note that different conventions exist, e.g. [19] excludes the charge sign, while [21], [22] include it. Here it has been chosen to go with the latter as it makes the maths slightly more succinct.

$$Q = \begin{pmatrix} \frac{1}{\Omega} \sin(\Omega\tau) & \frac{1}{\Omega} [\cos(\Omega\tau) - 1] & 0 \\ \frac{1}{\Omega} [1 - \cos(\Omega\tau)] & \frac{1}{\Omega} \sin(\Omega\tau) & 0 \\ 0 & 0 & \tau \end{pmatrix}.$$

The velocity space gradient of  $f_0$  can be written as follows:

$$\begin{aligned} \nabla_v f_0(\mathbf{v}) &= \frac{\partial f_0}{\partial v_\perp} \frac{\partial v_\perp}{\partial v_x} \mathbf{e}_x + \frac{\partial f_0}{\partial v_\perp} \frac{\partial v_\perp}{\partial v_y} \mathbf{e}_y + \frac{\partial f_0}{\partial v_z} \mathbf{e}_z \\ &= \frac{\partial f_0}{\partial v_\perp} \frac{v_x}{v_\perp} \mathbf{e}_x + \frac{\partial f_0}{\partial v_\perp} \frac{v_y}{v_\perp} \mathbf{e}_y + \frac{\partial f_0}{\partial v_z} \mathbf{e}_z. \end{aligned} \quad (2.24)$$

In a homogeneous plasma  $v'_z = v_z$ ,  $v'_\perp = v_\perp$ , so the only thing that needs to be changed to use this in Eq. (2.20) is to add a prime to  $v_x, v_y$ . The perturbed distribution function can thus be written as:

$$\begin{aligned} \tilde{f}_1 &= -\frac{q}{m} \int_0^\infty d\tau \left\{ \left[ \tilde{E}_x v'_x + \tilde{E}_y v'_y \right] \left[ \frac{k_z f_{0z}}{\omega} + \frac{f_{0\perp}}{v_\perp} \left( 1 - \frac{v_z k_z}{\omega} \right) \right] \right. \\ &\quad \left. + \tilde{E}_z \left[ \left( \frac{f_{0\perp} v_z}{v_\perp} - f_{0z} \right) \frac{v'_x k_x + v'_y k_y}{\omega} + f_{0z} \right] \right\} \exp[i(\omega - k_z v_z)\tau - i v_x \chi_x - i v_y \chi_y]. \end{aligned} \quad (2.25)$$

To avoid clutter, the following quantities have been defined:

$$\begin{aligned} f_{0\perp} &= \frac{\partial f_0}{\partial v_\perp}, & f_{0z} &= \frac{\partial f_0}{\partial v_z}, \\ \chi_x &= [k_x \sin(\Omega\tau) + k_y (1 - \cos(\Omega\tau))] / \Omega, \\ \chi_y &= [k_x (\cos(\Omega\tau) - 1) + k_y \sin(\Omega\tau)] / \Omega. \end{aligned}$$

Also for convenience the species subscript  $s$  has been suppressed, but this can be placed on any species dependent quantity  $f, \Omega, m, q$ .

The exponent from Eq. (2.25) can be rewritten as follows:

$$\begin{aligned} i\mathbf{k} \cdot (\mathbf{r}' - \mathbf{r}) + i\omega\tau &= i \frac{k_x}{\Omega} [-v_x \sin(\Omega\tau) + v_y (1 - \cos(\Omega\tau))] \\ &\quad + i \frac{k_y}{\Omega} [-v_x (1 - \cos(\Omega\tau)) - v_y \sin(\Omega\tau)] \\ &\quad + i\tau(\omega - k_z v_z) \\ &= -i \frac{k_\perp v_\perp}{\Omega} [\sin(\phi - \psi + \Omega\tau) - \sin(\phi - \psi)] \\ &\quad + i\tau(\omega - k_z v_z), \end{aligned} \quad (2.26)$$

using the polar coordinates:

$$v_x = v_\perp \cos(\phi) \quad (2.27a)$$

$$v_y = v_\perp \sin(\phi) \quad (2.27b)$$

$$k_x = k_\perp \cos(\psi) \quad (2.27c)$$

$$k_y = k_\perp \sin(\psi). \quad (2.27d)$$

The variables  $\phi, \psi$  represent the gyro angle and wave phase, respectively, which at this stage are not yet locked down. The  $x, y$  directions are just two Cartesian directions in the perpendicular plane, which can be defined later on.

In conclusion, Eq. (2.25) becomes

$$\begin{aligned} \tilde{f}_1 = & -\frac{q}{m} \int_0^\infty d\tau \left\{ [\tilde{E}_x \cos(\phi + \Omega\tau) + \tilde{E}_y \sin(\phi + \Omega\tau)] \left[ \frac{k_z v_\perp f_{0z}}{\omega} + f_{0\perp} \left( 1 - \frac{v_z k_z}{\omega} \right) \right] \right. \\ & + E_z \left[ \left( \frac{f_{0\perp} v_z}{v_\perp} - f_{0z} \right) \frac{k_\perp v_\perp}{\omega} \cos(\phi - \psi + \Omega\tau) + f_{0z} \right] \left. \right\} \\ & \times \exp \left[ -i \frac{k_\perp v_\perp}{\Omega} [\sin(\phi - \psi + \Omega\tau) - \sin(\phi - \psi)] + i\tau(\omega - k_z v_z) \right] \\ = & -\frac{q}{m} \int_0^\infty d\tau \mathbf{a} \cdot \tilde{\mathbf{E}}_1, \end{aligned} \quad (2.28)$$

where the last line defines the auxiliary vector  $\mathbf{a}$ , making Eq. (2.31) more succinct.

### 2.2.2 Dielectric tensor

The moments of the perturbed distribution function are:

$$\rho_p = q \int_{\mathbb{R}^3} d^3 v f_1 \quad (2.29a)$$

$$\mathbf{J}_p = q \int_{\mathbb{R}^3} d^3 v \mathbf{v} f_1. \quad (2.29b)$$

From Eq. (2.28) it is seen that in  $k$ -space,

$$\tilde{\mathbf{J}}_p = q \int_{\mathbb{R}^3} d^3 v \mathbf{v} \tilde{f}_1 = -\frac{q^2}{m} \int_{\mathbb{R}^3} d^3 v \mathbf{v} \int_0^\infty d\tau \mathbf{a} \cdot \tilde{\mathbf{E}}_1 = \tilde{\sigma} \cdot \tilde{\mathbf{E}}_1, \quad (2.30)$$

where  $\tilde{\sigma}$  is the conductivity tensor. It can be computed in wavenumber space using:

$$\tilde{\sigma} = -\frac{q^2}{m} \int_{\mathbb{R}^3} d^3 v \mathbf{v} \int_0^\infty d\tau \mathbf{a} = -\frac{q^2}{m} \int_0^\infty d\tau \int_{-\infty}^\infty dv_\perp v_\perp \int_{-\infty}^\infty dv_z \int_0^{2\pi} d\phi \mathbf{v} \mathbf{a}. \quad (2.31)$$

It is convenient to perform the integral also in cylindrical coordinates, and integrate over gyro angle first. To deal with the exponent, it must first be expanded into a series of Bessel functions, using Eq. (A.17a). Since there are two sines in the exponent this trick will be repeated twice,

resulting in a double sum.

$$\begin{aligned}
 & \int_0^{2\pi} d\phi e^{-ib[\sin(\phi-\psi+\Omega\tau)-\sin(\phi-\psi)]} f(\phi) \\
 &= \int_0^{2\pi} d\phi e^{-ib[\sin(\phi+\Omega\tau)-\sin(\phi)]} f(\phi+\psi) \\
 &= \sum_{n=-\infty}^{\infty} e^{-in\Omega\tau} J_n(b) \sum_{m=-\infty}^{\infty} J_m(b) \int_0^{2\pi} d\phi e^{i(m-n)\phi} f(\phi+\psi),
 \end{aligned}$$

using change of variables  $\phi - \psi \rightarrow \phi$ , and shifting the integration limits by an angle  $\psi$ , which is allowed since  $f(\phi)$  is periodic. Integration over  $\phi$  then kills off all terms except where the new exponent is zero, hence only one sum remains. This can be summarised in the following identities (based on [21, chapter 10, Eq. 43]):

$$\begin{aligned}
 & \int_0^{2\pi} d\phi e^{-ib[\sin(\phi-\psi+\Omega\tau)-\sin(\phi-\psi)]} \begin{pmatrix} \sin(\phi) \sin(\phi + \Omega\tau) \\ \sin(\phi) \cos(\phi + \Omega\tau) \\ \cos(\phi) \sin(\phi + \Omega\tau) \\ \cos(\phi) \cos(\phi + \Omega\tau) \\ 1 \\ \sin(\phi) \\ \cos(\phi) \\ \sin(\phi + \Omega\tau) \\ \cos(\phi + \Omega\tau) \\ \cos(\phi - \psi + \Omega\tau) \\ \sin(\phi) \cos(\phi - \psi + \Omega\tau) \\ \cos(\phi) \cos(\phi - \psi + \Omega\tau) \end{pmatrix} \\
 &= 2\pi \sum_{n=-\infty}^{\infty} e^{-in\Omega\tau} \begin{pmatrix} (J'_n(b))^2 \cos^2(\psi) + \frac{n^2}{b^2} J_n^2(b) \sin^2(\psi) \\ -\frac{in}{b} J_n(b) J'_n(b) + \left[ \frac{n^2}{b^2} J_n^2(b) - (J'_n(b))^2 \right] \cos(\psi) \sin(\psi) \\ \frac{in}{b} J_n(b) J'_n(b) + \left[ \frac{n^2}{b^2} J_n^2(b) - (J'_n(b))^2 \right] \cos(\psi) \sin(\psi) \\ (J'_n(b))^2 \sin^2(\psi) + \frac{n^2}{b^2} J_n^2(b) \cos^2(\psi) \\ J_n^2(b) \\ -i J_n(b) J'_n(b) \cos(\psi) + \frac{n}{b} J_n^2(b) \sin(\psi) \\ i J_n(b) J'_n(b) \sin(\psi) + \frac{n}{b} J_n^2(b) \cos(\psi) \\ i J_n(b) J'_n(b) \cos(\psi) + \frac{n}{b} J_n^2(b) \sin(\psi) \\ -i J_n(b) J'_n(b) \sin(\psi) + \frac{n}{b} J_n^2(b) \cos(\psi) \\ \frac{n}{b} J_n^2(b) \\ -\frac{in}{b} J_n(b) J'_n(b) \cos(\psi) + \frac{n^2}{b^2} J_n^2(b) \sin(\psi) \\ \frac{in}{b} J_n(b) J'_n(b) \sin(\psi) + \frac{n^2}{b^2} J_n^2(b) \cos(\psi) \end{pmatrix}, \quad (2.32)
 \end{aligned}$$

where  $b = k_{\perp} v_{\perp} / \Omega$ , and  $J_n$  are the Bessel functions of the first kind of order  $n$ . So the conductivity is written as:

$$\tilde{\sigma} = -2\pi \frac{q^2}{m} \sum_{n=-\infty}^{\infty} \int_0^{\infty} dv_{\perp} v_{\perp} \int_{-\infty}^{\infty} dv_z Y \int_0^{\infty} d\tau e^{i(\omega - n\Omega - k_z v_z)\tau}, \quad (2.33)$$

where the sum over  $n$  indicates the sum over all cyclotron harmonics. And  $Y$  is a  $3 \times 3$  matrix, with entries:

$$Y_{11} = \left[ \left( J'_n(b)^2 - \frac{n^2}{b^2} J_n^2(b) \right) \sin^2(\psi) + \frac{n^2}{b^2} J_n^2(b) \right] G_{\perp} \quad (2.34a)$$

$$Y_{12} = \left[ \frac{in}{b} J_n(b) J'_n(b) + \left( \frac{n^2}{b^2} J_n^2(b) - (J'_n(b))^2 \right) \cos(\psi) \sin(\psi) \right] G_{\perp} \quad (2.34b)$$

$$Y_{13} = \left[ i J_n(b) J'_n(b) \sin(\psi) + \frac{n}{b} J_n^2(b) \cos(\psi) \right] \frac{v_{\perp}}{v_z} G_z \quad (2.34c)$$

$$Y_{21} = \left[ -\frac{in}{b} J_n(b) J'_n(b) + \left( \frac{n^2}{b^2} J_n^2(b) - (J'_n(b))^2 \right) \cos(\psi) \sin(\psi) \right] G_{\perp} \quad (2.34d)$$

$$Y_{22} = \left[ \left( J'_n(b)^2 - \frac{n^2}{b^2} J_n^2(b) \right) \cos^2(\psi) + \frac{n^2}{b^2} J_n^2(b) \right] G_{\perp} \quad (2.34e)$$

$$Y_{23} = \left[ -i J_n(b) J'_n(b) \cos(\psi) + \frac{n}{b} J_n^2(b) \sin(\psi) \right] \frac{v_{\perp}}{v_z} G_z \quad (2.34f)$$

$$Y_{31} = \left[ -i J_n(b) J'_n(b) \sin(\psi) + \frac{n}{b} J_n^2(b) \cos(\psi) \right] \frac{v_z}{v_{\perp}} G_{\perp} \quad (2.34g)$$

$$Y_{32} = \left[ i J_n(b) J'_n(b) \cos(\psi) + \frac{n}{b} J_n^2(b) \sin(\psi) \right] \frac{v_z}{v_{\perp}} G_{\perp} \quad (2.34h)$$

$$Y_{33} = J_n^2(b) G_z, \quad (2.34i)$$

and

$$G_{\perp} = v_{\perp} \left[ f_{0z} \frac{k_z v_{\perp}}{\omega} + f_{0\perp} \left( 1 - \frac{v_z k_z}{\omega} \right) \right] \quad (2.35a)$$

$$G_z = v_z \left[ f_{0z} + \frac{n\Omega}{\omega} \left( \frac{v_z}{v_{\perp}} f_{0\perp} - f_{0z} \right) \right]. \quad (2.35b)$$

In case  $f_0$  is a Maxwellian it simplifies dramatically,  $G_z = v_z f_{0z}$ ,  $G_{\perp} = v_{\perp} f_{0\perp}$ . The next step is to integrate over  $\tau$ . Here we use that  $\text{Im}(\omega) > 0$ , corresponding to an antenna that has been ramping up infinitely slowly since  $t = -\infty$ ,

$$\tilde{\sigma} = -2i\pi \frac{q^2}{m} \sum_{n=-\infty}^{\infty} \int_0^{\infty} dv_{\perp} v_{\perp} \int_{-\infty}^{\infty} dv_z \frac{Y}{\omega - n\Omega - k_z v_z}. \quad (2.36)$$

The denominator that appears reveals the wave-particle resonance condition,

$$\omega - n\Omega - k_z v_z = 0, \quad (2.37)$$

with  $n \in \mathbb{Z}$  (so including negative integers).



The dielectric tensor is defined as

$$\tilde{K} = I + \frac{i\tilde{\sigma}}{\omega\epsilon_0}. \quad (2.38)$$

Hence, in configuration space, the double curl equation (Eq. (2.3)) can be succinctly written as:

$$\nabla \times (\nabla \times \mathbf{E}_1) - \frac{\omega^2}{c^2} K \cdot \mathbf{E}_1 = i\mu_0\omega \mathbf{J}_{ant}. \quad (2.39)$$

In a general plasma  $K$  is an integral operator, but in a homogeneous plasma it simplifies to a convolution operator. Continuing with the homogeneous approximation, the dielectric tensor for a general  $f_0(v_\perp, v_\parallel)$  is given in  $k$ -space by:

$$\tilde{K} = \begin{pmatrix} K_1 + K_0 \sin^2(\psi) & K_2 - K_0 \cos(\psi) \sin(\psi) & K_4 \cos(\psi) + K_5 \sin(\psi) \\ -K_2 - K_0 \cos(\psi) \sin(\psi) & K_1 + K_0 \cos^2(\psi) & K_4 \sin(\psi) - K_5 \cos(\psi) \\ K_6 \cos(\psi) - K_7 \sin(\psi) & K_6 \sin(\psi) + K_7 \cos(\psi) & K_3 \end{pmatrix}, \quad (2.40)$$

where the elements are given by the following expressions:

$$K_0 = \sum_s \frac{2\pi\omega_{ps}^2}{\omega} \sum_{n=-\infty}^{\infty} \int_0^\infty dv_\perp v_\perp \int_{-\infty}^\infty dv_z \frac{(b_s J'_n(b_s))^2 - n^2 J_n^2(b_s)}{b_s^2(\omega - n\Omega_s - k_z v_z)} F_{\perp,s} \quad (2.41a)$$

$$K_1 = 1 + \sum_s \frac{2\pi\omega_{ps}^2}{\omega} \sum_{n=-\infty}^{\infty} \int_0^\infty dv_\perp v_\perp \int_{-\infty}^\infty dv_z \frac{n^2 J_n^2(b_s)}{b_s^2(\omega - n\Omega_s - k_z v_z)} F_{\perp,s} \quad (2.41b)$$

$$K_2 = i \sum_s \frac{2\pi\omega_{ps}^2}{\omega} \sum_{n=-\infty}^{\infty} \int_0^\infty dv_\perp v_\perp \int_{-\infty}^\infty dv_z \frac{n J_n(b_s) J'_n(b_s)}{b_s(\omega - n\Omega_s - k_z v_z)} F_{\perp,s} \quad (2.41c)$$

$$K_3 = 1 + \sum_s \frac{2\pi\omega_{ps}^2}{\omega} \sum_{n=-\infty}^{\infty} \int_0^\infty dv_\perp v_\perp \int_{-\infty}^\infty dv_z \frac{J_n^2(b_s)}{\omega - n\Omega_s - k_z v_z} F_{z,s} \quad (2.41d)$$

$$K_4 = \sum_s \frac{2\pi\omega_{ps}^2}{\omega} \sum_{n=-\infty}^{\infty} \int_0^\infty dv_\perp v_\perp \int_{-\infty}^\infty dv_z \frac{n J_n^2(b_s)}{b_s(\omega - n\Omega_s - k_z v_z)} \frac{v_\perp}{v_z} F_{z,s} \quad (2.41e)$$

$$K_5 = i \sum_s \frac{2\pi\omega_{ps}^2}{\omega} \sum_{n=-\infty}^{\infty} \int_0^\infty dv_\perp v_\perp \int_{-\infty}^\infty dv_z \frac{J_n(b_s) J'_n(b_s)}{\omega - n\Omega_s - k_z v_z} \frac{v_\perp}{v_z} F_{z,s} \quad (2.41f)$$

$$K_6 = \sum_s \frac{2\pi\omega_{ps}^2}{\omega} \sum_{n=-\infty}^{\infty} \int_0^\infty dv_\perp v_\perp \int_{-\infty}^\infty dv_z \frac{n J_n^2(b_s)}{b_s(\omega - n\Omega_s - k_z v_z)} \frac{v_z}{v_\perp} F_{\perp,s} \quad (2.41g)$$

$$K_7 = i \sum_s \frac{2\pi\omega_{ps}^2}{\omega} \sum_{n=-\infty}^{\infty} \int_0^\infty dv_\perp v_\perp \int_{-\infty}^\infty dv_z \frac{J_n(b_s) J'_n(b_s)}{\omega - n\Omega_s - k_z v_z} \frac{v_z}{v_\perp} F_{\perp,s}, \quad (2.41h)$$

where  $s$  indicates the species index to be summed over, and

$$F_\perp = G_\perp / N$$

$$F_z = G_z / N,$$

with  $N$  the number density. And the plasma frequency  $\omega_{ps}$  is defined in:

$$\omega_{ps}^2 = \frac{N_s q_s^2}{\epsilon_0 m_s}. \quad (2.42)$$

The  $K$  elements match those in [19, Eqs. 4.184-4.191], but note that a different charge sign convention in  $\Omega$  has been used. It may be convenient to normalise Eqs. (2.41a)-(2.41h) using  $x = v_z / v_{T\parallel}$ ,  $y = v_{\perp} / v_{T\perp}$ :

$$K_0 = - \sum_s \frac{2\pi\omega_p^2 v_{T\perp}^2}{\omega k_z a_s^2} \sum_{n=-\infty}^{\infty} \int_0^{\infty} dy \frac{(a_s y J'_n(a_s y))^2 - n^2 J_n^2(a_s y)}{y} \int_{-\infty}^{\infty} dx \frac{F_{\perp,s}}{x - x_{n,s}} \quad (2.43a)$$

$$K_1 = 1 - \sum_s \frac{2\pi\omega_p^2 v_{T\perp}^2}{\omega k_z a_s^2} \sum_{n=-\infty}^{\infty} \int_0^{\infty} dy \frac{n^2 J_n^2(a_s y)}{y} \int_{-\infty}^{\infty} dx \frac{F_{\perp,s}}{x - x_{n,s}} \quad (2.43b)$$

$$K_2 = -i \sum_s \frac{2\pi\omega_p^2 v_{T\perp}^2}{\omega k_z a_s} \sum_{n=-\infty}^{\infty} \int_0^{\infty} dy n J_n(a_s y) J'_n(a_s y) \int_{-\infty}^{\infty} dx \frac{F_{\perp,s}}{x - x_{n,s}} \quad (2.43c)$$

$$K_3 = 1 - \sum_s \frac{2\pi\omega_p^2 v_{T\perp}^2}{\omega k_z} \sum_{n=-\infty}^{\infty} \int_0^{\infty} dy y J_n^2(a_s y) \int_{-\infty}^{\infty} dx \frac{F_{z,s}}{x - x_{n,s}} \quad (2.43d)$$

$$K_4 = - \sum_s \frac{2\pi\omega_p^2 v_{T\perp}^3}{\omega k_z v_{T\parallel} a_s} \sum_{n=-\infty}^{\infty} \int_0^{\infty} dy y n J_n^2(a_s y) \int_{-\infty}^{\infty} dx \frac{F_{z,s}}{x(x - x_{n,s})} \quad (2.43e)$$

$$K_5 = -i \sum_s \frac{2\pi\omega_p^2 v_{T\perp}^3}{\omega k_z v_{T\parallel}} \sum_{n=-\infty}^{\infty} \int_0^{\infty} dy y^2 J_n(a_s y) J'_n(a_s y) \int_{-\infty}^{\infty} dx \frac{F_{z,s}}{x(x - x_{n,s})} \quad (2.43f)$$

$$K_6 = - \sum_s \frac{2\pi\omega_p^2 v_{T\perp} v_{T\parallel}}{\omega k_z a_s} \sum_{n=-\infty}^{\infty} \int_0^{\infty} dy \frac{n J_n^2(a_s y)}{y} \int_{-\infty}^{\infty} dx \frac{x F_{\perp,s}}{x - x_{n,s}} \quad (2.43g)$$

$$K_7 = -i \sum_s \frac{2\pi\omega_p^2 v_{T\perp} v_{T\parallel}}{\omega k_z} \sum_{n=-\infty}^{\infty} \int_0^{\infty} dy J_n(a_s y) J'_n(a_s y) \int_{-\infty}^{\infty} dx \frac{x F_{\perp,s}}{x - x_{n,s}}, \quad (2.43h)$$

where  $a_s = k_{\perp} v_{T\perp} / \Omega_s$ , and  $x_n = \frac{\omega - n\Omega}{k_z v_{T\parallel}} = \text{sign}(k_z) \zeta_n$ , so  $\zeta_n = \frac{\omega - n\Omega}{|k_z| v_{T\parallel}}$ . Writing the sign of  $k_z$  explicitly also differs from the convention used in [19], but this is exceptionally useful when computing the inverse Fourier transform in chapter 3. Integration over  $x$  is actually not fully along the real axis, a tiny detour must be made around the singularity, always going below the pole if  $k_z$  is positive, and above it if  $k_z < 0$ . This contour comes from the formal derivation using a Laplace transform in time, instead of the Fourier transform. In case  $f_0$  is Maxwellian or bi-Maxwellian, the integral over  $x$  leads to the PDF in its original definition, without the need to define auxiliary functions that pass on the correct sign of  $k_z$  to the PDF. See [23] for a thorough discussion on this topic.

### 2.2.3 Bi-Maxwellian

In case  $f_0$  is a normal bi-Maxwellian, see Eq. (4.2), the two remaining integrals in Eqs. (2.43a)-(2.43h) can be computed analytically. First, notice that  $F_{\perp}, F_z$  can be written as follows:

$$F_{\perp} = - \frac{2y^2 e^{-(x^2+y^2)}}{\pi^{3/2} v_{T\parallel} v_{T\perp}^2} \left[ 1 + x \frac{k_z v_{T\parallel}}{\omega} \left( \frac{T_{\perp}}{T_{\parallel}} - 1 \right) \right] \quad (2.44a)$$

$$F_z = - \frac{2x^2 e^{-(x^2+y^2)}}{\pi^{3/2} v_{T\parallel} v_{T\perp}^2} \left[ 1 + \frac{n\Omega}{\omega} \left( \frac{T_{\parallel}}{T_{\perp}} - 1 \right) \right]. \quad (2.44b)$$

In order to compute the integral over the parallel velocity, use the following identities:

$$\frac{1}{\sqrt{\pi}} \int_{-\infty}^{\infty} dx \frac{e^{-x^2}}{x - x_n} \begin{pmatrix} 1 \\ x \\ x^2 \end{pmatrix} = \text{sign}(k_z) \begin{pmatrix} Z(\zeta_n) \\ -\frac{1}{2} \text{sign}(k_z) Z'(\zeta_n) \\ -\frac{1}{2} \zeta_n Z'(\zeta_n) \end{pmatrix}. \quad (2.45)$$

The first row comes from [23], for higher powers of  $x$  use the trick in Eq. (A.37). So Eqs. (2.43a)-(2.43h) become:

$$K_0 = \sum_s \frac{4\omega_{ps}^2}{\omega |k_z| v_{T_{\parallel s}} a_s^2} \sum_{n=-\infty}^{\infty} \left[ Z(\zeta_{n,s}) + \frac{|k_z| v_{T_{\parallel s}}}{\omega} \left( 1 - \frac{T_{\perp s}}{T_{\parallel s}} \right) \frac{Z'(\zeta_{n,s})}{2} \right] \times \int_0^{\infty} dy y e^{-y^2} [(a_s y J'_n(a_s y))^2 - n^2 J_n^2(a_s y)] \quad (2.46a)$$

$$K_1 = 1 + \sum_s \frac{4\omega_{ps}^2}{\omega |k_z| v_{T_{\parallel s}} a_s^2} \sum_{n=-\infty}^{\infty} n^2 \left[ Z(\zeta_{n,s}) + \frac{|k_z| v_{T_{\parallel s}}}{\omega} \left( 1 - \frac{T_{\perp s}}{T_{\parallel s}} \right) \frac{Z'(\zeta_{n,s})}{2} \right] \times \int_0^{\infty} dy y e^{-y^2} J_n^2(a_s y) \quad (2.46b)$$

$$K_2 = i \sum_s \frac{4\omega_{ps}^2}{\omega |k_z| v_{T_{\parallel s}} a_s} \sum_{n=-\infty}^{\infty} n \left[ Z(\zeta_{n,s}) + \frac{|k_z| v_{T_{\parallel s}}}{\omega} \left( 1 - \frac{T_{\perp s}}{T_{\parallel s}} \right) \frac{Z'(\zeta_{n,s})}{2} \right] \times \int_0^{\infty} dy y^2 e^{-y^2} J_n(a_s y) J'_n(a_s y) \quad (2.46c)$$

$$K_3 = 1 - \sum_s \frac{2\omega_{ps}^2}{\omega |k_z| v_{T_{\parallel s}}} \sum_{n=-\infty}^{\infty} \left[ 1 + \frac{n\Omega_s}{\omega} \left( \frac{T_{\parallel s}}{T_{\perp s}} - 1 \right) \right] \zeta_{n,s} Z'(\zeta_{n,s}) \times \int_0^{\infty} dy y e^{-y^2} J_n^2(a_s y) \quad (2.46d)$$

$$K_4 = - \sum_s \frac{2\omega_{ps}^2 v_{T_{\perp s}}}{\omega k_z v_{T_{\parallel s}}^2 a_s} \sum_{n=-\infty}^{\infty} n \left[ 1 + \frac{n\Omega_s}{\omega} \left( \frac{T_{\parallel s}}{T_{\perp s}} - 1 \right) \right] Z'(\zeta_{n,s}) \times \int_0^{\infty} dy y e^{-y^2} J_n^2(a_s y) \quad (2.46e)$$

$$K_5 = -i \sum_s \frac{2\omega_{ps}^2 v_{T_{\perp s}}}{\omega k_z v_{T_{\parallel s}}^2} \sum_{n=-\infty}^{\infty} \left[ 1 + \frac{n\Omega_s}{\omega} \left( \frac{T_{\parallel s}}{T_{\perp s}} - 1 \right) \right] Z'(\zeta_{n,s}) \times \int_0^{\infty} dy y^2 e^{-y^2} J_n(a_s y) J'_n(a_s y) \quad (2.46f)$$

$$K_6 = - \sum_s \frac{2\omega_{ps}^2}{\omega k_z v_{T_{\perp s}} a_s} \sum_{n=-\infty}^{\infty} n \left[ 1 + \zeta_{n,s} \frac{|k_z| v_{T_{\parallel s}}}{\omega} \left( \frac{T_{\perp s}}{T_{\parallel s}} - 1 \right) \right] Z'(\zeta_{n,s}) \times \int_0^{\infty} dy y e^{-y^2} J_n^2(a_s y) \quad (2.46g)$$

$$K_7 = -i \sum_s \frac{2\omega_{ps}^2}{\omega k_z v_{T_{\perp s}}} \sum_{n=-\infty}^{\infty} \left[ 1 + \zeta_{n,s} \frac{|k_z| v_{T_{\parallel s}}}{\omega} \left( \frac{T_{\perp s}}{T_{\parallel s}} - 1 \right) \right] Z'(\zeta_{n,s}) \times \int_0^{\infty} dy y^2 e^{-y^2} J_n(a_s y) J'_n(a_s y). \quad (2.46h)$$

Note that  $K_6 = K_4$  and  $K_7 = K_5$ , since

$$\frac{T_{\parallel}}{T_{\perp}} \left[ 1 + \zeta_n \frac{|k_z| v_{T_{\parallel}}}{\omega} \left( \frac{T_{\perp}}{T_{\parallel}} - 1 \right) \right] = 1 + \frac{n\Omega}{\omega} \left( \frac{T_{\parallel}}{T_{\perp}} - 1 \right). \quad (2.47)$$

To proceed with the integration over  $y$ , use the following identities:

$$\int_0^{\infty} dy y e^{-y^2} J_n^2(ay) = \frac{1}{2} e^{-\lambda} I_n(\lambda) \quad (2.48a)$$

$$\int_0^{\infty} dy y^2 e^{-y^2} J_n(ay) J'_n(ay) = -\frac{a}{4} e^{-\lambda} (I_n(\lambda) - I'_n(\lambda)) \quad (2.48b)$$

$$\int_0^{\infty} dy y e^{-y^2} [(ay J'_n(ay))^2 - n^2 J_n^2(ay)] = \lambda^2 e^{-\lambda} (I_n(\lambda) - I'_n(\lambda)), \quad (2.48c)$$

where  $\lambda$  represents the FLR parameter

$$\lambda = \frac{1}{2} k_{\perp}^2 \rho_{T_{\perp}}^2 = \frac{k_{\perp}^2 v_{T_{\perp}}^2}{2\Omega^2}. \quad (2.49)$$

In conclusion, the  $K$  elements can be simplified to:

$$K_0 = 2 \sum_s \mathcal{W}_s \sum_{n=-\infty}^{\infty} \lambda_s (I_n(\lambda_s) - I'_n(\lambda_s)) \left[ Z(\zeta_{n,s}) + \frac{|k_z| v_{T_{\parallel s}}}{\omega} \left( 1 - \frac{T_{\perp s}}{T_{\parallel s}} \right) \frac{Z'(\zeta_{n,s})}{2} \right] \quad (2.50a)$$

$$K_1 = 1 + \sum_s \mathcal{W}_s \sum_{n=-\infty}^{\infty} \frac{n^2 I_n(\lambda_s)}{\lambda_s} \left[ Z(\zeta_{n,s}) + \frac{|k_z| v_{T_{\parallel s}}}{\omega} \left( 1 - \frac{T_{\perp s}}{T_{\parallel s}} \right) \frac{Z'(\zeta_{n,s})}{2} \right] \quad (2.50b)$$

$$K_2 = -i \sum_s \mathcal{W}_s \sum_{n=-\infty}^{\infty} n (I_n(\lambda_s) - I'_n(\lambda_s)) \left[ Z(\zeta_{n,s}) + \frac{|k_z| v_{T_{\parallel s}}}{\omega} \left( 1 - \frac{T_{\perp s}}{T_{\parallel s}} \right) \frac{Z'(\zeta_{n,s})}{2} \right] \quad (2.50c)$$

$$K_3 = 1 - \sum_s \mathcal{W}_s \sum_{n=-\infty}^{\infty} I_n(\lambda_s) \left[ 1 - \frac{n\Omega_s}{\omega} \left( 1 - \frac{T_{\perp s}}{T_{\parallel s}} \right) \right] \zeta_{n,s} Z'(\zeta_{n,s}) \quad (2.50d)$$

$$K_4 = -\text{sign}(k_z) \sum_s \mathcal{W}_s \frac{k_{\perp} v_{T_{\parallel s}}}{\Omega_s} \sum_{n=-\infty}^{\infty} \frac{n I_n(\lambda_s)}{\lambda_s} \left[ \frac{T_{\perp s}}{T_{\parallel s}} + \frac{n\Omega_s}{\omega} \left( 1 - \frac{T_{\perp s}}{T_{\parallel s}} \right) \right] \frac{Z'(\zeta_{n,s})}{2} \quad (2.50e)$$

$$K_5 = i \text{sign}(k_z) \sum_s \mathcal{W}_s \frac{k_{\perp} v_{T_{\parallel s}}}{\Omega_s} \sum_{n=-\infty}^{\infty} (I_n(\lambda_s) - I'_n(\lambda_s)) \left[ \frac{T_{\perp s}}{T_{\parallel s}} + \frac{n\Omega_s}{\omega} \left( 1 - \frac{T_{\perp s}}{T_{\parallel s}} \right) \right] \frac{Z'(\zeta_{n,s})}{2}, \quad (2.50f)$$

with

$$\mathcal{W} = \frac{\omega_p^2 e^{-\lambda}}{\omega |k_z| v_{T_{\parallel}}}. \quad (2.51)$$

Also, beware that all expressions have  $T_{\perp}/T_{\parallel}$ , but  $K_3$  has  $T_{\parallel}/T_{\perp}$ . The form of Eq. (2.50) is not unique, since the derivative of the PDF can also be expressed in terms of the PDF itself (A.26), and the modified Bessel functions can be rewritten, see section A.2.

In the special case of an isotropic Maxwellian  $f_0$ , i.e. setting  $T_{\perp} = T_{\parallel} = T$  in Eq. (2.50), the  $K$

elements reduce further:

$$K_0 = 2 \sum_s \mathcal{W}_s \sum_{n=-\infty}^{\infty} \lambda_s (I_n(\lambda_s) - I'_n(\lambda_s)) Z(\zeta_{n,s}) \quad (2.52a)$$

$$K_1 = 1 + \sum_s \mathcal{W}_s \sum_{n=-\infty}^{\infty} \frac{n^2 I_n(\lambda_s)}{\lambda_s} Z(\zeta_{n,s}) \quad (2.52b)$$

$$K_2 = -i \sum_s \mathcal{W}_s \sum_{n=-\infty}^{\infty} n (I_n(\lambda_s) - I'_n(\lambda_s)) Z(\zeta_{n,s}) \quad (2.52c)$$

$$K_3 = 1 - \sum_s \mathcal{W}_s \sum_{n=-\infty}^{\infty} I_n(\lambda_s) \zeta_{n,s} Z'(\zeta_{n,s}) \quad (2.52d)$$

$$K_4 = -\text{sign}(k_z) \sum_s \mathcal{W}_s \frac{k_{\perp} v_{Ts}}{\Omega_s} \sum_{n=-\infty}^{\infty} \frac{n I_n(\lambda_s)}{\lambda_s} \frac{Z'(\zeta_{n,s})}{2} \quad (2.52e)$$

$$K_5 = i \text{sign}(k_z) \sum_s \mathcal{W}_s \frac{k_{\perp} v_{Ts}}{\Omega_s} \sum_{n=-\infty}^{\infty} (I_n(\lambda_s) - I'_n(\lambda_s)) \frac{Z'(\zeta_{n,s})}{2}. \quad (2.52f)$$

These dielectric tensors (Eqs. (2.50), (2.52)) are also implemented in LEMan, see chapter 4.

## 2.3 Cold plasma

In order to gain some intuition, let us first study some properties of cold plasma, which describes wave propagation in the limit  $T \rightarrow 0$ . It must be noted that cold plasma theory has some serious deficiencies compared to the more complete hot model from section 2.2. Nevertheless, it is able to capture the essence of many ICRH schemes. Therefore it is still useful today in designing experimental scenarios and explaining observations, if one keeps in mind the inherent limitations.

### 2.3.1 Dispersion relation

In an infinite, homogeneous plasma, the dielectric tensor has no spatial dependence, and all of the modes decouple. Of course the right hand side of Eq. (2.39) is zero as there is no antenna current inside of the plasma. Using orthogonality of the basis reveals:

$$\mathbf{k} \times (\mathbf{k} \times \mathbf{E}) + \frac{\omega^2}{c^2} K \cdot \mathbf{E} = \mathbf{0}. \quad (2.53)$$

The tilde is dropped to lighten notation. Define the refractive index (vector):

$$\mathbf{n} = \frac{c\mathbf{k}}{\omega} = \frac{c}{v_p^2} \mathbf{v}_p, \quad (2.54)$$

with the phase velocity  $\mathbf{v}_p = \frac{\omega}{k^2} \mathbf{k}$ . Note, the choice of phase velocity is not unique. It is simply the velocity at which the observed phase is constant, where the plane wave phase is defined as  $\Phi = (\mathbf{k} \cdot \mathbf{r} - \omega t)$ . Requiring  $d\Phi/dt = 0$  implies  $\mathbf{k} \cdot \mathbf{v}_p - \omega = 0$ , which is just one equation for three unknowns. This locks in the velocity parallel to  $\mathbf{k}$ , but any arbitrary velocity perpendicular to  $\mathbf{k}$

can be added without modifying the phase. In other words, this perpendicular velocity would just introduce a movement in the plane of the plane wave.

Using the triple product expansion, the Laplace-Fourier transformed wave equation, inside the plasma, becomes:

$$(\mathbf{n}\mathbf{n} - n^2 \mathbf{I} + K) \cdot \mathbf{E} = \mathbf{0}. \quad (2.55)$$

For an infinite, homogeneous plasma, and completely neglecting any thermal effects ( $T \rightarrow 0$ ), the dielectric tensor can be derived from a fluid model, see Stix [21, section 1.2] or Freidberg [3, section 15.5] for a derivation. Alternatively, it can be recovered by taking the limit  $T \rightarrow 0$  in Eq. (2.52) of the previous section, yielding:

$$K = \begin{pmatrix} S & -iD & 0 \\ iD & S & 0 \\ 0 & 0 & P \end{pmatrix}. \quad (2.56)$$

The elements  $S, P, D$  are solely functions of the antenna, cyclotron and plasma frequencies:

$$S = \frac{1}{2}(R + L) = 1 - \sum_s \frac{\omega_{ps}^2}{\omega^2 - \Omega_s^2} \quad (2.57a)$$

$$D = \frac{1}{2}(R - L) = \sum_s \frac{\Omega_s \omega_{ps}^2}{\omega(\omega^2 - \Omega_s^2)} \quad (2.57b)$$

$$R = 1 - \sum_s \frac{\omega_{ps}^2}{\omega(\omega + \Omega_s)} \quad (2.57c)$$

$$L = 1 - \sum_s \frac{\omega_{ps}^2}{\omega(\omega - \Omega_s)} \quad (2.57d)$$

$$P = 1 - \sum_s \frac{\omega_{ps}^2}{\omega^2}. \quad (2.57e)$$

Cold plasma is a good approximation as long as the finite Larmor radius (FLR) parameter is small, i.e.  $\lambda_s \ll 1$ . Introducing FLR effects modifies all tensor elements, including the ones that are zero in Eq. (2.56).

For any non-trivial solution to Eq. (2.55), the determinant of the matrix<sup>6</sup> on the left hand side must be zero. This leads to the cold plasma dispersion relation:

$$\begin{vmatrix} S - n_{\parallel}^2 & -iD & n_{\perp} n_{\parallel} \\ iD & S - n^2 & 0 \\ n_{\perp} n_{\parallel} & 0 & P - n_{\perp}^2 \end{vmatrix} = 0. \quad (2.58)$$

When  $n^2 > 0$  the wave can propagate, if  $n^2 < 0$  the wave is said to be evanescent. This means that the wave amplitude decays as a function of the distance into the evanescent layer. If

---

<sup>6</sup>Note, without loss of generality we may choose a Cartesian coordinate system, with  $\mathbf{e}_z$  aligned with  $\mathbf{B}_0$ , and rotated such that  $\mathbf{n}$  lies in the  $Oxz$  plane. So  $\mathbf{B}_0 = B_0 \mathbf{e}_z$  and  $n^2 = n_x^2 + n_z^2 = n_{\perp}^2 + n_{\parallel}^2$ .

said layer is small enough, part of the wave amplitude will tunnel through, and the wave continues to propagate. This dispersion relation only permits real solutions for  $n^2$ , so either propagating or decaying. In a hot plasma it is possible to have  $n^2 \in \mathbb{C}$ , so propagating and decaying. Some more definitions are needed: a cut-off is encountered when  $n^2 \rightarrow 0$ , and the wave will (partially) reflect; on the opposite end, a wave resonance is defined as  $n^2 \rightarrow \infty$ . If there is a physical mechanism for absorption at this point, power is effectively transferred to the plasma (wave-particle resonance). Otherwise, the wave may reflect or convert to another mode.

Solving for the perpendicular component ( $n_{\parallel}$  is assumed to be given by the antenna geometry), gives:

$$An_{\perp}^4 + Bn_{\perp}^2 + C = 0, \quad (2.59)$$

with coefficients,

$$A = S \quad (2.60a)$$

$$B = D^2 - (P + S)(S - n_{\parallel}^2) \quad (2.60b)$$

$$C = P((S - n_{\parallel}^2)^2 - D^2). \quad (2.60c)$$

Where the solution is given by

$$n_{\perp}^2 = \frac{-B \pm \sqrt{B^2 - 4AC}}{2A}. \quad (2.61)$$

Assuming  $B \neq 0$ , this can be written as:

$$n_{\perp}^2 = -\frac{B}{2A} \left( 1 \mp \text{sign}(B) \sqrt{1 - 4AC/B^2} \right).$$

These two solutions are used so often they have been given specific names. However, this labelling is arbitrary, and one could redefine the labelling based on the sign of  $B$ . We choose:

$$n_{\perp}^2 = -\frac{B}{2A} \begin{cases} 1 - \sqrt{1 - 4AC/B^2} & \text{fast wave} \\ 1 + \sqrt{1 - 4AC/B^2} & \text{slow wave.} \end{cases} \quad (2.62)$$

The names “fast” and “slow” come from the difference in their phase velocity. In the ICRF the term  $P$  typically dominates over  $S$  and  $D$  because of the large electron contribution (ignoring here the edge case where  $\omega \approx \Omega_s$ ). So the square root can be expanded for large  $P$ ,

$$n_{\perp}^2 \approx -\frac{B}{2A} \begin{cases} 2AC/B^2 \\ 2 - 2AC/B^2 \end{cases} \approx \begin{cases} -C/B \\ -B/A. \end{cases}$$

For the fast wave (FW) the zeroth order term cancels. Then, dropping terms not proportional

to  $P$  in the denominator yields:

$$n_{\perp}^2 = \frac{(S - n_{\parallel}^2)^2 - D^2}{S - n_{\parallel}^2} = \frac{(R - n_{\parallel}^2)(L - n_{\parallel}^2)}{S - n_{\parallel}^2} \quad \text{fast wave.} \quad (2.63)$$

For the slow wave (SW) the zeroth order term survives, and thus the first order term is dropped. Simplifying the numerator by dropping terms not proportional to  $P$  in the numerator yields:

$$n_{\perp}^2 = \frac{P(S - n_{\parallel}^2)}{S} \quad \text{slow wave.} \quad (2.64)$$

This retrieves the well known FW and SW dispersion relations, see [21, section 2.5] and [24, section 3.4]. Note these are even more approximative than the general solution to Eq. (2.59), but they are often still sufficiently accurate, and provide some guidance in designing heating schemes. In the ICRF only the FW is of interest for heating purposes, as it is able to reach the core of the plasma. The slow wave on the other hand does not propagate into the core. This is one of the reasons that typically a Faraday screen is installed, which is essentially a grating, aligned with the background magnetic field. It effectively filters out the SW because the SW usually has a large parallel electric field [25], [26].

### 2.3.2 ICRH schemes

Given the choice of the coordinate system, the parallel field is  $E_z$ , and the two components in the plane perpendicular to  $\mathbf{B}_0$  are  $E_x, E_y$ . The latter two can be combined into a convenient form<sup>7</sup>:

$$E^{\pm} = \frac{1}{2} (E_x \pm iE_y), \quad (2.65)$$

with  $E^+$  the left-handed component, rotating with the ion gyro motion. And  $E^-$  the right-handed component, rotating with the electrons. The second row of Eq. (2.55) reads  $iDE_x + (S - n^2)E_y = 0$ , from which the following ratio can be derived:

$$\frac{E^+}{E^-} = \frac{R - n^2}{L - n^2}. \quad (2.66)$$

This is referred to as the polarisation of the wave. For ion heating one wants to maximize  $|E^+ / E^-|$ , as collisionless volumetric power absorption on thermal ions is approximately  $P_{abs} \propto |E^+|^2$ . But Eq. (2.66) can still be simplified further. The third row of Eq. (2.55) reads  $n_{\perp} n_{\parallel} E_x + (P - n_{\perp}^2)E_z = 0$ . Since  $P$  dominates over all other terms in the ICRF, this row is approximately  $PE_z = 0$ , indicating  $E_z = 0$ . Indeed, in the ICRF the parallel electric field is negligible compared to the perpendicular components. This is because the RF frequency is low enough so that electrons can short circuit the parallel component (their thermal velocity is comparable to the wave's phase velocity). Using the first row of Eq. (2.55), and neglecting  $E_z$ , the polarisation can

---

<sup>7</sup>Note, different definitions for  $E^{\pm}$  exist in literature, the factor  $\frac{1}{2}$  is commonly omitted.



be written as:

$$\frac{E^+}{E^-} = -\frac{R - n_{\parallel}^2}{L - n_{\parallel}^2}. \quad (2.67)$$

From this equation it can already be seen why heating the bulk ion species at the fundamental cyclotron frequency is not efficient: At  $\omega \rightarrow \Omega_i$ ,  $|L| \rightarrow \infty$  while  $R$  remains finite, and so the polarisation is zero. This means the wave is fully right-handed polarised, resulting in very little power absorption by ions. However, in real life the power is not exactly zero for a number of reasons: Due to the Doppler effect, bulk ions can also resonate a small distance away from the cold resonant surface ( $\omega = \Omega_i$ ), where the polarisation is more favourable. Secondly, if thermal effects are included,  $|L|$  remains finite at  $\omega = \Omega_i$ , so  $|E^+ / E^-| > 0$ . Moreover, the ions can absorb some power from  $E^-$  as well. But the original conclusion remains: bulk ion heating at the fundamental frequency is not efficient, and most power goes to the electrons. The wave will mode convert to short wavelength modes, such as the ion Bernstein wave (IBW), which is then damped by electrons via Landau damping. This is why in practice other heating schemes are used, such as minority -, higher harmonic -, three-ion - or Doppler shifted heating.

A good ion heating scheme has these four requirements:

- 1 Wave resonance
- 2 Wave-particle resonance
- 3 Good wave polarisation ( $|E^+ / E^-|$  as large as possible)
- 4 Good accessibility

To clarify the above, a wave resonance is when  $n^2 \rightarrow \infty$ , at which point the wavelength shrinks to zero, and power transfer to the plasma is very efficient, **if** there is a physical mechanism to transfer this power. See [3, section 15.4.3] for more details. For example: cyclotron heating, Landau damping and transit time magnetic pumping are such mechanisms. These are all special cases of wave-particle resonances, which satisfy the condition in Eq. (2.37). The thermal ions absorb power mainly from the left-handed polarised component (see Quasi-linear theory), hence the polarisation should be maximised. Note that fast ions can also interact with  $E^-$ . Point (4) highlights that the wave must be able to propagate into the core. In practice there is often a small evanescent region at the edge through which it must tunnel.

For plasmas with only one ion species  $\omega_{pi}^2 / \Omega_i^2 \gg n_{\parallel}^2$ , so the polarisation is approximately  $-R/L$  [27] (away from a cut-off). Also the 1 in  $R, L$  can be neglected because  $\omega_{pi}^2 / \Omega_i^2 \gg 1$  for a

typical tokamak plasma, so:

$$\frac{E^+}{E^-} \approx -\frac{\frac{\omega_{pi}^2}{\omega(\omega+\Omega_i)} + \frac{\omega_{pe}^2}{\omega(\omega+\Omega_e)}}{\frac{\omega_{pi}^2}{\omega(\omega-\Omega_i)} + \frac{\omega_{pe}^2}{\omega(\omega-\Omega_e)}} = -\frac{\omega - \Omega_i}{\omega + \Omega_i} \left[ \frac{1 + \frac{\omega_{pe}^2}{\omega_{pi}^2} \frac{\omega + \Omega_i}{\omega + \Omega_e}}{1 + \frac{\omega_{pe}^2}{\omega_{pi}^2} \frac{\omega - \Omega_i}{\omega - \Omega_e}} \right] \approx \frac{\omega - \Omega_i}{\omega + \Omega_i}, \quad (2.68)$$

where in the last step  $\omega \ll |\Omega_e|$  and quasi-neutrality has been used:

$$\frac{\omega_{pe}^2}{\omega_{pi}^2} \frac{\Omega_i}{\Omega_e} = -\frac{N_e}{N_i Z_i} \approx -1,$$

with  $q_i = eZ_i$ . So the term in brackets in Eq. (2.68) then reduces to  $-1$ . It is again clear, that  $E^+/E^- = 0$  at the fundamental, but heating at higher harmonics does provide a non-zero polarisation, namely  $(M-1)/(M+1)$ , with  $M$  the harmonic. The issue is that higher harmonic heating is a FLR effect, the higher the harmonic, the less efficient the absorption [3, Section 15.8.2].

The idea of minority heating is to add a small ( $N_{i2}/N_e$  of a few percent) quantity of a second ion species, and heat at the fundamental of that species. Since only a “small” amount is added, the effect on the dielectric tensor is neglected, hence the result from Eq. (2.68) can still be applied. E.g. for heating hydrogen minorities in a  $^4\text{He}$  plasma:

$$\frac{E^+}{E^-} = \frac{\Omega_H - \Omega_{He}}{\Omega_H + \Omega_{He}} \neq 0. \quad (2.69)$$

It is a simple, yet effective approach, and therefore minority heating is one of the go-to schemes in tokamaks and stellarators. To distinguish the species, minority heating schemes are usually written using the template Majority-(Minority), e.g.  $^4\text{He}-(\text{H})$ .

An even more advanced method, is to add yet another ion species, and optimally tune the concentrations of the two majority ion species, in order to line up the L cut-off ( $L - n_{\parallel}^2 = 0$ ) with the cyclotron resonance of the third ion species (and thus get very good polarisation). These layers can never truly line up, as  $|L| \rightarrow \infty \neq n_{\parallel}^2$  at the resonance, but it can get close enough to achieve effective plasma heating. This is the so called three-ion heating scheme [27], [28].

Lastly, it is also possible to exploit the significant Doppler shifted resonance of an NBI population, dubbed “RF-NBI synergetic heating”. This can even be used for majority ion species heating, see e.g. Refs. [29]–[31]. But it can also be used in combination with the aforementioned schemes, e.g. minority [32], or using the fast ion population from the beam as a third “species” [33], [34].

## 2.4 LEMan

LEMan is a full-wave code that has been used to study waves in the ICRF and Alfvén range of frequencies. This section briefly describes the mathematical basis used in the code. For more details see [16], [17].

### 2.4.1 Weak form

The model equations are given in the strong form by Eqs. (2.6). They can also be written in the weak form, which has some benefits: Only first order derivatives appear, instead of second order. So the requirements on continuity of  $\phi, \mathbf{A}$  are relaxed. And secondly, there is an elegant way to impose the so called “natural” boundary conditions. In order to obtain this weak form, multiply by a test function, and integrate over the modelling domain, which yields:

$$\int_{\Omega} dV [-(\nabla \times \mathbf{F}^*) \cdot (\nabla \times \mathbf{A}) - (\nabla \cdot \mathbf{F}^*)(\nabla \cdot \mathbf{A}) + \omega^2 c^{-2} \mathbf{F}^* \cdot \mathbf{A} + i\omega c^{-2} \mathbf{F}^* \cdot \nabla \phi + \mu_0 \mathbf{F}^* \cdot \mathbf{J}_p] + \int_{\partial\Omega} dS [\mathbf{F}^* \times (\nabla \times \mathbf{A}) + \mathbf{F}^* (\nabla \cdot \mathbf{A})] \cdot \mathbf{n} = -\mu_0 \int_{\Omega} dV \mathbf{F}^* \cdot \mathbf{J}_{ant} \quad (2.70a)$$

$$\int_{\Omega} dV [-\nabla G^* \cdot \nabla \phi + i\omega \nabla G^* \cdot \mathbf{A} + i\varepsilon_0^{-1} \omega^{-1} \nabla G^* \cdot \mathbf{J}_p] + \int_{\partial\Omega} dS [G^* \nabla \phi - i\omega G^* \mathbf{A} - i\varepsilon_0^{-1} \omega^{-1} G^* \mathbf{J}_p] \cdot \mathbf{n} = -\varepsilon_0^{-1} \int_{\Omega} dV G^* \rho_{ant}, \quad (2.70b)$$

with  $\Omega$  the modelling domain,  $\partial\Omega$  its boundary, and  $\mathbf{n}$  the normal vector on this boundary. The second order derivative terms are integrated by parts (use divergence theorem). Also, the following vector identities have been used:

$$\begin{aligned} \mathbf{a} \cdot [\nabla \times (\nabla \times \mathbf{b})] &= (\nabla \times \mathbf{a}) \cdot (\nabla \times \mathbf{b}) - \nabla \cdot [\mathbf{a} \times (\nabla \times \mathbf{b})] \\ \mathbf{a} \cdot \nabla (\nabla \cdot \mathbf{b}) &= \nabla \cdot (\mathbf{a} (\nabla \cdot \mathbf{b})) - (\nabla \cdot \mathbf{a}) (\nabla \cdot \mathbf{b}). \end{aligned}$$

Note, the complex conjugate in Eq. (2.70) coming from the inner product has been indicated explicitly with an asterisk. The charge density  $\rho_p$  has been eliminated using charge conservation. Note, this weak form is not unique as the first order derivatives may or may not be integrated by parts.

The functions  $\mathbf{F}, G$  are test functions from the same function space as that of the approximate solution (Galerkin method). Equation (2.70b) has the wrong sign in [17], however this never caused an issue in LEMan because the antenna current has been assumed divergence free, so  $\rho_{ant} = 0$ . Also noteworthy, LEMan uses cgs units, not SI.

It is now time to apply the BCs: usually Dirichlet = essential, and Neumann = natural, as it is in

this case. But beware, that classification is not always true. The weak form can be written as:

$$\begin{aligned} \int_{\Omega} dV & \left[ -(\nabla \times \mathbf{F}^*) \cdot (\nabla \times \mathbf{A}) - (\nabla \cdot \mathbf{F}^*)(\nabla \cdot \mathbf{A}) + \omega^2 c^{-2} \mathbf{F}^* \cdot \mathbf{A} + i\omega c^{-1} \mathbf{F}^* \cdot \nabla \Phi + \mu_0 \mathbf{F}^* \cdot \mathbf{J}_p \right. \\ & \quad \left. - \nabla G^* \cdot \nabla \Phi + i\omega c^{-1} \nabla G^* \cdot \mathbf{A} + i\mu_0 \omega^{-1} c \nabla G^* \cdot \mathbf{J}_p \right] \\ & = -\mu_0 \int_{\Omega} dV [(\mathbf{F}^* + i\omega^{-1} c \nabla G^*) \cdot \mathbf{J}_{ant}], \quad \Phi = 0, \quad \mathbf{A} \times \mathbf{n} = \mathbf{0}. \end{aligned} \quad (2.71)$$

with  $\Phi = \phi/c$ , so units of Vs/m, same as the vector potential. The reason for this rescaling is better matrix conditioning<sup>8</sup>, which the cgs version gets for free. Also, without loss of generality the two weak forms can be added (completely general because it holds for any  $\mathbf{F}, G$ ). Using the conductivity operator  $\mathbf{J}_p = \sigma \cdot (-c \nabla \Phi + i\omega \mathbf{A})$  the weak form can also be written as:

$$\begin{aligned} \int_{\Omega} dV & \left[ -(\nabla \times \mathbf{F}^*) \cdot (\nabla \times \mathbf{A}) - (\nabla \cdot \mathbf{F}^*)(\nabla \cdot \mathbf{A}) + \omega^2 c^{-2} \mathbf{F}^* \cdot (K \cdot \mathbf{A}) + i\omega c^{-1} \mathbf{F}^* \cdot (K \cdot \nabla \Phi) \right. \\ & \quad \left. - \nabla G^* \cdot (K \cdot \nabla \Phi) + i\omega c^{-1} \nabla G^* \cdot (K \cdot \mathbf{A}) \right] \\ & = -\mu_0 \int_{\Omega} dV [(\mathbf{F}^* + i\omega^{-1} c \nabla G^*) \cdot \mathbf{J}_{ant}], \quad \Phi = 0, \quad \mathbf{A} \times \mathbf{n} = \mathbf{0}. \end{aligned} \quad (2.72)$$

To actually solve this equation, a basis must be chosen. In the case of LEMan, a complex Fourier series in poloidal and toroidal directions, and cubic Hermite splines in radial direction are used. In order to speed up the expensive volume integrals, LEMan uses a poloidal and toroidal grid, in addition to the poloidal and toroidal modes of the basis functions. On this grid (in configuration space) all of the necessary coefficients are sampled. Then, using a fast Fourier transform (FFT) the volume integrals are readily found. In the radial direction five point Gauss-Legendre quadrature is used for the integration. A detailed explanation of the matrix building is found in [16, chapter 3].

LEMan uses a locally-homogeneous approximation, so for evaluation of the dielectric tensor, the local values of the background quantities are used. Initially LEMan was developed to study cold plasma, thus the dielectric tensor did not depend on wavenumber. Later updates introduced warm and hot plasma effects, which do depend on  $\mathbf{k}$ . In principle this can be accounted for by using the mode numbers of the basis functions to compute what the wavenumbers are supposed to be. However, this requires a significant re-write of the code, and so a more pragmatic approach was used. Namely, at every point on the grid a local wavenumber is assumed to dominate, found self-consistently from the gradient of the scalar potential [35]. The program then iterates until an equilibrium is found. This approximation has some serious consequences: as only one mode is considered, mode conversion is ruled out from the simulation. Secondly, the plasma response is a simple multiplication, which respects the

<sup>8</sup>This is because the entries in the assembly matrix, related to the coupling between different components of the four potential, will be of a similar magnitude after rescaling. More explicitly, the relatively small term  $\propto \omega c^{-2}$  in Eq. (2.6a) and the large term  $\propto \omega$  in Eq. (2.6b) are replaced by  $\omega/c$ , which is approximately  $1 \text{ m}^{-1}$  in the ICRF.

non-local nature in  $\mathbf{k}$  space. But the Fourier series is only used for the two angular directions, not in radial direction. This means that the model is local in radial direction. This limitation is not too restrictive, as the non-local length scale of the plasma response in the direction perpendicular to the background magnetic field is on the order of a Larmor radius, see chapter 3. Note, this applies regardless of the frequency of the wave, since particles are constrained to move in the perpendicular direction. To be clear, due to the approximations made in LEMan the FEM is local in radial direction, but in general FEM models can be used to study non-local physics, and mode conversion as well, see chapter 3 for an example.

### 2.4.2 Optimisations for axisymmetry

If the plasma is axisymmetric, its dielectric response is a convolution in terms of geometric toroidal angle. This is effectively studied using a Fourier series in toroidal angle  $\sim e^{in_{tor}\varphi}$ . The wave field for each toroidal mode  $n_{tor}$  can be solved for independently. The total field can be reconstructed in the end using a weighted sum of the modes, where the weighting is determined by the antenna spectrum. This is a good choice of optimisation for two reasons: The original problem is split into a number of smaller, independent problems, which is more suitable for parallelisation and reduces total runtime<sup>9</sup>. Secondly, the antenna spectrum typically has only a few peaks, and using just a few, or even only one “dominant” toroidal mode can provide a relatively accurate approximation of the total field in a tokamak [36].

Unfortunately, in the general 3D case  $f_0, \mathbf{B}_0$  have a  $\varphi$  dependency which results in all toroidal modes coupling together. This can be easily seen from the linearised Vlasov equation, Eq. (2.16): Plug in the  $\sim e^{in_{tor}\varphi}$  dependence, multiply by  $e^{-in'_{tor}\varphi}$  and integrate over  $\varphi$ . In 2D, all terms of the sum drop out, except for  $n'_{tor} = n_{tor}$ , due to the orthogonality of the basis functions. However, in 3D mixed terms will appear, coming from  $f_0$  and  $\mathbf{B}_0$  which now depend on toroidal angle. In other words, in 3D the conductivity kernel is not simply a difference kernel in terms of toroidal angle. This means that the kernel is of the form  $\sigma(\varphi, \varphi')$  instead of  $\sigma(\varphi - \varphi')$ , so it is not a convolution. A Fourier series can of course still be used, however, it will need to be solved as a single (large) problem. Note that other optimisations are still possible in special cases, e.g. for stellarators with a periodicity mode families can be used.

### 2.4.3 Mode families

In order to improve the resolution of the simulation (in poloidal/toroidal direction), the number of Fourier modes needs to be increased. The computational cost associated with this can be prohibitive: memory consumption is  $O(N^2)$ , with  $N$  the number of modes, and LU decomposition of the dense matrix blocks is  $O(N^3)$ . This raises the question if perhaps a different algorithm is more suitable, see chapter 3. Nevertheless, an optimisation can be applied in special cases that extend the limit of the current algorithm (besides just waiting for faster computers).

<sup>9</sup>Even when running in serial, see section 2.4.3 for a discussion on the solver's time complexity.

The optimisation can be applied in 3D plasma configurations which have a toroidal periodicity  $N_p$ . Meaning that to describe any background quantity (derived from  $f_0, \mathbf{B}_0$ ) in terms of a Fourier series in toroidal angle only every  $N_p$  modes are needed (e.g.  $N_p = 5$  for W7-X). In this case the problem of computing the wave field can be split up into  $N_p$  independent simulations, each having only every  $N_p$  toroidal modes (mode families). This translates into a factor  $N_p^2$  times less memory and a runtime that is  $N_p^3$  times smaller, per family. This optimisation has been applied to the AORSA code [37] in the past. Although this code is quite different from LEMan, and much richer in physics, this optimisation can be applied to LEMan as well.

More explicitly, the LHS operator in Eq. (2.39) is  $N_p$ -fold periodic. Plug in the  $\sum_n e^{in\varphi}$  dependence of the potentials, as well as the source term on the RHS, and  $\sum_s e^{isN_p\varphi}$  for the dielectric tensor (only every  $N_p$  modes). Multiplying by  $e^{-ik\varphi}$  and integrating only picks out the  $n = k$  and  $n + sN_p = k$  terms due to orthogonality. This demonstrates that mode  $n$  only couples to a subset of other modes, staggered by  $N_p$  modes. For example in W7-X, the first family would contain  $n \in \{\dots, -15, -10, -5, 0, 5, 10, 15, \dots\}$ , the next would have  $n \in \{\dots, -14, -9, -4, 1, 6, 11, 16, \dots\}$ , ...etc..., and the last (fifth)  $n \in \{\dots, -11, -6, -1, 4, 9, 14, 19, \dots\}$ .

In practice this implies a solution needs to be found on the domain  $\varphi \in [0, 2\pi/N_p]$  for each family  $M \in \{0, 1, 2, \dots, N_p - 1\}$ . Once such a solution is obtained, the total electric field can be reconstructed in each period  $p \in \{0, 1, 2, \dots, N_p - 1\}$ . For period  $p$ ,  $\varphi \in \left[\frac{2\pi p}{N_p}, \frac{2\pi(p+1)}{N_p}\right]$ , and the electric field is found through,

$$\mathbf{E}(s, \theta, \varphi) = \frac{1}{N_p} \sum_{M=0}^{N_p-1} \mathbf{E}_M(s, \theta, \varphi) = \frac{1}{N_p} \sum_{M=0}^{N_p-1} e^{-2\pi i M p / N_p} \mathbf{E}_M(s, \theta, \varphi - 2\pi p / N_p). \quad (2.73)$$

In addition, in LEMan, each  $\mathbf{E}_M$  is divided by the square root of the absorbed power for that family. The exponent appears in the last part of Eq. (2.73) because  $\mathbf{E}_M$  is only computed in the first period ( $p = 0$ ), so a shift has to be applied to all families to obtain the solution in period  $p$ . Note that this assumption on periodicity only applies to the background quantities, not the solution to the wave equation itself, nor the antenna current. But in case the latter is also  $N_p$ -fold periodic, only the trivial solution exists for any family other than the first.

## 2.5 SCENIC

Finally, the main tool used for the ICRH simulations is now described, called SCENIC (Self-Consistent Ion Cyclotron). It is a code package that aims to self-consistently solve for the magnetic equilibrium, the wave field coming from ICRH, and the fast ion distribution function [35], [38]. The motivation for this approach is described below.

The use of ICRH changes the background distribution function of the plasma, after all, that is the purpose of heating/current drive. This implies that over time the wave propagation/absorption and also the magnetic equilibrium change. Solving for these self-consistently can be a daunting task. However, separation of time scales enables optimisation: the background

distribution function  $f_0$  changes on the collisional time scale, which is typically considerably longer than the time scale of the wave  $1/\omega$ . This allows decoupling of the physics and iteratively solving for  $\mathbf{E}_1, f_0, \mathbf{B}_0$  to find a steady state solution.

SCENIC does precisely that. It combines the codes ANIMEC [39], LEMan and VENUS-LEVIS<sup>10</sup> [40]. For simplicity, the magnetic equilibrium code has been left out of the iterative loop, unless indicated otherwise. Besides SCENIC, coupled full-wave and Fokker-Planck codes have been used before, e.g. AORSA-CQL3D [41], TORIC-SSFPQL [42], EVE-SPOT[31] and SELFO [43].

SCENIC can be applied to study both tokamaks and stellarators. It computes a 3D equilibrium which can account for the temperature anisotropy in  $f_0$ . In addition, its full-wave code is also 3D, and includes hot plasma effects. Lastly, the orbit following code accounts for finite orbit width (no bounce averaging applied), particle losses, and has excellent energy conservation.

To be clear, VENUS-LEVIS is only applied to study the evolution of  $f_0$  of the fast ion population, not the distribution function of the other plasma species. This is sufficient, as in many scenarios most of the wave power is absorbed by a small ion population. Any power going to the bulk species is typically distributed over many particles, so those populations are Maxwellian to good approximation. Their associated plasma profiles are assumed to be provided by experiments or other simulation tools.

## 2.6 Summary

In summary, the computation of EM wave propagation requires solving Maxwell's equations, which couple to the linearised Vlasov equation. The latter leads to a constitutive relation which can be solved for analytically under certain conditions. This forms the foundation of the developments in the next chapter. In the cold limit the constitutive relation simplifies considerably, which reveals four requirements for an ICRH scheme. These heating scenarios can be described with LEMan, or more generally SCENIC (when the background distribution function is allowed to change). The SCENIC code will be applied to study a JET-like plasma in section 4.5, and W7-X in 5.4.

<sup>10</sup>Originally SCENIC used the VENUS code, but later on this was replaced by the newer VENUS-LEVIS code.





## 3 Configuration space conductivity kernel

The previous chapter introduced the plasma response in wavenumber-space ( $k$ -space). This is most useful in plasma theory, where the domain is often assumed to be infinite. All of the Fourier modes of the  $\mathbf{E}_1$  field (or equivalently the potentials) decouple, and thus can be solved for independently. Real plasmas on the other hand are bounded, and the topology is not necessarily periodic either. For instance, in the case of a torus shape, the domain is only periodic in the two angular directions but not the radial one. Spectral or pseudo-spectral methods can still be applied, but the modes do not decouple in general. Moreover, there may be regions in the modelling domain requiring very high resolution, while other areas are non-interesting (where the field is essentially zero).

Alternatively, the finite element method (FEM) may be used. This technique has experienced a rapid growth of different versions over the last few decades, but they all share some favourable traits: Flexible meshing, which implies it can handle flexible geometry. Also, FEM uses local basis functions which means elements only need to be refined where the fine scales are found (such as near the antenna structure or in the plasma core). Another beneficial property of FEM is that its basis functions have compact support, which normally results in sparse assembly matrices. Unfortunately, this property is lost since the plasma response is non-local (integral term). However, the conductivity kernel (as will become clear later on), decays rapidly when moving away from the reference point. So the matrix may be dense, but it will contain many small entries of negligible amplitude. These can in principle be pruned to recover good sparsity.

In order to construct a model built on FEM the conductivity kernel (or dielectric kernel) is needed in configuration space. This will be derived in the following section, probably for the first time, as attested by the referees of [20]. An example application in 1D will also be constructed based on this new formulation, which demonstrates mode conversion. Although this model is just 1D, the fundamental basis goes beyond that of LEMan and many other full-wave codes. Which can in principle be used for a 2D or 3D code in the future.

This chapter is adapted from the following article: M. Machielsen et al., 2023, “Exact expression

for the hot plasma conductivity kernel in configuration space”, [20], licensed under CC BY 4.0.

## 3.1 Inverse Fourier transform

For simplicity an isotropic Maxwellian is assumed here, in which case the elements of the dielectric tensor are known exactly in  $k$ -space, see Eq. (2.52). However, the approach in this section may easily be generalised to other distribution functions. The conductivity tensor  $\tilde{\sigma}$  is easily found using Eq. (2.38). Arguably, the most arduous task is already completed, what remains is “just” to apply the inverse Fourier transform.

Firstly, the necessary integral transforms are defined. Fourier transform (FT) in 3D:

$$\tilde{g}(\mathbf{k}) = \mathcal{F}_{\mathbf{r}}(g(\mathbf{r})) = \int_{\mathbb{R}^3} d^3r g(\mathbf{r}) e^{-i\mathbf{k}\cdot\mathbf{r}}. \quad (3.1a)$$

Inverse Fourier transform (IFT) in 3D:

$$g(\mathbf{r}) = \mathcal{F}_{\mathbf{k}}^{-1}(\tilde{g}(\mathbf{k})) = \left(\frac{1}{2\pi}\right)^3 \int_{\mathbb{R}^3} d^3k \tilde{g}(\mathbf{k}) e^{i\mathbf{k}\cdot\mathbf{r}}. \quad (3.1b)$$

In addition, the Hankel transform of order  $p$  and its inverse will be needed. Hankel transform (HT):

$$\tilde{g}(k) = \mathcal{H}_{s,p}(g(s)) = \int_0^\infty ds s g(s) J_p(ks). \quad (3.2a)$$

Inverse Hankel transform (IHT):

$$g(s) = \mathcal{H}_{k,p}^{-1}(\tilde{g}(k)) = \int_0^\infty dk k \tilde{g}(k) J_p(ks), \quad (3.2b)$$

where the subscript indicates which variable is to be integrated over. Each component  $\mu, \nu$  of the conductivity kernel can be written as follows:

$$\sigma_{\mu,\nu}(\mathbf{s}) = \mathcal{F}^{-1}(\tilde{\sigma}_{\mu,\nu})(\mathbf{s}) = \left(\frac{1}{2\pi}\right)^3 \int_{-\infty}^\infty dk_z e^{ik_z d} \int_0^\infty dk_\perp k_\perp \int_0^{2\pi} d\psi \tilde{\sigma}_{\mu,\nu}(k_\perp, \psi, k_z) e^{ik_\perp s_\perp \cos(\alpha - \psi)}, \quad (3.3)$$

with the difference vector defined as  $\mathbf{s} = \mathbf{r} - \mathbf{r}'$ , where  $\mathbf{r}$  is the reference point. The vector  $\mathbf{s}$  can be written in terms of cylindrical coordinates  $(s_\perp, \alpha, s_z)$  for convenience:

$$x - x' = s_\perp \cos(\alpha) \quad (3.4a)$$

$$y - y' = s_\perp \sin(\alpha) \quad (3.4b)$$

$$z - z' = s_z. \quad (3.4c)$$

Notice that  $\tilde{\sigma}_{\mu,\nu}$  is a separable function, so it can be refactored into:

$$\tilde{\sigma}_{\mu,\nu}(k_\perp, \psi, k_z) = \sum_{l=1}^5 P_l(\psi) \sum_{n=-\infty}^{\infty} N_{\mu,\nu,l,n}(k_\perp) M_{\mu,\nu,l,n}(k_z), \quad (3.5)$$

where  $n$  is the cyclotron harmonic, see Eq. (2.52). In configuration space this can thus be written as follows:

$$\sigma_{\mu,v}(s_{\perp}, \alpha, s_z) = \sum_{l=1}^5 \sum_{n=-\infty}^{\infty} \left( \frac{1}{2\pi} \right)^3 \int_{-\infty}^{\infty} dk_z e^{ik_z s_z} M_{\mu,v,l,n}(k_z) \int_0^{\infty} dk_{\perp} k_{\perp} N_{\mu,v,l,n}(k_{\perp}) \int_0^{2\pi} d\psi P_l(\psi) e^{ik_{\perp} s_{\perp} \cos(\alpha-\psi)}, \quad (3.6)$$

with  $P_l$  is defined as:

$$\{P_1(\psi), P_2(\psi), P_3(\psi), P_4(\psi), P_5(\psi)\} = \{1, \cos(\psi), \sin(\psi), \cos(2\psi), \sin(2\psi)\}. \quad (3.7)$$

In order to perform the integral over  $\psi$ , expand the exponent into a series using Eq. (A.17b). Then realise that all terms disappear, except where  $p$  matches a mode of  $P$  (convert trig to exp first). Finally, use Eq. (A.14b) to flip the negative order Bessel functions, and convert exp back to trig. In the end the original values  $P_l$  are recovered, except they are rescaled by a value  $Q_l$ , as summarised below.

$$\frac{1}{2\pi} \int_0^{2\pi} d\psi P_l(\psi) e^{ik_{\perp} s_{\perp} \cos(\alpha-\psi)} = \sum_{p=-\infty}^{\infty} i^p J_p(k_{\perp} s_{\perp}) e^{ip\alpha} \frac{1}{2\pi} \int_0^{2\pi} d\psi e^{-ip\psi} P_l(\psi) = P_l(\alpha) Q_l(k_{\perp} s_{\perp}),$$

with  $Q$  defined as follows:

$$\{Q_1(x), Q_2(x), Q_3(x), Q_4(x), Q_5(x)\} = \{J_0(x), iJ_1(x), iJ_1(x), -J_2(x), -J_2(x)\}. \quad (3.8)$$

In conclusion,  $\sigma_{\mu,v}$  is also found to be a separable function,

$$\begin{aligned} \sigma_{\mu,v}(s_{\perp}, \alpha, s_z) &= \sum_{l=1}^5 P_l(\alpha) \sum_{n=-\infty}^{\infty} \left( \frac{1}{2\pi} \right)^2 \int_{-\infty}^{\infty} dk_z e^{ik_z s_z} M_{\mu,v,l,n}(k_z) \int_0^{\infty} dk_{\perp} k_{\perp} N_{\mu,v,l,n}(k_{\perp}) Q_l(k_{\perp} s_{\perp}) \\ &= \sum_{l=1}^5 P_l(\alpha) \sum_{n=-\infty}^{\infty} F_{\mu,v,l,n}(s_z) G_{\mu,v,l,n}(s_{\perp}), \end{aligned} \quad (3.9)$$

where

$$F_{\mu,v,l,n}(s_z) = \frac{1}{2\pi} \int_{-\infty}^{\infty} dk_z e^{ik_z s_z} M_{\mu,v,l,n}(k_z) \quad (3.10a)$$

$$G_{\mu,v,l,n}(s_{\perp}) = \frac{1}{2\pi} \int_0^{\infty} dk_{\perp} k_{\perp} N_{\mu,v,l,n}(k_{\perp}) Q_l(k_{\perp} s_{\perp}). \quad (3.10b)$$

Notice that  $F$  can be written as the 1D IFT of  $M$ ,  $F_{\mu,v,l,n}(s_z) = \mathcal{F}_{k_z}^{-1}(M_{\mu,v,l,n})$ , and  $G$  can be expressed as an IHT of  $N$ . The exact definition of  $M, N$  has been brushed over. However, it is unimportant because  $M, N$  will not be used going forward, these were merely used to make the separable form explicit. What remains now is to compute the inverse transforms in Eq. (3.10).

Table 3.1: Definitions of the  $H$  functions.

Component	Transformation Required
$K_0$	$H_{0,n}(\xi) = \frac{1}{64} \mathcal{H}_{v,0}^{-1} \left[ v^2 e^{-v^2/8} (I_n(v^2/8) - I'_n(v^2/8)) \right]$ $\check{H}_{0,n}(\xi) = \frac{1}{64} \mathcal{H}_{v,2}^{-1} \left[ v^2 e^{-v^2/8} (I_n(v^2/8) - I'_n(v^2/8)) \right]$
$K_1$	$H_{1,n}(\xi) = \mathcal{H}_{v,0}^{-1} \left[ v^{-2} e^{-v^2/8} n^2 I_n(v^2/8) \right]$
$K_2$	$H_{2,n}(\xi) = \frac{1}{8} \mathcal{H}_{v,0}^{-1} \left[ e^{-v^2/8} n (I_n(v^2/8) - I'_n(v^2/8)) \right]$
$K_3, C_3$	$H_{3,n}(\xi) = \frac{1}{8} \mathcal{H}_{v,0}^{-1} \left[ e^{-v^2/8} I_n(v^2/8) \right]$
$K_4, C_4$	$H_{4,n}(\xi) = \frac{1}{\sqrt{8}} \mathcal{H}_{v,1}^{-1} \left[ v^{-1} e^{-v^2/8} n I_n(v^2/8) \right]$
$K_5, C_5$	$H_{5,n}(\xi) = \frac{1}{8\sqrt{8}} \mathcal{H}_{v,1}^{-1} \left[ v e^{-v^2/8} (I_n(v^2/8) - I'_n(v^2/8)) \right]$

### 3.1.1 Transform perpendicular direction

Judging from the  $k_\perp$  dependence of  $N$ , seven distinct versions can be identified, see table 3.1. For example, the  $N$  function in the term  $K_1$  in Eq. (2.52) has the following  $k_\perp$  dependency

$$\lambda^{-1} e^{-\lambda} n^2 I_n(\lambda),$$

where  $\lambda$  is defined in Eq. (2.49). However, a Maxwellian has  $T_\perp = T_\parallel = T$ , so there is no distinction between these two temperatures. The integral over  $k_\perp$  becomes,

$$\begin{aligned} \int_0^\infty dk_\perp k_\perp J_0(k_\perp s_\perp) \left( \lambda^{-1} e^{-\lambda} n^2 I_n(\lambda) \right) &= \int_0^\infty dv v J_0(v\xi) \left( v^{-2} e^{-v^2/8} n^2 I_n(v^2/8) \right) \\ &= \mathcal{H}_{0,v}^{-1} \left[ v^{-2} e^{-v^2/8} n^2 I_n(v^2/8) \right] = H_{1,n}(\xi), \end{aligned}$$

where the change of variables  $v = 2\rho_T k_\perp$ ,  $\xi = \frac{s_\perp}{2\rho_T}$  was used, so  $k_\perp s_\perp = v\xi$ . This procedure can be repeated for the other components to map out the needed  $H$  functions in table 3.1. Since the actual expressions were derived using the program Mathematica, it was found to be somewhat easier to do the transformation using yet another set of variables. This is why the original paper [20] used  $u = v/\sqrt{8}$ . To avoid confusion, this intermediate step is not shown here, but in order to remain consistent with the conventions in [20] some additional factors of 8 appear in the definition of the  $H$  functions.

The  $H$  functions can actually be computed analytically in terms of so called generalised hypergeometric functions, see appendix A.5. To illustrate, some of the  $H$  functions are plotted in Fig. 3.1. For integer order  $n$  these simplify to combinations of Gaussians and error functions. With this comes a characteristic decay length  $\rho_T$ , which is not surprising given that charged particles in a magnetised plasma are constrained to move perpendicular to  $\mathbf{B}_0$ . How far they can deviate from the reference point in perpendicular direction  $s_\perp$  is dictated by their perpendicular speed. And since a Maxwellian  $f_0 \propto e^{-v_\perp^2/v_T^2}$ , there are fewer particles at higher speed, hence the decay with  $s_\perp$ .

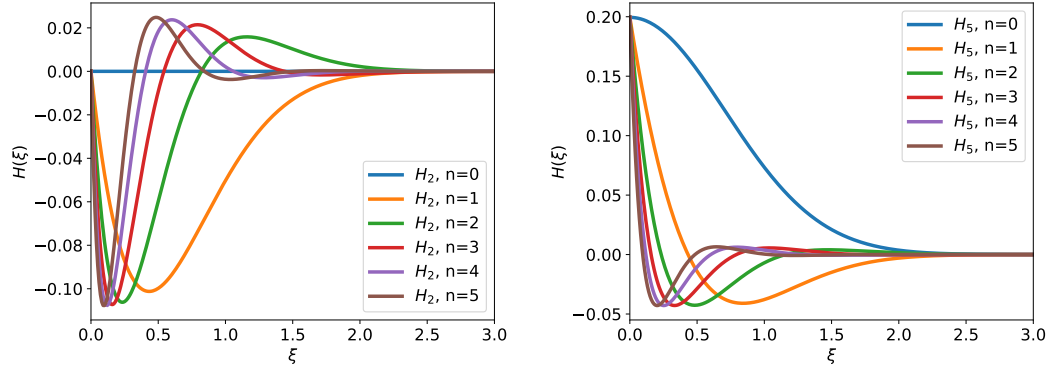


Figure 3.1: Some examples of what the  $H$  functions look like, in this case  $H_2, H_5$  plotted vs  $\xi$  for several harmonics.

Table 3.2: Definition of the  $S$  functions.

Component	Transformation Required
$K_0, K_1, K_2, C_4, C_5$	$S_1(\mu_n) = \mathcal{F}_{w_n}^{-1} \left( \frac{1}{ w_n } Z \left( \frac{\epsilon_n}{2 w_n } \right) \right)$
$K_4, K_5, C_3$	$S_2(\mu_n) = \mathcal{F}_{w_n}^{-1} \left( \frac{1}{w_n} Z' \left( \frac{\epsilon_n}{2 w_n } \right) \right)$
$K_3$	$S_3(\mu_n) = \frac{\epsilon_n}{2} \mathcal{F}_{w_n}^{-1} \left( \frac{1}{w_n^2} Z' \left( \frac{\epsilon_n}{2 w_n } \right) \right)$

### 3.1.2 Transform parallel direction

The  $M$  functions come in three flavours, the necessary transforms are defined in table 3.2. Before beginning the transformation, it is convenient to normalise the variables<sup>1</sup>:

$$\mu_n = \frac{s_z}{2L_n} \quad (3.11a)$$

$$w_n = 2L_n k_z, \quad (3.11b)$$

so that  $w_n \mu_n = k_z s_z$ . The parallel length scale  $L_n$  is defined as follows:

$$L_n = \frac{v_T}{|\omega - n\Omega|} = \frac{\rho_T}{|\omega/\Omega - n|}. \quad (3.12)$$

Clearly, this change of variables only works as long as  $\omega \neq n\Omega$ , otherwise we divide by zero. The resonance parameter can be rewritten as well:

$$\zeta_n = \frac{\omega - n\Omega}{|k_z| v_T} = \frac{\epsilon_n}{|k_z| L_n} = \frac{\epsilon_n}{2|w_n|}, \quad (3.13)$$

where  $\epsilon_n = \text{sign}(\omega - n\Omega)$ .

<sup>1</sup>Note, this definition varies slightly from what was used in [20].

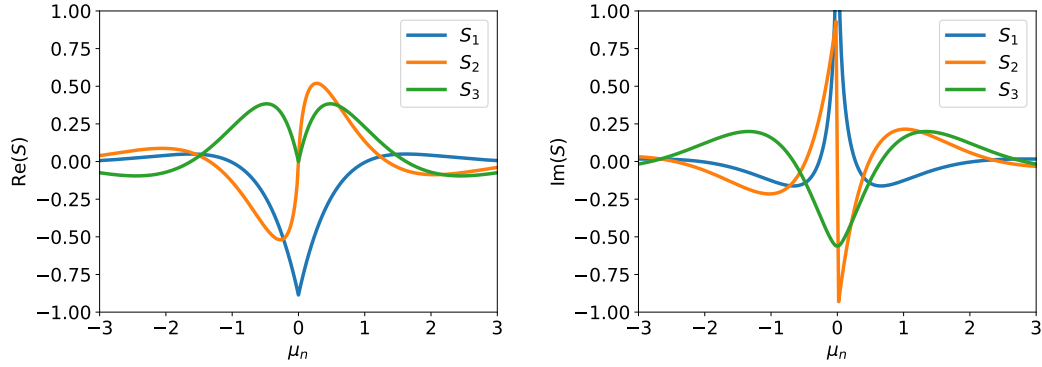


Figure 3.2: Plot of Re and Im parts of the functions  $S_1, S_2, S_3$  for  $\epsilon_n = 1$ .

To give an example, the  $k_z$  dependency of the  $M$  function in  $K_1$  is

$$\frac{1}{|k_z|} Z(\zeta_n) = \frac{2L_n}{|w_n|} Z\left(\frac{\epsilon_n}{2|w_n|}\right).$$

The integral over  $k_z$  then becomes

$$\begin{aligned} \frac{1}{2\pi} \int_{-\infty}^{\infty} dk_z e^{ik_z s_z} \frac{1}{|k_z|} Z(\zeta_n) &= \frac{1}{2\pi} \int_{-\infty}^{\infty} dw_n e^{iw_n \mu_n} \frac{1}{|w_n|} Z\left(\frac{\epsilon_n}{2|w_n|}\right) \\ &= \mathcal{F}_{w_n}^{-1}\left(\frac{1}{|w_n|} Z\left(\frac{\epsilon_n}{2|w_n|}\right)\right) = S_1(\mu_n). \end{aligned}$$

These IFTs can also be computed analytically, see appendix A.6. This results in more generalised hypergeometric functions, and so called Meijer G-functions. The latter are a class of even more general special functions. The  $S$  functions are plotted in Fig. 3.2. The characteristic decay length in parallel direction is  $L_n$ , which is typically on the order of a thermal Larmor radius. However, it can be considerably larger if the reference point is near a cyclotron resonance, see Eq. (3.12).

In order to investigate further into the nature of this decay, revisit Eq. (2.18). Imagine computing the conductivity kernel by releasing a collection of test particles from the reference point  $\mathbf{r}$  and following them along their characteristics. The velocity of these particles is sampled randomly from the distribution function  $f_0$  at point  $\mathbf{r}$ . More precisely, the probability density function related to  $v_\perp$  is

$$f_{V_z}(v_z) = \frac{1}{\sqrt{\pi} v_T} \exp(-v_z^2 / v_T^2), \quad (3.14)$$

where  $V_z$  represents a randomly chosen value with probability density  $f_{V_z}(v_z)$ , and  $v_z$  is a fixed input to evaluate the function at. The cumulative distribution function (CDF) is computed as follows:

$$F_{V_z}(v_z) = \Pr[V_z \leq v_z] = \int_{-\infty}^{v_z} dx f_{V_z}(x) = \frac{1}{2} (1 + \text{Erf}(v_z / v_T)), \quad (3.15)$$

where  $\Pr$  means probability. Of course  $F_{V_z}(\infty) = 1$  since the probability to find a particle with

any velocity is 1. The goal is to find  $f_{S_z}(s_z)$ , which can be obtained by first constructing its CDF; considering that when following along the characteristics of the particles,  $s_z = v_z \tau$ . Thus,

$$\begin{aligned} F_{S_z}(s_z) &= \Pr[S_z \leq s_z] = \Pr[V_z \tau \leq s_z] = \Pr[V_z \leq s_z / \tau] \\ &= F_{V_z}(s_z / \tau) = \frac{1}{2} \left[ 1 + \operatorname{Erf} \left( \frac{s_z}{\tau v_T} \right) \right]. \end{aligned} \quad (3.16)$$

The probability density can be found by taking the derivative,

$$f_{S_z}(s_z) = \frac{dF_{S_z}(s_z)}{ds_z} = \frac{1}{\sqrt{\pi} \tau v_T} \exp \left( -\frac{s_z^2}{\tau^2 v_T^2} \right). \quad (3.17)$$

So initially these particles start clumped together at  $\mathbf{r}' = \mathbf{r}$  (a delta function, Eq. (4.13)), but as  $\tau$  increases (so marching backwards in time), the particles fan out in parallel direction. An observer standing at fixed  $s_z$  measuring the integrand of Eq. (2.18) will notice it decays as a function of  $\tau$ . When keeping  $\tau$  fixed, and moving the observation point  $s_z$  it decays as well.

The velocities  $v_\perp$  and  $v_z$  are independent, so the same procedure can be applied to the perpendicular velocity. A random variable  $V_\perp$  is sampled from  $f_{V_\perp}(v_\perp)$ , where

$$f_{V_\perp}(v_\perp) = \frac{2v_\perp}{v_T^2} \exp(-v_\perp^2 / v_T^2), \quad (3.18)$$

which has the following CDF,

$$F_{V_\perp}(v_\perp) = \int_0^{v_\perp} dx f_{V_\perp}(x) = 1 - \exp(-v_\perp^2 / v_T^2). \quad (3.19)$$

This can be converted to  $f_\Xi(\xi)$ . First, using Eq. (2.23) notice that along the characteristics of the particles

$$s_\perp^2 = \frac{4v_\perp^2}{\Omega^2} \sin^2(\Omega\tau/2), \quad (3.20)$$

so

$$\begin{aligned} F_\Xi(\xi) &= \Pr[\Xi \leq \xi] = \Pr \left[ \frac{V_\perp}{v_T} |\sin(\omega_c \tau / 2)| \leq \xi \right] = \Pr \left[ V_\perp \leq \frac{v_T \xi}{|\sin(\omega_c \tau / 2)|} \right] \\ &= F_{V_\perp} \left( \frac{v_T \xi}{|\sin(\omega_c \tau / 2)|} \right) = 1 - \exp \left( -\frac{\xi^2}{\sin^2(\omega_c \tau / 2)} \right). \end{aligned} \quad (3.21)$$

Taking the derivative results in  $f_\Xi(\xi)$ :

$$f_\Xi(\xi) = \frac{dF_\Xi(\xi)}{d\xi} = \frac{2\xi}{\sin^2(\omega_c \tau / 2)} \exp \left( -\frac{\xi^2}{\sin^2(\omega_c \tau / 2)} \right), \quad (3.22)$$

which demonstrates that the integrand of Eq. (2.18) also decays as a function of  $\xi$ . On the contrary, the perpendicular motion does not contribute to the decay in time, which is in line with expectations because the particles are not free to move in that direction; every cyclotron

period they regroup into a single point when viewing in the plane perpendicular to  $\mathbf{B}_0$ .

### 3.1.3 Explicit form of the configuration space kernel

Putting it all together, the conductivity kernel in configuration space can be written as follows:

$$\sigma(s_\perp, \alpha, s_z) = -i \frac{\varepsilon_0 \omega_p^2 \Omega^2}{\pi v_T^3} \begin{pmatrix} R_1 + \frac{1}{2} R_0 - \frac{1}{2} \check{R}_0 \cos(2\alpha) & R_2 - \frac{1}{2} \check{R}_0 \sin(2\alpha) & R_4 \cos(\alpha) + R_5 \sin(\alpha) \\ -R_2 - \frac{1}{2} \check{R}_0 \sin(2\alpha) & R_1 + \frac{1}{2} R_0 + \frac{1}{2} \check{R}_0 \cos(2\alpha) & R_4 \sin(\alpha) - R_5 \cos(\alpha) \\ R_4 \cos(\alpha) - R_5 \sin(\alpha) & R_4 \sin(\alpha) + R_5 \cos(\alpha) & R_3 \end{pmatrix}, \quad (3.23)$$

with

$$R_0 = 2 \sum_{n=-\infty}^{\infty} H_{0,n}(\xi) S_1(\mu_n) \quad (3.24a)$$

$$\check{R}_0 = -2 \sum_{n=-\infty}^{\infty} \check{H}_{0,n}(\xi) S_1(\mu_n) \quad (3.24b)$$

$$R_1 = \sum_{n=-\infty}^{\infty} H_{1,n}(\xi) S_1(\mu_n) \quad (3.24c)$$

$$R_2 = -i \sum_{n=-\infty}^{\infty} H_{2,n}(\xi) S_1(\mu_n) \quad (3.24d)$$

$$R_3 = - \sum_{n=-\infty}^{\infty} H_{3,n}(\xi) S_3(\mu_n) \quad (3.24e)$$

$$R_4 = -\frac{i}{2} \sqrt{2} \text{sign}(\Omega) \sum_{n=-\infty}^{\infty} H_{4,n}(\xi) S_2(\mu_n) \quad (3.24f)$$

$$R_5 = -\frac{1}{2} \sqrt{2} \text{sign}(\Omega) \sum_{n=-\infty}^{\infty} H_{5,n}(\xi) S_2(\mu_n). \quad (3.24g)$$

This result can be applied anywhere, as long as  $\omega \neq n\Omega$ . A  $4 \times 3$  and  $4 \times 4$  version of  $\sigma$  that also computes the plasma charge can be found in [20]. To be clear, the expressions in Eq. (3.23) are for one species only. To get the total plasma response it will need to be summed over all plasma species. Several components of  $\sigma$  are illustrated in Fig. 3.3. Notice the difference in scale on the axes. This is because  $L_n \gg \rho_T$  near a cyclotron resonance, as discussed before. The plasma response can be found using Eq. (2.30), which in configuration space corresponds to

$$j_{1,\mu}(\mathbf{r}) = \int_{\mathbb{R}^3} d^3 r' \sum_{v=1}^3 \sigma_{\mu,v}(\mathbf{r}-\mathbf{r}') E_{1,v}(\mathbf{r}') = \sum_{v=1}^3 (\sigma_{\mu,v} * E_{1,v})(\mathbf{r}). \quad (3.25)$$

Special care must be taken in order to evaluate the integrals in Eq. (3.25) because there are singularities in  $\sigma$ : The functions  $H_{0,n}, \check{H}_{0,n}, H_{3,n}$  have a  $1/\xi$  type singularity at  $\xi = 0$ , and  $S_1$  has a logarithmic singularity at  $\mu_n = 0$ . However, this does not pose a problem because integrating the  $H$  functions in polar coordinates brings out a factor  $\xi$  (Jacobian determinant) which cancels out the singularity at the origin. As for the function  $S_1$ , the logarithmic type singularity



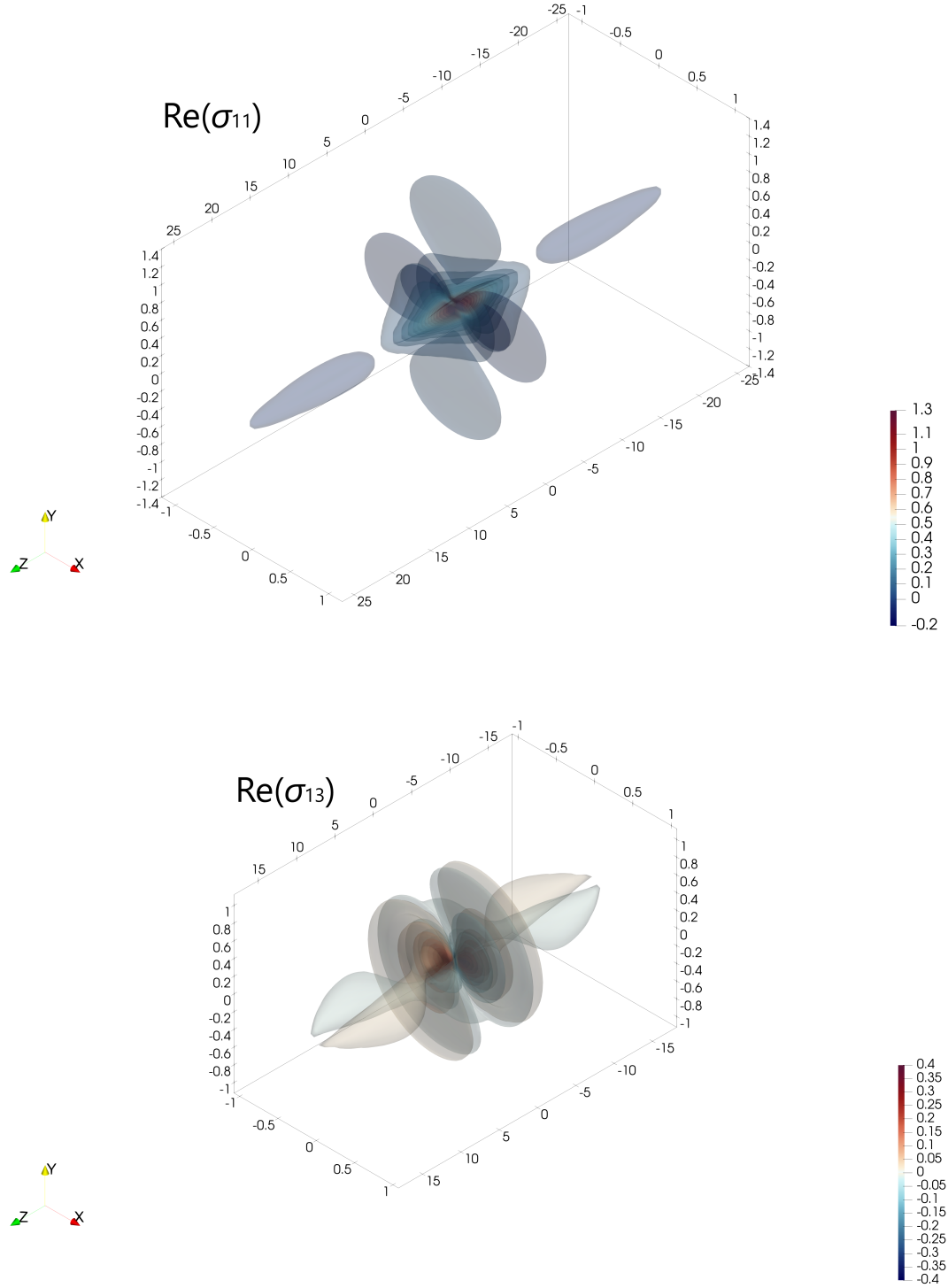


Figure 3.3: 3D contour plot of some selected entries in  $\sigma$ , without the prefactor of Eq. (3.23), so only the part in parenthesis is plotted. The values  $\omega/\Omega = 0.9$ ,  $\text{sign}(\Omega) = 1$  are chosen, and cyclotron harmonics  $n = -3, -2, \dots, 2, 3$  are summed over. The axes indicate the  $x, y, z$  components of the normalised relative distance  $\mathbf{s}/\xi$ .

is already integrable.

A few remarks about the result in Eq. (3.23): This was derived from hot plasma theory without making additional approximations. This means that it inherits the same physics model, including wave reflection, mode conversion, and power dissipation via various mechanisms (including FLR effects). However, one limitation is that it is based on the assumption of a homogenous plasma with uniform magnetic field. Of course this is not the case in a real plasma. However, if the background quantities are varying slowly in space w.r.t. the length scale of the kernel, the so called “locally homogeneous” approximation (LHA) may be used. This works as follows,  $\sigma(\mathbf{r} - \mathbf{r}')$  is extended by prepending an additional argument which keeps track of the slow variation of the background quantities:  $\sigma(\mathbf{r}, \mathbf{r} - \mathbf{r}')$ . When implementing this in a computer model, the homogeneous expression for  $\sigma$  will be used, but wherever it is evaluated it will use the local values of  $\omega_p^2, \Omega, v_T$ . The validity of this approach can be summarised with the following criterion:

$$L_k \ll L_p, \quad (3.26)$$

where  $L_p$  is the length scale of the plasma; e.g. the gradient length of the density, temperature, or magnetic field strength in the plasma. And  $L_k$  is the length scale of the kernel, which was found to be  $\rho_T$  in perpendicular direction, and  $L_n$  in parallel direction. In a magnetised plasma  $\rho_T \ll L_p$  by definition, otherwise particles would not be well confined. On the other hand,  $L_n \ll L_p$  is usually satisfied, but fails near a cyclotron resonance.

There is one more caveat related to the LHA: in a real plasma the  $\mathbf{B}_0$  field will not be perfectly uniform, but the derivation of  $\sigma$  used coordinates based on the direction of  $\mathbf{B}_0$ . If this is varying in space it becomes unclear what definition of  $(x', y', z')$  ought to be used. However, in the LHA the magnetic field varies only slowly compared to the decay of the kernel. This implies that  $\mathbf{B}_0(\mathbf{r}') \approx \mathbf{B}_0(\mathbf{r})$  for any point  $\mathbf{r}'$  that can still contribute significantly towards generating the plasma response at  $\mathbf{r}$ . Thus the ambiguity is resolved by defining the coordinate axes based on the reference point  $\mathbf{B}_0(\mathbf{r})$  alone.

## 3.2 Application in 1D

In order to illustrate the power of the LHA, a very simplified 1D ICRH model is presented that implements the plasma response from Eq. (3.23). It concerns an annulus geometry, described with cylindrical coordinates  $(R, \varphi, Z)$  with  $R \in [R_w, R_e]$  the major radius,  $\varphi \in [0, 2\pi]$  the toroidal angle and  $Z \in \mathbb{R}$  the vertical position. The inside of the modelling domain is filled with plasma, where the density and temperature profiles are given below:

$$N(R) = N_{min} + (N_{max} - N_{min}) \left[ 1 - \left( \frac{R - R_c}{a} \right)^2 \right]^{\alpha_N} \quad (3.27a)$$

$$T(R) = T_{min} + (T_{max} - T_{min}) \left[ 1 - \left( \frac{R - R_c}{a} \right)^2 \right]^{\alpha_T}, \quad (3.27b)$$

with  $R_c$  is the major radius of the magnetic axis,  $a$  the minor radius, and  $\alpha_N, \alpha_T$  the profile peaking factors. In this example the magnetic axis is not exactly in-between the east  $R_e$  and west  $R_w$  walls, so  $a$  has the following definition:

$$a = \begin{cases} R_c - R_w, & R < R_c \\ R_e - R_c, & R \geq R_c. \end{cases} \quad (3.28)$$

The background magnetic field is

$$\mathbf{B}_0(R) = \frac{B_c R_c}{R} \mathbf{e}_\varphi, \quad (3.29)$$

with  $B_c$  being the central magnetic field strength. The perturbations are assumed to be independent of  $Z$ . In addition, a Fourier series can be used to decompose the perturbations in terms of toroidal angle:

$$f(R, \varphi) = \sum_{n_{tor}} f_{n_{tor}}(R) e^{i n_{tor} \varphi}, \quad (3.30)$$

where  $f$  stands for any of the four potentials. Since  $f_0, \mathbf{B}_0$  are independent of toroidal angle, the plasma response is a normal convolution in the  $\varphi$  direction. This means that all modes  $f_{n_{tor}}$  decouple, and can be independently solved for. So the problem reduces to a series of 1D problems. In this case only one mode will be used,  $n_{tor} = 26$ . But in principle the function  $f(R, \varphi)$  can be recovered from the weighted sum in Eq. (3.30).

Maxwell's equations are solved in the weak form, very similar to Eq. (2.71), see [20] for the precise details. In addition the following values for the parameters are chosen:  $N_{min} = 3 \cdot 10^{17} \text{ m}^{-3}$ ,  $N_{max} = 3 \cdot 10^{19} \text{ m}^{-3}$ ,  $T_{min} = 100 \text{ eV}$ ,  $T_{max} = 3 \text{ keV}$ ,  $\alpha_N = 1$ ,  $\alpha_T = 3/2$  for electrons. The rest of the plasma consists of a mix of deuterium (95%) and hydrogen (5%) and  $T_i = T_e$ . In addition,  $R_c = 3 \text{ m}$ ,  $B_c = 3.45 \text{ T}$ ,  $R_w = 2.3 \text{ m}$ ,  $R_e = 4.0 \text{ m}$  and the antenna is modelled as a current sheet at  $R_{ant} = 3.9 \text{ m}$ , with frequency  $\frac{\omega}{2\pi} = 51 \text{ MHz}$ .

The result is shown in Fig. 3.4. Notice that all potentials go to zero on the boundary, except for the normal component of  $\mathbf{A}$  which used a Neumann boundary condition. The wave that is launched from the LFS reaches the cyclotron resonance of H in the core (and 2nd harmonic for D), beyond which some of the energy is transferred to a shorter wavelength mode. Since the model is linear, the values on the vertical axis may be rescaled arbitrarily based on the desired input power.

Although the model geometry is rather simplistic compared to a real tokamak, this model is relatively easily extended to 2D or even 3D. Moreover, the most important dimension to resolve is arguably the  $R$  direction, since in a tokamak (axisymmetry) a slice through the mid-plane cuts through all resonances (and usually all cut-offs as well). Resolving the full poloidal plane would be better of course, but the 1D model at least samples all the important layers in the plasma.

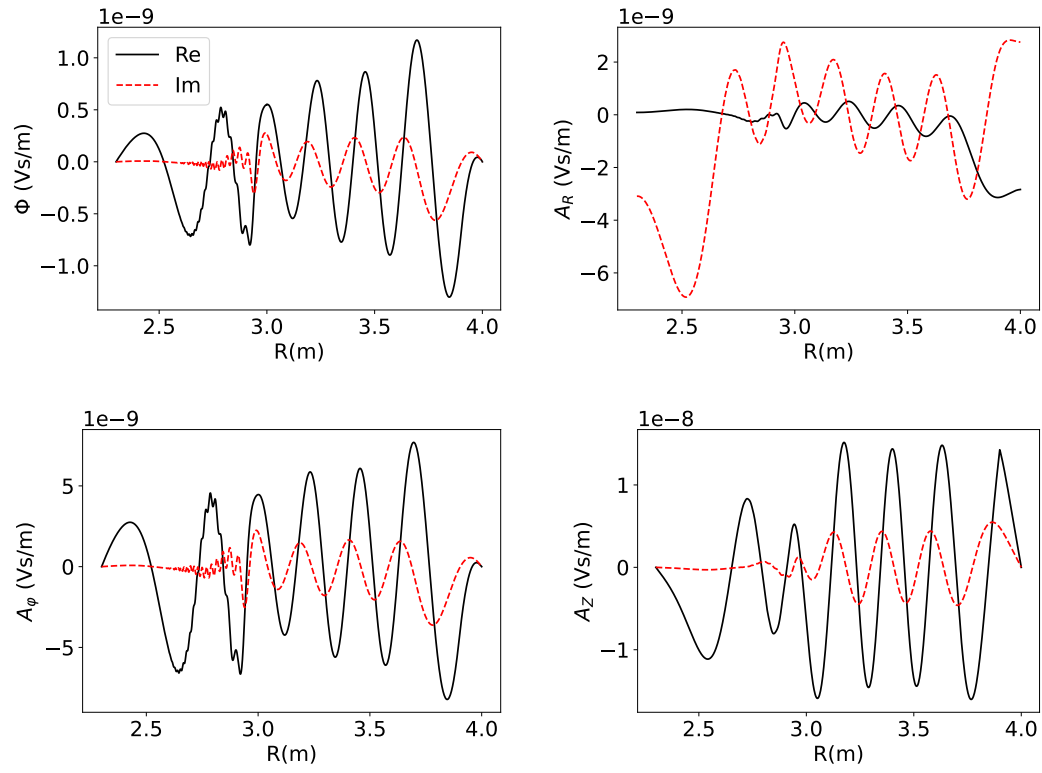


Figure 3.4: All four potentials plotted vs major radius.

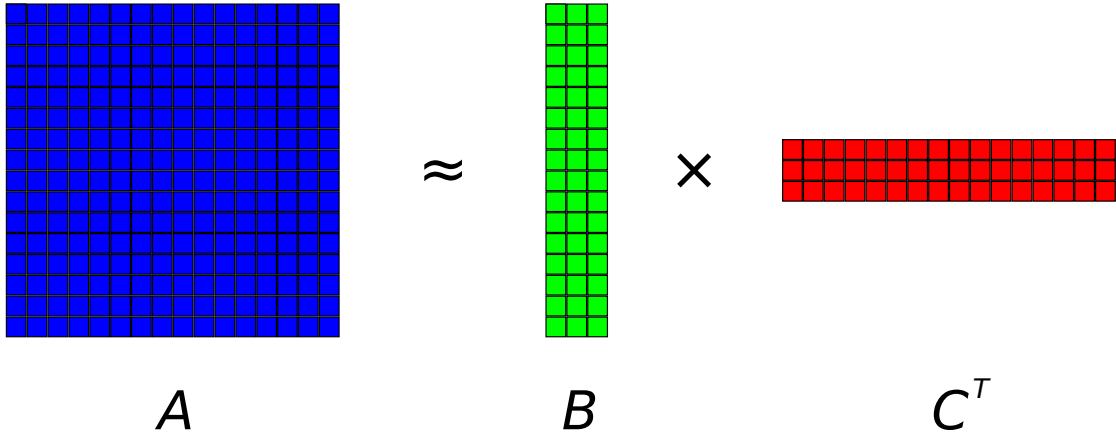


Figure 3.5: Example of a low rank approximation,  $A \approx BC^T$ , where  $A$  is  $N \times N$ , and  $B, C$  are just  $N \times r$ , with  $r \ll N$ .

### 3.3 Hierarchical matrices

Many physical phenomena present themselves in the form of a partial differential equation (PDE), or a system of PDEs. These PDEs can often be converted to integral equations using a Green's function. The integral formulation is often advantageous when dealing with shocks (where the partial derivative may not be defined), excessive noise, or open domains which extend to infinity. Some examples that use an integral formulation are: retarded potentials, boundary element method, and peridynamics. When such an integral operator is discretised with a FEM, the assembly matrix  $A$  will in general be dense. With  $N$  rows, it takes  $O(N^2)$  amount of storage, and  $O(N^3)$  amount of work to solve  $Ax = b$ . However, in many cases the actual information stored in it is much less, also known as “data-sparse” (not to be confused with a sparse matrix). By then approximating the integral kernel, a low-rank approximation of  $A$  can be found, which is significantly cheaper to compute and do operations on. Of course, the solution for  $x$  will not be exact, but we were never hoping on getting an exact solution anyway. Thus, if the error due to this low-rank approximation is less than some tolerance, it is acceptable. An illustration of low rank approximation is given in Fig. 3.5. Of course in practice one wants to avoid constructing  $A$  in the first place, by assembling  $B$  and  $C$  directly. In addition, using a low-rank approximation for the entire matrix  $A$  is often inaccurate, therefore, it is only applied to specific blocks of the matrix, while other blocks remain in full-rank form. This is referred to as a hierarchical matrix, or  $\mathcal{H}$ -matrix. See Hackbush for an introduction into the topic [44]. Nowadays there are libraries available that implement these ideas, e.g. STRUMPACK (C++), HLIBpro (C++) and hm-toolbox [45] (MATLAB).

Equations (2.6) are integro-differential because the plasma response provides an integral term. However, the associated conductivity kernel is relatively smooth, and so it may be approximated using a degenerate kernel. In this example a specific type of  $\mathcal{H}$ -matrix is used, a so called hierarchically off-diagonal low rank (HODLR) matrix. The reason for choosing this format is twofold: It is a simple format for which optimised routines exist, and a user only

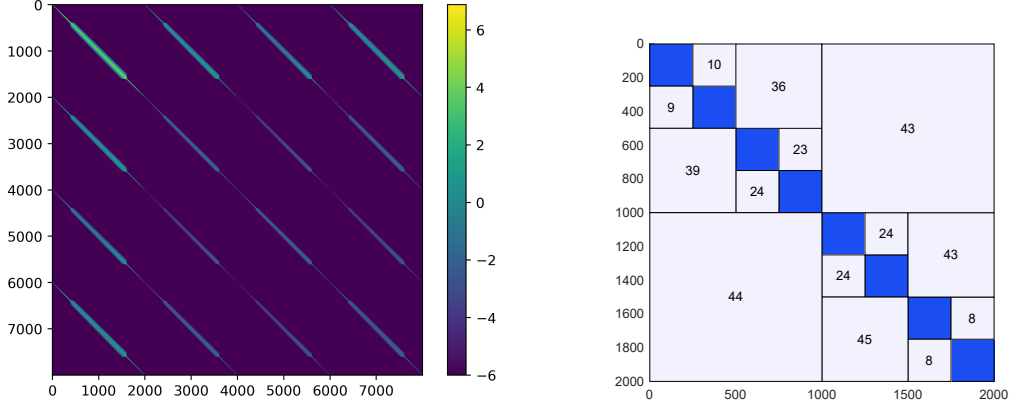


Figure 3.6: On the left, a plot of the assembly matrix  $A$ . The colourbar indicates  $\max(-6, \log_{10}|A_{ij}|)$ . On the right, the approximate form of the top-left  $2000 \times 2000$  block of  $A$ , as given by `hm-toolbox`. The numbers indicate the rank of the compressed blocks, while the blue blocks are full-rank.

needs to provide an element extraction routine, i.e. a function that returns  $A_{ij}$  for a given row index  $i$  and column index  $j$ .

$\mathcal{H}$ -matrices can be applied to the FEM model from the previous section. Since in this case the matrix  $A$  consists of  $4 \times 4$  blocks, associated with the potentials, a HODLR approximation is used for each of the four blocks, illustrated in Fig. 3.6. The structure of  $A$  is relatively smooth, starting from the diagonal and tapering off: The discretised version of the differential operator gives a contribution near the diagonal (only interaction with nearest neighbours), because it is a 1D model and the nodes are arranged in ascending order. The plasma response on the other hand interacts with nodes much further away, see Fig. 3.6. However, this effect drops off rapidly, moving away from the diagonal. In principle this response could be truncated, and a sparse matrix can be used. However, if the mesh resolution becomes large enough to resolve the length scale of the conductivity kernel, the number of non-zeros per row grows with matrix size.  $\mathcal{H}$ -matrices provide a possible way out; as demonstrated, the rank can be reduced significantly, which will help to accelerate the LU decomposition.

Define  $x_1$  to be the approximate solution by solving  $Ax = b$  using standard LU decomposition with a full matrix  $A$ , and  $x_2$  to be the approximate solution when approximating blocks of  $A$  with HODLR format. The quality of the  $\mathcal{H}$  matrix solver can be quantified by defining  $\delta = \|x_2 - x_1\| / \|x_1\|$ . In the test case described above, with 2000 grid points, it was found that  $\delta = 2 \cdot 10^{-9}$  (using the  $L^2$  norm). Some additional parameters are compared in table 3.3. Note that at this scale the savings are limited, but the reduction in resources will be significantly bigger at larger matrix size due to the better time complexity of HODLR matrices. However, the full matrix building already took more than a week on an intel i7-8700 CPU (using 12 threads), so unfortunately it was not feasible to investigate these larger problems. Moreover, recall that

Table 3.3: Comparison of resources for full matrix and HODLR matrix versions of  $A$ . The number of grid points is 2000, which corresponds to 8000 DOFs.

	Full matrix	HODLR matrix
Memory (bit)	$8.192 \cdot 10^9$	$1.553 \cdot 10^9$
Build time (days)	$\approx 8$	-
Factorisation time (s)	8.5	5.2
Solve time (s)	0.04	2.2

the used code [46] is a proof of concept, currently all elements of the matrix  $A$  are computed first, then elements of  $A$  are sampled to construct the  $\mathcal{H}$  matrix. But in a real application this first step would be skipped by directly constructing the HODLR matrix, avoiding the large build time. Such a modification is beyond the scope of this exploratory study, but should not be too difficult to implement<sup>2</sup>.

### 3.4 Summary

For reasons mentioned in this chapter's introduction, it may be beneficial to solve Maxwell's equations in configuration space, as opposed to wavenumber space. However, this requires  $\sigma$  instead of  $\tilde{\sigma}$ . The first has now been found, by making use of the inverse Fourier transform. The relevant length scales of the kernel appear naturally. The kernel  $\sigma$  has furthermore been applied to a simplified example in annulus geometry. Although successful, solving the resulting dense linear algebra problem can be expensive. Therefore more work should be done to optimise the solver. One such strategy has already been hinted at: hierarchical matrices.

---

<sup>2</sup>All that is needed is compiling the C++ code as a library, and making the element extraction routine public. This can then be called directly from within Matlab. The hm-toolbox provides a constructor for HODLR matrices using handle functions.





## 4 Applications of the hot plasma dielectric tensor

LEMan was originally developed for cold plasma [17], however, in order to properly account for power deposition a warm model was added [47], followed by a hot plasma implementation (Maxwellian) [48]. Which was later extended to other distribution functions [49]. Implementation of these later models in LEMan requires a more advanced description of the dielectric tensor, as was derived in chapter 2. For some specific distributions  $f_0$  the dielectric tensor is readily available. However, in plasmas heated by ICRF waves the minority distribution function is often more complicated than a regular bi-Maxwellian. This chapter starts by introducing two additional distribution functions. The corresponding dielectric tensor can be found by substituting  $f_0$  into Eqs. (2.41a) - (2.41h). The new expressions are implemented in LEMan, and then demonstrated for a number of heating scenarios.

This chapter is adapted from the following article, with permission from the publisher. M. Machielsen et al. 2021 Plasma Phys. Control. Fusion **63** 094002, “ICRF modelling in 2D and 3D magnetic configurations using a hot plasma model” [49].

### 4.1 Distribution functions

In order to derive an expression for the dielectric tensor, the background distribution function  $f_0$  must first be known, for each plasma species. A few common types are given here.

#### 4.1.1 Maxwellian and its variations

$$f_0(s, v) = \frac{N(s)}{\pi^{3/2} v_T^3(s)} \exp \left[ -\frac{v^2}{v_T^2(s)} \right], \quad (4.1)$$

with  $N$  the number density,  $v_T = \sqrt{2T/m}$  the thermal velocity and  $s$  the flux surface label. This is the standard Maxwell-Boltzmann distribution, also known as a “Maxwellian”. It is isotropic, meaning the temperature  $T$  is the same for every coordinate direction. And it is non-drifting,

meaning that the bulk flow is zero:

$$\int_{\mathbb{R}^3} d^3 v \mathbf{v} f_0 = \mathbf{0}.$$

If  $f_0$  is non-Maxwellian, collisions attempt to drive it back towards Maxwellian. This does not imply that all distribution functions are Maxwellian in steady state; a balance can set in where the collisional drag is compensated by some external mechanism, such as NBI or ICRH. In those cases an enhanced fast ion population can be sustained, even in steady state. ICRH is also known for creating populations of fast ions with considerably enhanced perpendicular velocity. Such a distribution function is often modelled as the sum of a low energy Maxwellian part, plus a high energy bi-Maxwellian part. The latter can be modelled as follows:

$$f_0(s, v_{\parallel}, v_{\perp}) = \frac{N(s)}{\pi^{3/2} v_{T_{\parallel}}(s) v_{T_{\perp}}^2(s)} \exp \left[ - \left( \frac{v_{\parallel}^2}{v_{T_{\parallel}}^2(s)} + \frac{v_{\perp}^2}{v_{T_{\perp}}^2(s)} \right) \right], \quad (4.2)$$

where  $T_{\parallel}, T_{\perp}$  represent the parallel and perpendicular temperatures respectively. Equation (2.11) indicates that  $f_0$  is conserved when moving along the u.p.t., but the two distribution functions mentioned above do not satisfy this requirement. One way of ensuring  $df/dt|_{u.p.t.} = 0$  is by defining the distribution function  $f_0$  only in terms of constants of motion. Instead of a normal “local” Maxwellian, a so called “canonical” Maxwellian can be defined, which satisfies  $df/dt|_{u.p.t.} = 0$ . However, the difference is often so minute that a local Maxwellian is sufficiently accurate.

To lowest order in gyro-radius, the u.p.t. follows a field line, which thus implies the following requirement,

$$\mathbf{B} \cdot \nabla f_0 = 0. \quad (4.3)$$

The local Maxwellian from Eq. (4.1) does satisfy this. But it is easy to see why the bi-Maxwellian from Eq. (4.2) does not even satisfy the less stringent requirement in Eq. (4.3). Take for example a trapped particle that is placed at its bounce point; it has perpendicular velocity  $v_{\perp}(0) = v_0$ , and no parallel velocity,  $v_{\parallel}(0) = 0$ . Assuming that  $f_0$  is constant along the u.p.t., this requires

$$\frac{v_{\parallel}^2}{v_{T_{\parallel}}^2} + \frac{v_{\perp}^2}{v_{T_{\perp}}^2} = \frac{v_0^2}{v_{T_{\perp}}^2},$$

at any time. As it bounces back some of the perpendicular velocity is converted to parallel velocity. Constant energy requires  $v_{\parallel}^2 = v_0^2 - v_{\perp}^2$ , but constant  $f_0$  requires:

$$v_{\parallel}^2 = \frac{v_{T_{\parallel}}^2}{v_{T_{\perp}}^2} (v_0^2 - v_{\perp}^2),$$

which is contradicting unless  $v_{T_{\parallel}} = v_{T_{\perp}}$ . A modified bi-Maxwellian distribution that satisfies

Eq. (4.3) is given by [39], [50], [51]:

$$f_0(s, E, \mu) = \frac{N_c(s)}{\pi^{3/2} \nu_{T_\parallel}(s) \nu_{T_\perp}^2(s)} \exp \left[ - \left( \frac{\mu B_C}{T_\perp(s)} + \frac{|E - \mu B_C|}{T_\parallel(s)} \right) \right], \quad (4.4)$$

with the magnetic moment (ratio of perpendicular kinetic energy to magnetic field strength)  $\mu = \frac{1}{2} m v_\perp^2 / B$ , energy  $E = \frac{1}{2} m v^2$  and  $N_c$  is the “critical” density<sup>1</sup>. The “critical” magnetic field indicates where the wave-particle resonance occurs. Assuming this happens at the cold cyclotron harmonic  $n$ , the critical field is defined as

$$B_C = \frac{m\omega}{n|q|}. \quad (4.5)$$

In this context, the high field side (HFS) and low field side (LFS) will be defined with respect to this resonance, so HFS ( $B \geq B_C$ ), LFS ( $B < B_C$ ). The local particle density is found by taking the 0<sup>th</sup> moment of the distribution function, and can be related to the critical density:

$$N(s, B) = \int_{\mathbb{R}^3} d^3 v f_0 = N_c(s) \mathcal{C}(s, B), \quad (4.6)$$

with

$$\mathcal{C}(s, B) = \begin{cases} \frac{B/B_C}{1 - (T_\perp/T_\parallel)(1 - B/B_C)} & B \geq B_C \\ \frac{B}{B_C} \frac{1 + (T_\perp/T_\parallel)(1 - B/B_C) - 2(T_\perp/T_\parallel)^{3/2}(1 - B/B_C)^{3/2}}{1 - (T_\perp/T_\parallel)^2(1 - B/B_C)^2} & B < B_C. \end{cases} \quad (4.7)$$

It becomes apparent that the true density  $N$  is not constant on a flux surface. In a real machine there are many reasons for poloidal density variation, one of them being that trapped particles tend to align their bounce tips at the resonant surface. This happens because each time an ion passes the resonance layer, it gets a kick that is predominantly in perpendicular direction. I.e. on average  $\nu_\perp$  is increased by each kick, but less so for  $\nu_\parallel$ , see Eq. (5.30). This means that ions are trapped more and more deeply, so the bounce tips slide from the HFS to the LFS. Once the bounce tips are fully on the LFS, the particle does not resonate anymore, and therefore no longer gets any kick. In the end this amounts to an accumulation on the LFS. Which is also seen in VENUS-LEVIS simulations, see e.g. Fig. 4.19.

Taking the flux surface average of Eq. (4.6) yields:

$$\langle N \rangle = N_c \langle \mathcal{C} \rangle \approx N_c = N(s, B_C), \quad (4.8)$$

with the averaging operator denoted by angle brackets  $\langle \rangle$ . The latter equality explains the name “critical” density, as it is equal to the number density wherever  $B = B_C$ , which is also approximately equal to the flux surface averaged density.

Note that the contours of constant  $f_0$  for the modified bi-Maxwellian are not smooth every-

<sup>1</sup>The notation of Eq. (4.4) follows that of [52], slightly deviating from what was used in [49]. This proves to be more convenient as some factors of  $\sqrt{T_\parallel/T_\perp}$  disappear, but it is completely equivalent in terms of the physics.

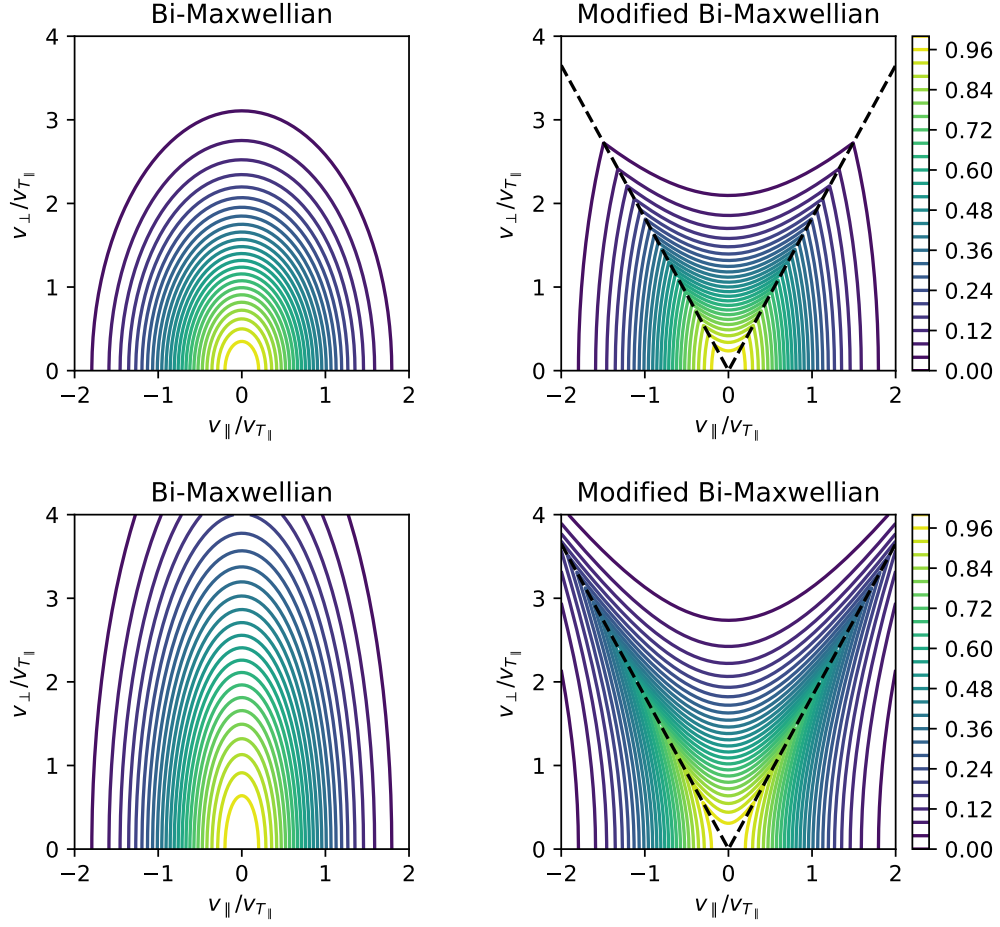


Figure 4.1: Comparison of the regular and modified bi-Maxwellian distributions. Contour plot of  $f_0(s, v_{\parallel}, v_{\perp})/f_0(s, 0, 0)$ , for  $B_C/B = 1.3$  and  $T_{\perp}/T_{\parallel} = 3$  (top row),  $T_{\perp}/T_{\parallel} = 10$  (bottom row). The contours of the regular bi-Maxwellian form ellipses, while those of the modified distribution only do so on the high field side. Note that both velocity components are normalised by  $v_{T_{\parallel}}$ .

where, see Fig. 4.1. The term  $|E - \mu B_C|$  is responsible for this, which is zero when

$$v_\perp = |v_\parallel| \sqrt{\frac{B}{B_C - B}}. \quad (4.9)$$

This expression describes the line on which the tips lie, indicated by the dashed line in Fig. 4.1. And if  $B_{\text{bounce}} = B_C$  it also coincides with the trapped-passing boundary. As the temperature anisotropy  $T_\perp / T_\parallel$  is increased, the contours become ever more stretched along the line in Eq. (4.9). These lobes are also seen in simulations, where they are more rounded [53]–[55], and are sometimes referred to as “rabbit ears”. Note also that in the isotropic case  $T_\perp / T_\parallel = 1$ , Eq. (4.4) recovers a Maxwellian on the HFS, but not on the LFS because of the absolute value. Although Eq. (4.4) is merely an approximation, it captures the essential physics, while still being analytically tractable. It is therefore useful to derive a dielectric tensor for this type of distribution function.

#### 4.1.2 Marker distribution function

The distribution function might not fit any of the above mentioned types. In case the distribution would come from a Monte Carlo code  $f_0$  is then given by the sum over a collection of test particles (markers), with weights  $w_k$ :

$$f_0(\mathbf{r}, v_\parallel, v_\perp, \phi) = \sum_k w_k \delta(\mathbf{r} - \mathbf{r}_k) \delta(v_\parallel - v_{\parallel,k}) \frac{\delta(v_\perp - v_{\perp,k})}{v_\perp} \delta(\phi - \phi_k), \quad (4.10)$$

where  $\delta$  indicates the Dirac delta function,  $\phi$  the gyro angle and  $k$  the marker index. The  $1/v_\perp$  appears because of the Jacobian determinant in cylindrical coordinates. Using this raw distribution function directly in the computation of the dielectric tensor would be unnecessarily expensive, and would suffer from noise. For this reason some level of averaging/smoothing will be introduced, but on a scale smaller than the typical scales in configuration and velocity space which may be expected from physical arguments. To this end,  $f_0$  at a point  $\mathbf{r}$  can be approximated as its average value in a volume  $V(\mathbf{r})$ . What this volume is precisely will be defined later on.

$$\bar{f}_0(\mathbf{r}, v_\parallel, v_\perp, \phi) = \frac{1}{V(\mathbf{r})} \sum_j w_j \delta(v_\parallel - v_{\parallel,j}) \frac{\delta(v_\perp - v_{\perp,j})}{v_\perp} \delta(\phi - \phi_j), \quad (4.11)$$

where the sum is only over markers  $j$  which are inside of the volume  $V$ . The function  $\bar{f}_0$  is to good approximation independent of gyro angle, see Eq. (2.15), so it can also be averaged over  $\phi$ :

$$\bar{f}_0(\mathbf{r}, v_\parallel, v_\perp) = \frac{1}{2\pi} \frac{1}{V(\mathbf{r})} \sum_j w_j \delta(v_\parallel - v_{\parallel,j}) \frac{\delta(v_\perp - v_{\perp,j})}{v_\perp}. \quad (4.12)$$

As touched on before, there is no need to resolve all velocity scales either. So the delta function in parallel velocity may be replaced by another sharply peaked shape function that decays with a standard deviation much less than  $v_{T_\parallel}$ . Reminder, the Dirac delta can be expressed as

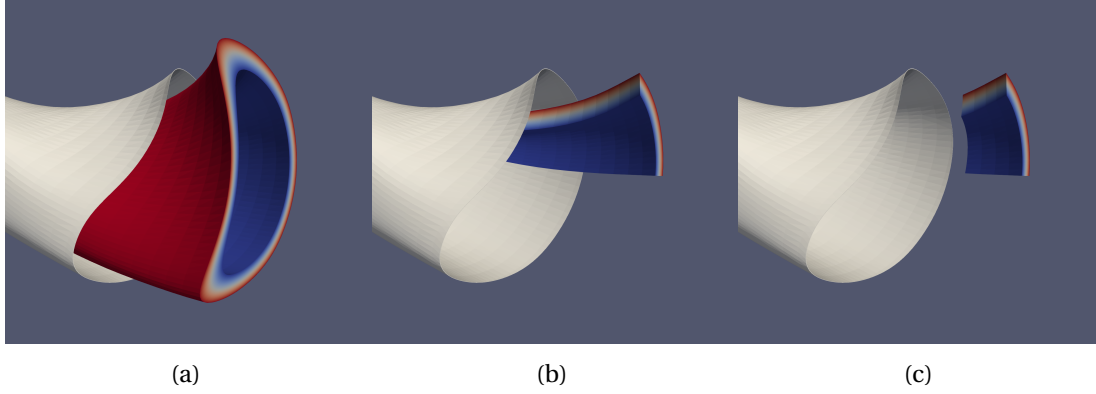


Figure 4.2: Three choices of averaging volume for W7-X. In white the LCFS, in colour the volume  $V$ , with blue indicating the radial inside, and red the radial outside. From left to right: a full flux tube, a filament, and a section of a filament. The size of the volume has been exaggerated in order to see it more clearly, so not to scale.

the limit of a Gaussian:

$$\delta(x) = \lim_{\sigma \rightarrow 0} \frac{1}{\sqrt{\pi}|\sigma|} \exp\left(-\frac{x^2}{\sigma^2}\right). \quad (4.13)$$

Swapping the term  $\delta(v_{\parallel} - v_{\parallel,j})$  with a Gaussian shape function gives

$$f_0(\mathbf{r}, v_{\parallel}, v_{\perp}) = \frac{1}{2\pi} \frac{1}{V(\mathbf{r})} \sum_j w_j \frac{1}{\sqrt{\pi}\sigma_j} \exp\left[-\left(\frac{v_{\parallel} - v_{\parallel,j}}{\sigma_j}\right)^2\right] \frac{\delta(v_{\perp} - v_{\perp,j})}{v_{\perp}}. \quad (4.14)$$

Choosing the parameter  $\sigma$  is a trade-off between precision and speed. A small  $\sigma$  allows for a very refined representation of  $f_0$ , at the cost of using many more samples. In order to avoid using unnecessary resources,  $\sigma$  should be chosen as large as possible, while still being smaller than the typical velocity scale  $v_{T_{\parallel}}$ . Also, in general  $\sigma_j$  can be chosen independently for each marker, hence the subscript  $j$ . Such optimisation may be useful in the high energy tail, but it has not been experimented with in this work.

Another reason to choose a different shape function for the  $v_{\parallel}$  term is the singularity of Eq. (2.37). By choosing a Gaussian, we can smooth over it. The integral over  $v_{\perp}$  has no such difficulty, hence it is kept in its raw form, a delta function.

#### 4.1.2.1 Choosing the averaging volume

The volume  $V(\mathbf{r})$  should be chosen as large as possible for improved statistics, while still being able to resolve the length scale on which moments (density, flow rate, pressure, etc...) of  $f_0$  change considerably. The choice therefore depends strongly on the scenario, several examples are shown in Fig. 4.2. These volumes can be described as: (a) the volume between two flux surfaces, with  $\mathbf{r}$  lying on the central flux surface, (b) a filament and (c) a section of a filament. In typical scenarios configuration (a) would suffice, as moments of  $f_0$  rapidly equilibrate on

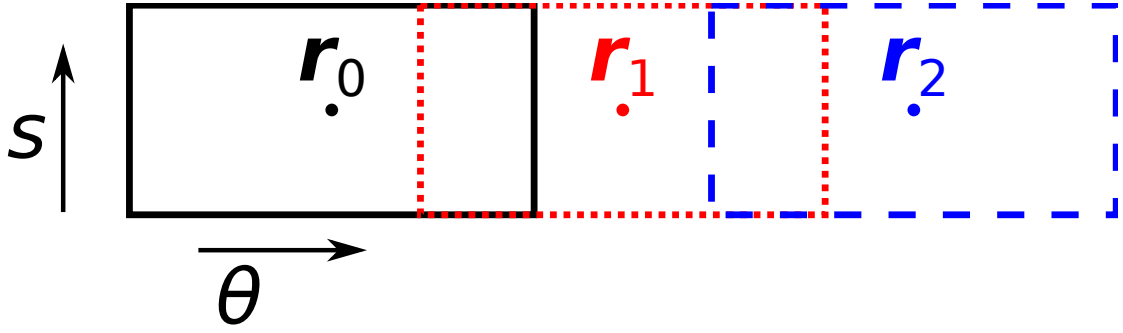


Figure 4.3: Cartoon showing three sample points, with their associated averaging volumes (filament type), in the poloidal plane.

a flux surface, thus it would make sense to average over both angular directions. However, this is not compatible with the modified bi-Maxwellian from Eq. (4.4) because of the poloidal density variation. In some cases even volume (b) may not suffice. Option (c) provides an even higher degree of refinement but it is unlikely to be used in practice. Even when there is very precise heating or fuelling with NBI for instance, the transport along the field lines is much faster than the time scale on which moments of  $f_0$  significantly change. However, it may be useful in case there are regions where lots of trapped particles reside. Note that the density variation is not just poloidal, but also toroidal in a stellarator:  $N(s, B) = N(s, B(s, \theta, \varphi))$ .

Note also that the domain is not cut up in a fixed number of volumes. Imagine instead the volume  $V(\mathbf{r})$  “centred” on the sample point  $\mathbf{r}$ , so as this point moves around, the volume also moves, see Fig. 4.3. Where the term “centred” is to be interpreted based on the volume type, e.g. for volume (a) the point  $\mathbf{r}$  is not the geometric centre. Hence, the size of the volume does not depend on the number of sample points, but on the number of available markers, and expected length scales of the moments of  $f_0$ .

## 4.2 Derivation of the dielectric tensor

### 4.2.1 Modified bi-Maxwellian

In order to compute the dielectric tensor given  $f_0$  from Eq. (4.4), it is convenient to look at the LFS and HFS separately. On the HFS, the absolute value in the exponent of  $f_0$  can be removed as  $E \geq \mu B_C$  is guaranteed. This yields an expression very similar to the normal bi-Maxwellian,

$$\begin{aligned} f_0(v_\perp, v_\parallel) &= \frac{N_c F(v_\parallel)}{\pi v_{T_\perp}^2} \exp\left(-\frac{v_\perp^2}{v_{T_\perp}^2} C_+\right) \\ F(v_\parallel) &= \frac{1}{\sqrt{\pi} v_{T_\parallel}} \exp\left(-\frac{v_\parallel^2}{v_{T_\parallel}^2}\right) \\ C_\pm &= \frac{B_C}{B} \pm \frac{T_\perp}{T_\parallel} \left(1 - \frac{B_C}{B}\right), \end{aligned} \tag{4.15}$$

## Chapter 4. Applications of the hot plasma dielectric tensor

for which the dielectric tensor is well established. On the HFS,  $\mathcal{C}C_+ = 1$ , so  $f_0$  can be written as:

$$f_0(v_\perp, v_\parallel) = \frac{N}{\pi^{3/2} v_{T_\parallel} u^2} \exp \left[ - \left( \frac{v_\parallel^2}{v_{T_\parallel}^2} + \frac{v_\perp^2}{u^2} \right) \right], \quad (4.16)$$

which matches exactly Eq. (4.2), except  $v_{T_\perp}$  has been replaced by  $u = v_{T_\perp}/C_+$ . So the previously derived dielectric tensor from Eq. (2.50) can be reused, with this simple substitution, yielding:

$$K_0 = 2\tilde{\mathcal{W}} \sum_{n=-\infty}^{\infty} \tilde{\lambda} (I_n(\tilde{\lambda}) - I'_n(\tilde{\lambda})) \left[ Z(\zeta_n) + \frac{|k_z|v_{T_\parallel}}{\omega} \left( 1 - \frac{T_\perp}{T_\parallel C_+} \right) \frac{Z'(\zeta_n)}{2} \right] \quad (4.17a)$$

$$K_1 = \tilde{\mathcal{W}} \sum_{n=-\infty}^{\infty} \frac{n^2 I_n(\tilde{\lambda})}{\tilde{\lambda}} \left[ Z(\zeta_n) + \frac{|k_z|v_{T_\parallel}}{\omega} \left( 1 - \frac{T_\perp}{T_\parallel C_+} \right) \frac{Z'(\zeta_n)}{2} \right] \quad (4.17b)$$

$$K_2 = -i\tilde{\mathcal{W}} \sum_{n=-\infty}^{\infty} n (I_n(\tilde{\lambda}) - I'_n(\tilde{\lambda})) \left[ Z(\zeta_n) + \frac{|k_z|v_{T_\parallel}}{\omega} \left( 1 - \frac{T_\perp}{T_\parallel C_+} \right) \frac{Z'(\zeta_n)}{2} \right] \quad (4.17c)$$

$$K_3 = -\tilde{\mathcal{W}} \sum_{n=-\infty}^{\infty} I_n(\tilde{\lambda}) \left[ 1 - \frac{n\Omega}{\omega} \left( 1 - \frac{T_\perp}{T_\parallel C_+} \right) \right] \zeta_n Z'(\zeta_n) \quad (4.17d)$$

$$K_4 = -\text{sign}(k_z) \tilde{\mathcal{W}} \frac{k_\perp v_{T_\parallel}}{\Omega} \sum_{n=-\infty}^{\infty} \frac{n I_n(\tilde{\lambda})}{\tilde{\lambda}} \left[ \frac{T_\perp}{T_\parallel C_+} + \frac{n\Omega}{\omega} \left( 1 - \frac{T_\perp}{T_\parallel C_+} \right) \right] \frac{Z'(\zeta_n)}{2} \quad (4.17e)$$

$$K_5 = i\text{sign}(k_z) \tilde{\mathcal{W}} \frac{k_\perp v_{T_\parallel}}{\Omega} \sum_{n=-\infty}^{\infty} (I_n(\tilde{\lambda}) - I'_n(\tilde{\lambda})) \left[ \frac{T_\perp}{T_\parallel C_+} + \frac{n\Omega}{\omega} \left( 1 - \frac{T_\perp}{T_\parallel C_+} \right) \right] \frac{Z'(\zeta_n)}{2}, \quad (4.17f)$$

with

$$\tilde{\lambda} = \lambda/C_+ \quad (4.18a)$$

$$\tilde{\mathcal{W}} = \frac{\omega_p^2 e^{-\tilde{\lambda}}}{\omega |k_z| v_{T_\parallel}}. \quad (4.18b)$$

In practice, these  $K$  elements will only be used for the contribution of the resonant minority ion species, for the other populations a Maxwellian distribution function is assumed. Therefore the species subscript is omitted. The identity matrix coming from the vacuum contribution is also not included. The form in which the elements of  $K$  are shown in Eq. (4.17) is not unique, they can be rewritten using identities of the modified Bessel functions. Remark also that  $\mathcal{C}, C_+$  are usually nearly equal to 1, thus the deformation from a normal bi-Maxwellian is not very large on the HFS.

Unfortunately, no analytical expression has been derived for the LFS. The main difficulty stems from the term  $|E - \mu B_C|$ , as it splits the velocity space integral in two. First define the following



quantities:

$$x = v_{\parallel} / v_{T_{\parallel}} \quad (4.19a)$$

$$y = \frac{v_{\perp}}{v_{T_{\perp}}} \sqrt{\frac{B_C}{B}} \quad (4.19b)$$

$$a = \frac{k_{\perp} v_{T_{\perp}}}{\Omega} \sqrt{\frac{B}{B_C}} \quad (4.19c)$$

$$s = \frac{T_{\perp}}{T_{\parallel}} \left( \frac{B}{B_C} - 1 \right). \quad (4.19d)$$

Also note that  $a^2 = 2\lambda B/B_C$ . On the LFS, the distribution function can be written as:

$$f_0(v_{\perp}, v_{\parallel}) = \frac{N}{\pi^{3/2} v_{T_{\parallel}} v_{T_{\perp}}^2 \mathcal{C}} e^{-y^2 - |x^2 + sy^2|}. \quad (4.20)$$

Since  $s < 0$  on the LFS, the absolute value cannot be simplified without splitting the integral in two parts. The variables  $F_{\perp}, F_z$  can be computed:

$$F_{\perp} = -\frac{2y^2 e^{-y^2 - |x^2 + sy^2|}}{\pi^{3/2} v_{T_{\parallel}} v_{T_{\perp}}^2 \mathcal{C}} \left[ 1 - \frac{k_z v_{T_{\parallel}}}{\omega} x + \text{sign}(x^2 + sy^2) \left( s + \frac{k_z v_{T_{\parallel}}}{\omega} \frac{T_{\perp}}{T_{\parallel}} x \right) \right] \quad (4.21a)$$

$$F_z = -\frac{2x^2 e^{-y^2 - |x^2 + sy^2|}}{\pi^{3/2} v_{T_{\parallel}} v_{T_{\perp}}^2 \mathcal{C}} \left[ \frac{n\Omega}{\omega} \frac{T_{\parallel} B_C}{T_{\perp} B} + \text{sign}(x^2 + sy^2) \left( 1 - \frac{n\Omega}{\omega} \frac{B_C}{B} \right) \right], \quad (4.21b)$$

using

$$\begin{aligned} \frac{\partial f_0}{\partial x} &= -2x f_0 \text{sign}(x^2 + sy^2) \\ \frac{\partial f_0}{\partial y} &= -2y f_0 [1 + s \text{sign}(x^2 + sy^2)]. \end{aligned}$$

Technically, these derivatives are not defined at  $x^2 + sy^2 = 0$ , but in real life there would not be such a perfect discontinuity anyway, it would be smoothed. The coefficients of the dielectric

tensor, Eqs. (2.41a)-(2.41h), can then be written in the following normalised form:

$$K_0 = \frac{4\Omega^2\omega_p^2}{\sqrt{\pi}\omega k_z k_\perp^2 v_{T_\parallel} v_{T_\perp}^2 \mathcal{C}} \sum_{n=-\infty}^{\infty} \int_{-\infty}^{\infty} \frac{dx}{x-x_n} \left[ \left(1 - \frac{k_z v_{T_\parallel}}{\omega} x\right) M_3(x) + \left(s + \frac{k_z v_{T_\parallel}}{\omega} \frac{T_\perp}{T_\parallel} x\right) N_3(x) \right] \quad (4.22a)$$

$$K_1 = \frac{4\Omega^2\omega_p^2}{\sqrt{\pi}\omega k_z k_\perp^2 v_{T_\parallel} v_{T_\perp}^2 \mathcal{C}} \sum_{n=-\infty}^{\infty} n^2 \int_{-\infty}^{\infty} \frac{dx}{x-x_n} \left[ \left(1 - \frac{k_z v_{T_\parallel}}{\omega} x\right) M_1(x) + \left(s + \frac{k_z v_{T_\parallel}}{\omega} \frac{T_\perp}{T_\parallel} x\right) N_1(x) \right] \quad (4.22b)$$

$$K_2 = i \frac{4\Omega\omega_p^2}{\sqrt{\pi}\omega k_z k_\perp v_{T_\parallel} v_{T_\perp}^2 \mathcal{C}} \sqrt{\frac{B}{B_C}} \sum_{n=-\infty}^{\infty} n \int_{-\infty}^{\infty} \frac{dx}{x-x_n} \left[ \left(1 - \frac{k_z v_{T_\parallel}}{\omega} x\right) M_2(x) + \left(s + \frac{k_z v_{T_\parallel}}{\omega} \frac{T_\perp}{T_\parallel} x\right) N_2(x) \right] \quad (4.22c)$$

$$K_3 = \frac{4\omega_p^2}{\sqrt{\pi}\omega k_z v_{T_\parallel} \mathcal{C}} \frac{B}{B_C} \sum_{n=-\infty}^{\infty} \int_{-\infty}^{\infty} \frac{dx x^2}{x-x_n} \left[ \frac{n\Omega}{\omega} \frac{T_\parallel B_C}{T_\perp B} M_1(x) + \left(1 - \frac{n\Omega}{\omega} \frac{B_C}{B}\right) N_1(x) \right] \quad (4.22d)$$

$$K_4 = \frac{4\Omega\omega_p^2}{\sqrt{\pi}\omega k_z k_\perp v_{T_\parallel}^2 \mathcal{C}} \frac{B}{B_C} \sum_{n=-\infty}^{\infty} n \int_{-\infty}^{\infty} \frac{dx x}{x-x_n} \left[ \frac{n\Omega}{\omega} \frac{T_\parallel B_C}{T_\perp B} M_1(x) + \left(1 - \frac{n\Omega}{\omega} \frac{B_C}{B}\right) N_1(x) \right] \quad (4.22e)$$

$$K_5 = i \frac{4\omega_p^2 v_{T_\perp}}{\sqrt{\pi}\omega k_z v_{T_\parallel}^2 \mathcal{C}} \left(\frac{B}{B_C}\right)^{3/2} \sum_{n=-\infty}^{\infty} \int_{-\infty}^{\infty} \frac{dx x}{x-x_n} \left[ \frac{n\Omega}{\omega} \frac{T_\parallel B_C}{T_\perp B} M_2(x) + \left(1 - \frac{n\Omega}{\omega} \frac{B_C}{B}\right) N_2(x) \right] \quad (4.22f)$$

$$K_6 = \frac{4\Omega\omega_p^2}{\sqrt{\pi}\omega k_z k_\perp v_{T_\perp}^2 \mathcal{C}} \sum_{n=-\infty}^{\infty} n \int_{-\infty}^{\infty} \frac{dx x}{x-x_n} \left[ \left(1 - \frac{k_z v_{T_\parallel}}{\omega} x\right) M_1(x) + \left(s + \frac{k_z v_{T_\parallel}}{\omega} \frac{T_\perp}{T_\parallel} x\right) N_1(x) \right] \quad (4.22g)$$

$$K_7 = i \frac{4\omega_p^2}{\sqrt{\pi}\omega k_z v_{T_\perp} \mathcal{C}} \sqrt{\frac{B}{B_C}} \sum_{n=-\infty}^{\infty} \int_{-\infty}^{\infty} \frac{dx x}{x-x_n} \left[ \left(1 - \frac{k_z v_{T_\parallel}}{\omega} x\right) M_2(x) + \left(s + \frac{k_z v_{T_\parallel}}{\omega} \frac{T_\perp}{T_\parallel} x\right) N_2(x) \right], \quad (4.22h)$$

with the functions  $M, N$  defined as follows:

$$M_1(x) = \int_0^\infty y e^{-|x^2+sy^2|-y^2} J_n^2(ay) dy \quad (4.23a)$$

$$M_2(x) = \int_0^\infty y^2 e^{-|x^2+sy^2|-y^2} J_n(ay) J'_n(ay) dy \quad (4.23b)$$

$$M_3(x) = \int_0^\infty y e^{-|x^2+sy^2|-y^2} [a^2 y^2 J_n'^2(ay) - n^2 J_n^2(ay)] dy \quad (4.23c)$$

$$N_1(x) = \int_0^\infty \text{sign}(x^2+sy^2) y e^{-|x^2+sy^2|-y^2} J_n^2(ay) dy \quad (4.23d)$$

$$N_2(x) = \int_0^\infty \text{sign}(x^2+sy^2) y^2 e^{-|x^2+sy^2|-y^2} J_n(ay) J'_n(ay) dy \quad (4.23e)$$

$$N_3(x) = \int_0^\infty \text{sign}(x^2+sy^2) y e^{-|x^2+sy^2|-y^2} [a^2 y^2 J_n'^2(ay) - n^2 J_n^2(ay)] dy. \quad (4.23f)$$

Clearly, these functions are even in  $x$ . This fact, combined with the trick from Eq. (A.37) can

be used to prove the following:

$$\begin{aligned} & \int_{-\infty}^{\infty} \frac{dx}{x-x_n} \left[ \left( 1 - \frac{k_z v_{T_{\parallel}}}{\omega} x \right) M(x) + \left( s + \frac{k_z v_{T_{\parallel}}}{\omega} \frac{T_{\perp}}{T_{\parallel}} x \right) N(x) \right] = \\ & \int_{-\infty}^{\infty} \frac{dx}{x-x_n} \left[ \left( 1 - \frac{k_z v_{T_{\parallel}}}{\omega} x_n \right) M(x) + \left( s + \frac{k_z v_{T_{\parallel}}}{\omega} \frac{T_{\perp}}{T_{\parallel}} x_n \right) N(x) \right] = \\ & \frac{T_{\perp} B}{T_{\parallel} B_C} \int_{-\infty}^{\infty} \frac{dx}{x-x_n} \left[ \frac{n\Omega}{\omega} \frac{T_{\parallel} B_C}{T_{\perp} B} M(x) + \left( 1 - \frac{n\Omega}{\omega} \frac{B_C}{B} \right) N(x) \right]. \end{aligned}$$

Thus, once again,  $K_6 = K_4$  and  $K_7 = K_5$ , hence these duplicates will not be shown going forward. In summary, the elements of  $K$  in Eq. (4.22a)-(4.22f) can be cast into the following common form:

$$\begin{aligned} K_l &= \Upsilon_l \sum_{n=-\infty}^{\infty} \varsigma_{l,n} \int_{\gamma} \left( p_{l,0} M_{h_l}(x) + p_{l,1} N_{h_l}(x) + \frac{q_{l,0} M_{h_l}(x) + q_{l,1} N_{h_l}(x)}{x-x_n} \right) dx \\ &= \Upsilon_l \sum_{n=-\infty}^{\infty} \varsigma_{l,n} (p_{l,0} \Gamma_{h_l} + p_{l,1} \Delta_{h_l} + q_{l,0} \Phi_{h_l}(\zeta_n) + q_{l,1} \Psi_{h_l}(\zeta_n)), \end{aligned} \quad (4.24)$$

with the coefficients given in table A.1 and

$$\Gamma_h = \int_{-\infty}^{\infty} M_h(x) dx = 2 \int_0^{\infty} M_h(x) dx \quad (4.25a)$$

$$\Delta_h = \int_{-\infty}^{\infty} N_h(x) dx = 2 \int_0^{\infty} N_h(x) dx \quad (4.25b)$$

$$\Phi_h(z) = \int_{\gamma} \frac{M_h(x)}{x-z} dx \quad (4.25c)$$

$$\Psi_h(z) = \int_{\gamma} \frac{N_h(x)}{x-z} dx. \quad (4.25d)$$

The integral over  $x$  in Eq. (4.24) can be written in terms of a Hilbert transform, analogous to that used in section A.3.1:

$$\Phi_h(z) = \int_{\gamma} \frac{M_h(x)}{x-z} dx = \pi (-\mathcal{H}(M_h(x))(z) + i M_h(z)). \quad (4.26)$$

However, this is not needed in practice, as the singularity is a removable one. Start by adding and subtracting  $M_h(z)$ , the extra integral that appears vanishes because of symmetry (real  $z$ ). Now the numerator and denominator both vanish as  $x \rightarrow z$ . Lastly, the integral can be “folded”, to save on sampling points when integrating numerically (using the fact that  $M$  is even):

$$\begin{aligned} \Phi_h(z) &= \int_{\gamma} \frac{M_h(x)}{x-z} dx = PV \int_{-\infty}^{\infty} \frac{M_h(x)}{x-z} dx + \pi i M_h(z) \\ &= PV \int_{-\infty}^{\infty} \frac{M_h(x) - M_h(z)}{x-z} dx + M_h(z) PV \int_{-\infty}^{\infty} \frac{1}{x-z} dx + \pi i M_h(z) \\ &= 2z PV \int_0^{\infty} \frac{M_h(x) - M_h(z)}{x^2 - z^2} dx + \pi i M_h(z). \end{aligned} \quad (4.27)$$

The same procedure can be applied to  $\Psi_h$ .

The implementation in LEMan combines the integrals of  $\Gamma_s, \Delta_s, \Phi_s, \Psi_s$  into one, in order to avoid numerical cancellation issues at large  $z$ . Secondly, most cpu time in computing these integrals is spent on evaluating the Bessel functions. Since these  $J_n$  depend just on  $ay$ , not  $x$ , it seems logical to pre-compute these on a  $y$  grid once, then re-using these for different  $x$  values. This however will not yield accurate results, as the term  $e^{-|x^2+sy^2|}$  in Eq. (4.23) becomes very sharply peaked around  $y = x/\sqrt{|s|}$  for  $s < 0, x > 1$ . Therefore it is more efficient to recompute the Bessel functions for every  $x$  value, on a new  $y$  grid with refinement around  $y = x/\sqrt{|s|}$ . Additionally, the upper limit of the integral over  $x$  can be truncated, as the integrand vanishes for large  $x$ . The infinite sum over all cyclotron harmonics remains, however, this sum can be truncated rapidly since typical ICRH scenarios do not involve resonances with  $n > 3$ .

The  $K$  elements from Eq. (4.24) will be applied to a JET-like plasma in section 4.3.

### 4.2.2 Marker distribution

The dielectric tensor associated with the distribution function from Eq. (4.14) is given by

$$\begin{aligned} K_\ell &= \frac{\omega_p^2 / (\omega |k_z|)}{\sum_j w_j} \sum_j \frac{w_j}{v_{\perp,j}} \sum_{n=-\infty}^{\infty} \left( c_{\ell,j} Z(\xi_{n,j}) - \frac{1}{2} d_{\ell,j} Z'(\xi_{n,j}) \right) \\ &= \frac{q^2}{\epsilon_0 \omega |k_z| m V} \sum_j \frac{w_j}{v_{\perp,j}} \sum_{n=-\infty}^{\infty} \left( c_{\ell,j} Z(\xi_{n,j}) - \frac{1}{2} d_{\ell,j} Z'(\xi_{n,j}) \right), \end{aligned} \quad (4.28)$$

which was derived by plugging in Eq. (4.14) into Eqs. (2.41a)-(2.41h). See section A.8 for the expressions of the coefficients. Contrary to the (modified) bi-Maxwellian, this type of distribution function does not guarantee  $K_6 = K_4$ ,  $K_7 = K_5$ , so  $K_6$  and  $K_7$  must be kept. Note that  $K_\ell$  in Eq. (4.28) is not the full dielectric tensor, but only the contribution of one species of markers. To find the total dielectric tensor we must sum over all species, and the vacuum contribution (identity matrix).

In order to validate this marker based approach, a comparison is made for D-(H) minority heating in the JET tokamak, see case A of table 4.2. A Maxwellian distribution function was assumed for all plasma species, and the H minority was sampled with markers. From Fig. 4.4 it is seen that the simulation converges to the reference model if a sufficient number of markers is used. Most notably are the regions with negative power density, which vanish with increased marker count. Total power fractions are given in table 4.1. The markers were generated using VENUS-LEVIS, and binned in volumes with  $\Delta s = 0.01, \Delta \theta = 0.16$  rad,  $\Delta \varphi = \infty$ , where  $s$  is the normalised toroidal flux. This means that the averaging volume is a filament, exploiting the toroidal symmetry. In this test  $\sigma_j = 40$  km/s was used, for all markers. In case the phase-space gradients of the distribution function are stronger, a smaller averaging volume and smoothing parameter  $\sigma_j$  may be required.

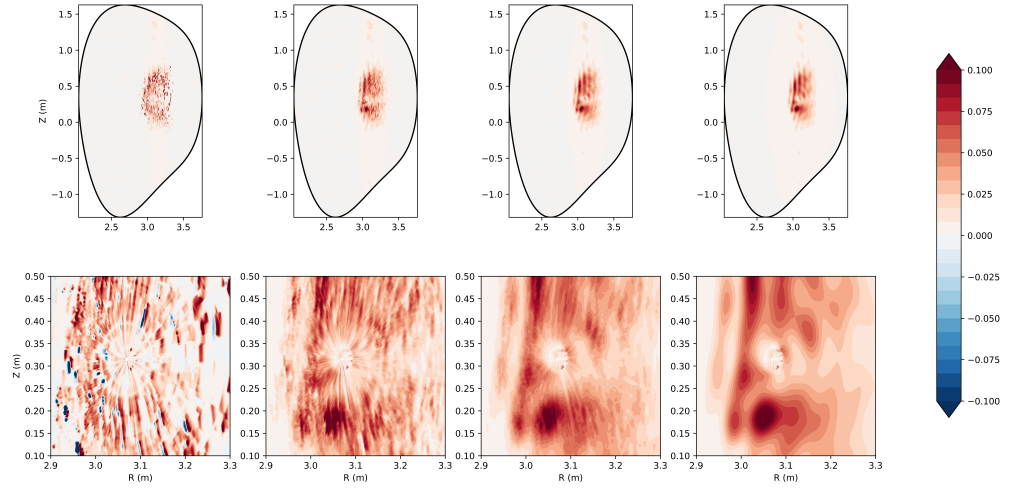


Figure 4.4: D-(H) minority heating, H power density shown. From left to right the columns correspond to cases with  $10^5$ ,  $10^6$ ,  $10^7$  markers using the marker dielectric tensor. The fourth column shows the Maxwellian reference case (no markers). The power density has been cropped at  $\pm 0.1$  in arbitrary units. The bottom row of panels shows a zoom of the core region. No data is available exactly on axis, hence the white dot in the centre.

Table 4.1: Power fractions for the marker dielectric tensor test run.

	Electrons	Deuterium	Hydrogen
$10^5$ markers	34 %	47 %	19 %
$10^6$ markers	30 %	43 %	28 %
$10^7$ markers	29 %	41 %	30 %
Reference	29 %	41 %	30 %

Table 4.2: Overview of the four JET cases studied in this section. Species concentration in parentheses,  $N(s)/N_e(s)$  for the regular (bi-)Maxwellian, and analogously  $N_c(s)/N_e(s)$  for the modified bi-Maxwellian. Note these plasmas are quasi-neutral because  $\sum_S q_S N_S = 0$ , with  $S$  the species, including electrons. And analogously  $\sum_S q_S \langle N_S \rangle = 0$  for the plasmas with a modified bi-Maxwellian as minority distribution.

Case	A	B	C	D
Bulk ion species ( $N/N_e$ )	D(0.99)	D(0.98)	D(0.49), T(0.49)	D(0.32), T(0.64)
Minority ion species ( $N/N_e$ or $N(s, B_C)/N_e(s)$ )	H(0.01)	$^3\text{He}$ (0.01)	$^3\text{He}$ (0.01)	$^9\text{Be}$ (0.01)

The downsides of this approach, compared to using an analytic distribution function, are threefold: Increased CPU time, introduction of noise and the model requires more user inputs. On the upside, no minority species profile needs to be prescribed, only the marker data is needed, which avoids fitting the distribution function.

### 4.3 Comparison of plasma models using axisymmetric JET-like geometry

The dielectric tensors derived in the section 4.2 describe a hot plasma, i.e. they include FLR effects. This happens by default when starting from the kinetic equation (2.10). However, in case  $\lambda \ll 1$ , it is justified to simplify the expressions by expanding in terms of the FLR parameter  $\lambda$  and truncating. Some texts also refer to this expansion as a “hot” plasma, but in this thesis it will be named a “warm” plasma model. This follows because it is a compromise between the full hot plasma theory, and the cold plasma limit  $T \rightarrow 0$ .

What follows is a comparison of the warm and hot models in LEMan. For simplicity a series of 2D tokamak scenarios is used, resembling the typical parameters for a JET plasma, see table 4.2. These cases are all minority heating scenarios. A and C are chosen because they involve second harmonic heating, so a large difference between warm and hot models is expected. B is a reference case without the 2<sup>nd</sup> harmonic resonance and case D is a three-ion scheme. In order to isolate the effect of changing the dielectric tensor, no iteration with SCENIC is included in this section.

Even to zeroth order in  $k_\perp$ , the warm plasma model already has extra physics compared to the cold version: The parallel dispersion is included (through the PDF), which avoids the singularities in the dielectric tensor that the cold plasma has at the cyclotron resonance. Also, it can be shown that the cold model exchanges exactly zero power with the plasma. To avoid the singularity, and include some damping, an artificial collision frequency is often added. However, in the warm model the collisionless power deposition arises naturally, in

### 4.3 Comparison of plasma models using axisymmetric JET-like geometry

the form of fundamental cyclotron and electron Landau damping. But higher harmonic heating and electron TTMP are still omitted. The damping of the right-handed polarised wave  $E^-$  on fast ions is also an FLR effect. This was the motivation to upgrade LEMan to the hot plasma model. Initial work was done by Patten [48] for a Maxwellian distribution and refined by Machielsens [49]. In particular Ref. [49] added the modified bi-Maxwellian and marker distribution function to LEMan.

The plasma profiles are shown in Fig. 4.5, based on hybrid shot 92398 [48, section 3.6.1]. All species used a Maxwellian distribution function, with the exception of the minority species, which is modelled as a modified bi-Maxwellian unless indicated otherwise. The temperature anisotropy is  $T_{\perp}/T_{\parallel} = 3$ , where  $T_{\parallel} = T_e$ . If the dielectric tensor is approximated using an expansion in  $k_{\perp}$  to some given order, then it has been applied consistently for all species up to that same order. E.g., if the warm model is applied, it is done so for electrons and all ion species. Moreover, all simulations of JET employed on axis fundamental heating of the indicated minority species, with  $B_0 = 2.7$  T on axis. In LEMan the antenna frequency is set based on this value,  $\omega = B_0 q_{min}/m_{min}$ . As dominant toroidal mode  $n_{tor} = 27$  has been selected for the JET simulations. LEMan employed a radial grid of 250 elements, and the plasma was sampled on a  $400 \times 20$  spatial grid (poloidal  $\times$  toroidal). In addition, 201 poloidal modes were used.

In comparing the warm and hot models there are several differences, the most important one being the discrepancy in the power fractions, see table 4.3. Cases A and C involve second harmonic heating, which is omitted by the warm model. This explains the lack of D and T heating respectively. In addition, the warm model severely underestimates the electrons' power fraction, which is particularly noticeable since the minority concentrations are only one percent. Adding FLR effects provides a new way of damping power on electrons in the ICRF, namely via TTMP. This is analogous to Landau damping, except the contribution due to the electric field is replaced by the mirror force.

The ion power fraction in cases A, B and C can be increased by using a larger minority concentration. However, if made too large, the minority species is no longer a "minority". Which means the favourable polarisation at the fundamental cyclotron resonance deteriorates. In addition, some of the power will be transferred to short-wavelength modes called ion Bernstein waves or ion cyclotron waves. These are effectively dissipated by electrons through Landau damping. The effect of mode conversion is not included in LEMan, since it assumes only one dominant mode exists.

The power deposition is shown for case A in more detail in Fig. 4.6. The wave field (and power) has been rescaled such that the total dissipation equals 4.5 MW. The model has some trouble resolving what happens exactly on axis, which results in a spike in power density. This is also clearly visible for case D in Fig. 4.10(b) for  $\rho < 0.05$ . The hot model is more sensitive to this numerical problem because the spike results in large gradients, thus large  $k_{\perp}$ , which in turn affects the dielectric tensor. Note that the electric field is still well behaved on axis, even in the

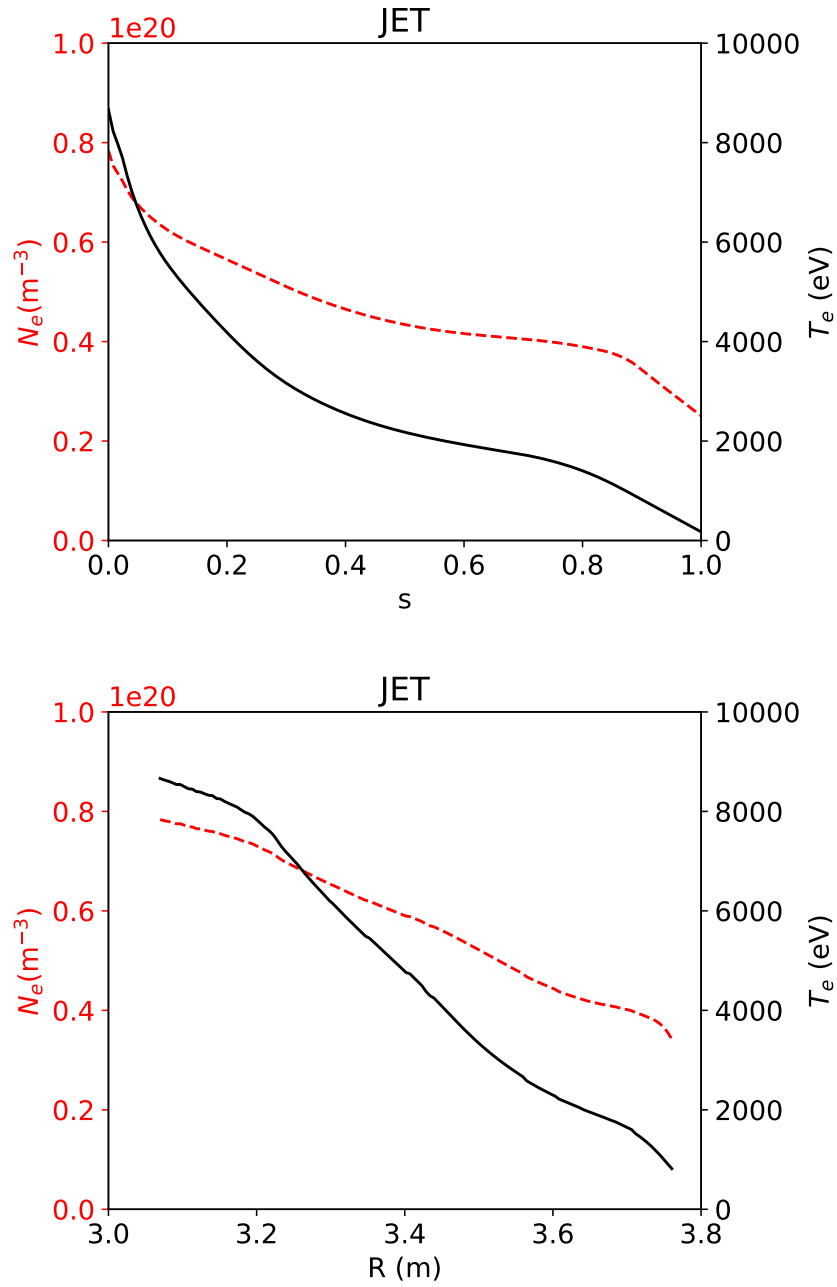


Figure 4.5: Plasma profiles used in the JET simulations. The left vertical axis corresponds to density, in red (dashed), and the right vertical corresponds to the temperature, in black (solid). In the bottom panel a projection on the mid-plane (on the LFS) is shown.



### 4.3 Comparison of plasma models using axisymmetric JET-like geometry

Table 4.3: Absorbed power fractions (%) on each of the species rounded to two significant figures. This is collisionless power deposition, so direct absorption by the wave. The dielectric tensor model for the minority ions is indicated within parentheses. Warm here refers the to the limiting case  $k_{\perp} \rightarrow 0$ . Hot includes FLR effects to all orders. “bi-Max” refers to the regular bi-Maxwellian from Eq. (4.2), and “mod bi-Max” is the distribution of Eq. (4.4).

Case	Electrons	H	D	T	$^3\text{He}$	$^9\text{Be}$
A (Warm mod bi-Max)	0.76	99	0.0	-	-	-
A (Hot Maxwellian)	29	30	41	-	-	-
A (Hot bi-Max)	29	29	42	-	-	-
A (Hot mod bi-Max)	29	29	42	-	-	-
B (Warm mod bi-Max)	1.2	-	3.9	-	95	-
B (Hot Maxwellian)	47	-	2.0	-	51	-
B (Hot bi-Max)	47	-	2.0	-	51	-
B (Hot mod bi-Max)	47	-	2.0	-	51	-
C (Warm mod bi-Max)	1.1	-	4.5	0.0	94	-
C (Hot Maxwellian)	31	-	2.9	15	51	-
C (Hot bi-Max)	31	-	2.9	15	51	-
C (Hot mod bi-Max)	31	-	3.0	15	51	-
D (Warm mod bi-Max)	0.80	-	51	0.18	-	48
D (Hot Maxwellian)	9.5	-	47	0.16	-	43
D (Hot bi-Max)	9.5	-	47	0.15	-	43
D (Hot mod bi-Max)	9.1	-	47	0.16	-	43

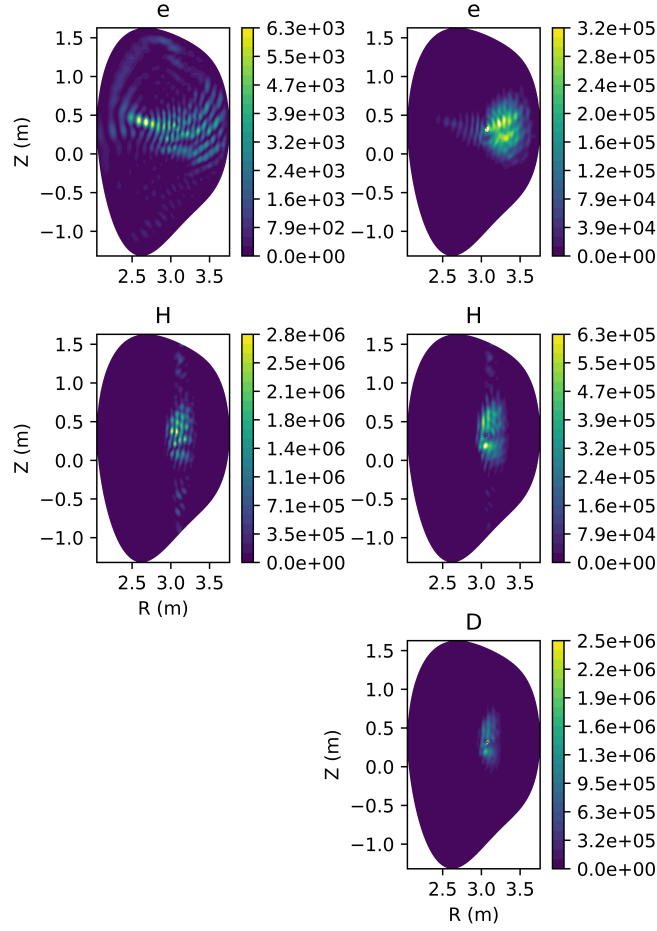


Figure 4.6: Absorbed power densities on each species in the contour plots for case A, in  $\text{MWm}^{-3}$ . The left column is for the warm model, the right for the hot model. Power on deuterium is not shown for the warm model as it is zero (no 2nd harmonic heating) up to machine precision errors.

hot model, the issue mainly comes from  $k_{\perp}$  on axis. Since (in this work) the warm model is to zeroth order in  $k_{\perp}$ , it is less sensitive to artefacts on axis. This artefact however does not significantly affect the overall behaviour of the power transfer, as indicated by the cumulative power fractions, see Fig. 4.7. Cumulative power is defined as the integral of power density over the volume of a flux surface positioned at a given radial position  $\rho$ . Since the volume of a flux surface near  $\rho = 0$  is vanishingly small, the effect of this spike in power density does not appear in the cumulative power plot.

Some additional notes about LEMan are given in the following. The modelling domain extends up to the LCFS, so  $\rho \in [0, 1]$ . This leaves two options for implementing a power source: One could modify the boundary conditions to excite a wave at the domain boundary, or the antenna

### 4.3 Comparison of plasma models using axisymmetric JET-like geometry

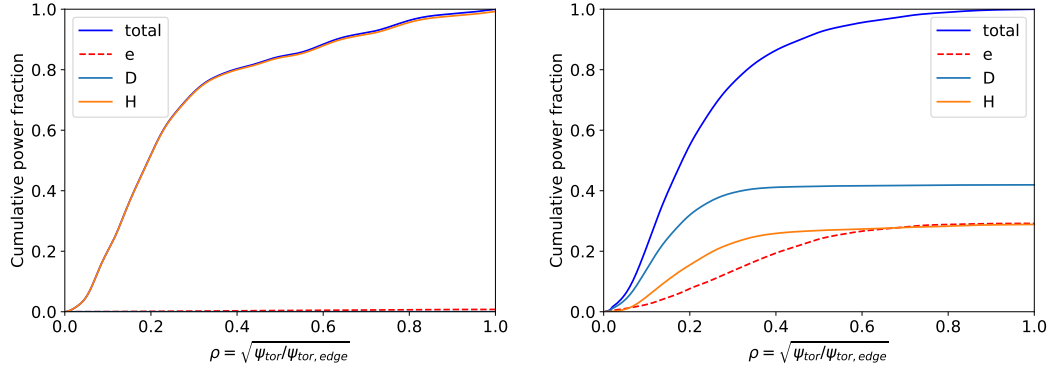


Figure 4.7: Cumulative power fractions for each species in case A, versus radial position. The warm model on the left, the hot model on the right.

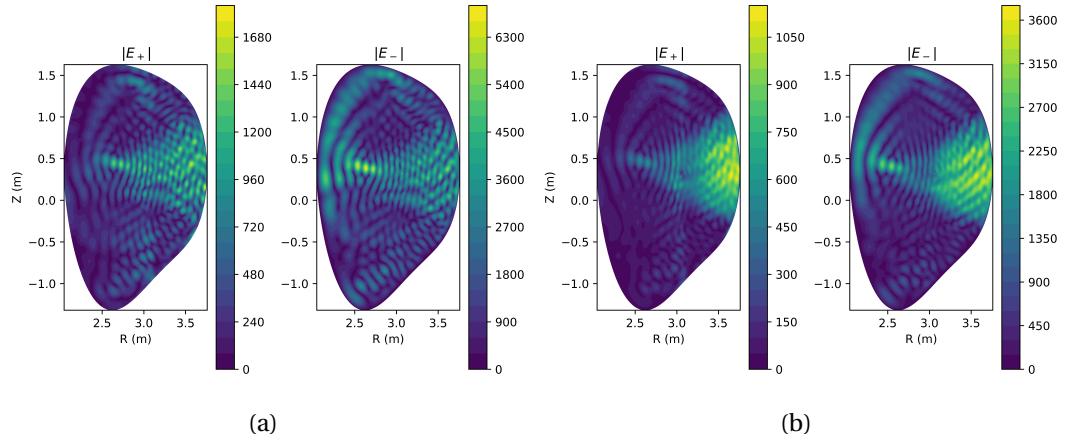


Figure 4.8: Left and right handed polarised wave components, in V/m, for case A. The warm model on the left, the hot model on the right.

(charge/current source) must be inside the LCFS. LEMan goes with the latter option<sup>2</sup>. In either case, the model does not solve the antenna-plasma coupling problem. In real life the fast wave is evanescent in the low density region near the antenna, so it will have to tunnel through this layer in order to reach the core plasma. This feature is not included in the modelling. Due to the chosen boundary conditions, the wave will reflect at the domain boundary, so all power is assumed to be absorbed in the plasma somewhere. In the warm model the damping is less strong, so the wave can propagate further, see Fig. 4.8. Also, the wave field appears to be more focussed (towards the core) in the hot vs the warm model.

JET uses a wall that is representative of what will be used in ITER, called the ITER like wall. This contains tiles made from or coated with tungsten, and others beryllium. Hence some metal impurities will inevitably end up in the plasma. Native impurities such as beryllium can be exploited for RF heating using a three-ion scheme D-(<sup>9</sup>Be)-T, this is case D. For this to

<sup>2</sup>How exactly the antenna is implemented can be read in [56, section 3.1] or [48, section 3.5].

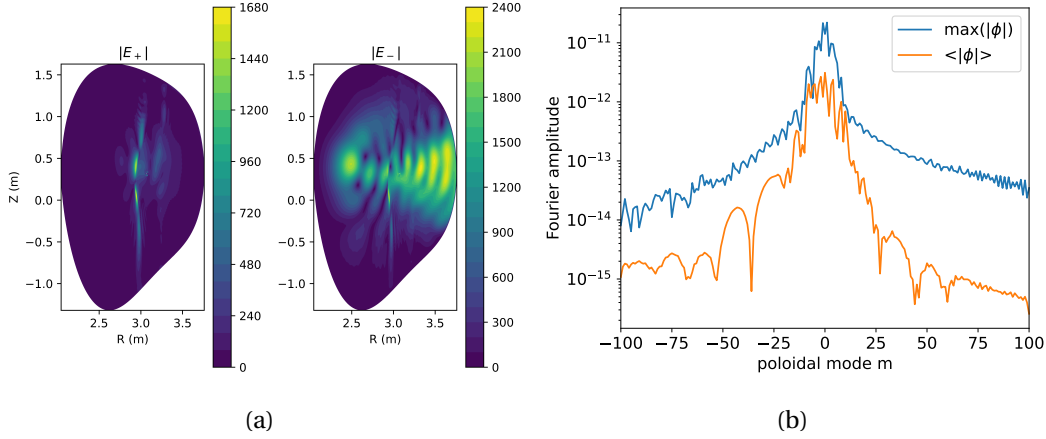


Figure 4.9: Left and right handed polarised wave components for case D, in V/m. On the right the Fourier mode amplitudes (arbitrary units) of the electric potential  $\phi$  are shown for the same simulation.

work the concentrations of the majority ions need to be carefully tuned. As predicted from the theory [27], the three-ion scheme results in greatly enhanced wave polarisation near the minority cyclotron resonance, see Fig. 4.9(a). The wave is launched from the LFS, and as it propagates inwards it encounters the fundamental resonance of D, Be and then T. Even though a considerable amount of deuterium is present, it still absorbs a significant fraction of the power since its resonance is close to that of Be. Once the wave reaches the T resonance little power is left to be absorbed, and also the polarisation is unfavourable. See Fig. 4.10 for the power deposition.

The convergence of the simulation (in terms of poloidal mode number) can be assessed from Fig. 4.9(b). The Fourier modes of the scalar potential (and also that of the vector potential) depend on the flux surface. So in order to condense this down to a 1D plot, the average and maximal value over the radial range have been selected.

#### 4.4 LEMan runs for W7-X

LEMan can also be applied to 3D configurations. Of particular interest is the  $^4\text{He}$ -(H) scenario in W7-X, which has been chosen as one of the ICRH schemes for the next operational phase OP2. The plasma is assumed to consist of 1% H, 0.5%  $^{12}\text{C}^{6+}$  and 48%  $^4\text{He}$ . For the majority ions it was assumed that  $T_i = T_e$ . In addition, the species densities have the same profile shape as electrons, but scaled up by a given factor. The electron profiles are estimates for what may be achieved in the second operational phase of W7-X:  $N_e = N_{e,0} (0.9(1 - s^{10})^2 + 0.1)$ ,  $N_{e,0} = 1.5 \cdot 10^{20} \text{ m}^{-3}$ , and  $T_e = (3995(1 - s) + 5) \text{ eV}$ , see Fig. 4.11.

It is important to use a hot plasma description (or higher order warm model) in order to accurately compute the power fractions of helium and carbon. The H species is described with

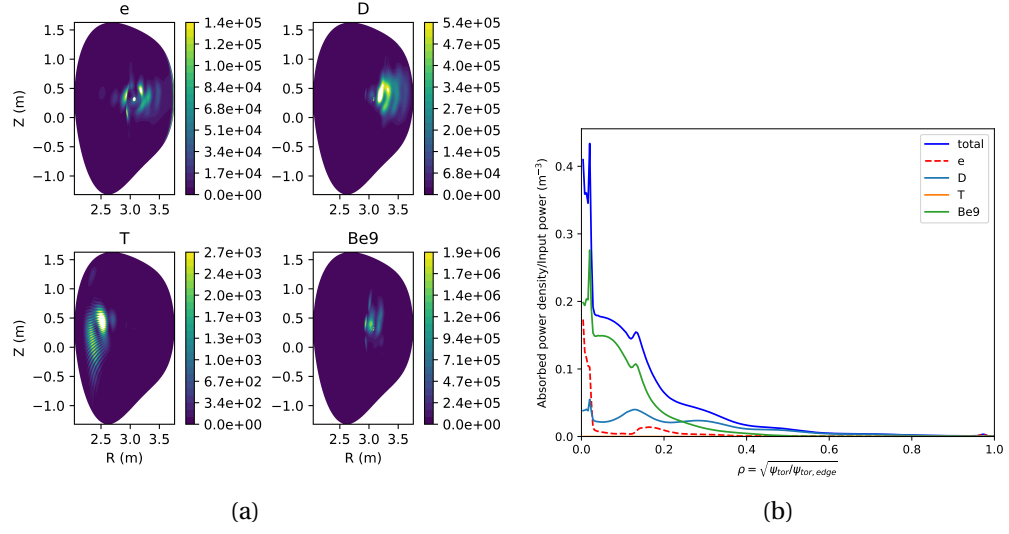


Figure 4.10: Absorbed RF power density in  $\text{MWm}^{-3}$ , for all of the plasma species, case D. In the right plot the volume averaged power density is shown versus radial coordinate  $\rho$ .

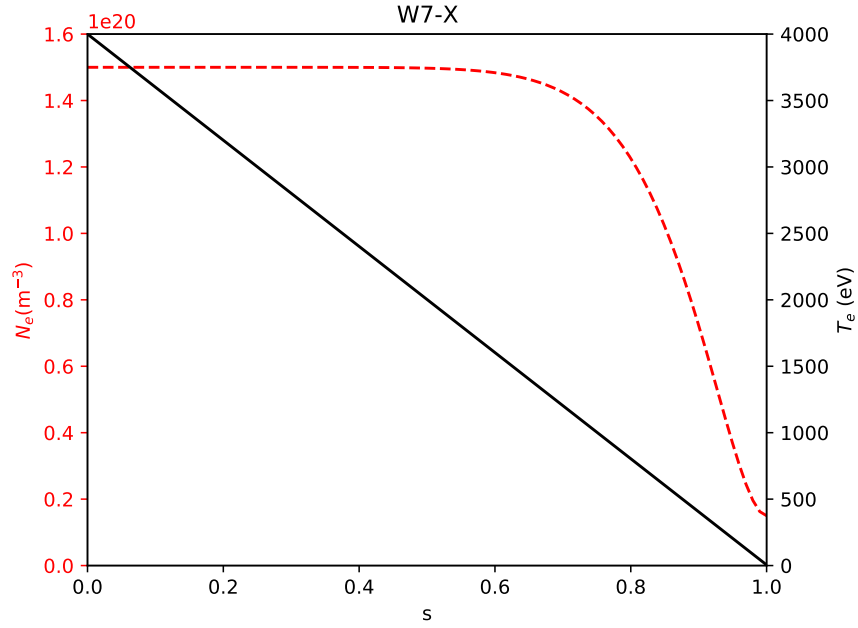


Figure 4.11: Plasma profiles used in the W7-X simulations. The left vertical axis corresponds to density, in red (dashed), and the right vertical corresponds to the temperature, in black (solid).

the modified bi-Maxwellian, with  $T_{\perp}/T_{\parallel} = 3$ . The standard magnetic equilibrium is used, with  $B_0 = 2.5$  T on axis at  $\varphi = 0$ . As before, this  $B_0$  value is used to set the antenna frequency in the model. In this high density scenario the wave is strongly damped and it does not propagate far from the antenna, see Figs. 4.12 and 4.13. The antenna model is described in [48, section 3.5], which corresponds approximately to dipole phasing.

The LEMan simulations in this section used 200 radial elements, sampling  $f_0, \mathbf{B}_0$  in a  $300 \times 250$  (poloidal  $\times$  toroidal) grid. The table of modes consists of 9000 Fourier modes:  $30 \times 300$  (poloidal  $\times$  toroidal). In order to use such a large number of modes, the mode family technique was used, see section 2.4.3. It is crucial to have a sufficient number of these Fourier modes for proper convergence, see Fig. 4.14 for an example of the spectrum.

If the large toroidal mode numbers are omitted the wave is able to propagate much further into the other field periods of the device. This is simply because the large  $n_{tor}$  are needed to resolve the small scales and thus obtain the highly localised field near the antenna. Additionally, the electron power will be underestimated because  $k_{\parallel}$  is limited when too few modes are used, which leads to a too high phase velocity. The  $n = 0$  resonance occurs when electrons have a velocity that matches the wave's phase velocity,  $v_{\parallel} \approx \omega/k_{\parallel}$ . So only electrons with  $v_{\parallel} \gg v_T$  are able to resonate, of which there are only very few since  $f_0 \propto \exp(-v_{\parallel}^2/v_T^2)$ .

In practice, the minority concentration cannot be controlled very precisely given that the carbon wall can absorb and release hydrogen. For this reason a scan of the H concentration was performed, see Fig. 4.15. Carbon absorbs only a negligible amount of power in this scheme because there is very little of it, and it has the same charge to mass ratio as helium. So apart from a different thermal velocity, there is very little change to the dielectric tensor when swapping 3 He for 1 C. It would play a bigger role if an inverted minority heating scheme was used, such as H-( $^4\text{He}$ ). Such a scheme relies on a low minority concentration, but 1 C effectively counts for 3 He (at the same density  $\omega_p^2$  is three times as large). This can easily lead to considerable mode conversion, see e.g. [57], [58].

Note that all W7-X simulations in this section have been redone with the latest version of LEMan (but using the same inputs as in [49]). It was found there was a bug in the code related to the mode family method, which has since been fixed. The problem had to do with the selection of the Fourier modes. In order to compute the integrals appearing in the weak form, LEMan first computes a number of coefficients related to the background quantities on a poloidal and toroidal grid (for each radial element). This data is then transformed using the fast Fourier transform (FFT). In addition to this grid, a user of LEMan must specify a table of poloidal and toroidal modes. Wherever the modes of the FFT data equal a mode from this table the data is stored. It was at this selection stage that a problem appeared. Modes are stored in their corresponding array index, e.g. toroidal mode 15 is stored in array index 15. But with the mode family method only every five modes is used (in each of the five runs), so this mode would be stored in index  $15/5 = 3$ . The automated selection mechanism was not aware of this though, so it still picked index 15, instead of index 3. This has resulted in selection of

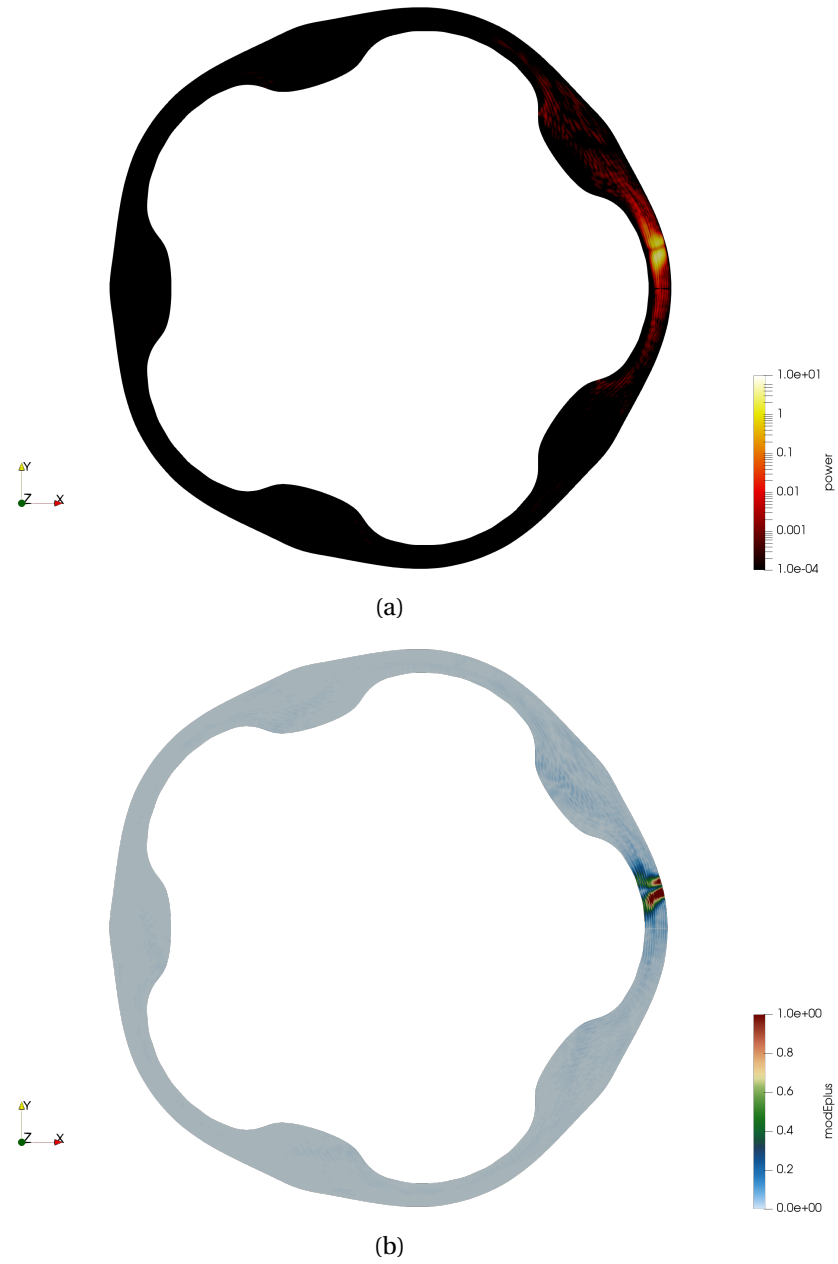


Figure 4.12: Absorbed power density on hydrogen minorities in W7-X on the top. Most absorption happens right in front of the antenna, which is placed roughly at a geometric toroidal angle of 8 degrees. On the bottom a plot of the left handed polarised wave component  $|E_+|$ . Arbitrary units.

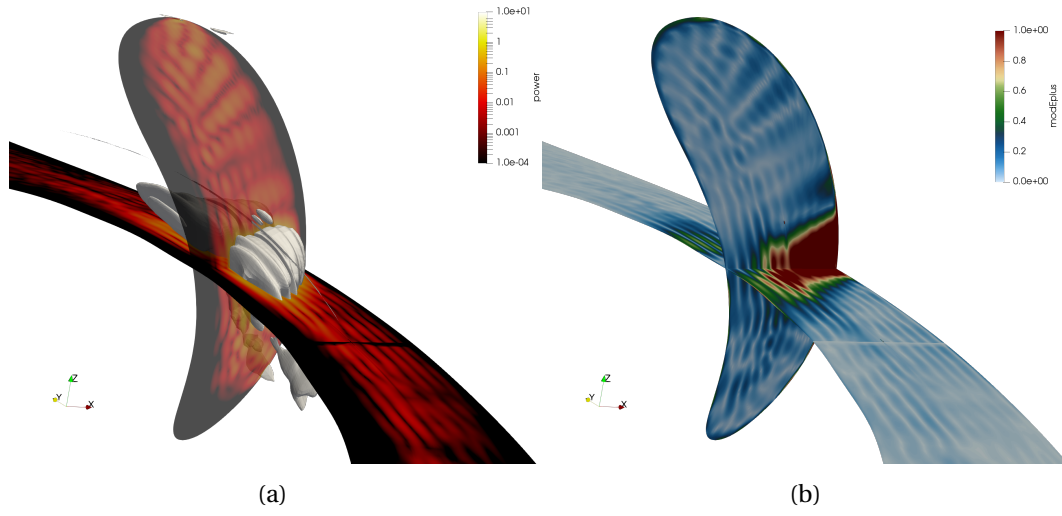


Figure 4.13: Zoom of the antenna region. The power deposition on hydrogen is shown on the left,  $|E_+|$  on the right. The white surface in the figure (a) highlights a sub volume where the power density exceeds 0.3 (A.U.). The poloidal slice is placed at a geometric toroidal angle of 8 degrees, which is approximately bisects the antenna.

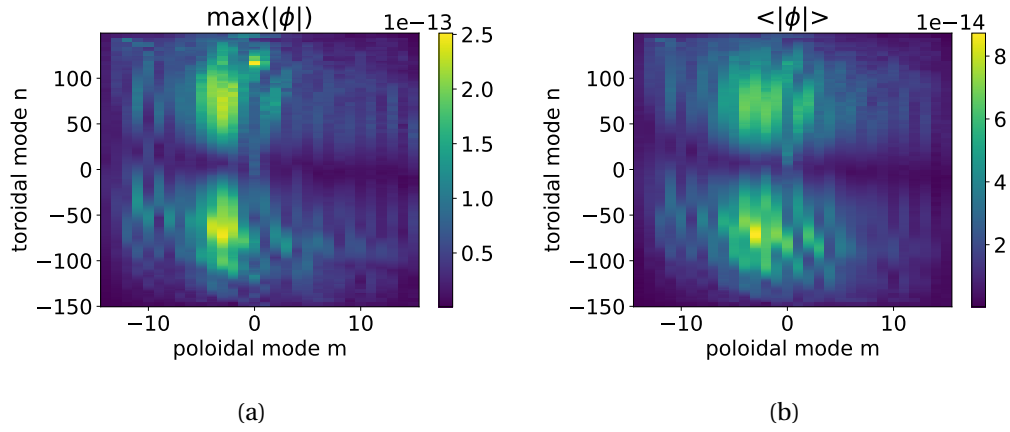


Figure 4.14: Fourier mode spectrum. Here  $\phi$  represents the  $m, n$  Fourier amplitude of the electric potential. The maximum of  $|\phi|$  over the radial domain is plotted on the left, and the average on the right.



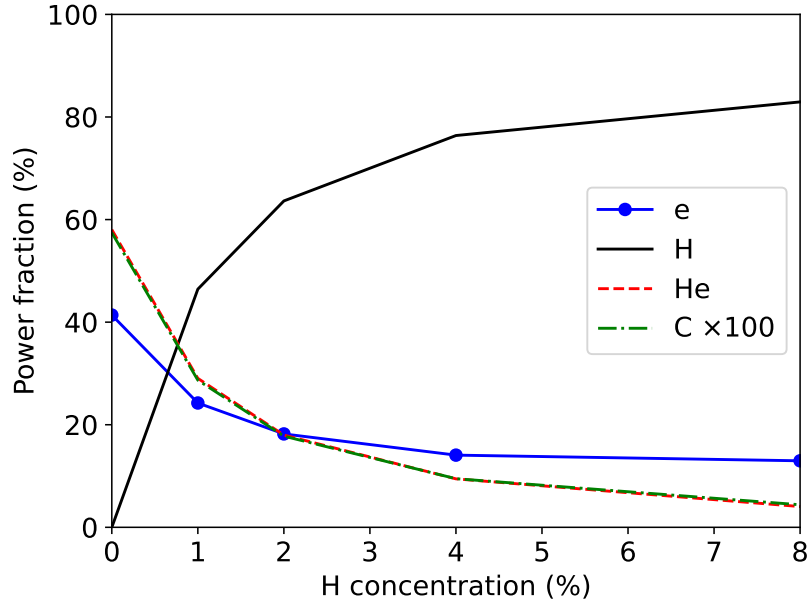


Figure 4.15: The RF heating power partitions for all plasma species given a H concentration of 0, 1, 2, 4 and 8%. The  $^{12}\text{C}^{6+}$  concentration was fixed to 0.5% and the rest is  $^4\text{He}$ . For visibility, the power fraction of carbon has been multiplied by 100 in this plot.

the wrong (too large) modes, which caused an enhanced electron power fraction. The LEMan simulations for JET were not affected, and the W7-X runs in chapter 5 were performed after this bug was patched.

## 4.5 Full SCENIC runs in JET

So far the background distribution function  $f_0$  and the magnetic equilibrium  $\mathbf{B}_0$  were assumed fixed. However, these can change over time due to the injection of RF waves. This will now be investigated for JET case A, using SCENIC (section 2.5) and including ANIMEC in the loop.

The toroidal modes used are  $n_{tor} = \pm 13, \pm 27$ , which is representative of  $(0\pi 0\pi)$  dipole phasing, see [48, table 3.2]. The main interest is in the steady state plasma, not necessarily the evolution towards it. To this end VENUS-LEVIS was iterated six times, 100 ms of physical time each. In the analysis only the last 50 ms was used (averaged), to rule out any start up behaviour. These runs assume a fixed total coupled power of 4.5 MW; the electric field amplitude is then rescaled accordingly to ensure fixed power over time in VENUS-LEVIS. This amplitude is multiplied by another factor to account for the power fraction of the minority species. (Recall that VENUS-LEVIS only evolves  $f_0$  for one species, not the whole plasma). The energy distribution for each of these iterations is shown in Fig. 4.16. This plot also functions as a way to check if the simulation has converged. A considerable amount of fast protons are produced, but they are

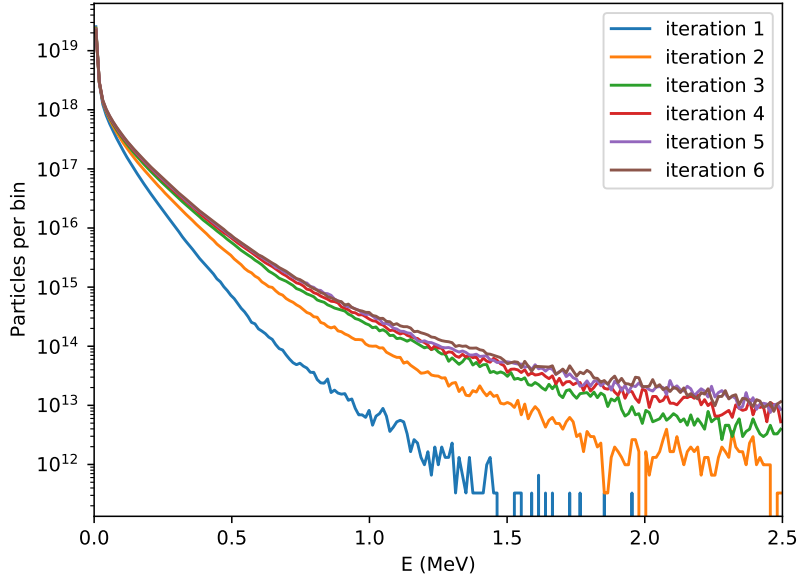


Figure 4.16: Energy histogram of H minority ions, after 6 consecutive SCENIC iterations, 200 bins used.

not isotropic in velocity space, see Fig. 4.17. In this case the markers are binned in terms of  $(v_{\parallel}, v_{\perp})$  or (energy, pitch). This analysis is applied to the entire plasma, not at a single point, so it includes all confined markers (2002944 total markers).

LEMan computes the collisionless power deposition, but if the goal is heating bulk ions (the fuel) collisional power must be considered as well. Using hydrogen as a minority results (in this case) in a substantial amount of fast ions, which transfer their power to the bulk plasma via collisions. But since the minority ions are so energetic, a lot of power will go to the electrons, see Fig. 4.18. This can be mitigated by using a heavier impurity such as  $^3\text{He}$ , since it is more collisional, which leads to a less energetic fast ion population. In simple terms, more power would be transferred to the bulk ions via friction before the  $^3\text{He}$  ions get a chance to become really fast. Another knob to play with is the minority concentration, increasing this usually results in less power per ion, thus less fast ions. For more details see e.g. [59]. However, if the goal is generating as many fast ions as possible, the large tail on the distribution is welcome.

Lastly, the fast ion density and pressure can be computed from the data produced by VENUS-LEVIS, see Fig. 4.19. These plots demonstrate a poloidal asymmetry, which is explained in section 4.1.1.

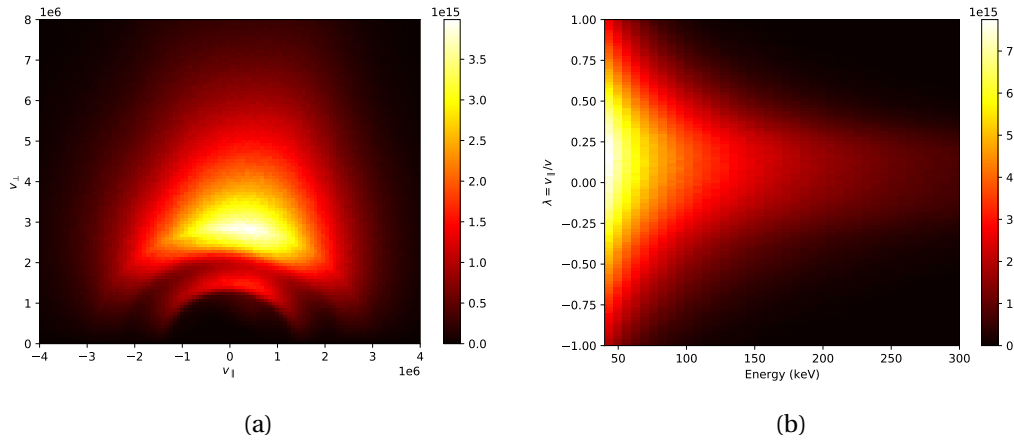


Figure 4.17: 2D histograms of the fast H minority population, markers with  $E/T_e < 5$  are omitted from the left plot. The colourbar shows the number of particles per bin. 40 Bins in energy space, 100 bins for the velocity components and the pitch angle.

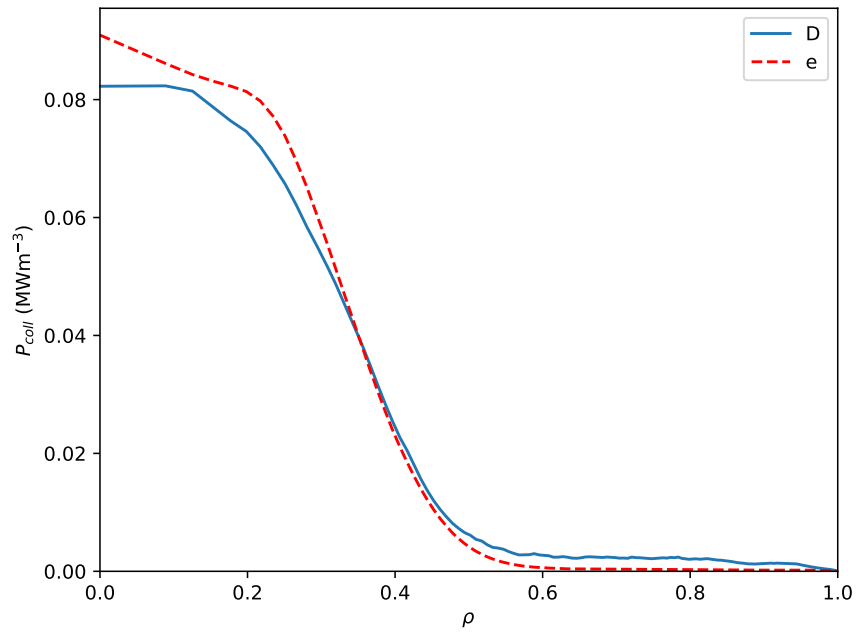


Figure 4.18: Collisional power density of hydrogen on bulk species versus radial position, averaged over angular coordinates.

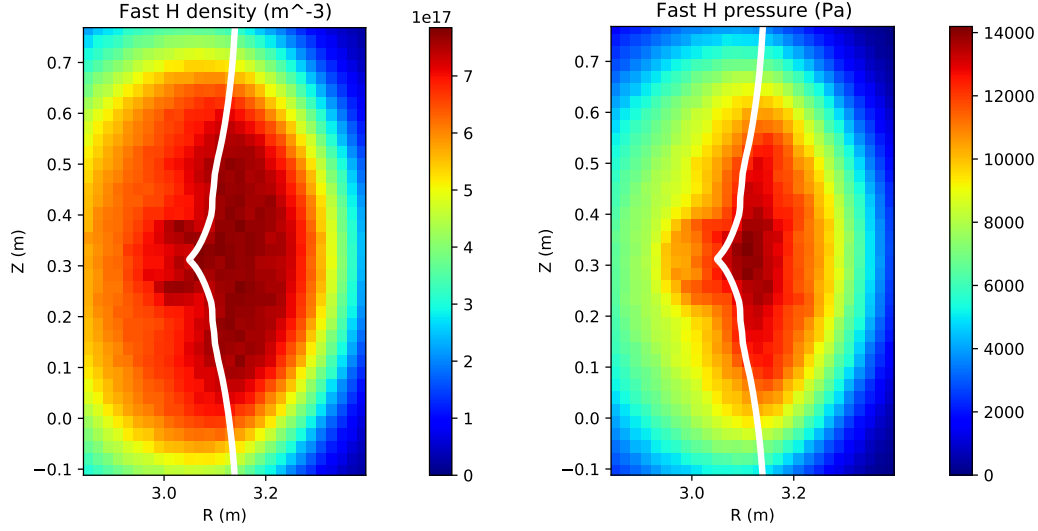


Figure 4.19: Fast ion density (left) and fast ion pressure (right) in the core (averaged over toroidal angle), protons with kinetic energy less than five times the local electron temperature are not plotted. The white line indicates the cold plasma resonance  $B = B_C$ .

## 4.6 Summary

The type of distribution function plays an important role in the wave propagation and absorption. Using the expressions from section 2.2, two new dielectric tensors have been derived, which are also implemented in the full-wave code LEMan. The new hot model is compared against the warm model for several cases in a JET-like plasma. The biggest difference is in the power fractions for each species, where the hot model predicts a considerably larger electron heating and damping on ions via second harmonic heating. Little difference is observed between the different kinds of hot models (Maxwellian, bi-Maxwellian, modified bi-Maxwellian), which may be because the minority concentration was kept rather low (1%). The updated version of LEMan has also been applied to W7-X for the  $^4\text{He}$ -(H) scheme, which predicts strong damping on hydrogen. Lastly, the full SCENIC suite has been used to study minority heating in JET. Simulations show that a significant number of fast ions are produced, which are highly anisotropic in pitch angle.

## 5 Combined RF-NBI heating

As alluded to in section 2.3.2, the large Doppler shift of neutral beams may be exploited for synergetic heating with ICRH. In this chapter the RF-NBI scheme is studied in W7-X using the SCENIC code. First the basics of computing the NBI deposition are explained. After the deposition, the test particles will need to be followed over time, during which they interact with both the bulk plasma and the waves. This is accounted for in VENUS-LEVIS via the use of Monte Carlo operators. A limitation of previous work [48] was the model deployed for the thermalised part of the beam population. These thermal ions have an important effect on the fast wave, and hence ultimately on the supra-thermal population. To this end, a radial diffusion model is added which enables VENUS-LEVIS to reach steady state even when thermal markers are included. Finally, all of these elements are brought together to study the effectiveness in generating fast ions using the synergetic scheme in W7-X.

This chapter is adapted from the following article: M. Machielsen et al., 2023, “Fast ion generation by combined RF-NBI heating in W7-X”, [60], licensed under CC BY 4.0.

### 5.1 Neutral beam injection

Besides ICRF waves, neutral beam injection (NBI) is another source of fast ions. The high energy beam is created in a linear accelerator, however, to be able to enter the magnetic field the particles must be neutralised again. This is typically done by sending the ions through a gas chamber where they pick up (or lose) an electron. The particles that did not manage to neutralise are deflected onto the ion dump. Most current day devices accelerate positive ions, hence the name PINIs (Positive Ion Neutral Injectors). The injection energy is typically on the order of 100 keV. For ITER the energy needs to be much higher ( $\sim 1$  MeV) in order to reach the plasma core. However, the efficiency of neutralisation of positive ions at these high energies is poor, so it is advantageous to use negative ion beams in ITER. Other devices have already demonstrated this negative ion technology, such as JT-60U and LHD.

Imagine a beam of  $N_0$  neutrals impinging on a plasma. After some penetration distance  $\ell$

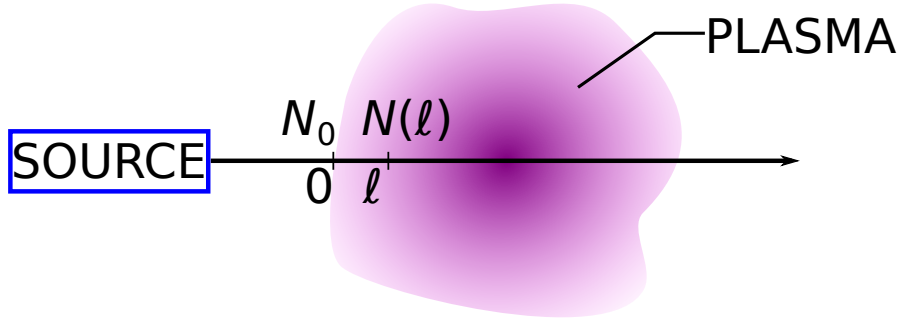


Figure 5.1: Schematic of a neutral particle beam (black line) impinging on a plasma (purple).

into the plasma, there are only  $N(\ell)$  neutrals left due to ionisation, see Fig. 5.1. This decay is described by the following ODE:

$$\frac{dN}{d\ell} = -N(\ell)n_e(\ell)\sigma(\ell), \quad (5.1)$$

where  $n_e$  is the electron density and  $\sigma$  the ionisation cross section, which in general both depend on the position within the plasma. Multiple ionisation effects can be incorporated into  $\sigma$ . The solution is given by

$$N(\ell) = N_0 \exp\left(-\int_0^\ell n_e(x)\sigma(x)dx\right). \quad (5.2)$$

### 5.1.1 NBI model

In practice the source is not a single point, it has a finite size. In addition, there will be some angular spread of the beam. However, such a realistic beam can be approximated by randomly sampling many beam lines. Where each of these lines will experience a slightly different plasma background. In this work a Monte Carlo approach is used to sample the ion distribution born from NBI: For each marker a uniform random number  $r \in [0, 1)$  is generated. Then, by stepping through the plasma along one beam line, the cumulative ionisation probability  $P_{ion}$  is computed. When  $P_{ion} \geq r$ , an ion is born and the loop is terminated.

Earlier versions of the NBI model distributed the markers equally (in terms of distance) along a beam line, after which the marker weights were adjusted based on the ionisation probability. However, it was found that this approach leads to markers with negligible weight at the edges. Using equal marker weight (at least per PINI and energy) was found to be more effective [48], [61]. The NBI program started out as a MATLAB routine, but it has since been incorporated into VENUS-LEVIS [62] under the name “VENUS-NBI”. This brought improvements both in code performance and physical accuracy. The MATLAB model traces a single central beam line for each PINI, then the ions are displaced perpendicularly to this line by a random amount (sampled from a normal distribution). The VENUS-NBI model traces each marker along a unique beam line. This more accurately samples the plasma and is arguably the biggest

improvement. Each marker's injection is completely independent, hence this type of model belongs to the “embarrassingly parallel” category. VENUS-NBI takes advantage of this using the Message Passing Interface (MPI).

Recently some technical upgrades have been applied: the model can now handle focusing of the beam (e.g. with a concave acceleration grid<sup>1</sup>). Secondly, markers are injected until the desired number of markers is reached, without losing the ability to compute shine-through power. This is accomplished by adjusting the marker weights at the end of the deposition stage. In order to have a fair representation of all PINIs and each energy fraction (1, 1/2, 1/3), the markers are equally divided over each PINI-energy combination. All markers associated with one such combination are assigned the same weight, however, the injection rate (atoms/s) varies per PINI and energy, thus marker weights of different combinations need not be equal. Nevertheless, weights are typically of the same order of magnitude, and thus do not become negligibly small.

In pseudo-code the model works as illustrated below. The indicated values are merely an example, in reality these may be different.

---

```
NPINI = 4; //number of PINIs
N = 2400000; // total number of markers
Nfrac = N/(3*NPINI); // number of markers per PINI, per energy fraction

for (p=0; p<NPINI; p++) {
    inject_count = 0; //array of 3 values, recorded for each PINI and energy separately
    shine_count = 0;
    for (m=0; m<Nfrac; m++) {
        for (energy=0; energy<3; energy++) {
            while(true) {
                generate random beam line;
                if (plasma puncture found) {
                    inject marker;
                    inject_count(energy)++;
                    if (ionised) {
                        store marker;
                        continue; //go to next energy, and thus the next marker
                    } else {
                        shine_count(energy)++;
                    }
                }
            }
        }
    }
}
```

---

<sup>1</sup>This is used for instance in W7-X, where the beam is focussed on the core of the plasma.

```
}  
sum inject_count over all processes with MPI_Allreduce;  
sum shine_count over all processes with MPI_Allreduce;  
for (energy=0; energy<3; energy++) {  
    compute weight = atom-flux(p,energy)/inject_count(energy);  
    compute shine-through power;  
}  
}
```

---

Note, the weight is set by dividing the atom flux of one particular PINI-energy combination, by the total number of injected markers for that particular combination. Thereby preserving the correct flux <sup>2</sup>. The sum of the weights of the stored markers is thus less than the atom flux, which is because of shine-through. Furthermore, the weight here is a flux, i.e. particles/s. Contrarily, in VENUS-LEVIS the unit of weight is particles, thus one simply has to multiply the weights by the simulated time.

### 5.1.2 Limitations of the NBI model

Although still rather general, the adopted model has some notable limitations, mainly related to the geometry:

- The source geometry is assumed to be a rectangle, instead of the actual geometry of the acceleration grid. The injection angle is set based on the normal vector of this rectangle, a random spread, and optionally a focus angle.
- The model has no knowledge of the wall and injector geometry, it treats it as non-existing. Thus beam lines intersecting with the sides of the injector just go through.
- All beam lines are assumed to intersect the plasma at least once. If the beam line has a deviation large enough to miss the plasma entirely, the beam line is rejected and a new random beam line is generated.
- The beam line can puncture the LCFS at most 4 times. I.e. it can enter the plasma, exit, re-enter and exit again. This is usually not needed, but it may be of use in some non-axisymmetric configurations in combination with tangential injection.
- Any plasma outside the LCFS is ignored. Although this is not a fundamental limitation, it is purely due to the use of a VMEC equilibrium. If an equilibrium magnetic field is provided that extends beyond the LCFS this outer region could in principle be incorporated as well.
- The neutral particles are assumed to move along straight lines until they ionise or shine-through, without losing energy. So scattering is not included.

---

<sup>2</sup>If the denominator was the number of ionised markers instead, the flux would be incorrect.



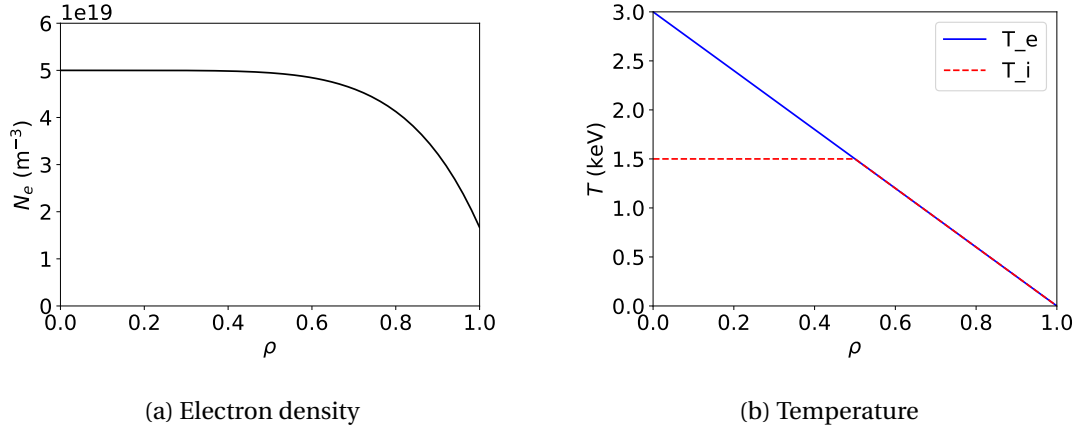


Figure 5.2: Plasma profiles versus flux label  $\rho$ . The latter being defined as the square root of the normalised toroidal flux.

- Currently, VENUS-NBI uses the Suzuki data [63, Eq. 28] for the ionisation cross sections, which is only valid for hydrogen beams in a H, D or T bulk plasma. However, this can easily be extended in the future using ADAS (atomic data and analysis structure) tables.

### 5.1.3 NBI deposition in W7-X

Using the latest version of VENUS-NBI, the deposition profile (also known as the birth-profile) for the W7-X stellarator can be accurately computed. The NBI system uses hydrogen beams with an energy of 55 keV. A bulk plasma consisting of deuterium is selected, see Fig. 5.2 for the plasma profiles. The so called high mirror magnetic equilibrium (KJM) is used here. In the following simulations balanced injection is applied, using a total of four PINIs (3,4,7,8) from beam boxes NI20 (3,4) & NI21 (7,8). This corresponds to an injection rate of about  $1.2 \cdot 10^{21}$  atoms per second, out of which about  $10^{21}$  per second are actually ionised (using these profiles and  $\mathbf{B}_0$ ). For more details on the NBI system see [64].

The ionised particles are binned to generate the deposition profiles, as seen for example in Fig. 5.3. Two humps are identified, which originate from the fact that PINIs (3,4) are placed in the bottom of box NI20, below the currently unused PINIs (1,2), and PINIs (7,8) are located at the top of NI21, above the unused (5,6). In addition, the beam boxes are aligned at slightly different angles.

Besides the location of ionisation, the type of particle orbit is important too. Consider a particle with velocity  $(v_{\parallel}, v_{\perp})$  and assume conservation of energy  $E$  and magnetic moment  $\mu$ . Then there exists a magnetic field strength such that the particle reflects, called  $B_{ref}$ . At this point  $v_{\parallel,ref} = 0$  by definition, and conservation of energy leads to  $v_{\perp,ref} = \sqrt{v_{\parallel}^2 + v_{\perp}^2}$ . Using

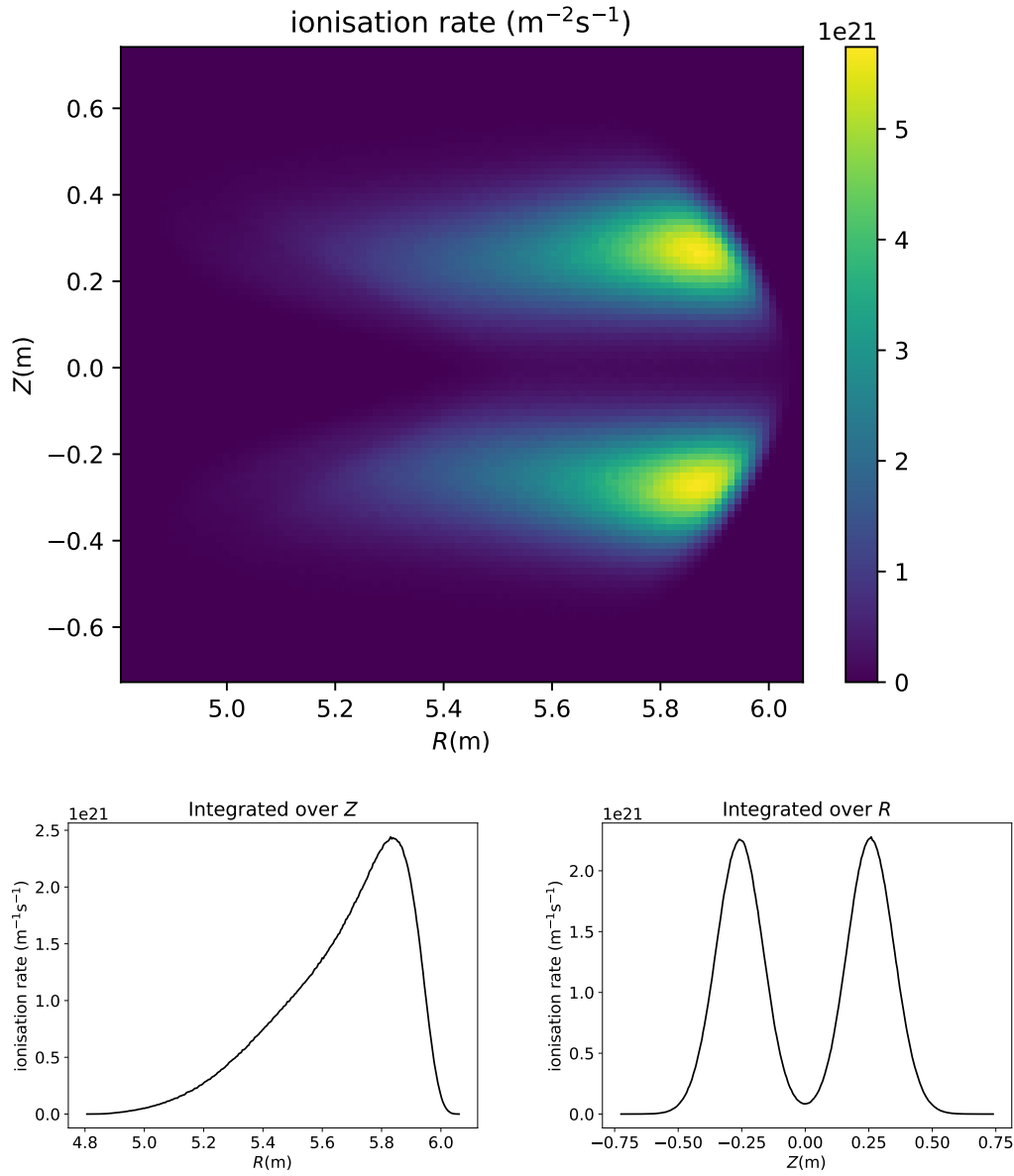


Figure 5.3: Ionisation rate vs position. Normalised such that the integral over space gives the total rate of new protons per second (about  $10^{21}\text{s}^{-1}$ ), which explains why the 2D map has units  $\text{m}^{-2}\text{s}^{-1}$ .

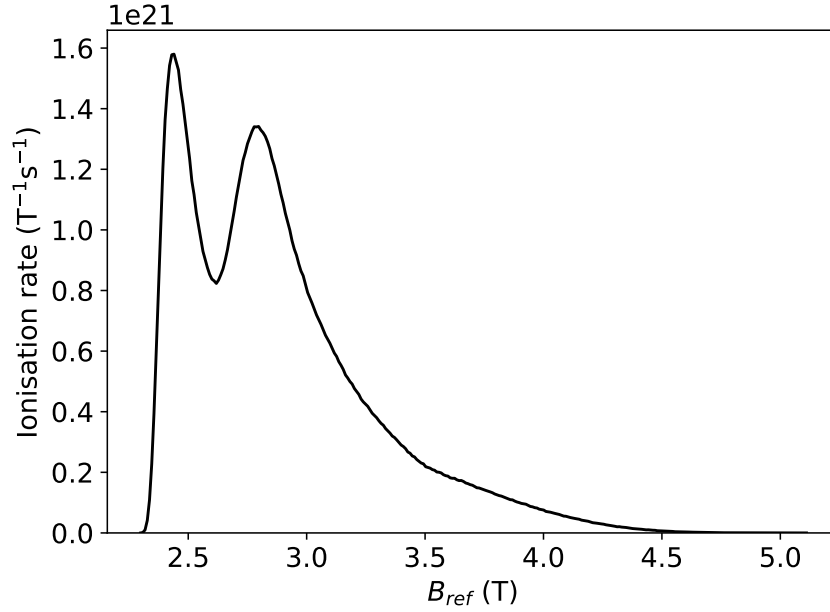


Figure 5.4: Distribution of  $B_{ref}$  values for the freshly injected beam ions. Normalised so that the integral over  $B_{ref}$  gives the total rate. For comparison, the value of the magnetic field strength on axis is roughly 2.43 T in front of the antenna.

conservation of  $\mu$  the following relation can be derived,

$$B_{ref} = E/\mu. \quad (5.3)$$

If a particle has  $B_{ref} > \max(B)$  it is passing, otherwise it is trapped (assuming sufficiently low collision frequency). Where the maximum is computed along the particle's full trajectory. The distribution of different  $B_{ref}$  is shown in Fig. 5.4. Most of the fresh beam ions are passing, which is by design because there are certain unfavourable trapped particle orbits which lead to rapid (collisionless) losses, see e.g. [10].

Similarly, the placement of the ICRH antenna is not a coincidence either. The wave enters the plasma in the bean cross section, which contains the highest magnetic field strength. Thus, the fast particles (generated by ICRH) essentially start on a “hill” in terms of magnetic field, which means that particles can always move away to other toroidal angles. Of course the generation of fast ions from RF waves is not an instant process, contrary to NBI where the ions are born fast. In wave heating a particle undergoes many interactions with the wave (kicks) before it becomes supra-thermal (fast). During this process it can move around, but the rationale is that most fast ions are generated in the poloidal cross section where the antenna is located. This is where the field is strongest (Fig. 5.13), and the most power is deposited.

Note that recently the deposition in VENUS-NBI has been benchmarked and confirmed favourably against other codes in a W7-X plasma [65]. Though it should be noted that the

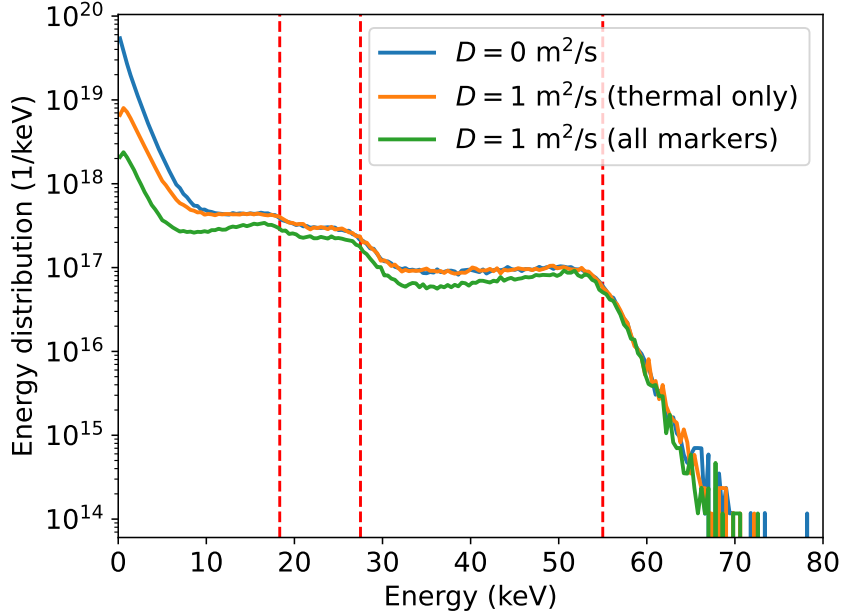


Figure 5.5: Comparison of the energy distribution for three cases: no diffusion, diffusion on thermal markers only, or diffusion on all markers. The data represents the NBI slowing down distribution using base case parameters after 200 ms. Normalised such that the integral over energy gives the total number of H ions in the plasma.

plasma profiles and PINI injection rates used for that study are not the same as used here.

#### 5.1.4 Slowing down distribution

Section 5.1.3 investigated the NBI deposition. But as time passes these beam ions will slow down on the bulk plasma due to collisions. The mix of slowed down and freshly injected ions will be referred to as the slowing down (SD) population. An example of the SD distribution, binned in energy is given in Fig. 5.5. There is still a signature visible of the three distinct injection energies, indicated by the red lines. Note that these simulations use the same plasma and magnetic equilibrium as in section 5.1.3, which will be called the “base case”.

A radial diffusion model has been added so that particle balance may be achieved, see section 5.3 for an explanation of this problem. In short, the thermal markers cannot just be removed because they are needed for the later RF-NBI simulation step, but in previous versions of SCENIC [48] their transport was not fully resolved, leading to accumulation of thermal density. It is for this reason that a diffusion model is implemented, see section 5.2.2 for details. This diffusion process can be enabled for thermal markers, for all markers, or for none. The differences are highlighted in Fig. 5.5.

In this context “thermal” markers are defined as those having  $E < 1.5T_e$  ( $s = \rho^2 = 0.5$ ), the rest

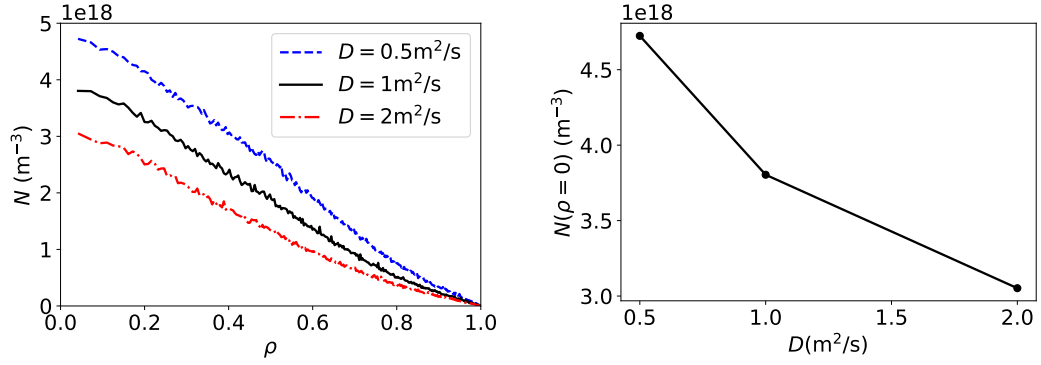


Figure 5.6: Hydrogen density profile vs radial position  $\rho$  for three different diffusion coefficients  $D$  (left). For comparison,  $N_e = 5 \cdot 10^{19} \text{ m}^{-3}$  in these simulations. And the hydrogen core density vs  $D$  (right).

are considered “fast”. The diffusion results in fewer thermal markers, but it also affects the fast population, to a lower degree. This is because beam ions do not exclusively slow down, the collisions are random in nature. The diffusion removes thermal markers that could have become fast at some point in the future. In addition, there is an indirect effect of diffusion on fast ions: the thermal population influences the RF wave propagation, polarisation and absorption. This affects the ability to generate fast ions. Note that this indirect effect is not included until section 5.4, where the wave field is incorporated.

The hydrogen density is controlled by setting the value of  $D$ , see Fig. 5.6. In principle a scan of simulations can be performed to tune the value of  $D$ , such that the best match with experiment can be found.

The SD distribution can also be binned in pitch  $\lambda$ , see Fig. 5.7. The fresh beam ions have four distinct peaks:  $\lambda = \pm 0.46$ , corresponding to PINIs 4,8 which are more tangential and  $\lambda = \pm 0.30$ , corresponding to PINIs 3,7 which are more radial. Over time the distribution becomes more isotropic due to collisions. Fully isotropic (in terms of polar and azimuthal angle) would show up as a flat line in Fig. 5.7, because  $f$  would be independent of  $(\lambda, \phi)$ . This binning can be slightly deceptive though. It works by filtering all markers based on a given criteria, in this case fixed width bins in pitch, and summing their weights. This means that the Jacobian determinant of the given coordinate system is **already** included. To illustrate this effect, note that a point in velocity space can be uniquely described using the coordinates  $(E, \lambda, \phi)$  (pitch, energy, gyro angle). Where  $\lambda = v_z/v = \cos(\theta)$  with  $\theta \in [0, \pi]$  the polar angle. Binning an isotropic distribution function in terms of  $\theta$  would not actually result in a flat line (when plotted vs  $\theta$ ) because of the Jacobian determinant  $\sin(\theta)$ .

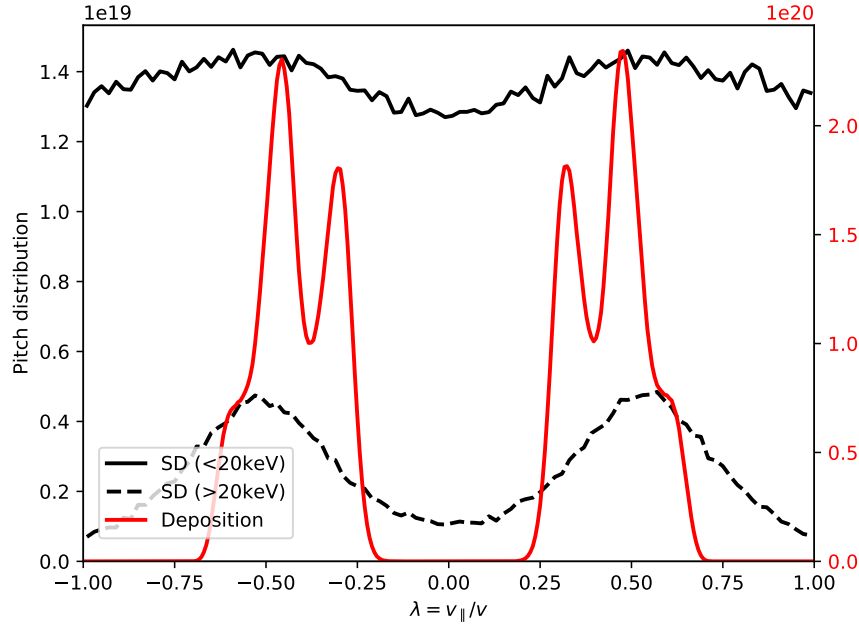


Figure 5.7: Particle pitch distribution for the slowing down (SD) distribution after 200 ms (2 cycles), normalised such that the integral over pitch gives the total number of H ions in the plasma. As a reference, the total deposition of particles for one whole cycle (100 ms of physical time) is plotted in red, with corresponding y-axis on the right.

## 5.2 Monte Carlo operators

Markers in VENUS-LEVIS are advanced in time by updating the 4 state variables (3 for position + parallel Larmor radius) using the guiding centre drift equations<sup>3</sup>. In addition to these updates, the following processes are included by using Monte Carlo operators: Coulomb collisions (scattering in pitch-angle and energy), interaction with the wave field, and anomalous diffusion. All except for the latter have already been used for the computations in section 4.5. However, the RF-NBI scheme requires all processes together, see section 5.3, which necessitates an update to VENUS-LEVIS. Thus, for completeness, all three relevant operators are described. Note, this section is based on [66], [62, section 4.5].

### 5.2.1 Coulomb collisions

The time derivative of the distribution function  $f$  due to collisions is given by:

$$\left(\frac{\partial f}{\partial t}\right)_{coll} = \sum_s C[f, f_s]. \quad (5.4)$$

<sup>3</sup>The code can also run in full 6D (full-orbit), but that is never used in this work because it would be too costly and also unnecessary for the purpose of ICRH.

It will be assumed that the bulk population  $f_s$  is a Maxwellian distribution. Also it is assumed that  $f$  is independent of gyro angle, see Eq. (2.15). The collision operator  $C$  can then be written as follows:

$$C[f, f_s] = \nu_\lambda^s \frac{1}{2} \frac{\partial}{\partial \lambda} \left[ (1 - \lambda^2) \frac{\partial f}{\partial \lambda} \right] + \frac{1}{\nu^2} \frac{\partial}{\partial \nu} \left[ \nu^2 \nu_E^s \left( \nu f + \frac{T_s}{m} \frac{\partial f}{\partial \nu} \right) \right], \quad (5.5)$$

with  $\nu_\lambda^s, \nu_E^s$  the frequencies of pitch-angle and energy scattering for species  $s$ . For both of these processes a Monte Carlo scheme can be derived. Take pitch angle scattering for example: Firstly, define a generic moment of the distribution function  $f$  function,

$$\langle h \rangle = \int_{-1}^1 f h d\lambda. \quad (5.6)$$

Note,  $h$  can be a function of position and velocity, but not of time. The moment  $\langle h \rangle$  on the other hand is only a function of time. In addition, in this derivation  $f$  is normalised such that  $\langle 1 \rangle = 1$ . The time derivative due to pitch-angle scattering can then be written as

$$\left( \frac{d\langle h \rangle}{dt} \right)_\lambda = \int_{-1}^1 \left( \frac{\partial f}{\partial t} \right)_\lambda h d\lambda = \int_{-1}^1 h \sum_s \nu_\lambda^s \frac{1}{2} \frac{\partial}{\partial \lambda} \left[ (1 - \lambda^2) \frac{\partial f}{\partial \lambda} \right] d\lambda. \quad (5.7)$$

This now has to be integrated by parts twice to eliminate derivatives of  $f$ , so that it may again be written using the angular brackets:

$$\begin{aligned} \left( \frac{d\langle h \rangle}{dt} \right)_\lambda &= \sum_s \nu_\lambda^s \underbrace{\left( h \frac{1}{2} \left[ (1 - \lambda^2) \frac{\partial f}{\partial \lambda} \right] \right) \Big|_{-1}^1}_{=0} - \sum_s \nu_\lambda^s \int_{-1}^1 \frac{\partial h}{\partial \lambda} \frac{1}{2} \left[ (1 - \lambda^2) \frac{\partial f}{\partial \lambda} \right] d\lambda \\ &= - \sum_s \nu_\lambda^s \underbrace{\left( f \frac{1}{2} (1 - \lambda^2) \frac{\partial h}{\partial \lambda} \right) \Big|_{-1}^1}_{=0} + \sum_s \nu_\lambda^s \int_{-1}^1 f \frac{1}{2} \frac{\partial}{\partial \lambda} \left[ \frac{\partial h}{\partial \lambda} (1 - \lambda^2) \right] d\lambda \\ &= \sum_s \nu_\lambda^s \left( \left\langle \frac{1}{2} (1 - \lambda^2) \frac{\partial^2 h}{\partial \lambda^2} \right\rangle - \left\langle \lambda \frac{\partial h}{\partial \lambda} \right\rangle \right). \end{aligned} \quad (5.8)$$

Now two special cases are computed:

$$\left( \frac{d\langle \lambda \rangle}{dt} \right)_\lambda = - \sum_s \nu_\lambda^s \langle \lambda \rangle \quad (5.9a)$$

$$\left( \frac{d\langle \lambda^2 \rangle}{dt} \right)_\lambda = \sum_s \nu_\lambda^s (1 - 3\langle \lambda^2 \rangle). \quad (5.9b)$$

The variance can be written as  $\sigma_\lambda^2 = \langle \lambda^2 \rangle - \langle \lambda \rangle^2$ , which has the following time derivative:

$$\left( \frac{d\sigma_\lambda^2}{dt} \right)_\lambda = \left( \frac{d\langle \lambda^2 \rangle}{dt} \right)_\lambda - 2\langle \lambda \rangle \left( \frac{d\langle \lambda \rangle}{dt} \right)_\lambda = \sum_s \nu_\lambda^s (1 - 3\langle \lambda^2 \rangle + 2\langle \lambda \rangle^2). \quad (5.10)$$

## Chapter 5. Combined RF-NBI heating

The next step is to assume  $f$  is initialised as a delta function  $\delta(\lambda - \lambda_0)$ , so at time  $t = 0$ ,  $\langle \lambda \rangle = \lambda_0$ ,  $\langle \lambda^2 \rangle = \lambda_0^2$  and hence,

$$\left( \frac{d\langle \lambda \rangle}{dt} \right)_{\lambda} \Big|_{t=0} = - \sum_s v_{\lambda}^s \lambda_0 \quad (5.11a)$$

$$\left( \frac{d\sigma_{\lambda}^2}{dt} \right)_{\lambda} \Big|_{t=0} = \sum_s v_{\lambda}^s (1 - \lambda_0^2). \quad (5.11b)$$

As explained in [66], after a brief time  $t$ , the distribution  $f$  is expected to have evolved into a Gaussian, centred around  $\lambda = \lambda_0(1 - \sum_s v_{\lambda}^s t)$  with standard deviation  $\sigma_{\lambda} = \sqrt{\sum_s v_{\lambda}^s (1 - \lambda_0^2) t}$  (integrate Eqs. (5.11)). This broadening process of the delta function can be approximated by applying many small kicks,

$$\Delta \lambda = - \sum_s v_{\lambda}^s \lambda_0 \Delta t + \mathcal{R} \sqrt{\sum_s v_{\lambda}^s (1 - \lambda_0^2) \Delta t}, \quad (5.12)$$

with  $\mathcal{R} = \pm 1$ , randomly chosen. This procedure works as long as the time step is small enough, i.e.  $\sum_s v_{\lambda}^s \Delta t \ll 1$ . Equation (5.12) describes how pitch-angle scattering is implemented in VENUS-LEVIS, but an expression for energy scattering can be derived along the same lines:

$$\Delta E = - \sum_s 2v_E^s \Delta t \left[ E_0 - T_s \left( \frac{3}{2} + \frac{E_0}{v_E^s} \frac{dv_E^s}{dE} \right) \right] + 2\mathcal{R} \sqrt{\sum_s v_E^s T_s E_0 \Delta t}. \quad (5.13)$$

Alternatively, these kicks can be found by casting the collision operator in the Fokker-Planck form<sup>4</sup>:

$$\sum_s C[f, f_s] = \frac{\partial}{\partial \lambda} \left[ \sum_s v_{\lambda}^s \frac{1}{2} (1 - \lambda^2) \frac{\partial f}{\partial \lambda} \right] + \frac{1}{\sqrt{E}} \frac{\partial}{\partial E} \left[ \sqrt{E} \sum_s 2v_E^s E \left( f + T_s \frac{\partial f}{\partial E} \right) \right], \quad (5.14)$$

which matches the form used in [67, Eq. 19]:

$$\left( \frac{\partial f}{\partial t} \right)_{coll} = \frac{1}{\sqrt{g}} \frac{\partial}{\partial v^i} \left[ \sqrt{g} \left( a^i f + d^{ij} \frac{\partial f}{\partial v^j} \right) \right], \quad (5.15)$$

with  $a, d$  representing advection and diffusion coefficients. Applied to  $\lambda, E$  these are

$$a^{\lambda} = 0 \quad (5.16a)$$

$$d^{\lambda\lambda} = \frac{1}{2} \sum_s v_{\lambda}^s (1 - \lambda^2) \quad (5.16b)$$

$$a^E = 2 \sum_s v_E^s E \quad (5.16c)$$

$$d^{EE} = 2 \sum_s v_E^s T_s E, \quad (5.16d)$$

<sup>4</sup>Using  $\partial/\partial v = mv\partial/\partial E$ , and the velocity space Jacobian determinant is  $v/m$  in  $(E, \lambda, \phi)$  coordinates.



so all off-diagonal entries in  $d^{ij}$  are zero. The change in the mean and covariance are related to the advection and diffusion coefficients via:

$$\frac{d\langle v^i \rangle}{dt} = -a^i + \frac{1}{\sqrt{g}} \frac{\partial}{\partial v^j} (\sqrt{g} d^{ij}) \quad (5.17a)$$

$$\frac{d\text{cov}(v^i, v^j)}{dt} = d^{ij} + d^{ji} = 2d^{ij}. \quad (5.17b)$$

Note that  $\text{cov}(v^i, v^i) = \sigma_i^2$ . More explicitly, e.g. for energy:

$$\left( \frac{d\langle E \rangle}{dt} \right)_{\lambda} \Big|_{t=0} = - \sum_s 2v_E^s \left[ E_0 - T_s \left( \frac{3}{2} + \frac{E_0}{v_E^s} \frac{dv_E^s}{dE} \right) \right] \quad (5.18a)$$

$$\left( \frac{d\sigma_E^2}{dt} \right)_{\lambda} \Big|_{t=0} = 4 \sum_s v_E^s T_s E_0, \quad (5.18b)$$

which recovers Eq. (5.13).

### 5.2.2 Anomalous diffusion

Modelling anomalous diffusion was already explored for tokamaks in VENUS [61, sections 4.3, 4.4] (note: VENUS is the predecessor of VENUS-LEVIS). However, in order to apply this to more general magnetic equilibria, the approach of ASCOT is used instead [68]. This radial diffusion model is implemented as a Monte Carlo collision operator, similar to how the Coulomb collisions (as well as the ICRH kick) work in VENUS-LEVIS. Akin to the other Monte Carlo operators in VENUS-LEVIS, this process can be enabled/disabled with a simple modification to the input files.

It will be assumed that the collision processes responsible for pitch angle scattering, energy scattering,... etc are independent, hence they can be applied separately. The term responsible for radial diffusion can be written as:

$$\left( \frac{\partial f}{\partial t} \right)_d = \nabla \cdot (D \nabla f). \quad (5.19)$$

where  $D$  represents the diffusion coefficient. Defining a generic moment as follows,

$$\langle h \rangle = \int_{\Omega} f h dV. \quad (5.20)$$

Note, this differs from the definition of Eq. (5.6) since the integration is not over pitch angle, but over the entire plasma volume  $\Omega$ . The time derivative, due to diffusion alone, is

$$\left( \frac{d\langle h \rangle}{dt} \right)_d = \int_{\Omega} \left( \frac{\partial f}{\partial t} \right)_d h dV = \int_{\Omega} h \nabla \cdot (D \nabla f) dV. \quad (5.21)$$

Integrating by parts (twice) gives

$$\left(\frac{d\langle h \rangle}{dt}\right)_d = \int_{\Omega} f \nabla \cdot (D \nabla h) dV + \int_{\partial\Omega} D (h \nabla f - f \nabla h) \cdot \mathbf{n} dS = \langle \nabla \cdot (D \nabla h) \rangle. \quad (5.22)$$

The surface integral appears due to the divergence theorem, but because  $f$  vanishes on the boundary, this surface term is eliminated. To be precise,  $f$  does not need to be zero on  $\partial\Omega$ , but later on it will be approximated as a delta function which does disappear on the boundary.

Define the coordinate system to be  $(u^1, u^2, u^3)$ , where  $u^1$  is the radial flux label, and  $u^2, u^3$  two angular coordinates. Substitution of  $h = u^1$  or  $h = (u^1)^2$  in Eq. (5.22) yields the following in curvilinear coordinates:

$$\left(\frac{d\langle u^1 \rangle}{dt}\right)_d = \left\langle \frac{1}{\sqrt{g}} \frac{\partial}{\partial u^i} \left( \sqrt{g} D g^{1i} \right) \right\rangle \quad (5.23a)$$

$$\left(\frac{d\langle (u^1)^2 \rangle}{dt}\right)_d = 2 \left\langle \frac{1}{\sqrt{g}} \frac{\partial}{\partial u^i} \left( \sqrt{g} D u^1 g^{1i} \right) \right\rangle, \quad (5.23b)$$

where the Einstein summation convention is applied,  $g^{ij}$  is the metric tensor (see Appendix A.1) and  $\sqrt{g}$  is the Jacobian determinant. The time evolution of the variance  $\sigma^2$  can be written as

$$\left(\frac{d\sigma^2}{dt}\right)_d = \left(\frac{d}{dt} \left[ \langle (u^1)^2 \rangle - \langle u^1 \rangle^2 \right]\right)_d. \quad (5.24)$$

The initial distribution function is assumed to be a delta function in terms of  $u^1$ , i.e.  $\delta(u^1 - u^1(0))$ . Also this delta function is weighted such that  $\langle 1 \rangle = 1$ , so

$$\left(\frac{d\langle u^1 \rangle}{dt}\right)_d \Big|_{t=0} = \frac{1}{\sqrt{g}} \frac{\partial}{\partial u^i} \left( \sqrt{g} D g^{1i} \right) \quad (5.25a)$$

$$\left(\frac{d\sigma^2}{dt}\right)_d \Big|_{t=0} = 2 D g^{11}. \quad (5.25b)$$

From this the stochastic radial kick is constructed:

$$\begin{aligned} \Delta u^1 &= \Delta t \left(\frac{d\langle u^1 \rangle}{dt}\right)_d \Big|_{t=0} + \mathcal{R} \sqrt{\Delta t \left(\frac{d\sigma^2}{dt}\right)_d \Big|_{t=0}} \\ &= \frac{1}{\sqrt{g}} \frac{\partial}{\partial u^i} \left( \sqrt{g} D g^{1i} \right) \Delta t + \mathcal{R} \sqrt{2 D g^{11} \Delta t}. \end{aligned} \quad (5.26)$$

Equation (5.26) is the anomalous diffusion kick implemented in the new version of VENUS-LEVIS. The degree of anomalous diffusion can be controlled with the parameter  $D$ . Note that in this derivation no assumption has been made on the magnetic equilibrium, nor on the spatial dependence of  $D$ . Along the same lines a Monte Carlo operator for diffusion in the angular directions  $u^2, u^3$  can also be derived. However, this type of diffusive transport is negligible compared to the normal transport channels in the angular directions, hence it is omitted in VENUS-LEVIS.

### 5.2.3 Wave-particle interaction

Incorporating the effect of a radio frequency perturbation of the electromagnetic fields is easy in 6D. It is just added to the equilibrium fields and the state of the markers is advanced in time using the Lorentz force. However, this would require resolving the gyro period, which is rather expensive. Also it is unnecessary for the purpose of ICRH modelling since the change in an ion's momentum during one such period is typically small compared to its total momentum. So in this thesis VENUS-LEVIS is run in 4D mode. In which case the perturbation is accounted for via a own Monte Carlo operator representation, instead of modifying the  $\mathbf{E}, \mathbf{B}$  fields in the guiding centre equations.

Armed with the knowledge that the wave-particle interaction is highly localised near the resonance layer, see Eq. (2.37), so called “resonant diffusion” can be applied. This assumes that the interaction is fully confined to the exact resonant surface, with zero interaction elsewhere. In practice this is implemented in VENUS-LEVIS by checking if the sign of  $\omega - n\Omega - k_z v_z$  has flipped. It does so when the marker has crossed the resonant surface, at which point a kick is applied. This so called “RF kick” can be split into a parallel and perpendicular contribution, the latter is:

$$\Delta v_{\perp} = \langle \Delta v_{\perp} \rangle + \mathcal{R} \sqrt{2 \langle \Delta v_{\perp}^2 \rangle}. \quad (5.27)$$

For harmonic  $n$  the kick is given by

$$\langle \Delta v_{\perp}^2 \rangle = \alpha \frac{q^2}{m^2} \tau^2 |E^+ J_{n-1}(k_{\perp} v_{\perp} / \Omega) + E^- J_{n+1}(k_{\perp} v_{\perp} / \Omega)|^2 \quad (5.28a)$$

$$\langle \Delta v_{\perp} \rangle = \frac{\langle \Delta v_{\perp}^2 \rangle}{2 v_{\perp}}. \quad (5.28b)$$

In this case  $\tau$  represents the wave-particle interaction time, and  $\alpha$  is a scaling parameter. Note, the derivation of Eq. (5.28) is rather lengthy so it will not be reproduced here, but it can be found in e.g. [35, section 6.2.2] and references therein. The computation of  $E^{\pm}$  comes from a full-wave code, LEMan in this case, as seen in earlier chapters. Since the wave model is linear, the solution for  $E^{\pm}$  only needs to be computed once per plasma and magnetic field scenario. It can then be rescaled arbitrarily (using  $\alpha$ ) to any input power, e.g. 1.5 MW. In addition, there will always be a slight discrepancy between the power computed by LEMan and that reported by VENUS-LEVIS since the fundamental physics models are not the same: the plasma response in LEMan uses the 6D orbits, but in a homogeneous plasma. VENUS-LEVIS uses a realistic magnetic topology, but employs a 4D model and resonant diffusion.

Also, the distribution function  $f_0$ , which is sampled using markers, evolves over time. In some cases rather dramatically during one simulation run. However, something that is typically kept approximately constant during an experiment is the input power, which is why  $\alpha$  is also adjusted during the VENUS-LEVIS simulation to maintain a fixed input power. In real life, constant power does not necessarily imply that the whole wave field scales up or down in amplitude, which is what happens when  $\alpha$  is varied. As  $f_0$  changes, the wave field could

also rearrange itself in other ways that lead to a constant power. Playing with  $\alpha$  is merely an approximation, which is sufficient on short time scales, but if  $f_0$  has changed significantly it will be required to recompute  $E^\pm$ , which is precisely why SCENIC iterates its codes.

It can be shown that in the limit of resonant diffusion the following constraint holds [69],

$$v_\perp^2 + (v_z - \omega/k_z)^2 = \text{const.} \quad (5.29)$$

In combination with Eq. (2.37) this leads to

$$\frac{dv_z}{dv_\perp} = \frac{k_z v_\perp}{n\Omega} = \frac{v_\perp}{v_z} \frac{\omega - n\Omega}{n\Omega}. \quad (5.30)$$

Intuitively one might think that the RF kick only applies to  $v_\perp$ , given that it is the perpendicular motion of the particle that is in sync with the wave, but Eq. (5.30) disproves this. Because of the Doppler effect the numerator is not exactly zero, so the kick also applies to  $v_z$ . However, the frequency difference between  $\omega$  and  $n\Omega$  is typically not too large, only a few percent, which means that ICRH usually still results in (highly) anisotropic fast ion populations. Combining Eqs. (5.30), (5.27) provides an expression for the kick in parallel velocity:

$$\Delta v_z = \frac{k_z v_\perp}{n\Omega} \Delta v_\perp. \quad (5.31)$$

Using these increments, the change in energy can be made explicit:

$$\begin{aligned} \Delta E &= \frac{1}{2} m ((v_z + \Delta v_z)^2 + (v_\perp + \Delta v_\perp)^2) - \frac{1}{2} m (v_z^2 + v_\perp^2) \\ &= \frac{\omega}{n\Omega} m v_\perp \Delta v_\perp + \frac{1}{2} m ((\Delta v_z)^2 + (\Delta v_\perp)^2). \end{aligned} \quad (5.32)$$

Given that for ions, the resonance is only for  $n > 0$ , the net energy transfer is from the wave to the plasma,  $\langle \Delta E \rangle > 0$ . That does not mean that all particles gain energy, remember that  $\Delta v_\perp$  can be negative. So some particles will lose energy and some will gain, but on average their energy is increased by the RF kick.

To conclude this section, it has been shown that there are multiple Monte Carlo operators that modify  $(v_\perp, v_z)$ , either directly, or indirectly through  $(\lambda, E)$ . As mentioned before, these processes are assumed to be independent, yet they modify the same variables. The term “independent” here just means that the value of the kick of one Monte Carlo operator does not depend on the value of another operator. In other words, the value of the kick in each operator can be found independently (decoupled), so instead of one combined operator the kicks can all be conveniently applied in succession, or in demand for the problems investigated. For example, in practice the only heating scenario investigated in this thesis that requires the anomalous diffusion operator is the RF-NBI scheme explored next. Meanwhile, all the RF-only scenarios only require Coulomb collisions and the RF kick.

### 5.3 Model difficulties with combined RF-NBI

A primary goal is the study of fast ions, for which resources spent on the detailed dynamics of the thermal markers is wasteful. Unfortunately this may be unavoidable for specific scenarios, as will be explained in this section. In the case of NBI-only modelling, the markers are born fast, and slow down on the bulk plasma. At some point these markers are lost from the plasma, or thermalise, at which point they can be removed from the simulation. As mentioned before, removing thermal markers does have some up-stream effect; it also lowers the fast ion concentration to some extent. But this is a small effect in the energy range of interest (approximately 60 keV for mimicking fusion alphas [9]), so it is justified to remove thermal markers. However, in case ICRH is involved the wave provides a mechanism for accelerating ions to significantly higher energy. Thermal markers form the seed ions, some of which are going to be fast in the future. Hence they cannot simply be removed without substituting in an appropriate particle/energy source.

The thermal population experiences a higher collision frequency, so their distribution is typically well approximated by a Maxwellian. Given the wave field and the fraction of the RF input power that is absorbed by the thermal population, such a particle/energy source can in principle be derived. However, it would not be easy to do this in a consistent way. So to be pragmatic, in this thesis the thermal markers are not removed from the simulation (also in the NBI-only scenarios<sup>5</sup>). But that too has its problems if suitable transport channels are absent for the thermalised markers: for example, previous simulations observed accumulation of thermal ions reaching unphysically high concentrations [48].

VENUS-LEVIS is developed for modelling fast ions, and the guiding centre equations in combination with Coulomb collisions provide an accurate description of their motion. The supra-thermal ions are assumed to be fast enough so that turbulence does not have a significant effect on them, at least not in a direct way. This is because they move so rapidly that their interaction with any individual eddy of the background flow is short-lived. Thermal ions on the other hand can experience a considerably enhanced radial transport due to turbulence. Accurately modelling this type of transport is exceptionally challenging. Which is why a simplified model using radial anomalous diffusion (see section 5.2.2) has been implemented instead. With diffusion enabled, an equilibrium can be reached, see Fig. 5.8.

Since it is not known at the start of the VENUS-LEVIS simulation when the steady state will be reached, the simulation is divided up in so called “cycles” for numerical reasons. Markers are pre-generated for all cycles, and once a cycle finishes the next one can resume where the previous one left off. Note that most markers will be thermal, see Fig. 5.5. This means that for a reasonable total number of markers the fast ion tail will be rather noisy, which is another downside of including the thermal markers.

<sup>5</sup>Side note on RF-only simulations: as explained, thermal markers are not removed, but there are still particle losses. Since there is no actual particle source in the model in the absence of NBI, lost markers are re-spawned by sampling from the starting distribution. Of course at some point this starting distribution will need to be updated since VENUS-LEVIS evolves  $f_0$ . But this happens natively as SCENIC already iterates the codes.

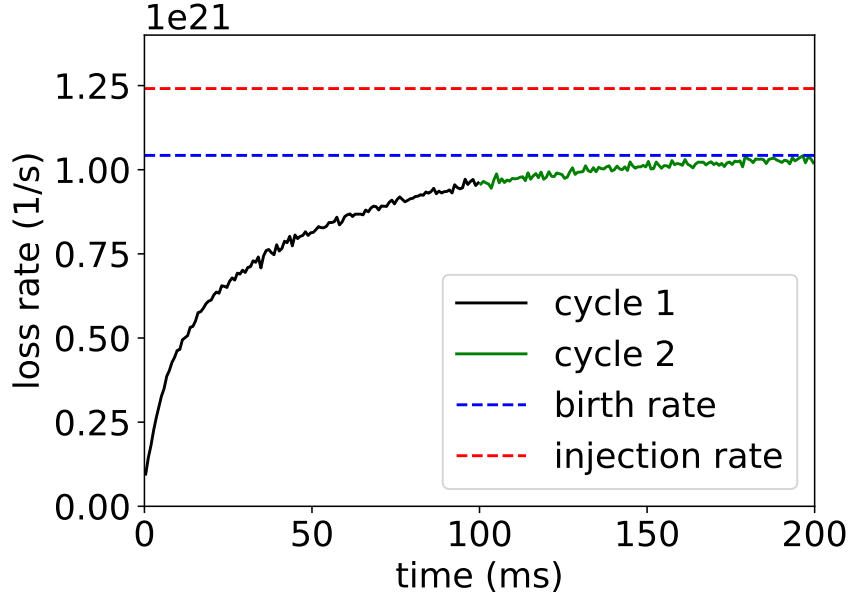


Figure 5.8: Loss rate of beam particles vs time. Using base case parameters, Table 5.1. Because of shine-through, birth rate < injection rate.

## 5.4 RF-NBI results W7-X

The synergetic RF-NBI scenario is now ready to be investigated. Several cases will be studied, see table 5.1. Note that the goal here is to generate as many fast ions as possible, which can be used for studies into e.g. their confinement, excitation of Alfvén waves and suppression of transport. Recall that not all beam ions start out with full energy (55 keV), about two thirds of the protons have half or third energy. To this end the RF-NBI scheme is promising because it is able to boost the beam ions to even higher energy, as was already demonstrated on Heliotron-J for instance [70]. Compared to schemes that only use RF there are a number of advantageous features as well: Typical minority heating results in fast ions with considerably larger perpendicular than parallel velocity. In a stellarator like W7-X these can be lost rapidly without even colliding [10], [71], which makes it hard in practice to form an energetic tail. However, because of the large  $v_z$  of the beam ions (and thus Doppler shift), the kicks in parallel velocity are not negligible, see Eq. (5.30). This means the heating is more isotropic, leading to a smaller trapped fast ion fraction. Lastly, there is more power available: the ICRH antenna is expected to couple about 1.5 MW to the plasma [72], the addition of four PINIs will add another 6.8 MW of power. One of the consequences is that instead of accelerating minority ions from thermal energy, the beam ions already start with  $E > T_e$ .

To be clear, as the name implies, ICRH exploits a resonant phenomenon and so a large fast ion population can also be obtained with RF-only schemes if it is ensured that most of the power goes to a tiny population of ions. This is what the three ion scheme does, which has an

Table 5.1: Description of the various test cases used. The density  $N$  and temperature  $T$  are on-axis values. For the profiles used see Fig. 5.2. The magnetic equilibrium is generated using base case parameters.

Case	$N_e$ ( $10^{19}\text{m}^{-3}$ )	$T_e$ (keV)	$T_i$ (keV)	$D$ ( $\text{m}^2/\text{s}$ )
Base case	5.0	3.0	1.5	1.0
$N \times 2$	10.0	3.0	1.5	1.0
$N \times 3$	15.0	3.0	1.5	1.0
$T \times 0.5$	5.0	1.5	0.75	1.0
$T \times 2$	5.0	6.0	3.0	1.0
$D \times 0.5$	5.0	3.0	1.5	0.5
$D \times 2$	5.0	3.0	1.5	2.0

impressively high power per ion. However, given the time constraints this scheme was not further investigated in this work.

#### 5.4.1 Wave field

After running VENUS-LEVIS with NBI-only and reaching steady state<sup>6</sup>, the density and temperature profiles of the beam species can be constructed. The hydrogen is first split into a thermal and fast population, which are then fitted with a Maxwellian and modified bi-Maxwellian respectively. Note that this classification of “thermal” and “fast” need not be the same as that used for the diffusion. It is chosen such that a good fit can be obtained, in this particular case the split is set at  $E > 6T_e$ , so six times the local electron temperature. Using this data the full-wave code is ready to be run. The same resolution as in section 4.4 is used for LEMan.

The antenna frequency is set indirectly in LEMan by controlling the parameter  $B_{res} = \frac{m\omega}{nq}$ . Initially, the value  $B_{res} = 2.5$  T is chosen; this is already a small shift w.r.t. the on-axis value  $B = 2.43$  T (in front of the antenna). Ideally, the frequency  $\omega$  is chosen such that the Doppler shifted resonance, near the antenna, is placed in the core (where confinement is best), see Fig. 5.9. But the optimal value is not obvious given that the magnetic field strength depends on all three spatial coordinates. In addition, the particle pitch of the SD population has a large spread as well. So the dashed red line in the cartoon is actually a broad zone. By shifting the antenna frequency up/down the layers can be moved. The bigger the shift, the more favourable the heating will be for the very fastest ions. Due to the Doppler effect, only they have a large enough  $v_z$  so resonance in the core is possible. By modifying the antenna frequency we are effectively selecting a population of ions to accelerate with ICRH. Note that there is an optimum, if  $B_{res}$  is approximately equal to the on-axis value most of the RF power will just go to heating thermal hydrogen. If the frequency shift is too high there will be some very fast

<sup>6</sup>To remain consistent with the assumption that fast ion transport is accurately modelled, the diffusion is only applied to the thermal population.

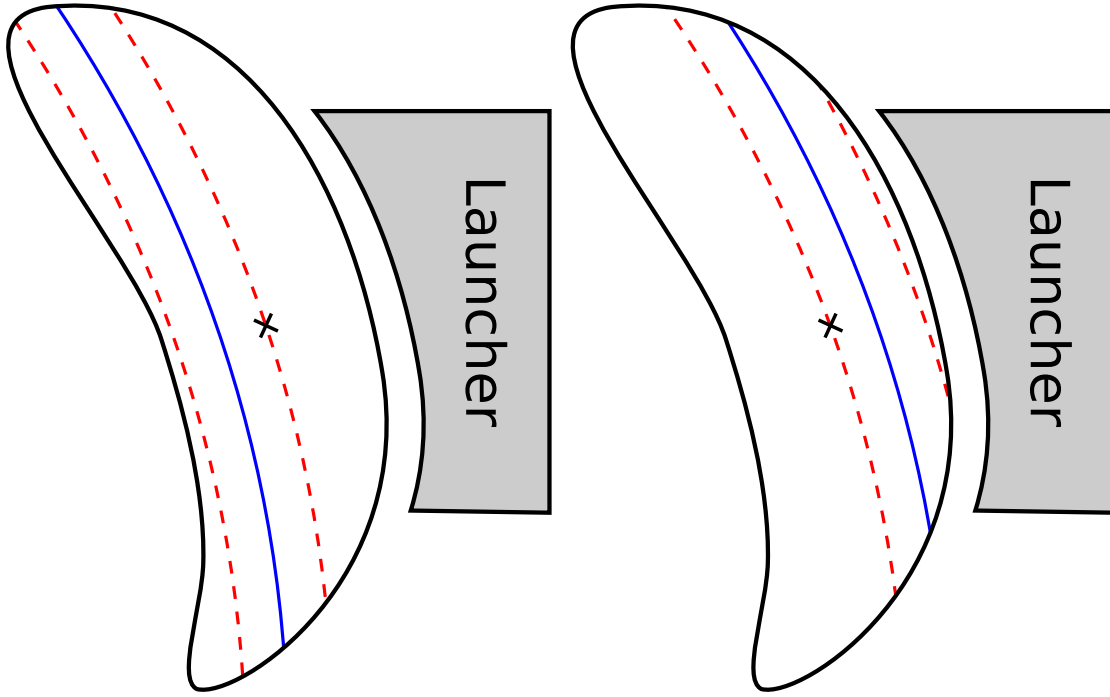


Figure 5.9: Simple cartoon to illustrate where the resonance is. The thermal ions resonate near the cold resonance ( $\omega = \Omega$ ), indicated in blue. The red dashed lines indicate where the beam ions resonate, and the  $\times$  highlights the magnetic axis. On the left, the antenna frequency is shifted up, on the right it is shifted down.

ions becoming even faster, but the small amount of ions starting at this high energy will be restrictive. In other words, too little power would go to the moderately fast ions, which are needed to get the “very fast” seed ions in the first place.

The power fractions for the various species are given in Fig. 5.10. If the bulk density is increased the hydrogen power fraction goes down, which is unsurprising given that the injection rate is unchanged. This means that the concentration of hydrogen w.r.t. the electron density decreases. A too high minority concentration can deteriorate the wave polarisation at the cyclotron resonance, but these simulations were still in the regime where even the base case with about 7.3% H in the core did not result in poor polarisation. From a related scan (Fig. 4.15) it is seen that this concentration can be quite large. At higher temperature (compared to the base case), the deuterium absorbs more power, which is because the second harmonic heating is an FLR effect; electrons also absorb more power. Lastly, if the diffusion coefficient is increased (section 5.1.4), more thermal H is lost which results in a lower power fraction of  $H_{th}$ . Note that the NBI deposition depends on the plasma density and temperature, thus VENUS-NBI had to be rerun for each case (except when modifying the diffusion coefficient).

With modern visualisation tools (Paraview in this case) it is easy to slice datasets in various ways. The wave field in the poloidal plane in front of the antenna is depicted in Fig. 5.11 for the base case, and in Fig. 5.12 for the  $N \times 3$  case. A top-down view of the device is shown in



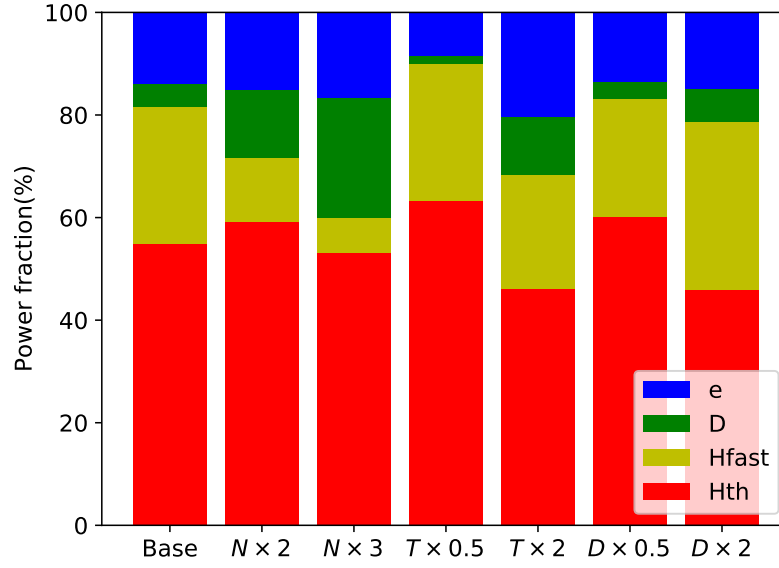


Figure 5.10: Fraction of the RF power directly deposited on the various plasma species. A distinction is made between the thermal (Maxwellian) hydrogen, and the fast hydrogen.

Figs. 5.13, 5.14, which reveals that the wave propagates less far toroidally in the higher density plasma. This is because of the stronger wave damping. It is clear that the amplitude is not homogeneous in space, also it does not focus perfectly on axis. Moreover, the magnetic field is fully 3D, so at some toroidal angles the cold resonant surface ( $\omega = \Omega$ ) cuts through the core plasma while at other angles it does not. Hence the power deposition is also not necessarily peaked on axis, see Fig. 5.15.

Another difference between these two cases is the wavelength, see Fig. 5.16. Cold plasma theory can be used to give a rough estimate of the wavelength. The slow wave does not propagate into the core, so this region is dominated by the fast wave. The parallel wavenumber is mainly determined by the antenna geometry and phasing, so this leaves the perpendicular wavenumber. For the fast wave the dispersion relation (2.63) can be written as follows:

$$k_{\perp}^2 \approx \frac{\omega^2}{c^2} \frac{(R - n_{\parallel}^2)(L - n_{\parallel}^2)}{S - n_{\parallel}^2}. \quad (5.33)$$

Far away from any cut-off or resonance the contribution of the parallel wavenumber ( $k_{\parallel} = \omega n_{\parallel} / c$ ) can be neglected,

$$k_{\perp}^2 \approx \frac{\omega^2}{c^2} \frac{RL}{S} \propto N. \quad (5.34)$$

So the perpendicular wavelength is roughly proportional to  $1/\sqrt{N}$ , with  $N$  the density. LEMan was also run for the other cases in table 5.1. But to keep the results of this section concise their

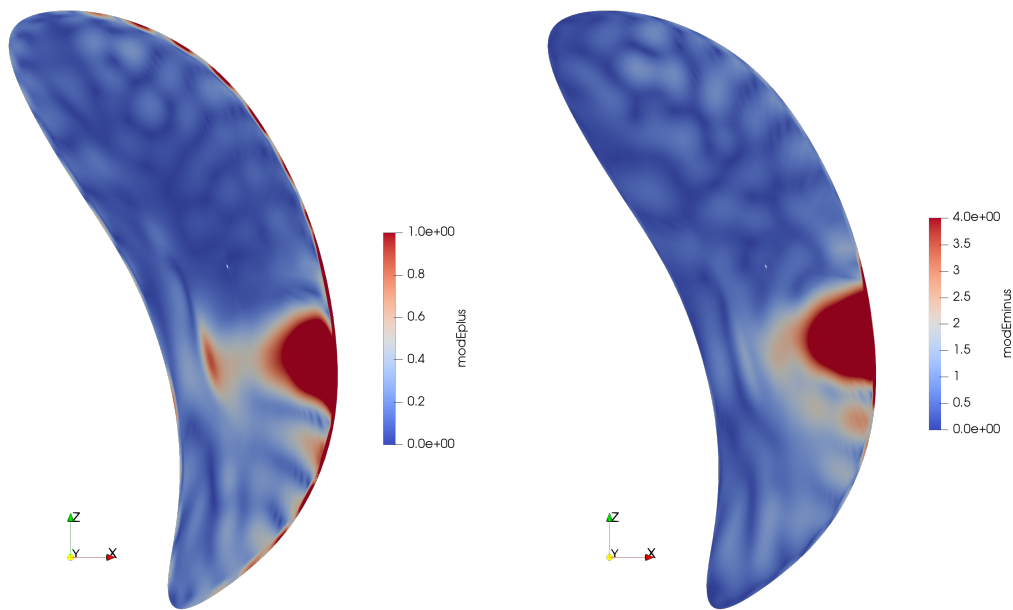


Figure 5.11: A plot of the amplitudes of the left (+) and right (-) handed polarised component of the electric field of the wave in front of the antenna (base case). Note,  $E^+$  is mainly responsible for heating H. (arbitrary units used)

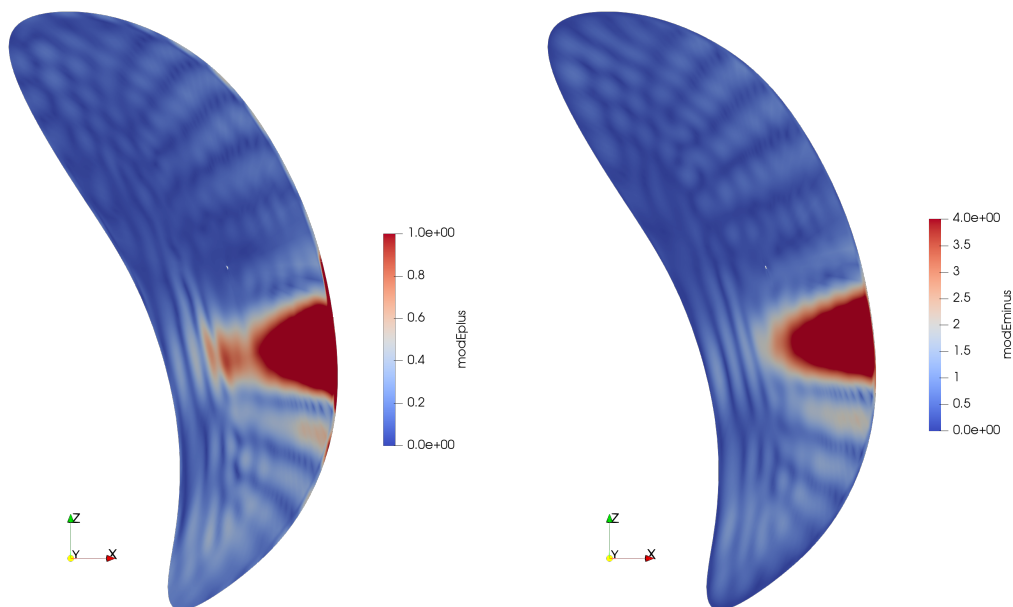


Figure 5.12: Plot of left and right handed polarised components of the wave field (density x3).

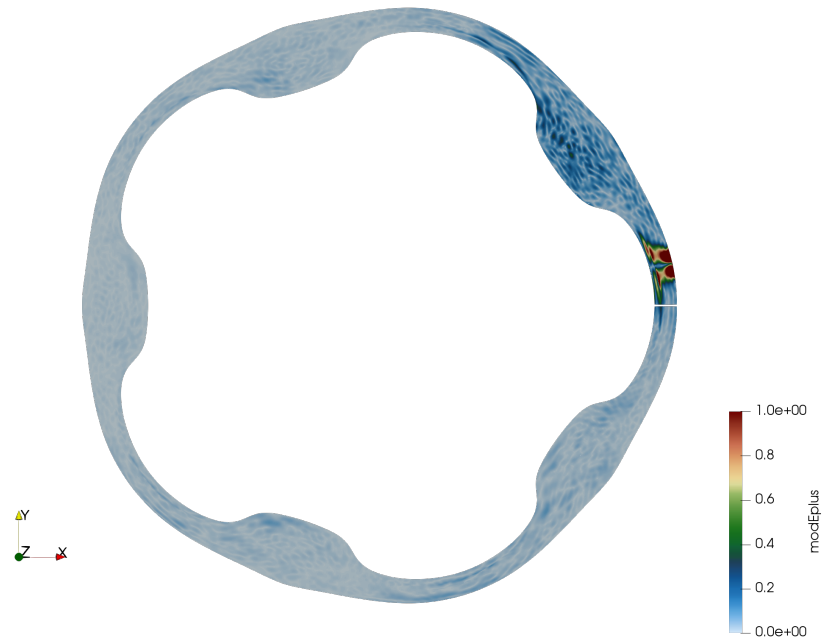


Figure 5.13: Cross section of the plasma, top-down view, colour indicates  $|E^+|$  in arbitrary units. The hotspot is located just in front of the antenna.

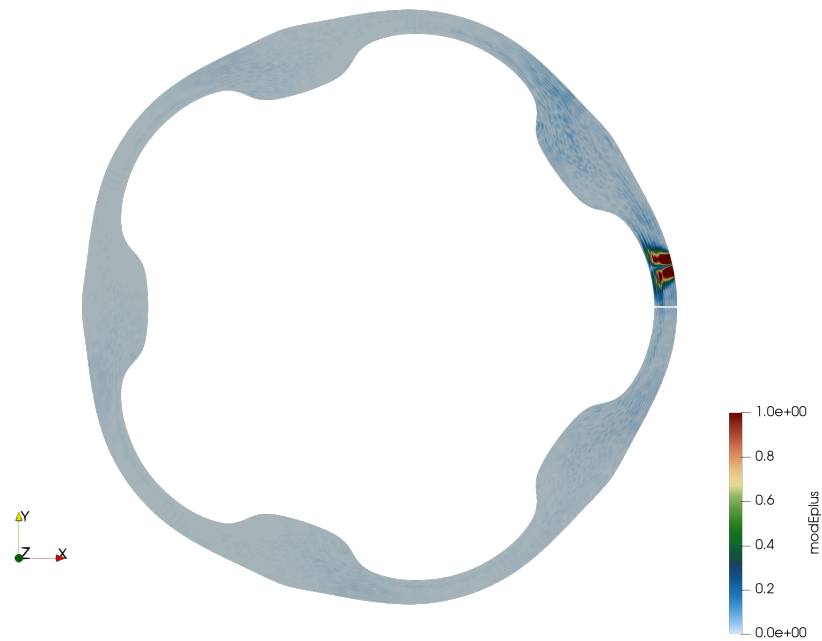


Figure 5.14: Same, but for density x3 case.

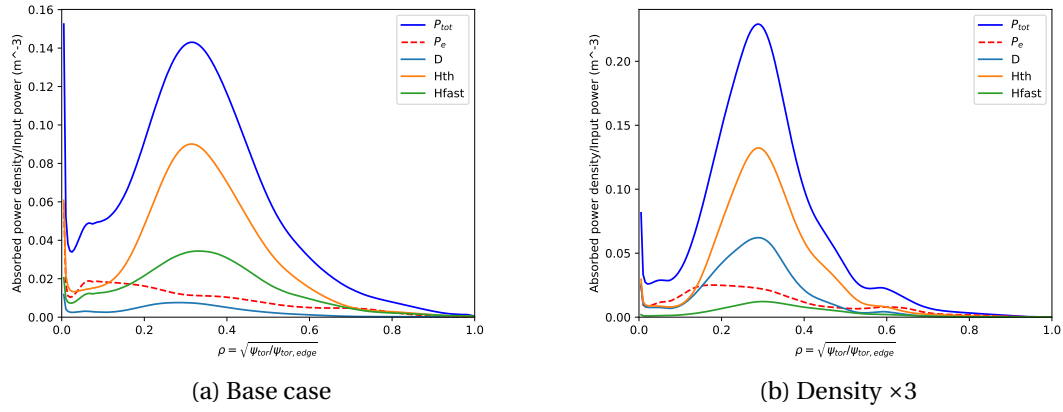


Figure 5.15: Flux surface averaged power density vs radial position.

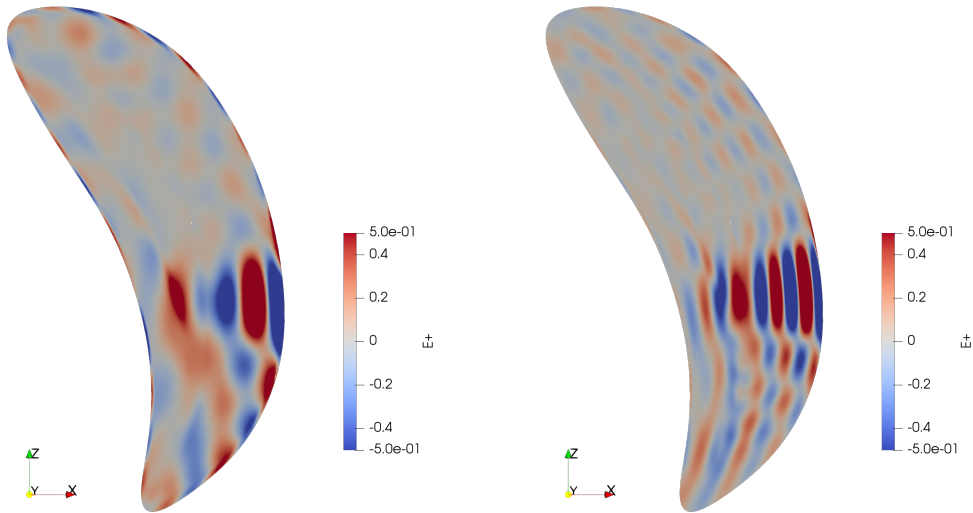


Figure 5.16: Left-hand polarised component of the electric field,  $\text{Re}(E^+)$ , in the poloidal plane in front of the antenna (arbitrary units). The base case on the left, the  $N \times 3$  case on the right.

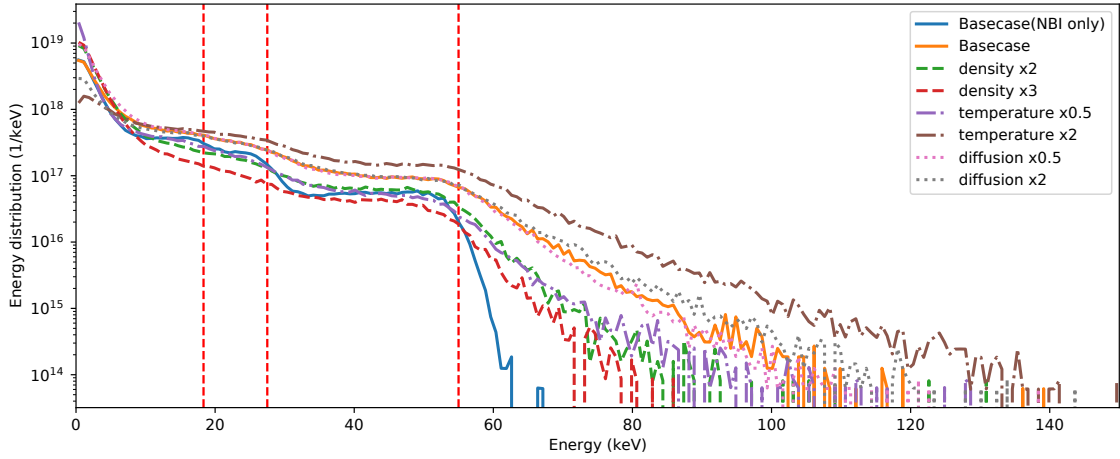


Figure 5.17: Comparison of the H particle energy distributions.

wave fields are not shown here.

### 5.4.2 Fast ions

After the wave field is computed, VENUS-LEVIS is run for another cycle of 100 ms, but now with both ICRH and beams enabled. (Reminder: in this chapter, VENUS-LEVIS did not include the wave field until now). The performance of the cases in table 5.1 can be compared with each other, and that of NBI-only, see Fig. 5.17. The addition of ICRH led to enhanced fast ion tails (meaning more fast ions) above 55 keV for any of the tested scenarios. However, the ability to generate fast ions strongly depends on the simulation settings. The best runs used low collisionality, which is achieved by making the density as low as possible, and the temperature as high as possible. The higher diffusion is also a good thing because more RF power will go to the fast hydrogen. Of course these settings may not be achievable, let alone controllable in a real experiment. E.g. temperature can be increased by applying more heating power, but that will affect transport as well (diffusion coefficient), and as a result the density profile. Also the profile shapes will change, and the ratio of ion/electron temperature may be modified.

Another important parameter is the antenna frequency, which determines which population is heated and where. As discussed it is not trivial to determine which value is best, without doing an extensive scan [48, section 5.2.3]. See Fig. 5.18 for the results of varying  $B_{res}$ . A noticeable improvement is seen at higher  $B_{res}$ . In practice the ICRH antenna can vary its frequency in the range of 25-38 MHz [72]. The frequencies used in this section go beyond that, e.g. a value of  $B_{res} = 2.5$  T corresponds to 38.1 MHz and  $B_{res} = 2.7$  T would need 41.2 MHz. Reaching these higher frequencies may be possible in the future with a different antenna, or more practically, a similar experiment can be designed at a lower magnetic field strength (and thus a lower antenna frequency). It would be beneficial if the optimal parameters could be directly fed into an experiment, however, that was not the aim of the study. The goal was to find the overall trends when varying specific parameters which reveal what the important quantities

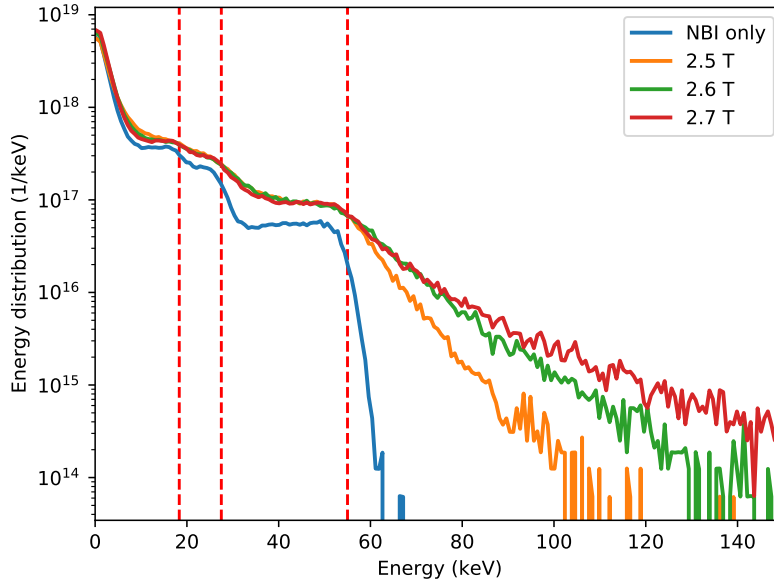


Figure 5.18: H particle energy distributions for the base case, but repeated with different resonant magnetic field strengths.

are. Finding the precise optimum would require vastly more resources (simulations).

The effect of changing the resonance position is exhibited in Fig. 5.19, where the dependence with pitch-angle and energy is shown to change. The fast ions are clearly not isotropic in pitch angle. In terms of  $\lambda$  the distribution is similar to that of NBI-only (Fig. 5.7), except at higher energy. The lost particles are binned in  $(\lambda, E)$  as well, see Fig. 5.20. The losses are mainly at low pitch angle because these particles are more likely to be trapped and subsequently lost in W7-X.

Lastly, VENUS-LEVIS also keeps track of the power transfer to/from the bulk plasma via collisions. See Fig. 5.21 for the power transfer in the base case. Mainly the ions are heated in the core, with a rather flat power density profile for electrons. Both ion and electron heating via collisions is enhanced at all radii by the addition of ICRH. However, the difference with NBI-only is not dramatic. A remark is in order regarding the power at the edge, see the spike in Fig. 5.21. This artefact is a consequence of the rather large ratio of beam to electron temperature, see [60] for a more detailed explanation. Most likely this would not appear in real life as the heating rapidly increases the local plasma temperature. As a result the temperature ratio would decrease and the spike would vanish.

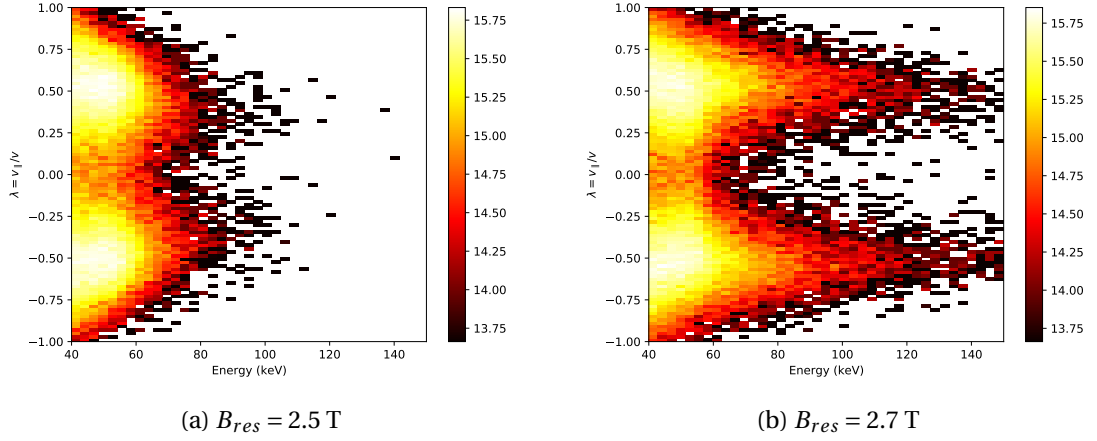


Figure 5.19: Fast ions binned in pitch and energy, the colour indicates  $\log_{10}$  of the total number of particles per bin. Base case used.

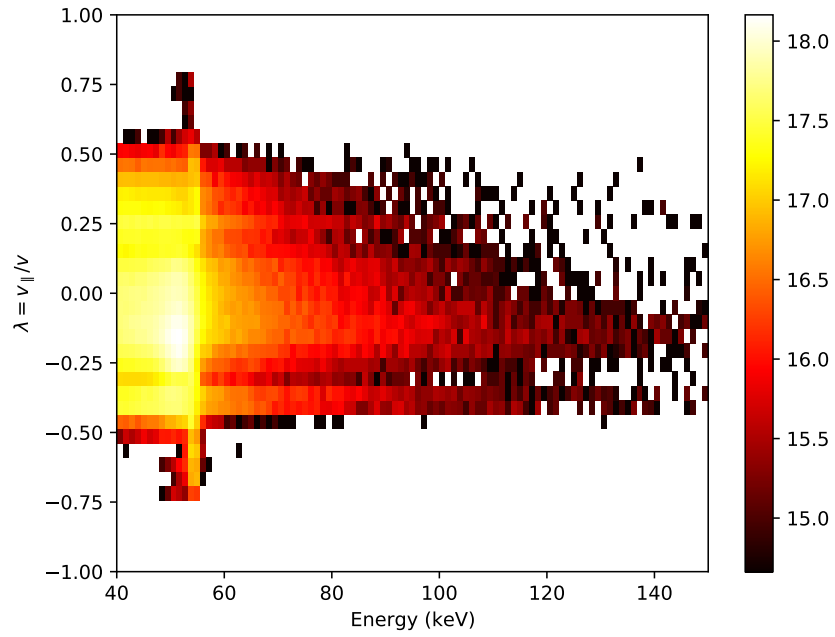


Figure 5.20: Fast ion losses binned in pitch and energy. Base case, but with  $B_{res} = 2.7$  T. The colour of a bin indicates  $\log_{10}$  of the lost particles per second in that bin.

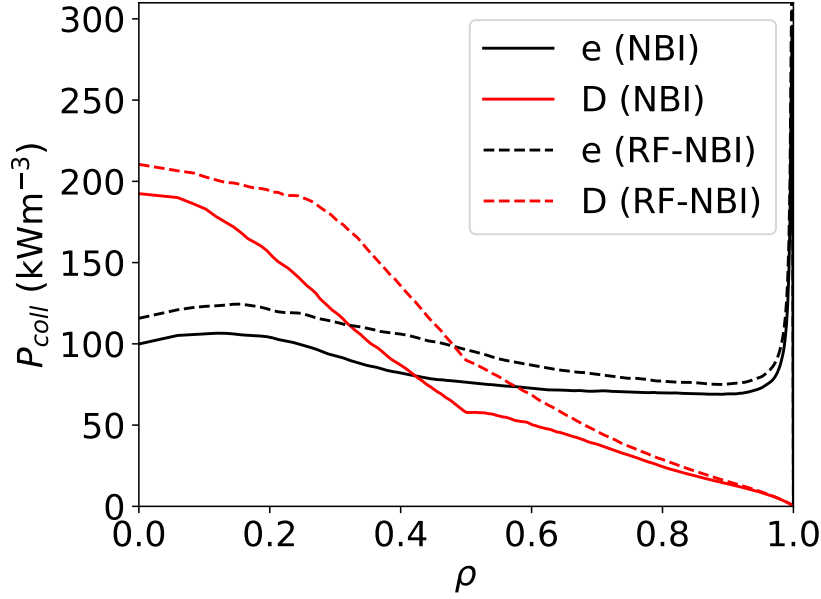


Figure 5.21: Collisional power density vs radial position (base case). As a reference, the second cycle (only NBI) has been plotted as well (solid lines).

## 5.5 Discussion

A few remarks regarding the limitations of the study: Due to the ambipolarity condition many tokamaks and stellarators have a steady state radial electric field  $E_r$ , Wendelstein 7-X is no exception. This field can have a significant effect on the fast ion confinement, see [10], [73]. The radial electric field causes an  $\mathbf{E} \times \mathbf{B}$  drift, which typically results in improved confinement for trapped ions at low energy where drifts are not dominated by magnetic drifts. This is because the additional poloidal drift motion helps particles to move out of bad confinement regions before they are lost. The profile of  $E_r$  depends on the plasma scenario, which is different for each case in table 5.1, so for simplicity it has been omitted in this work. Even though the very fast trapped ions are not strongly affected by  $E_r$ , we have seen that the fast ions arise from the thermal and moderately energetic NBI ions. Hence, neglecting  $E_r$  will cause an underestimation of the fast trapped ions too. Note however that the RF-NBI scheme provides heating of passing ions too, which are well confined without the radial electric field. So the neglect of  $E_r$  is not likely a very serious one. Nevertheless, note that fast passing particles originate from two channels: acceleration of thermal passing particles, or de-trapping of fast trapped particles (via collisions). If there are fewer trapped ions, the latter channel is underestimated as well. Though this is likely a small effect.

Secondly, the antenna placement in the simulation does not correspond with its position in the experiment. It was located at  $\varphi = 8^\circ$ , but should actually be mirrored, so at  $-8^\circ$ . The latter would place it somewhat further away from the injection sites of the beams.



There are also some notable improvements over previous RF-NBI SCENIC simulations of W7-X [48]: Most importantly, the problem of accumulating thermal markers has been addressed. With sufficient computational resources the diffusion coefficient can potentially be tuned to ensure that the beam concentration matches that of an experiment. Secondly, the newly introduced “cycles” allow continuation of the simulation in a way that permits the number of confined markers to change. In addition, LEMan now accounts for higher harmonic heating, see chapter 4, which means that the RF power fraction of hydrogen is computed more accurately. Moreover, the simulations in this chapter have been performed using more up to date plasma profiles. Lastly, the NBI deposition is calculated using the more accurate and performant VENUS-NBI.

## 5.6 Summary

In this chapter the synergetic RF-NBI scheme has been studied in the plasma of W7-X. The simulation procedure consists of multiple steps: computing the NBI deposition, followed by the slowing down simulation. In order to reach a steady state a diffusion term has been added. After calculating the profiles of the slowing down population, the wave field is computed. And finally it is all combined by enabling both NBI and ICRH in VENUS-LEVIS. These steps have been performed for a series of different parameters, where the best performance was found at low density and high temperature. In addition, it is essential to exploit the Doppler shift which requires shifting the antenna frequency so that the fast ions resonate in the core. However, obtaining the precise optimum is challenging and certainly more simulations and also experiments need to be done to find it.



## 6 Conclusion & summary

Generating fast ions in a quasi-isodynamic stellarator such as W7-X is important for the validation of the QI approach to building a stellarator reactor. For this purpose beams and ICRF waves can be used. The nature of these waves is complicated, but the work of chapter 3 has provided more insight. It is important to realise that the wave problem can be split into two smaller parts: first, mapping out the conductivity kernel, which is only a property of the background quantities, not of the wave. And secondly, using this kernel to solve Maxwell's equations. The kernel contains all the effects of a homogenous hot plasma, such as higher harmonic heating, TTMP and mode conversion. In addition, the two relevant length scales of the conductivity kernel appear naturally. Based on these a criterion for the validity of the locally homogeneous approximation can be formulated.

For the purpose of investigating the RF schemes in this thesis LEMan needed to be upgraded with new dielectric tensors, see chapter 4. Notably, expressions are derived for the dielectric tensor of a modified bi-Maxwellian, accurate to all orders in Larmor radius, and arbitrary cyclotron harmonic. Compared to the older warm model, the hot model predicts stronger damping of the wave. In addition, the power fraction of electrons is greatly enhanced, and higher harmonic heating is included. Moreover, minority heating of hydrogen in a helium-4 plasma is investigated for W7-X, which demonstrates strong damping, as attested by the low wave amplitude in field periods other than that of the antenna. While this means it will make a good heating scheme, it is not suitable unfortunately for fast ion generation in W7-X. For this purpose the more advanced three-ion or RF-NBI scheme could be used.

Modelling of the synergetic RF-NBI scheme has specific challenges compared to NBI-only and RF-only simulations. Since ICRH is involved, the thermal markers can no longer be removed from the simulation, as they are needed as seed ions which can be accelerated to higher energies. However, in the previous version of VENUS-LEVIS the transport of these ions was not sufficiently resolved, which in turn led to an accumulation of thermal markers. In order to avoid this behaviour a new diffusion model has been added to VENUS-LEVIS, see chapter 5. In addition, the code assumes a fixed number of total markers, which is not compatible with NBI since (at least initially) the particle influx need not equal the losses. A simple workaround was

to allocate memory for markers of multiple full runs of VENUS-LEVIS, and shift the starting index of the array. These runs are referred to as “cycles”. With all of these additions it is at last possible to reach steady state in VENUS-LEVIS, and proceed with the remaining iterations of SCENIC. Finally, the results predict that under the right conditions the RF-NBI scheme can generate a considerable increase in the number of fast ions in W7-X, at the NBI energy and beyond.

### 6.1 Future work

#### 6.1.1 ICRF waves

RF wave modelling in plasmas is a difficult problem because all of the following aspects couple together: antenna, wave propagation, absorption, plasma response and modification of the background plasma and magnetic equilibrium. However, separation of time scales of the items in this list enables a tractable approach: many of these “modules” can be simulated separately, linked together only by an iterative scheme. This also implies that upgrades to one module can be performed without requiring changes to the others. One possible upgrade to the core module is described in chapter 3. Although the implementation is only demonstrated in 1D, it can relatively easily be extended to higher dimensions. Advantages over LEMan would be numerous: The configuration space description enables to use of the FEM. This enables flexible meshing which may reduce the number of DOFs, and it can easily handle accurate antenna and vessel geometry. Moreover, the spatial dispersion of the plasma response is most important in the two angular directions, as particles fan out over a flux surface. LEMan can account for this non-locality, but it is local in radial direction. The new model on the other hand is fully non-local, i.e. in all three dimensions. Lastly, it does not assume a dominant wavenumber; a full spectrum is used, which allows mode conversion to be modelled. This process is always present to some extent in an inhomogeneous plasma whenever there is a wave resonance [74], but it becomes more prominent when the minority concentration is large. This may be of importance in W7-X since it has a carbon wall. Because this can bind and release hydrogen, it may be hard to keep the H concentration low in  $^4\text{He}$ -(H) scenarios for example. Hence, including mode conversion in the simulation would make a valuable addition. However, if one refuses to make further approximations on the nature of the plasma response, it appears that it is unavoidable that the assembly matrix of section 3.2 remains dense (non-local FEM). There are several possible paths forward in order to accelerate the solution process, some examples (as well as different approaches entirely) are given in appendix A.9.

#### 6.1.2 Fast ions

When it comes to fast ion generation in W7-X, more study is needed to find the optimal scenario. As explained in [60] the parameter space is vast, and it is not obvious which settings are best. In a tokamak the cyclotron resonance layer is nearly vertical, which makes it easier to

find the most suitable antenna frequency. In a stellarator however this layer is fully 3D and so it is not immediately evident what works best. Therefore more simulations and experiments are needed.

Moreover, the computational cost of running SCENIC is substantial, dominated by the run time of VENUS-LEVIS. It is unfortunate that most of this time is spent on pushing thermal markers (if ICRH is involved); ideally markers that thermalise are ejected from the simulation. However, the model will then need to be supplemented by an additional particle and energy source, see section 5.3. Alternatively, it might be possible to account for the thermal population by modifying the RF kick operator itself. Regardless if these thermal markers can be removed or not, adaptive marker weighting could be used to better resolve the high energy tail. This was already demonstrated in ASCOT [75].



# A Appendix

## A.1 Metric tensor

The metric tensor is used to compute the distance between two points:

$$(ds)^2 = g_{ij} du^i du^j. \quad (\text{A.1})$$

To compute the elements of the metric the following definition is used

$$g_{ij} = \mathbf{e}_i \cdot \mathbf{e}_j \quad (\text{A.2a})$$

$$g^{ij} = \mathbf{e}^i \cdot \mathbf{e}^j, \quad (\text{A.2b})$$

where  $\mathbf{e}_i$  are the covariant basis vectors, and  $\mathbf{e}^i = \nabla u^i$  the contra variant basis. Note, from this definition it is seen that the metric tensor is symmetric. Let  $G$  be the matrix containing  $g_{ij}$ , then  $G^{-1}$  has  $g^{ij}$  as its elements. In a Cartesian coordinate system  $G$  equals the identity matrix, so  $g_{ij} = \delta_{ij}$  and  $g^{ij} = \delta^{ij}$ .

To transform from one set of coordinates  $(u^1, u^2, u^3)$  to  $(v^1, v^2, v^3)$ , the Jacobian matrix is defined as

$$J = \frac{\partial(u^1, u^2, u^3)}{\partial(v^1, v^2, v^3)} = \begin{pmatrix} \frac{\partial u^1}{\partial v^1} & \frac{\partial u^1}{\partial v^2} & \frac{\partial u^1}{\partial v^3} \\ \frac{\partial u^2}{\partial v^1} & \frac{\partial u^2}{\partial v^2} & \frac{\partial u^2}{\partial v^3} \\ \frac{\partial u^3}{\partial v^1} & \frac{\partial u^3}{\partial v^2} & \frac{\partial u^3}{\partial v^3} \end{pmatrix}, \quad (\text{A.3})$$

and its inverse  $J^{-1} = \frac{\partial(v^1, v^2, v^3)}{\partial(u^1, u^2, u^3)}$ .

Consider a small displacement from  $u^i(\mathbf{v})$  to  $u^i(\mathbf{v} + d\mathbf{v}) = u^i(\mathbf{v}) + \frac{\partial u^i}{\partial v^j} dv^j$ , so  $du^i = \frac{\partial u^i}{\partial v^j} dv^j$ . Distance should be equal in both coordinate systems:

$$\begin{aligned} (ds)^2 &= g_{ij} du^i du^j \\ &= g_{ij} \frac{\partial u^i}{\partial v^k} \frac{\partial u^j}{\partial v^l} dv^k dv^l \\ &= g'_{kl} dv^k dv^l, \end{aligned} \quad (\text{A.4})$$

## Appendix A. Appendix

---

with  $g_{ij}$  the metric in coordinate system  $u$ , and  $g'_{ij}$  the metric in coordinate system  $v$ . Hence,

$$g'_{kl} = g_{ij} \frac{\partial u^i}{\partial v^k} \frac{\partial u^j}{\partial v^l}. \quad (\text{A.5})$$

Which can be written in matrix form:

$$G' = J^T G J. \quad (\text{A.6})$$

In Venus-Levis ( $u^1, u^2, u^3$ ) corresponds to the cylindrical coordinate system (major radius, vertical position, geometric toroidal angle),  $(R, Z, \phi_{geo})$ , so

$$G = \begin{pmatrix} 1 & 0 & 0 \\ 0 & 1 & 0 \\ 0 & 0 & R \end{pmatrix}^2. \quad (\text{A.7})$$

Defining  $\tilde{J}$  as

$$\tilde{J} = \begin{pmatrix} 1 & 0 & 0 \\ 0 & 1 & 0 \\ 0 & 0 & R \end{pmatrix} J = \begin{pmatrix} 1 & 0 & 0 \\ 0 & 1 & 0 \\ 0 & 0 & R \end{pmatrix} \begin{pmatrix} \frac{\partial R}{\partial v^1} & \frac{\partial R}{\partial v^2} & \frac{\partial R}{\partial v^3} \\ \frac{\partial Z}{\partial v^1} & \frac{\partial Z}{\partial v^2} & \frac{\partial Z}{\partial v^3} \\ \frac{\partial \phi_{geo}}{\partial v^1} & \frac{\partial \phi_{geo}}{\partial v^2} & \frac{\partial \phi_{geo}}{\partial v^3} \end{pmatrix}, \quad (\text{A.8})$$

so  $G' = \tilde{J}^T \tilde{J}$ . And the Jacobian determinant is computed as follows:

$$\sqrt{g'} = \sqrt{\det G'} = \det \tilde{J}. \quad (\text{A.9})$$

To compute derivatives of the metric tensor elements the product rule can be used:

$$\frac{\partial}{\partial u^i} G' = \left( \frac{\partial}{\partial u^i} \tilde{J} \right)^T \tilde{J} + \tilde{J}^T \left( \frac{\partial}{\partial u^i} \tilde{J} \right). \quad (\text{A.10})$$

However, Eq. (5.26) requires derivatives of  $g'^{ij}$ , which can be expressed in terms of derivatives of  $g'_{ij}$ :

$$\frac{\partial}{\partial u^i} (G')^{-1} = - (G')^{-1} \left( \frac{\partial}{\partial u^i} G' \right) (G')^{-1}. \quad (\text{A.11})$$

In VENUS-LEVIS the derivatives of  $G'$  are computed first using Eq. (A.10). Then the inverse of  $G'$  is found, and using Eq. (A.11) the derivatives of  $(G')^{-1}$  are obtained. To see where Eq. (A.11) comes from, consider an invertible matrix  $M$  where its elements are functions of a variable  $x$ ,

$$\frac{d}{dx} I = \frac{d}{dx} (M M^{-1}) = \left( \frac{d}{dx} M \right) M^{-1} + M \left( \frac{d}{dx} M^{-1} \right).$$

Obviously the derivative of the identity matrix is zero. Solving for  $\frac{d}{dx} M^{-1}$  then gives:

$$\frac{d}{dx} M^{-1} = -M^{-1} \left( \frac{d}{dx} M \right) M^{-1}. \quad (\text{A.12})$$



## A.2 Bessel functions

By definition, the Bessel function of the first kind is:

$$J_n(z) = \sum_{k=0}^{\infty} \frac{(-1)^k}{\Gamma(k+n+1)k!} \left(\frac{z}{2}\right)^{2k+n}, \quad (\text{A.13})$$

for any  $z \in \mathbb{C}$ . Since only integer order  $n \in \mathbb{Z}$  Bessel functions are used in the dielectric tensor, let us focus on just those. These symmetry properties hold:

$$J_n(-z) = (-1)^n J_n(z) \quad (\text{A.14a})$$

$$J_{-n}(z) = (-1)^n J_n(z). \quad (\text{A.14b})$$

Derivatives can be rewritten using the following relation:

$$J'_n(z) = J_{n-1}(z) - \frac{n}{z} J_n(z) \quad (\text{A.15a})$$

$$= \frac{n}{z} J_n(z) - J_{n+1}(z) \quad (\text{A.15b})$$

$$= \frac{1}{2} (J_{n-1}(z) - J_{n+1}(z)). \quad (\text{A.15c})$$

And so:

$$J_{-n}^2(z) = J_n^2(z) \quad (\text{A.16a})$$

$$J_{-n}'^2(z) = J_n'^2(z) \quad (\text{A.16b})$$

$$J_{-n}(z) J_{-n}'(z) = J_n(z) J_n'(z). \quad (\text{A.16c})$$

Some generating functions are:

$$e^{iz \sin \theta} = \sum_{n=-\infty}^{\infty} J_n(z) e^{in\theta} \quad (\text{A.17a})$$

$$e^{iz \cos \theta} = \sum_{n=-\infty}^{\infty} i^n J_n(z) e^{in\theta}. \quad (\text{A.17b})$$

The modified Bessel function of the first kind can be written as:

$$I_n(z) = \sum_{k=0}^{\infty} \frac{1}{\Gamma(k+n+1)k!} \left(\frac{z}{2}\right)^{2k+n}. \quad (\text{A.18})$$

For integer order  $n$  the following properties can be derived:

$$I_n(-z) = (-z)^n z^{-n} I_n(z) \quad (\text{A.19a})$$

$$I_{-n}(z) = I_n(z) \quad (\text{A.19b})$$

$$I_n'(z) = I_{-n}'(z). \quad (\text{A.19c})$$

Derivatives can be rewritten using the following:

$$I'_n(z) = \frac{n}{z} I_n(z) + I_{n+1}(z) \quad (\text{A.20a})$$

$$= I_{n-1}(z) - \frac{n}{z} I_n(z) \quad (\text{A.20b})$$

$$= \frac{1}{2} (I_{n-1}(z) + I_{n+1}(z)) . \quad (\text{A.20c})$$

For large arguments with positive real value, i.e.  $|z| \gg 1$ ,  $\text{Re}(z) > 0$ , the modified Bessel functions take on a simpler form:

$$I_n(z) \approx \frac{e^z}{\sqrt{2\pi z}} \left( 1 - \frac{4n^2 - 1}{8z} + \dots \right) \approx \frac{e^z}{\sqrt{2\pi z}} . \quad (\text{A.21})$$

Using a recurrence relation a similar expression can be found for its derivative:

$$I'_n(z) \approx \frac{e^z}{\sqrt{2\pi z}} \left( 1 - \frac{4n^2 + 3}{8z} + \dots \right) \approx \frac{e^z}{\sqrt{2\pi z}} , \quad (\text{A.22})$$

which comes in handy when numerically computing the exponentially scaled modified Bessel functions  $e^{-z} I_n(z)$  (avoid overflow). Lastly, sums over the modified Bessel functions crop up when computing the dielectric tensor, these may be rewritten using the following identity:

$$\sum_{n=-\infty}^{\infty} n I_n(z) = \sum_{n=-\infty}^{\infty} (I_n(z) - I'_n(z)) = 0 . \quad (\text{A.23})$$

### A.3 Plasma dispersion function

The plasma dispersion function (PDF) often appears in kinetic plasma theory, it is defined below [76].

$$Z(\zeta) = \frac{1}{\sqrt{\pi}} \int_{-\infty}^{\infty} \frac{e^{-s^2}}{s - \zeta} ds, \quad \text{Im}(\zeta) > 0. \quad (\text{A.24})$$

It can also be defined for  $\text{Im}(\zeta) \leq 0$  through analytic continuation. The PDF can also be written in terms of other familiar special functions:

$$Z(\zeta) = i\sqrt{\pi} e^{-\zeta^2} (1 + \text{Erf}(i\zeta)) = \sqrt{\pi} e^{-\zeta^2} (i - \text{Erfi}(\zeta)) = i\sqrt{\pi} e^{-\zeta^2} - 2D(\zeta), \quad (\text{A.25})$$

with  $D$  the Dawson function (`DawsonF` in Mathematica) and  $\text{Erfi}$  the imaginary error function. The derivatives of can be rewritten using the identity:

$$Z'(\zeta) = -2(1 + \zeta Z(\zeta)) . \quad (\text{A.26})$$

Lastly, note that the PDF can be written in terms of the Hilbert transform of a Gaussian.

### A.3.1 Hilbert transform

First, define the Fourier transform (FT) pair:

$$F(\omega) = \int_{-\infty}^{\infty} dt f(t) e^{-i\omega t} = \mathcal{F}(f) \quad (\text{A.27a})$$

$$f(t) = \frac{1}{2\pi} \int_{-\infty}^{\infty} d\omega F(\omega) e^{i\omega t} = \mathcal{F}^{-1}(F), \quad (\text{A.27b})$$

and let the convolution be defined as follows:

$$(f * g)(t) = \int_{-\infty}^{\infty} ds f(s) g(t-s) = \int_{-\infty}^{\infty} ds f(t-s) g(s). \quad (\text{A.28})$$

The convolution theorem then states:

$$\mathcal{F}(f * g) = \mathcal{F}(f) \mathcal{F}(g). \quad (\text{A.29})$$

Note that different definitions exist for Eqs. (A.27a) - (A.28), both in terms of the prefactor  $2\pi, \sqrt{2\pi}, \dots$  as well as the sign of the exponent. Alternative definitions work just as well, as long as one is consistent. But be aware that an alternative definition of the FT can lead to a different normalisation in the convolution theorem.

The Hilbert transform can be defined as the convolution between a function  $f(t)$  and  $1/(\pi t)$ :

$$\mathcal{H}(f)(t) = \frac{1}{\pi} PV \int_{-\infty}^{\infty} \frac{f(s)}{t-s} ds = \frac{1}{\pi t} * f(t) = \mathcal{F}^{-1}(-i \text{sign}(\omega) \mathcal{F}(f)), \quad (\text{A.30})$$

where  $PV$  is the principal value. Using the convolution theorem, this can be written (in Fourier space) as the product of  $-i \text{sign}(\omega)$  and the Fourier transform of  $f(t)$ . Optimised libraries exist for computing the discrete Hilbert transform, given an array with a time series sample of  $f(t)$ . This avoids directly computing the convolution. Usually, these libraries use the FFT (fast Fourier transform) of  $f(t)$ , multiply by  $-i \text{sign}(\omega)$ , and transform back with the IFFT. In this way the PDF can be computed as the Hilbert transform of a Gaussian plus the contribution from the residue,

$$Z(\zeta) = i\sqrt{\pi} \left( i \mathcal{H}(e^{-s^2})(\zeta) + e^{-\zeta^2} \right). \quad (\text{A.31})$$

The combination of these two parts is called the “analytic signal”, and effectively cuts out the negative half of the frequency range. A proof of this claim would go as follows: for a function  $f(t)$ , the analytic representation is defined as

$$f_a(t) = i \mathcal{H}(f)(t) + f(t). \quad (\text{A.32})$$

Taking the FT gives

$$\mathcal{F}(f_a) = i \cdot -i \text{sign}(\omega) \mathcal{F}(f) + \mathcal{F}(f) = \mathcal{F}(f) (1 + \text{sign}(\omega)), \quad (\text{A.33})$$

which is indeed zero for negative  $\omega$ .

Several strategies on numerically computing the Hilbert transform are given in [77]. In case just a single value is needed instead of a whole spectrum, one could use the Goertzel algorithm.

### A.3.2 Generalised plasma dispersion function

The generalised plasma dispersion function is defined as:

$$Z_p(\zeta) = \frac{1}{\sqrt{\pi}} \int_{-\infty}^{\infty} \frac{x^p e^{-x^2}}{x - \zeta} dx, \quad \text{Im}(\zeta) > 0, \quad p \geq 0. \quad (\text{A.34})$$

Analytic continuation is again used to extend the domain to arbitrary  $\text{Im}(\zeta)$ . These integrals can be related to derivatives of the PDF [78]:

$$Z_p(\zeta) = \frac{1}{2^p} \sum_{l=0}^p (-1)^l d_l(p) \frac{d^l Z(\zeta)}{d\zeta^l}, \quad (\text{A.35})$$

where  $d_l(p)$  are the coefficients that satisfy

$$x^p = \frac{1}{2^p} \sum_{l=0}^p d_l(p) H_l(x), \quad (\text{A.36})$$

with  $H_l(x)$  the Hermite polynomial of order  $l$ .

The generalised PDF from Eq. (A.34) may also be expressed differently for  $p > 0$  using

$$\frac{x^p}{x - \zeta} = x^{p-1} + \zeta \frac{x^{p-1}}{x - \zeta} = x^{p-1} + \underbrace{\zeta x^{p-2} + \zeta^2 x^{p-3} + \dots + \zeta^{p-1} \cdot 1}_{=\sum_{k=0}^{p-1} \zeta^k x^{p-k-1}} + \frac{\zeta^p}{x - \zeta}, \quad (\text{A.37})$$

so we find

$$Z_p(\zeta) = \frac{1}{\sqrt{\pi}} \int_{-\infty}^{\infty} \frac{x^p e^{-x^2}}{x - \zeta} dx = \frac{1}{\sqrt{\pi}} \sum_{k=0}^{p-1} \zeta^k \int_{-\infty}^{\infty} x^{p-k-1} e^{-x^2} dx + \frac{\zeta^p}{\sqrt{\pi}} \int_{-\infty}^{\infty} \frac{e^{-x^2}}{x - \zeta} dx. \quad (\text{A.38})$$

Half of the integrals drop out, because their integrand is odd:

$$\frac{1}{\sqrt{\pi}} \int_{-\infty}^{\infty} x^{2k} e^{-x^2} dx = \frac{(2k-1)!!}{2^k} = \frac{1}{\sqrt{\pi}} \Gamma\left(k + \frac{1}{2}\right). \quad (\text{A.39})$$

For non-negative integer  $m$ , the Gamma function is

$$\Gamma\left(m + \frac{1}{2}\right) = \sqrt{\pi} \frac{(2m)!}{2^{2m} m!}, \quad (\text{A.40})$$

so we find

$$Z_p(\zeta) = \zeta^p Z(\zeta) + \sum_{k=0}^{(p+(p \bmod 2))/2-1} \zeta^{p-2k-1} \frac{(2k-1)!!}{2^k}. \quad (\text{A.41})$$

Note that for  $k = 0, -1$ , the double factorial  $k!! = 1$ .

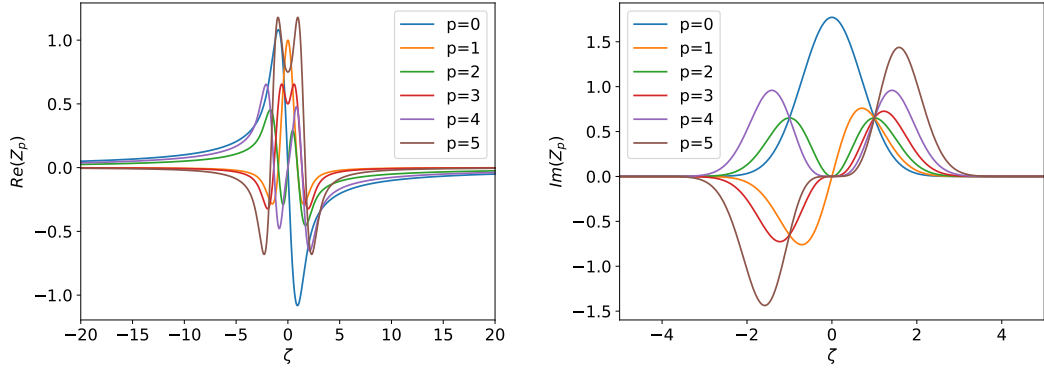


Figure A.1: Real and imaginary parts of  $Z_p$  for several  $p$ . As can be seen these alternate between even and odd functions. Additionally, the real part drops off faster for odd  $p$  than even  $p$ , as explained before.

See Fig. A.1 for a plot of the  $Z_p$  functions, for real valued  $\zeta$ . Arbitrary precision arithmetic (50 significant digits) was used to generate Fig. A.1. This was necessary to avoid issues with cancellation errors (at large  $|\zeta|$ ) in Eq. (A.41). This is why developing the asymptotic series is useful, since the cancellation becomes apparent. See Eq. (A.43) where the first terms in the sum over  $k$  have been eliminated.

The asymptotic series (i.e. for large  $|\zeta|$ ) of  $Z(\zeta)$  is given by:

$$Z(\zeta) \approx -\frac{1}{\zeta} \sum_{k=0}^N \frac{(2k-1)!!}{2^k} \zeta^{-2k} + i\sigma\sqrt{\pi}e^{-\zeta^2}, \quad (\text{A.42})$$

with

$$\sigma = \begin{cases} 0, & \text{Im}(\zeta) > 0 \\ 1, & \text{Im}(\zeta) = 0 \\ 2, & \text{Im}(\zeta) < 0. \end{cases}$$

At some  $k$ , the double factorial exceeds the  $2^k$ , and thus the series is truncated at  $k = N$ , where the terms do not decrease in magnitude anymore. It is clear that  $Z(\zeta)$  approaches zero as  $\zeta$  goes to infinity. It can easily be shown this holds true for  $Z_p(\zeta)$  as well. Plugging Eq. (A.42) into Eq. (A.41) yields:

$$Z_p(\zeta) \approx -\sum_{k=(p+p \bmod 2)/2}^N \frac{(2k-1)!!}{2^k} \zeta^{p-2k-1} + i\sigma\sqrt{\pi}\zeta^p e^{-\zeta^2}, \quad (\text{A.43})$$

where the highest power in the sum is  $\zeta^{-1}$  for even  $p$ , and  $\zeta^{-2}$  for odd  $p$ .

## A.4 Hot plasma dispersion relation

The hot plasma dispersion relation (HPDR) can be derived similarly to what was done in section 2.3.1 for cold plasma. Starting from the wave equation, non trivial solutions require

$$\det(\mathbf{nn} - n^2 I + K) = 0. \quad (\text{A.44})$$

Then plug in the general expression for the dielectric tensor, Eq. (2.40), and orient the  $x, y$  axes such that  $\psi = 0$ . So the HPDR becomes:

$$\begin{aligned} (K_3 - n_\perp^2) \left[ K_2^2 + (K_1 - n_\parallel^2) (K_0 + K_1 - n_\parallel^2 - n_\perp^2) \right] + K_7 \left[ K_5 (K_1 - n_\parallel^2) - K_2 (K_4 + n_\parallel n_\perp) \right] \\ - (K_6 + n_\parallel n_\perp) \left[ K_2 K_5 + (K_4 + n_\parallel n_\perp) (K_0 + K_1 - n_\parallel^2 - n_\perp^2) \right] = 0. \end{aligned} \quad (\text{A.45})$$

At first glance this appears to be a fourth order polynomial in  $n_\perp$ , however, this is not the case due to the wavenumber dependence inside of the  $K$  elements.

Here the procedure described by Swanson [19, section 4.3.7.2] is followed: assuming Maxwellian distributions, and expanding the  $K$  elements up to second order in  $k_\perp$  (first order in  $\lambda$ ) gives an approximate dispersion relation<sup>1</sup>:

$$A_1 n_\perp^6 + B_1 n_\perp^4 + C_1 n_\perp^2 + D_1 = 0. \quad (\text{A.46})$$

No odd order powers of  $n_\perp$  are present, as the modified Bessel functions have  $k_\perp^2$  in their argument. Analytical solutions can be found for polynomials up to 4th order, so this can be solved analytically for  $n_\perp^2$ . Repeating the same procedure, but to zeroth order in  $k_\perp$  yields the even simpler dispersion relation:

$$A_0 n_\perp^4 + B_0 n_\perp^2 + C_0 = 0, \quad (\text{A.47})$$

which is very similar to the cold plasma result, Eq. (2.59), except that some finite temperature effects are retained. The coefficients are,

$$A_0 = K_{1,0} \quad (\text{A.48a})$$

$$B_0 = -K_{2,0}^2 - (K_{1,0} + K_{3,0})(K_{1,0} - n_\parallel^2) \quad (\text{A.48b})$$

$$C_0 = K_{3,0}((K_{1,0} - n_\parallel^2)^2 + K_{2,0}^2), \quad (\text{A.48c})$$

---

<sup>1</sup>Notice the keyword ‘‘up to’’ here, not all  $K$  elements will have  $k_\perp^2$  terms.

with the zeroth order approximations to  $K$  for a Maxwellian:

$$K_{1,0} = 1 + \sum_s \frac{\omega_{ps}^2}{2\omega|k_z|v_{Ts}} (Z(\zeta_{-1,s}) + Z(\zeta_{1,s})) \quad (\text{A.49a})$$

$$K_{2,0} = i \sum_s \frac{\omega_{ps}^2}{2\omega|k_z|v_{Ts}} (Z(\zeta_{1,s}) - Z(\zeta_{-1,s})) \quad (\text{A.49b})$$

$$K_{3,0} = 1 - \sum_s \frac{\omega_{ps}^2}{\omega|k_z|v_{Ts}} \zeta_{0,s} Z'(\zeta_{0,s}). \quad (\text{A.49c})$$

## A.5 Expressions H functions

It is convenient to first eliminate the derivative of the modified Bessel functions using the identity of Eq. (A.20c). Secondly, the following auxiliary functions are derived using a symbolic algebra system (Mathematica in this case) [20]:

$$h_{1,n}(\xi) = \mathcal{H}_0^{-1} \left( v^{-2} e^{-v^2/8} I_n(v^2/8) \right) = \frac{1}{2\sqrt{\pi}} G_{3,2}^{1,2} \left( \frac{1}{\xi^2} \middle| \begin{matrix} \frac{1}{2}, 1, 1 \\ |n|, -|n| \end{matrix} \right) = \frac{{}_2F_2\left(-|n|, |n|; \frac{1}{2}, 1; -\xi^2\right)}{2|n|} - \frac{2\xi {}_2F_2\left(\frac{1}{2} - |n|, |n| + \frac{1}{2}; \frac{3}{2}, \frac{3}{2}; -\xi^2\right)}{\sqrt{\pi}}, n \in \mathbb{Z} \setminus \{0\} \quad (\text{A.50a})$$

$$h_{2,n}(\xi) = \frac{1}{\sqrt{8}} \mathcal{H}_1^{-1} \left( v^{-1} e^{-v^2/8} I_n(v^2/8) \right) = \frac{1}{2\sqrt{2\pi}\xi} G_{3,2}^{1,2} \left( \frac{1}{\xi^2} \middle| \begin{matrix} 0, \frac{1}{2}, 1 \\ |n|, -|n| \end{matrix} \right) = \frac{{}_2F_2\left(\frac{1}{2} - |n|, |n| + \frac{1}{2}; \frac{1}{2}, \frac{3}{2}; -\xi^2\right)}{\sqrt{2\pi}} - \frac{|n|\xi {}_2F_2\left(1 - |n|, |n| + 1; \frac{3}{2}, 2; -\xi^2\right)}{\sqrt{2}}, n \in \mathbb{Z} \quad (\text{A.50b})$$

$$h_{3,n}(\xi) = \frac{1}{8} \mathcal{H}_0^{-1} \left( e^{-v^2/8} I_n(v^2/8) \right) = \frac{1}{4\sqrt{\pi}} G_{3,2}^{1,2} \left( \frac{1}{\xi^2} \middle| \begin{matrix} 1, \frac{3}{2}, 1 \\ |n| + 1, 1 - |n| \end{matrix} \right) = \frac{{}_2F_2\left(\frac{1}{2} - |n|, |n| + \frac{1}{2}; \frac{1}{2}, \frac{1}{2}; -\xi^2\right)}{4\sqrt{\pi}\xi} - \frac{1}{2}|n| {}_2F_2\left(1 - |n|, |n| + 1; 1, \frac{3}{2}; -\xi^2\right), n \in \mathbb{Z} \quad (\text{A.50c})$$

$$h_{4,n}(\xi) = \frac{1}{8\sqrt{8}} \mathcal{H}_1^{-1} \left( v e^{-v^2/8} I_n(v^2/8) \right) = \frac{1}{4\sqrt{2\pi}\xi^3} G_{3,2}^{1,2} \left( \frac{1}{\xi^2} \middle| \begin{matrix} -1, \frac{1}{2}, 0 \\ |n|, -|n| \end{matrix} \right) = \frac{|n|(n^2 - 1)\xi {}_2F_2\left(2 - |n|, |n| + 2; 2, \frac{5}{2}; -\xi^2\right)}{3\sqrt{2}} + \frac{{}_2F_2\left(\frac{1}{2} - |n|, |n| + \frac{1}{2}; -\frac{1}{2}, \frac{1}{2}; -\xi^2\right)}{8\sqrt{2\pi}\xi^2}, n \in \mathbb{Z} \quad (\text{A.50d})$$

$$h_{5,n}(\xi) = \frac{1}{64} \mathcal{H}_0^{-1} \left( v^2 e^{-v^2/8} I_n(v^2/8) \right) = \frac{1}{8\sqrt{\pi}\xi^4} G_{3,2}^{1,2} \left( \frac{1}{\xi^2} \middle| \begin{matrix} -1, \frac{1}{2}, -1 \\ |n|, -|n| \end{matrix} \right) =$$

$$\frac{1}{6} |n|(n^2 - 1) {}_2F_2 \left( 2 - |n|, |n| + 2; 1, \frac{5}{2}; -\xi^2 \right) - \frac{{}_2F_2 \left( \frac{1}{2} - |n|, |n| + \frac{1}{2}; -\frac{1}{2}, -\frac{1}{2}; -\xi^2 \right)}{32\sqrt{\pi}\xi^3}, n \in \mathbb{Z} \quad (\text{A.50e})$$

$$h_{6,n}(\xi) = \frac{1}{64} \mathcal{H}_2^{-1} \left( v^2 e^{-v^2/8} I_n(v^2/8) \right) = \frac{1}{8\sqrt{\pi}\xi^4} G_{3,2}^{1,2} \left( \frac{1}{\xi^2} \middle| \begin{matrix} -2, \frac{1}{2}, 0 \\ |n|, -|n| \end{matrix} \right) =$$

$$\frac{{}_3F_2 \left( \frac{1}{2} - |n|, |n| + \frac{1}{2}; -\frac{3}{2}, \frac{1}{2}; -\xi^2 \right)}{32\sqrt{\pi}\xi^3} - \frac{1}{30} |n|(4 - 5n^2 + n^4) \xi^2 {}_2F_2 \left( 3 - |n|, |n| + 3; 3, \frac{7}{2}; -\xi^2 \right), n \in \mathbb{Z}, \quad (\text{A.50f})$$

where  ${}_pF_q$  are generalised hypergeometric functions, and  $G$  are Meijer G-functions. Although the equations (A.50) were derived using computer software,  $h_1, h_2$  can also be derived using identity ET II 68(8) of [79], followed by EH I 208(6) to simplify. Using these auxiliary functions, the original  $H$  functions can be found:

$$H_{0,n} = h_{5,n} - \frac{1}{2} h_{5,n-1} - \frac{1}{2} h_{5,n+1} \quad (\text{A.51a})$$

$$\check{H}_{0,n} = h_{6,n} - \frac{1}{2} h_{6,n-1} - \frac{1}{2} h_{6,n+1} \quad (\text{A.51b})$$

$$H_{1,n} = n^2 h_{1,n} \quad (\text{A.51c})$$

$$H_{2,n} = n \left( h_{3,n} - \frac{1}{2} h_{3,n-1} - \frac{1}{2} h_{3,n+1} \right) \quad (\text{A.51d})$$

$$H_{3,n} = h_{3,n} \quad (\text{A.51e})$$

$$H_{4,n} = n h_{2,n} \quad (\text{A.51f})$$

$$H_{5,n} = h_{4,n} - \frac{1}{2} h_{4,n-1} - \frac{1}{2} h_{4,n+1}. \quad (\text{A.51g})$$

Note that the auxiliary functions are symmetric in  $n$ , and so are the  $H$  functions. With the exception of  $H_{2,n}$  and  $H_{4,n}$  which are antisymmetric, i.e.  $H_{2,-n}(\xi) = -H_{2,n}(\xi)$ ,  $H_{4,-n}(\xi) = -H_{4,n}(\xi)$ .

In order to be sure these transforms were done correctly, a comparison with the expected result is in order. This is done by taking the Fourier transform of the kernel  $\sigma$  and comparing against  $\tilde{\sigma}$ . However, given the kernel is separable, it is easier to validate the perpendicular and parallel parts in isolation. This is done by sampling the  $H$  functions on a grid, and taking the Hankel transform. For example, the perpendicular contribution of  $\sigma_{11}$  is in  $R_1 + \frac{1}{2} R_0 - \frac{1}{2} \check{R}_0 \cos(2\alpha)$ . When comparing one harmonic at a time, the function  $S_1$  can be factored out since  $R_0, \check{R}_0, R_1$  all contain it. The expected value for  $\tilde{\sigma}_{11}$  is  $K_1 + K_0 \sin^2(\psi)$ , which can also be split up into the contribution of each harmonic, and since both  $K_0, K_1$  contain the same parallel contribution  $Z(\zeta_n)/|k_z|$  this will also be factored out. In summary, the comparison is between the transform



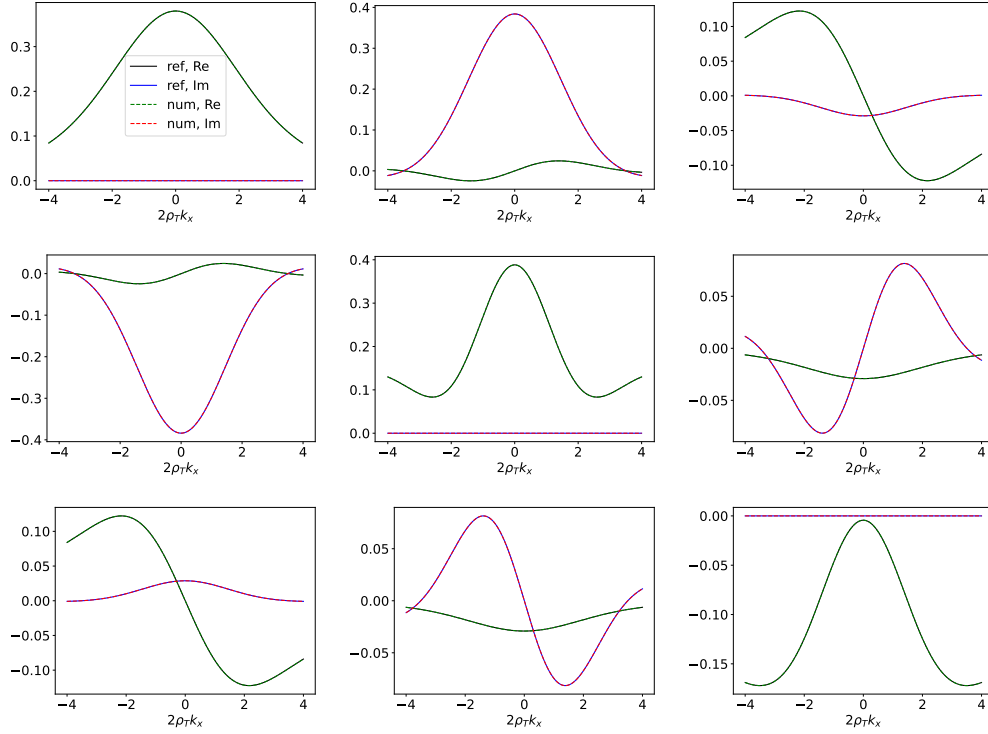


Figure A.2: All nine components of  $\tilde{\sigma}$ , “perpendicular contribution” only (as defined in the text). Using  $\omega/\Omega = 0.9$ ,  $n = 1$  and  $2\rho_T k_y = 0.3$ .

of

$$H_{1,n}(\xi) + H_{0,n}(\xi) + \check{H}_{0,n}(\xi) \cos(2\alpha),$$

and

$$\frac{\pi}{2} e^{-\lambda} \left[ \frac{n^2 I_n(\lambda)}{2\lambda} + \lambda (I_n(\lambda) - I'_n(\lambda)) \sin^2(\psi) \right].$$

These results are shown in Fig. A.2, which demonstrate agreement.

## A.6 Expressions S functions

In order to compute the inverse transforms of table 3.2 it is convenient to first split the PDF in terms of a Dawson function and a Gaussian, see Eq. (A.25). The transforms are again performed using Mathematica, see [20]:

$$\mathcal{F}_{w_n}^{-1} \left( \frac{1}{|w_n|} \exp \left[ -\frac{1}{4w_n^2} \right] \right) = \frac{1}{2\sqrt{\pi}} G_{0,3}^{2,0} \left( \mu_n^2 \mid 0, 0, \frac{1}{2} \right), \quad (\text{A.52})$$

where  $G_{p,q}^{m,n}$  is the Meijer G-function.

$$\begin{aligned} \mathcal{F}_{w_n}^{-1} \left( \frac{1}{|w_n|} D \left[ \frac{1}{2|w_n|} \right] \right) &= \mathcal{F}_{w_n}^{-1} \left( \frac{1}{w_n} D \left[ \frac{1}{2w_n} \right] \right) \\ &= \frac{1}{4} \left( \sqrt{\pi} {}_0F_2 \left( ; \frac{1}{2}, 1; \mu_n^2 \right) - 4|\mu_n| {}_0F_2 \left( ; \frac{3}{2}, \frac{3}{2}; \mu_n^2 \right) \right). \end{aligned} \quad (\text{A.53})$$

Note that the Gaussian is an even function, and the Dawson function is odd. This allows easy manipulation of the sign of  $w_n$ , using  $w_n = |w_n| \text{sign}(w_n)$ . In addition,  $\epsilon_n^2 = 1$ , so  $\zeta_n^2 = \frac{1}{4w_n^2}$ . These equations can now be used to construct  $S_1$ :

$$S_1(\mu_n) = \frac{i}{2} G_{0,3}^{2,0} \left( \mu_n^2 \mid 0, 0, \frac{1}{2} \right) + \frac{1}{2} \epsilon_n \left[ 4|\mu_n| {}_0F_2 \left( ; \frac{3}{2}, \frac{3}{2}; \mu_n^2 \right) - \sqrt{\pi} {}_0F_2 \left( ; \frac{1}{2}, 1; \mu_n^2 \right) \right]. \quad (\text{A.54a})$$

By integrating this expression with respect to  $\mu_n$  we can bootstrap our way up to find  $S_2$  and then  $S_3$ , as was done in [20]:

$$S_2(\mu_n) = \epsilon_n \mu_n G_{0,3}^{2,0} \left( \mu_n^2 \mid 0, 0, -\frac{1}{2} \right) + i \text{sign}(\mu_n) \left( 2\sqrt{\pi} |\mu_n| {}_0F_2 \left( ; 1, \frac{3}{2}; \mu_n^2 \right) - {}_0F_2 \left( ; \frac{1}{2}, \frac{1}{2}; \mu_n^2 \right) \right) \quad (\text{A.54b})$$

$$S_3(\mu_n) = -i G_{0,3}^{2,0} \left( \mu_n^2 \mid 0, 1, \frac{1}{2} \right) + 2\epsilon_n \left( |\mu_n| {}_0F_2 \left( ; \frac{1}{2}, \frac{3}{2}; \mu_n^2 \right) - \sqrt{\pi} \mu_n^2 {}_0F_2 \left( ; \frac{3}{2}, 2; \mu_n^2 \right) \right). \quad (\text{A.54c})$$

Just as in appendix A.5, a comparison is made with the expected results. To this end the  $S$  functions are Fourier transformed numerically and compared against the original functions relating to the PDF, see Fig. A.3. This numerical FT was performed by sampling the  $S$  functions on a grid, and integrating using the composite Simpson's rule. In order to accurately resolve the singularity, a very fine mesh around the origin was used. Good agreement is obtained, which suggests that the analytical result is correct.

## A.7 Modified bi-Maxwellian coefficients

The coefficients of the dielectric tensor for a modified bi-Maxwellian on the LFS are given in table A.1. With  $\eta = \frac{B_C}{B} \frac{n\Omega}{\omega}$ ,  $\Lambda = \frac{T_\perp}{T_\parallel} (1 - \eta)$ ,  $\zeta_n = \frac{\omega - n\Omega}{|k_z| v_{T_\parallel}}$ .

### A.7.1 Warm plasma limit LFS

In the limit of  $k_\perp \rightarrow 0$ , the components  $K_0, K_4, K_5$  vanish, but  $K_1, K_2, K_3$  remain. Care must be taken as  $k_\perp$  is present in the pre factors  $Y_l$  too. The lowest order terms are  $n = \pm 1, n = 0$  for

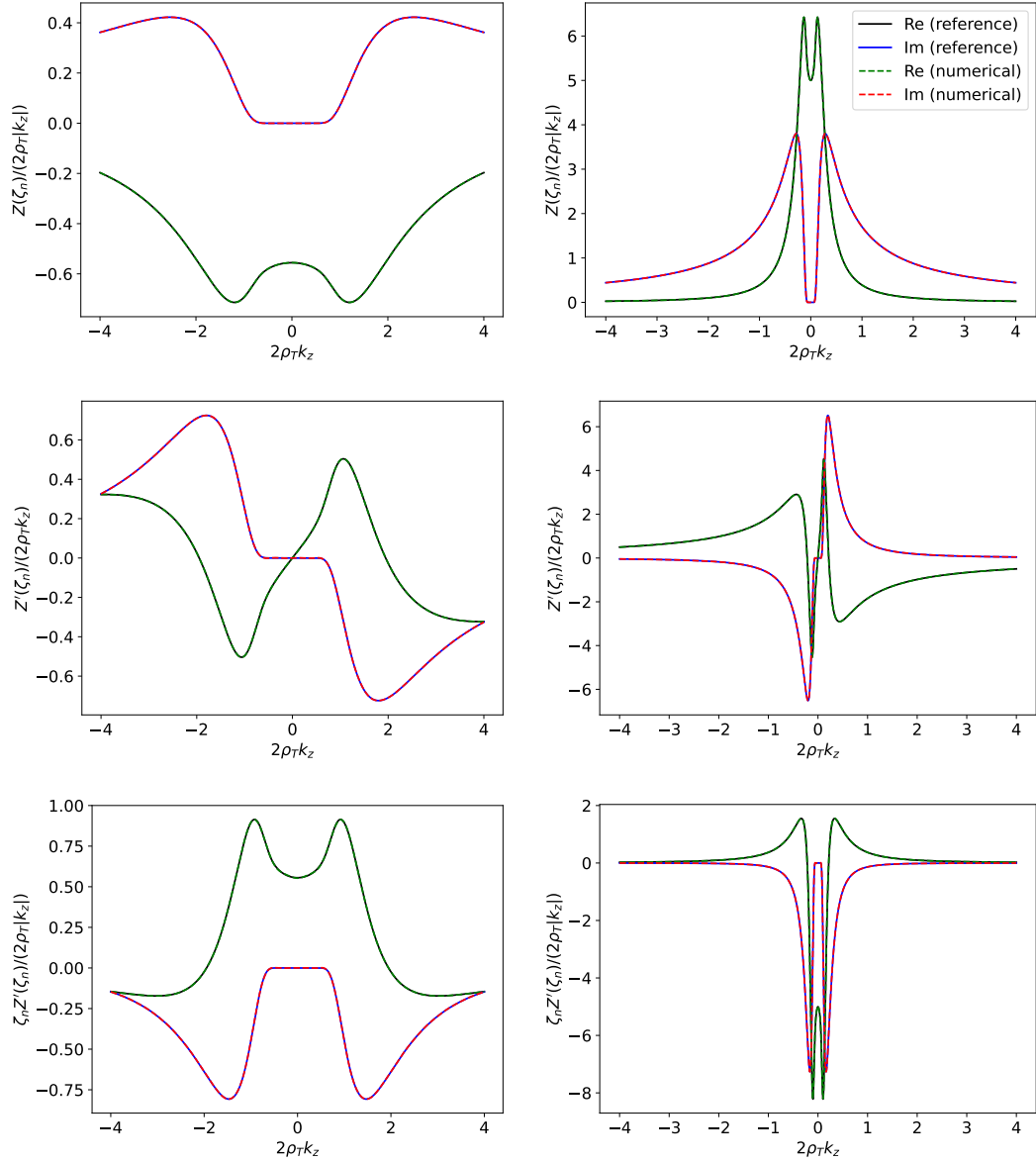


Figure A.3: From top to bottom, the FT of  $S_1$ ,  $S_2$ ,  $S_3$  respectively. The left column used cyclotron harmonic  $n = 0$ , the right one used  $n = 1$ . In addition, a frequency ratio of  $\omega/\Omega = 0.9$  was chosen.

Table A.1: Coefficients from Eq. (4.24).

	$\Upsilon_l$	$\zeta_{l,n}$	$p_{l,0}$	$p_{l,1}$	$q_{l,0}$	$q_{l,1}$	$h_l$
$K_0$	$\frac{4\omega_p^2 \Omega^2 B}{\sqrt{\pi}\omega  k_z  k_\perp^2 v_{T\parallel} v_{T\perp}^2 B_C \mathcal{C}}$	1	$-\frac{B_C}{B} \frac{ k_z  v_{T\parallel}}{\omega}$	$\frac{B_C}{B} \frac{ k_z  v_{T\parallel}}{\omega} \frac{T_\perp}{T_\parallel}$	$\eta$	$\Lambda$	3
$K_1$	$\frac{4\omega_p^2 \Omega^2 B}{\sqrt{\pi}\omega  k_z  k_\perp^2 v_{T\parallel} v_{T\perp}^2 B_C \mathcal{C}}$	$n^2$	$-\frac{B_C}{B} \frac{ k_z  v_{T\parallel}}{\omega}$	$\frac{B_C}{B} \frac{ k_z  v_{T\parallel}}{\omega} \frac{T_\perp}{T_\parallel}$	$\eta$	$\Lambda$	1
$K_2$	$\frac{4i\omega_p^2 \Omega B^{3/2}}{\sqrt{\pi}\omega  k_z  k_\perp v_{T\parallel} v_{T\perp} B_C^{3/2} \mathcal{C}}$	$n$	$-\frac{B_C}{B} \frac{ k_z  v_{T\parallel}}{\omega}$	$\frac{B_C}{B} \frac{ k_z  v_{T\parallel}}{\omega} \frac{T_\perp}{T_\parallel}$	$\eta$	$\Lambda$	2
$K_3$	$\frac{4\omega_p^2 v_{T\parallel} B}{\sqrt{\pi}\omega  k_z  v_{T\parallel}^2 B_C \mathcal{C}}$	$\zeta_n$	$\eta$	$\Lambda$	$\eta \zeta_n$	$\Lambda \zeta_n$	1
$K_4$	$\frac{4\omega_p^2 \Omega B}{\sqrt{\pi}\omega k_z k_\perp v_{T\parallel}^2 B_C \mathcal{C}}$	$n$	$\eta$	$\Lambda$	$\eta \zeta_n$	$\Lambda \zeta_n$	1
$K_5$	$\frac{4i\omega_p^2 B^{3/2}}{\sqrt{\pi}\omega k_z v_{T\parallel} B_C^{3/2} \mathcal{C}}$	1	$\eta$	$\Lambda$	$\eta \zeta_n$	$\Lambda \zeta_n$	2

$K_1, K_2$  and  $K_3$  respectively. The following lowest order approximations are used:

$$J_0^2(ay) \approx 1 \quad (\text{A.55a})$$

$$J_{\pm 1}(ay) J'_{\pm 1}(ay) \approx ay/4 \quad (\text{A.55b})$$

$$J_{\pm 1}^2(ay) \approx a^2 y^2/4. \quad (\text{A.55c})$$

In this limit the integration in Eq. (4.24) can be performed analytically:

$$K_1 = \frac{\omega_p^2}{2\omega |k_z| v_{T\parallel}} \frac{1}{\mathcal{C} C_+} \sum_{n=-1,1} \left[ Z(\zeta_n) + \frac{|k_z| v_{T\parallel}}{\omega} \left( 1 - \frac{T_\perp}{T_\parallel} \right) \frac{1}{C_+} \frac{B_C}{B} \frac{Z'(\zeta_n)}{2} \right. \\ \left. - \sqrt{-s} \frac{|k_z| v_{T\parallel}}{\omega} \frac{T_\perp}{T_\parallel} \frac{1}{C_-} - 2 \frac{s}{C_-} \frac{B_C}{B} Z(\tilde{\zeta}_n) \right] \quad (\text{A.56a})$$

$$+ \frac{|k_z| v_{T\parallel}}{\omega} \sqrt{-s} \frac{1}{C_-} \frac{B_C}{B} \left( 2s \frac{B_C^2}{B^2} \frac{1}{C_+ C_-} + \frac{T_\perp}{T_\parallel} \left( \frac{1}{C_-} + \tilde{\zeta}_n^2 \frac{B_C}{B} \right) \right) Z'(\tilde{\zeta}_n) \Big] \\ K_2 = \frac{i\omega_p^2}{2\omega |k_z| v_{T\parallel}} \frac{1}{\mathcal{C} C_+} \sum_{n=-1,1} n \left[ Z(\zeta_n) + \frac{|k_z| v_{T\parallel}}{\omega} \left( 1 - \frac{T_\perp}{T_\parallel} \right) \frac{1}{C_+} \frac{B_C}{B} \frac{Z'(\zeta_n)}{2} \right. \\ \left. - \sqrt{-s} \frac{|k_z| v_{T\parallel}}{\omega} \frac{T_\perp}{T_\parallel} \frac{1}{C_-} - 2 \frac{s}{C_-} \frac{B_C}{B} Z(\tilde{\zeta}_n) \right] \quad (\text{A.56b})$$

$$+ \frac{|k_z| v_{T\parallel}}{\omega} \sqrt{-s} \frac{1}{C_-} \frac{B_C}{B} \left( 2s \frac{B_C^2}{B^2} \frac{1}{C_+ C_-} + \frac{T_\perp}{T_\parallel} \left( \frac{1}{C_-} + \tilde{\zeta}_n^2 \frac{B_C}{B} \right) \right) Z'(\tilde{\zeta}_n) \Big] \\ K_3 = -\frac{\omega_p^2}{\omega |k_z| v_{T\parallel}} \frac{1}{\mathcal{C} C_+} \zeta_0 \left[ Z'(\zeta_0) - 2 \frac{B_C}{B} \frac{\sqrt{-s}}{C_-} Z'(\tilde{\zeta}_0) \right], \quad (\text{A.56c})$$

with  $\tilde{\zeta}_n = \zeta_n / \sqrt{-s}$  and note that  $C_\pm = \frac{B_C}{B} (1 \pm s)$ , so  $s = \frac{1}{2} \frac{B}{B_C} (C_+ - C_-)$ . This can of course be rewritten in countless ways, given that also the derivatives of the PDF can be written differently. Note, care must be taken if  $C_+ \rightarrow 0$ .

## A.8 Marker distribution coefficients

The coefficients for the dielectric tensor, using the marker distribution function are given below [49].

$$c_{0,j} = -2b_j \frac{v_{\perp,j}}{\sigma_j} \left( 1 - \frac{k_z v_{\parallel,j}}{\omega} \right) J_n(b_j) J'_n(b_j) \quad (\text{A.57a})$$

$$c_{1,j} = 2n^2 \frac{\Omega}{k_{\perp} \sigma_j} \left( 1 - \frac{k_z v_{\parallel,j}}{\omega} \right) J_n(b_j) J'_n(b_j) \quad (\text{A.57b})$$

$$c_{2,j} = i n \frac{v_{\perp,j}}{\sigma_j} \left( 1 - \frac{k_z v_{\parallel,j}}{\omega} \right) \left[ \left( \frac{n^2}{b_j^2} - 1 \right) J_n^2(b_j) + (J'_n(b_j))^2 \right] \quad (\text{A.57c})$$

$$c_{3,j} = 2n \frac{k_{\perp} v_{\parallel,j}^2}{\omega \sigma_j} J_n(b_j) J'_n(b_j) \quad (\text{A.57d})$$

$$c_{4,j} = 2n^2 \frac{\Omega v_{\parallel,j}}{\omega \sigma_j} J_n(b_j) J'_n(b_j) \quad (\text{A.57e})$$

$$c_{5,j} = i n \frac{k_{\perp} v_{\parallel,j} v_{\perp,j}}{\omega \sigma_j} \left[ \left( \frac{n^2}{b_j^2} - 1 \right) J_n^2(b_j) + (J'_n(b_j))^2 \right] \quad (\text{A.57f})$$

$$c_{6,j} = 2n \frac{v_{\parallel,j}}{\sigma_j} \left( 1 - \frac{k_z v_{\parallel,j}}{\omega} \right) J_n(b_j) J'_n(b_j) \quad (\text{A.57g})$$

$$c_{7,j} = i b_j \frac{v_{\parallel,j}}{\sigma_j} \left( 1 - \frac{k_z v_{\parallel,j}}{\omega} \right) \left[ \left( \frac{n^2}{b_j^2} - 1 \right) J_n^2(b_j) + (J'_n(b_j))^2 \right], \quad (\text{A.57h})$$

$$d_{0,j} = 2b_j \frac{|k_z|v_{\perp,j}}{\omega} J_n(b_j) J'_n(b_j) + 2 \frac{v_{\perp,j}^2}{\sigma_j^2} \frac{|k_z|v_{\perp,j}}{\omega} \left[ (J'_n(b_j))^2 - \frac{n^2}{b_j^2} J_n^2(b_j) \right] \quad (\text{A.58a})$$

$$d_{1,j} = -2n^2 \frac{\Omega |k_z|}{\omega k_{\perp}} J_n(b_j) J'_n(b_j) + 2n^2 \frac{\Omega^2 |k_z|v_{\perp,j}}{\omega k_{\perp}^2 \sigma_j^2} J_n^2(b_j) \quad (\text{A.58b})$$

$$d_{2,j} = -in \frac{|k_z|v_{\perp,j}}{\omega} \left[ \left( \frac{n^2}{b_j^2} - 1 \right) J_n^2(b_j) + (J'_n(b_j))^2 \right] + 2in \frac{\Omega |k_z|v_{\perp,j}^2}{\omega k_{\perp} \sigma_j^2} J_n(b_j) J'_n(b_j) \quad (\text{A.58c})$$

$$d_{3,j} = 2 \frac{v_{\perp,j} (\text{sign}(k_z) v_{\parallel,j} + \sigma_j \xi_{n,j})}{\sigma_j^2} \left( 1 - \frac{n\Omega}{\omega} \right) J_n^2(b_j) \quad (\text{A.58d})$$

$$+ 2n \frac{k_{\perp} (2\text{sign}(k_z) v_{\parallel,j} + \sigma_j \xi_{n,j})}{\omega} J_n(b_j) J'_n(b_j) \quad (\text{A.58e})$$

$$d_{4,j} = \text{sign}(k_z) \left( 2n^2 \frac{\Omega}{\omega} J_n(b_j) J'_n(b_j) + 2n \frac{\Omega v_{\perp,j}}{k_{\perp} \sigma_j^2} \left( 1 - \frac{n\Omega}{\omega} \right) J_n^2(b_j) \right) \quad (\text{A.58f})$$

$$d_{5,j} = \text{sign}(k_z) \left( in \frac{k_{\perp} v_{\perp,j}}{\omega} \left[ \left( \frac{n^2}{b_j^2} - 1 \right) J_n^2(b_j) + (J'_n(b_j))^2 \right] \right. \quad (\text{A.58g})$$

$$\left. + 2i \frac{v_{\perp,j}^2}{\sigma_j^2} \left( 1 - \frac{n\Omega}{\omega} \right) J_n(b_j) J'_n(b_j) \right) \quad (\text{A.58h})$$

$$d_{6,j} = 2n \text{sign}(k_z) \left( 1 - \frac{|k_z| (2\text{sign}(k_z) v_{\parallel,j} + \sigma_j \xi_{n,j})}{\omega} \right) J_n(b_j) J'_n(b_j) \quad (\text{A.58i})$$

$$+ 2n \frac{\Omega |k_z| v_{\perp,j} (v_{\parallel,j} + \sigma_j \text{sign}(k_z) \xi_{n,j})}{\omega k_{\perp} \sigma_j^2} J_n^2(b_j) \quad (\text{A.58j})$$

$$d_{7,j} = ib_j \text{sign}(k_z) \left( 1 - \frac{|k_z| (2\text{sign}(k_z) v_{\parallel,j} + \sigma_j \xi_{n,j})}{\omega} \right) \left[ \left( \frac{n^2}{b_j^2} - 1 \right) J_n^2(b_j) + (J'_n(b_j))^2 \right] \quad (\text{A.58k})$$

$$+ 2i \frac{|k_z| v_{\perp,j}^2 (v_{\parallel,j} + \sigma_j \text{sign}(k_z) \xi_{n,j})}{\omega \sigma_j^2} J_n(b_j) J'_n(b_j), \quad (\text{A.58l})$$

with

$$\xi_{n,j} = \frac{\omega - n\Omega - k_z v_{\parallel,j}}{|k_z| \sigma_j} \quad (\text{A.59})$$

$$b_j = \frac{k_{\perp} v_{\perp,j}}{\Omega}. \quad (\text{A.60})$$

The coefficients in Eq. (A.57) and (A.58) can be derived starting from Eq. (4.14), which gives

$$F_{\perp} = \frac{1}{2\pi \sum_j w_j} \sum_j \frac{w_j}{\sqrt{\pi} \sigma_j} \exp \left[ - \left( \frac{v_z - v_{zj}}{\sigma_j} \right)^2 \right] \times \left[ -2 \frac{v_z - v_{zj}}{\sigma_j^2} \frac{k_z v_{\perp}}{\omega} \delta(v_{\perp} - v_{\perp j}) + \left( 1 - \frac{k_z v_z}{\omega} \right) v_{\perp} \frac{d}{dv_{\perp}} \left( \frac{\delta(v_{\perp} - v_{\perp j})}{v_{\perp}} \right) \right] \quad (\text{A.61a})$$

$$F_z = \frac{1}{2\pi \sum_j w_j} \sum_j \frac{w_j}{\sqrt{\pi} \sigma_j} \exp \left[ - \left( \frac{v_z - v_{zj}}{\sigma_j} \right)^2 \right] \times \frac{v_z}{v_\perp} \left[ 2 \frac{v_z - v_{zj}}{\sigma_j^2} \left( \frac{n\Omega}{\omega} - 1 \right) \delta(v_\perp - v_{\perp j}) + \frac{n\Omega}{\omega} v_z \frac{d}{dv_\perp} \left( \frac{\delta(v_\perp - v_{\perp j})}{v_\perp} \right) \right]. \quad (\text{A.61b})$$

Here the density was eliminated using  $N = V^{-1} \sum_j w_j$ . During the derivation the following identity may be used to perform the integral over  $v_\perp$  (using integration by parts):

$$\int_0^\infty dx x f(x) \frac{d}{dx} \left( \frac{\delta(x - x_0)}{x} \right) = - \int_0^\infty dx \frac{\delta(x - x_0)}{x} \frac{d}{dx} (x f(x)) = - \frac{1}{x_0} \frac{d}{dx_0} (x_0 f(x_0)), \quad (\text{A.62})$$

with  $\delta$  the Dirac delta function, and it is assumed that  $0 < x_0 < \infty$ . The second derivative of the Bessel function is eliminated using the Bessel equation itself. Then the integral over parallel velocity is performed, which results in the PDFs.

In the limit  $k_\perp \rightarrow 0$ , the coefficients (A.57), (A.58) reduce to:

$$b_j = c_0 = c_3 = c_4 = c_5 = c_6 = c_7 = d_0 = d_4 = d_5 = d_6 = d_7 = 0 \quad (\text{A.63a})$$

$$c_1 = \frac{v_{\perp,j}}{2\sigma_j} \left( 1 - \frac{k_z v_{z,j}}{\omega} \right) \delta_{(\pm 1),n} \quad (\text{A.63b})$$

$$c_2 = in \frac{v_{\perp,j}}{2\sigma_j} \left( 1 - \frac{k_z v_{z,j}}{\omega} \right) \delta_{(\pm 1),n} = inc_1 \quad (\text{A.63c})$$

$$d_1 = \frac{|k_z| v_{\perp,j}}{2\omega} \left( \frac{v_{\perp,j}^2}{\sigma_j^2} - 1 \right) \delta_{(\pm 1),n} \quad (\text{A.63d})$$

$$d_2 = in \frac{|k_z| v_{\perp,j}}{2\omega} \left( \frac{v_{\perp,j}^2}{\sigma_j^2} - 1 \right) \delta_{(\pm 1),n} = ind_1 \quad (\text{A.63e})$$

$$d_3 = 2 \frac{v_{\perp,j} (\text{sign}(k_z) v_{z,j} + \sigma_j \xi_{n,j})}{\sigma_j^2} \delta_{0,n}. \quad (\text{A.63f})$$

Here  $\delta_{x,y}$  represents the Kronecker delta, so  $\delta_{(\pm 1),n}$  equals 1 if  $n = \pm 1$ , and 0 otherwise.

## A.9 Future ICRH models

Given the rapid growth in compute power, the ICRH models of the future will likely use different algorithms. Enabling a more truthful description of the plasma response, and potentially optimising for things such as mass parallelism and arithmetic intensity to take full advantage of new hardware. Some possible ways forward are described here.

- 1 The assembly matrix of the 1D FEM model in section 3.2 may be dense, but it is data-sparse. Meaning, it can be well approximated by using a hierarchical matrix ( $\mathcal{H}$ -matrix). Such a matrix consists of a hierarchy of low-rank blocks that are more cheaply stored than the full matrix. Matrix multiplication and inversion are significantly sped up when using this format and libraries that implement these techniques are readily available, see section 3.3. However, there are several downsides: There are four degrees of freedom per node for linear FEM (the potentials), so the matrix will probably be need to split up into  $4 \times 4$  blocks where each block can be compressed on its own. Compressing the whole matrix without taking advantage of these sub blocks is likely not very effective. This issue is only exacerbated with a higher order basis, as more DOFs per node means more sub blocks. Also, in 1D the nodes can always be arranged in ascending/descending order, such that the most tightly coupled nodes are adjacent in the solution vector. This results in the relatively smooth decay away from the matrix diagonal. However, in 2D or 3D no such favourable ordering is possible.
- 2 Alternatively, a non-local equation can be solved with FEM while still producing a sparse matrix if the integral kernel is smooth enough and if we are willing to add additional DOFs. Start with a very coarse mesh, where successive refinements are applied: binary/quad/oct-tree (this is not unrelated to approach 1). The potentials on the coarser mesh can be expressed in terms of averages of the level below, and so on until the leaves of the tree. Each of these cell values becomes a DOF. If the finest mesh has  $N$  DOFs, then there are still only  $O(N)$  DOFs in total. The plasma response is non-local, but it can also be binned in a tree structure, and its larger cells only couple to larger cells of the potential mesh. So the assembly matrix will have  $O(1)$  entries per row<sup>2</sup>, meaning  $O(N)$  non-zeros in total, hence it is a sparse matrix. How well this would work in practice has yet to be determined.
- 3 In addition to the EM fields (or potentials), the perturbed distribution function can be considered a DOF itself. Both Maxwell's equations and the Vlasov equation can be solved in the Eulerian frame, so without integrating along the particle trajectories. Given a phase-space grid with  $N_x$  points in configuration space, and  $N_v$  points in velocity space, Maxwell's equations occupy  $O(N_x)$  rows with  $O(N_v)$  non-zeros. And the Vlasov equation occupies  $O(N_x N_v)$  rows with  $O(1)$  non-zeros, meaning  $O(N_x N_v)$  non-zeroes

---

<sup>2</sup>The plasma response will couple to  $O(M)$  DOFs, but  $M$  is purely based on the nature of the background plasma, not the first order quantities of the wave. So  $M$  is independent of  $N$ , therefore the non-zeros are still  $O(1)$  when talking about scaling in terms of  $N$ .



in total. So by adding extra dimensions the matrix becomes sparse again, but at the cost of having significantly more DOFs. One upside is that the matrix entries are easy to compute, and so a matrix-free approach could be used to save memory. However, that would only work well if an iterative solver is used. And it is unclear how well the matrix conditioning is.

- 4 Using the frequency domain is attractive, because the plasma response is a convolution in the time domain (Assuming the Vlasov equation is linearised). However, by abandoning the frequency domain, and going to the time domain the matrix sparsity can be recovered. The plasma response at one time step alone is not sufficient information to predict the plasma current at the next time step. However, the perturbed distribution function is. The way this method would work is by interleaving updates of the potentials (or fields) and the distribution function. Test particles are pushed along the u.p.t. and are binned in cells. Once the charge and current in these cells is known, the potentials are updated<sup>3</sup>. However, modelling waves that move on a grid in the time domain may have issues with numerical instabilities (CFL) and numerical dispersion/dissipation. Also, one has to ensure that all grid elements are sufficiently sampled with particles, which is not trivial since they move around.

---

<sup>3</sup>This is essentially a type of  $\delta f$  particle-in-cell code.



# Acknowledgements

Firstly I would like to thank Hamish Patten for his contribution to the project. Especially early on he was a tremendous help in getting me set up with the code (and learning about the wave/fast ion physics). Without him this work would not be in the state it is today.

Secondly, I would like to thank my parents, who have always supported me, stimulated my curiosity and provided me with the resources to grow.

I also appreciate the many discussions I have had with my supervisor, Jonathan Graves. At some point you realise you have been staring at some maths for far too long, and it helps to brainstorm with someone with a different point of view. I appreciate that I did not have to sugar-coat anything; I could always speak freely, even when it comes to poking fun at the British.

I also treasure the many discussions with others: Stephan Brunner, Cristian Sommariva and Eduardo Neto. I remember our exchanges about Fokker-Planck equations, particle in cell simulations, flux coordinates and much more.

Lastly, a special thanks the SPC community. Outside of work we did many other activities which truly made this a lively place. This includes hiking, cycling, swimming, barbecuing, gaming (tabletop and/or digital), and of course grabbing a pint in the pub every now and then.



## Bibliography

- [1] J. Wesson, *Tokamaks* (Oxford science publications), 3rd ed. Oxford : New York: Clarendon Press ; Oxford University Press, 2004.
- [2] S. Coda, T. P. Goodman, M. A. Henderson, *et al.*, “High-power ECH and fully non-inductive operation with ECCD in the TCV tokamak”, *Plasma Physics and Controlled Fusion*, vol. 42, no. 12B, B311–B321, Dec. 2000. DOI: 10.1088/0741-3335/42/12B/323.
- [3] J. P. Freidberg, *Plasma physics and fusion energy*. Cambridge: Cambridge University Press, 2007.
- [4] Y. Xu, “A general comparison between tokamak and stellarator plasmas”, *Matter and Radiation at Extremes*, vol. 1, no. 4, pp. 192–200, Jul. 2016. DOI: 10.1016/j.mre.2016.07.001.
- [5] P. Helander, C. D. Beidler, T. M. Bird, *et al.*, “Stellarator and tokamak plasmas: A comparison”, *Plasma Physics and Controlled Fusion*, vol. 54, no. 12, p. 124 009, Dec. 2012. DOI: 10.1088/0741-3335/54/12/124009.
- [6] S. Gori, W. Lotz, and J. Nührenberg, “Quasi-isodynamic stellarators”, in *Theory of Fusion Plasmas Conference Proceedings*, Varenna (Italy): Editrice Compositori, 1996, pp. 335–342.
- [7] C. Beidler, G. Grieger, F. Herrnegger, *et al.*, “Physics and engineering design for Wendelstein VII-X”, *Fusion Technology*, vol. 17, no. 1, pp. 148–168, Jan. 1990. DOI: 10.13182/FST90-A29178.
- [8] J. Nührenberg, W. Lotz, P. Merkel, *et al.*, “Overview on Wendelstein 7-X theory”, *Fusion Technology*, vol. 27, no. 3T, pp. 71–78, Apr. 1995. DOI: 10.13182/FST95-A11947048.
- [9] M. Drevlak, J. Geiger, P. Helander, and Y. Turkin, “Fast particle confinement with optimized coil currents in the W7-X stellarator”, *Nuclear Fusion*, vol. 54, no. 7, 2014. DOI: 10.1088/0029-5515/54/7/073002.
- [10] J. Faustin, W. Cooper, J. Graves, D. Pfefferlé, and J. Geiger, “Fast particle loss channels in Wendelstein 7-X”, *Nuclear Fusion*, vol. 56, no. 9, p. 092 006, Sep. 2016. DOI: 10.1088/0029-5515/56/9/092006.
- [11] B.-n. Jiang, J. Wu, and L. Povinelli, “The origin of spurious solutions in computational electromagnetics”, *Journal of Computational Physics*, vol. 125, no. 1, pp. 104–123, Apr. 1996. DOI: 10.1006/jcph.1996.0082.

## Bibliography

---

- [12] E. Jaeger, D. Batchelor, M. Carter, and H. Weitzner, “Global ICRF wave propagation in edge plasma and Faraday shield regions”, *Nuclear Fusion*, vol. 30, no. 3, pp. 505–519, Mar. 1990. DOI: 10.1088/0029-5515/30/3/012.
- [13] L. Villard, K. Appert, R. Gruber, and J. Vaclavik, “Global waves in cold plasmas”, *Computer Physics Reports*, vol. 4, no. 3–4, pp. 95–135, Aug. 1986. DOI: 10.1016/0167-7977(86)90027-4.
- [14] O. Sauter and J. Vaclavik, “Gyrokinetic approach to the propagation of electromagnetic waves in nonuniform bounded plasma slabs”, *Computer Physics Communications*, vol. 84, no. 1–3, pp. 226–242, Nov. 1994. DOI: 10.1016/0010-4655(94)90213-5.
- [15] A. Jaun, K. Appert, J. Vaclavik, and L. Villard, “Global waves in resistive and hot tokamak plasmas”, *Computer Physics Communications*, vol. 92, no. 2–3, pp. 153–187, Dec. 1995. DOI: 10.1016/0010-4655(95)00105-6.
- [16] P. Popovitch, “Low frequency electromagnetic wave propagation in 3D plasma configurations”, Ph.D. dissertation, EPFL, Lausanne, 2004, p. 152. DOI: 10.5075/epfl-thesis-3063.
- [17] P. Popovich, W. Cooper, and L. Villard, “A full-wave solver of the maxwell’s equations in 3D cold plasmas”, *Computer Physics Communications*, vol. 175, no. 4, pp. 250–263, Aug. 2006. DOI: 10.1016/j.cpc.2006.04.001.
- [18] P. Monk, *Finite element methods for Maxwell’s equations* (Numerical mathematics and scientific computation). Oxford : New York: Clarendon Press ; Oxford University Press, 2003.
- [19] D. G. Swanson, *Plasma waves* (Series in plasma physics), 2nd ed. Bristol ; Philadelphia: Institute of Physics Pub, 2003.
- [20] M. Machielsen, J. Rubin, and J. Graves, “Exact expression for the hot plasma conductivity kernel in configuration space”, *Fundamental Plasma Physics*, p. 100 008, Jan. 2023. DOI: 10.1016/j.fpp.2023.100008.
- [21] T. H. Stix, *Waves in plasmas*. New York: American Institute of Physics, 1992.
- [22] M. Brambilla, *Kinetic theory of plasma waves: homogeneous plasmas* (The International series of monographs on physics). Oxford ; New York: Clarendon Press, 1998.
- [23] P. Hunana, A. Tenerani, G. P. Zank, *et al.*, “An introductory guide to fluid models with anisotropic temperatures. part 2. kinetic theory, Padé approximants and Landau fluid closures”, *Journal of Plasma Physics*, vol. 85, no. 6, p. 205 850 603, Dec. 2019. DOI: 10.1017/S0022377819000850.
- [24] S. Bingren, “Southwestern institute of physics: Annual report 1998”, China, Tech. Rep. 7-5022-2032–1, 1999, CNIC–01376, pp. 72–74.
- [25] R. V. Nieuwenhove, R. Koch, G. V. Oost, *et al.*, “Comparison of the performance of ICRF antennas with and without faraday shield on TEXTOR”, *Nuclear Fusion*, vol. 32, no. 11, pp. 1913–1925, Nov. 1992. DOI: 10.1088/0029-5515/32/11/I03.

- 
- [26] A. Messiaen and R. Weynants, “Design of ICRH launching structures: Antenna and waveguide”, in *Heating in Toroidal Plasmas 1982*. Elsevier, 1982, pp. 1107–1116. DOI: 10.1016/B978-1-4832-8428-6.50132-6.
  - [27] Y. Kazakov, D. V. Eester, R. Dumont, and J. Ongena, “On resonant ICRF absorption in three-ion component plasmas: A new promising tool for fast ion generation”, *Nuclear Fusion*, vol. 55, no. 3, p. 032 001, Feb. 2015. DOI: 10.1088/0029-5515/55/3/032001.
  - [28] Y. O. Kazakov, J. Ongena, J. C. Wright, *et al.*, “Efficient generation of energetic ions in multi-ion plasmas by radio-frequency heating”, *Nature Physics*, vol. 13, no. 10, pp. 973–978, 2017. DOI: 10.1038/nphys4167.
  - [29] A. V. Krasilnikov, D. Van Eester, E. Lerche, *et al.*, “Fundamental ion cyclotron resonance heating of JET deuterium plasmas”, *Plasma Physics and Controlled Fusion*, vol. 51, no. 4, p. 044 005, Apr. 2009. DOI: 10.1088/0741-3335/51/4/044005.
  - [30] E. Lerche, D. Van Eester, A. Krasilnikov, J. Ongena, and P. Lamalle, “Modelling of D majority ICRH at JET: Impact of absorption at the Doppler-shifted resonance”, *Plasma Physics and Controlled Fusion*, vol. 51, no. 4, p. 044 006, Apr. 2009. DOI: 10.1088/0741-3335/51/4/044006.
  - [31] J. Joly, J. Garcia, F. Imbeaux, *et al.*, “Self-consistent modelling of heating synergy between NBI and ICRH in JET deuterium plasmas”, *Plasma Physics and Controlled Fusion*, vol. 61, no. 7, p. 075 017, Jul. 2019. DOI: 10.1088/1361-6587/ab1f54.
  - [32] H. W. Patten, J. P. Graves, W. A. Cooper, J. Eriksson, and D. Pfefferlé, “Identification of an optimized heating and fast ion generation scheme for the wendelstein 7-x stellarator”, *Phys. Rev. Lett.*, vol. 124, p. 155 001, 15 Apr. 2020. DOI: 10.1103/PhysRevLett.124.155001.
  - [33] J. Ongena, Y. O. Kazakov, Y. Baranov, *et al.*, “Synergetic heating of D-NBI ions in the vicinity of the mode conversion layer in H-D plasmas in JET with the ITER like wall.”, in *EPJ Web of Conferences*, vol. 157, 2017, pp. 1–7. DOI: 10.1051/epjconf/201715702006.
  - [34] K. K. Kirov, Y. Kazakov, M. Nocente, *et al.*, “Synergistic ICRH and NBI heating for fast ion generation and maximising fusion rate in mixed plasmas at JET”, in *AIP Conference Proceedings*, vol. 2254, 2020, p. 030 011. DOI: 10.1063/5.0014235.
  - [35] M. Jucker, “Self-consistent ICRH distribution functions and equilibria in magnetically confined plasmas”, Ph.D. dissertation, EPFL, Lausanne, 2010. DOI: 10.5075/epfl-thesis-4912.
  - [36] R. Dumont, “Variational approach to radiofrequency waves in magnetic fusion devices”, *Nuclear Fusion*, vol. 49, no. 7, p. 075 033, Jul. 2009. DOI: 10.1088/0029-5515/49/7/075033.
  - [37] E. F. Jaeger, L. A. Berry, E. D’Azevedo, *et al.*, “Advances in full-wave modeling of radio frequency heated, multidimensional plasmas”, *Physics of Plasmas*, vol. 9, no. 5, pp. 1873–1881, 2002. DOI: 10.1063/1.1455001.
  - [38] M. Jucker, J. Graves, W. Cooper, N. Mellet, T. Johnson, and S. Brunner, “Integrated modeling for ion cyclotron resonant heating in toroidal systems”, *Computer Physics Communications*, vol. 182, no. 4, pp. 912–925, Apr. 2011. DOI: 10.1016/j.cpc.2010.12.028.

## Bibliography

---

- [39] W. A. Cooper, S. P. Hirshman, P. Merkel, *et al.*, “Three-dimensional anisotropic pressure free boundary equilibria”, *Computer Physics Communications*, vol. 180, no. 9, pp. 1524–1533, 2009. DOI: 10.1016/j.cpc.2009.04.006.
- [40] D. Pfefferlé, W. Cooper, J. Graves, and C. Misev, “VENUS-LEVIS and its spline-fourier interpolation of 3D toroidal magnetic field representation for guiding-centre and full-orbit simulations of charged energetic particles”, *Computer Physics Communications*, vol. 185, no. 12, pp. 3127–3140, Dec. 2014. DOI: 10.1016/j.cpc.2014.08.007.
- [41] E. F. Jaeger, L. A. Berry, S. D. Ahern, *et al.*, “Self-consistent full-wave and Fokker-Planck calculations for ion cyclotron heating in non-Maxwellian plasmas”, *Physics of Plasmas*, vol. 13, no. 5, p. 056 101, May 2006. DOI: 10.1063/1.2173629.
- [42] R. Bilato, M. Brambilla, O. Maj, L. Horton, C. Maggi, and J. Stober, “Simulations of combined neutral beam injection and ion cyclotron heating with the TORIC-SSFPQL package”, *Nuclear Fusion*, vol. 51, no. 10, p. 103 034, Oct. 2011. DOI: 10.1088/0029-5515/51/10/103034.
- [43] J. Hedin, “Ion cyclotron resonance heating in toroidal plasmas”, Ph.D. dissertation, Alfvén Laboratory, Stockholm, 2001.
- [44] W. Hackbusch, *Hierarchical Matrices: Algorithms and Analysis* (Springer Series in Computational Mathematics). Berlin, Heidelberg: Springer Berlin Heidelberg, 2015, vol. 49. DOI: 10.1007/978-3-662-47324-5.
- [45] S. Massei, L. Robol, and D. Kressner, “Hm-toolbox: MATLAB software for HODLR and HSS matrices”, *SIAM Journal on Scientific Computing*, vol. 42, no. 2, pp. C43–C68, Jan. 2020. DOI: 10.1137/19M1288048.
- [46] PlatinumMike, *Platinummike/hotpk: Hotpk*, version v0.03, Oct. 2022. DOI: 10.5281/zenodo.7257874.
- [47] N. Mellet, “Propagation and absorption of low frequency waves in two and three dimensional warm plasmas”, p. 125, 2009. DOI: 10.5075/epfl-thesis-4398.
- [48] H. W. Patten, “Development and optimisation of advanced auxiliary ion heating schemes for 3D fusion plasma devices”, Ph.D. dissertation, EPFL, 2019.
- [49] M. Machielsen, J. P. Graves, and W. A. Cooper, “ICRF modelling in 2D and 3D magnetic configurations using a hot plasma model”, *Plasma Physics and Controlled Fusion*, vol. 63, no. 9, p. 094 002, Sep. 2021. DOI: 10.1088/1361-6587/ac11b2.
- [50] R. O. Dendy, R. J. Hastie, K. G. McClements, and T. J. Martin, “A model for ideal  $m=1$  internal kink stabilization by minority ion cyclotron resonant heating”, *Physics of Plasmas*, vol. 2, no. 5, pp. 1623–1636, 1995. DOI: 10.1063/1.871457.
- [51] W. Cooper, J. Graves, S. Hirshman, *et al.*, “Anisotropic pressure bi-maxwellian distribution function model for three-dimensional equilibria”, *Nuclear Fusion*, vol. 46, no. 7, pp. 683–698, May 2006. DOI: 10.1088/0029-5515/46/7/001.



- 
- [52] J. P. Graves, W. A. Cooper, S. Coda, L.-G. Eriksson, T. Johnson, and J.-E. Contributors, “Modelling ICCD experiments for sawtooth control in JET”, in *AIP Conference Proceedings*, vol. 871, Varenna (Italy): AIP, 2006, pp. 350–355. DOI: 10.1063/1.2404569.
- [53] G. D. Kerbel and M. G. McCoy, “Kinetic theory and simulation of multispecies plasmas in tokamaks excited with electromagnetic waves in the ion-cyclotron range of frequencies”, *Physics of Fluids*, vol. 28, no. 12, pp. 3629–3653, 1985. DOI: 10.1063/1.865319.
- [54] R. Harvey, M. McCoy, G. Kerbel, and S. Chiu, “ICRF fusion reactivity enhancement in tokamaks”, *Nuclear Fusion*, vol. 26, no. 1, pp. 43–49, Jan. 1986. DOI: 10.1088/0029-5515/26/1/004.
- [55] C. S. Chang and P. Colestock, “Anisotropic distribution function of minority tail ions generated by strong ion-cyclotron resonance heating”, *Physics of Fluids B: Plasma Physics*, vol. 2, no. 2, pp. 310–317, Jan. 1990, Citation Key: Chang1990. DOI: 10.1063/1.859319.
- [56] J. M. P. Faustin, “Self-consistent interaction of fast particles and ICRF waves in 3D applications of fusion plasma devices”, Ph.D. dissertation, Lausanne, EPFL, Jan. 2017. DOI: 10.5075/epfl-thesis-7283.
- [57] M.-L. Mayoral, P. Lamalle, D. V. Eester, *et al.*, “Hydrogen plasmas with ICRF inverted minority and mode conversion heating regimes in the JET tokamak”, *Nuclear Fusion*, vol. 46, no. 7, S550–S563, Jun. 2006. DOI: 10.1088/0029-5515/46/7/s14.
- [58] P. Lamalle, M. Mantsinen, J.-M. Noterdaeme, *et al.*, “Expanding the operating space of ICRF on JET with a view to ITER”, *Nuclear Fusion*, vol. 46, no. 2, pp. 391–400, Feb. 2006. DOI: 10.1088/0029-5515/46/2/021.
- [59] D. Gallart, M. J. Mantsinen, J. Manyer, *et al.*, “Prediction of ICRF minority heating schemes for JET D–T experiments”, *Plasma Physics and Controlled Fusion*, vol. 64, no. 12, p. 125 006, Dec. 2022. DOI: 10.1088/1361-6587/ac9925.
- [60] M. Machielsen, J. P. Graves, H. W. Patten, C. Slaby, and S. Lazerson, “Fast ion generation by combined RF-NBI heating in W7-X”, *Accepted by journal of plasma physics*, 2023. DOI: 10.1017/S0022377823000302.
- [61] M. Albergante, “Interaction between fast ions and microturbulence in thermonuclear devices theory and modelling”, Ph.D. dissertation, EPFL, Lausanne, 2011, p. 166. DOI: 10.5075/epfl-thesis-5164.
- [62] D. Pfefferlé, “Energetic ion dynamics and confinement in 3D saturated MHD configurations”, Ph.D. dissertation, Lausanne, EPFL, May 2015. DOI: 10.5075/epfl-thesis-6561.
- [63] S. Suzuki, T. Shirai, M. Nemoto, *et al.*, “Attenuation of high-energy neutral hydrogen beams in high-density plasmas”, *Plasma Physics and Controlled Fusion*, vol. 40, no. 12, pp. 2097–2111, Dec. 1998. DOI: 10.1088/0741-3335/40/12/009.

## Bibliography

---

- [64] N. Rust, B. Heinemann, B. Mendelevitch, A. Peacock, and M. Smirnow, “W7-X neutral-beam-injection: Selection of the NBI source positions for experiment start-up”, *Fusion Engineering and Design*, vol. 86, no. 6–8, pp. 728–731, 2011. DOI: 10.1016/j.fusengdes.2011.03.054.
- [65] S. A. Lazerson, O. P. Ford, C. Nuehrenberg, *et al.*, “Validation of the BEAMS3D neutral beam deposition model on Wendelstein 7-X”, *Nuclear Fusion*, vol. 60, no. 7, p. 076 020, Jul. 2020. DOI: 10.1088/1741-4326/ab8e61.
- [66] A. H. Boozer and G. Kuo-Petravic, “Monte Carlo evaluation of transport coefficients”, *The Physics of Fluids*, vol. 24, no. 5, pp. 851–859, 1981. DOI: 10.1063/1.863445.
- [67] L.-G. Eriksson and P. Helander, “Monte Carlo operators for orbit-averaged Fokker–Planck equations”, *Physics of Plasmas*, vol. 1, no. 2, pp. 308–314, Feb. 1994. DOI: 10.1063/1.870832.
- [68] E. Hirvijoki and T. Kurki-Suonio, “Monte carlo diffusion operator for anomalous radial transport in tokamaks”, *EPL (Europhysics Letters)*, vol. 97, no. 5, p. 55 002, Mar. 2012. DOI: 10.1209/0295-5075/97/55002.
- [69] C. F. Kennel and F. Engelmann, “Velocity space diffusion from weak plasma turbulence in a magnetic field”, *Physics of Fluids*, vol. 9, no. 12, p. 2377, 1966. DOI: 10.1063/1.1761629.
- [70] H. Okada, K. Murakami, Y. Jinno, *et al.*, “Fast ion generation by combination heating of ICRF and NBI in Heliotron J”, 2016.
- [71] J. M. Faustin, W. A. Cooper, J. P. Graves, D. Pfefferlé, and J. Geiger, “ICRH induced particle losses in Wendelstein 7-X”, *Plasma Physics and Controlled Fusion*, vol. 58, no. 7, p. 074 004, Jul. 2016. DOI: 10.1088/0741-3335/58/7/074004.
- [72] J. Ongena, A. Messiaen, Y. Kazakov, *et al.*, “The ICRH system for the stellarator Wendelstein 7-X”, 2020, p. 070 003. DOI: 10.1063/5.0014264.
- [73] Y. I. Kolesnichenko, V. V. Lutsenko, A. V. Tykhyy, *et al.*, “Effects of the radial electric field on the confinement of trapped fast ions in the Wendelstein 7-X and Helias reactor”, *Physics of Plasmas*, vol. 13, no. 7, p. 072 504, Jul. 2006. DOI: 10.1063/1.2210927.
- [74] D. G. Swanson, “Radio frequency heating in the ion-cyclotron range of frequencies”, *Physics of Fluids*, vol. 28, no. 9, pp. 2645–2677, Sep. 1985. DOI: 10.1063/1.865224.
- [75] C. Schuster, T. Johnson, G. Papp, *et al.*, “Moment-preserving and mesh-adaptive reweighting method for rare-event sampling in Monte-Carlo algorithms”, *Computer Physics Communications*, vol. 267, p. 108 041, Oct. 2021. DOI: 10.1016/j.cpc.2021.108041.
- [76] B. D. Fried and S. D. Conte, *The plasma dispersion function: the Hilbert transform of the Gaussian*. Academic Press, 1961.
- [77] C. Zhou, L. Yang, Y. Liu, and Z. Yang, “A novel method for computing the hilbert transform with haar multiresolution approximation”, *Journal of Computational and Applied Mathematics*, vol. 223, no. 2, pp. 585–597, Jan. 2009. DOI: 10.1016/j.cam.2008.02.006.

- [78] S. D. Baalrud, “The incomplete plasma dispersion function: Properties and application to waves in bounded plasmas”, *Physics of Plasmas*, vol. 20, no. 1, p. 012 118, 2013. DOI: 10.1063/1.4789387.
- [79] I. Gradshteyn and I. Ryzhik, *Table of Integrals, Series, and Products (7th edition)*. Academic Press, 2007.



# MIKE MACHIELSEN

Lausanne, Switzerland

[Mike.machielsen@epfl.ch](mailto:Mike.machielsen@epfl.ch) · [linkedin.com/in/mikemachielsen/](https://linkedin.com/in/mikemachielsen/)  
[orcid.org/0000-0003-2230-9896](https://orcid.org/0000-0003-2230-9896) · [github.com/PlatinumMike](https://github.com/PlatinumMike)

---

My main interest is in computation physics. As long as it's related to physics and it involves coding, I'm game. I am also enthusiastic about supercomputing. The massive increase in performance over the last decades has enabled lots of advances in STEM, but many more are still to come.

## EXPERIENCE

DEC 2018 – MAR 2023

**PHD STUDENT, EPFL**

Research on the topic of fast ions in fusion plasmas. These can be generated using particle beams and radio frequency waves, with the aim of mimicking fusion alphas. This involved a combination of particle orbit modelling, solving Maxwell's equations and computing magnetic equilibria.

## EDUCATION

AUG 2018

**MASTER DEGREE, TU/E**

Double degree, studied fluid dynamics and nuclear fusion program. The latter is what inspired me to pursue a PhD in fusion.

JUL 2015

**BACHELOR DEGREE, TU/E**

Applied physics.

## SKILLS

- Excellent English proficiency
- Solid physics background
- Well organised
- Good coding proficiency
- Comfortable using command line interface
- Using HPC on and off since 2015

## MISC

During my time at EPFL, I was a teaching assistant for numerical physics and mathematical methods for physicists. I also supervised two student semester projects. I also worked on Particle simulations, Monte Carlo, Maxwell equations, FEM, magnetic equilibrium (plasma), Vlasov equation and radio waves in plasma. Coding experience: python, C++, MATLAB, Mathematica, Fortran. And some experience with HDF5, make, CMake, OpenMP and MPI.